THE STRESS-STRAIN BEHAVIOUR OF SOILS CONTAINING GAS BUBBLES

A thesis submitted to

The University of Oxford

by

Simon Jonathan Wheeler M.A.

Balliol College

for

The Degree of Doctor of Philosophy

Hilary 1986

The Stress-Strain Behaviour Of Soils Containing Gas Bubbles

by

S.J. Wheeler

Balliol College

A thesis submitted to the University of Oxford
for the degree of Doctor of Philosophy

Hilary 1986

ABSTRACT

The stress-strain behaviour of unsaturated soils containing discrete bubbles of gas has been studied in a programme of experimental and theoretical research.

The research is of particular relevance to the offshore environment, where bubbles of methane, nitrogen and carbon dioxide are formed within the seabed by the decomposition of organic matter. The presence of these gas bubbles can have a major influence on the engineering properties of the soil. As gas bubbles in marine sediments are typically much larger than the normal void spaces, the bubbles cannot be considered as simply changing the compressibility of the pore fluid.

Chapters 2 to 4 describe a series of undrained triaxial tests on reconstituted samples of clayey silt from an estuarine site. Bubbles of methane were formed within the soil by using a chemical technique. The test results provide evidence of the effect of gas bubbles on the undrained shear strength, together with useful information on the stress-strain behaviour prior to failure, the generation of pore pressures during shearing, the elastic moduli and the isotropic consolidation behaviour.

A theoretical model for soils containing large gas bubbles is developed in Chapter 5. The model consists of spherical bubble cavities surrounded by a matrix of saturated soil. In the following three chapters various aspects of the soil behaviour are examined by analysing the theoretical model. Chapter 6 covers the elastic moduli, Chapter 7 the consolidation behaviour and Chapter 8 the undrained shear strength.

In Chapter 9 the predictions of the theoretical model are compared with the experimental results. The agreement between theory and experiment is excellent, suggesting that the theoretical approach developed and analysed in Chapters 5 to 8 is a reasonable model for the behaviour of soils containing large gas bubbles.

ACKNOWLEDGEMENTS

I am indebted to my supervisor Dr Gilliane Sills, who stimulated my interest in this field of study and provided help and encouragement throughout the research.

I would also like to thank the other members of the soil mechanics group at Oxford for the advice and discussion which created such a stimulating environment for research.

Invaluable assistance was provided by the technical support staff of the soil mechanics group, particularly Mr Robert Sawala who devoted such care and attention to the fabrication of the modified triaxial cells.

The financial support of SERC and McClelland Engineers is gratefully acknowledged, with special thanks to Dr R. Semple of McClelland Engineers for his interest in the research.

I am grateful to Miss Heather Stewart for typing the thesis, and Mrs Mina Tedford for preparing the diagrams.

Finally, I would like to thank my many friends at Holywell Manor, who are now scattered throughout the world. It was their presence which made the three years that I spent at Oxford such an enjoyable and educational period of my life.

CONTENTS

NOTATION

a	bubble radius
A	cross-sectional area of sample
B_o, B_1, B_2	constants in Gurson's yield curve
c'	cohesion intercept
C_t, C_m, D_t, D_m	compression indices for unsaturated soil
C_u	undrained shear strength
$(C_u)_{sat}$	undrained shear strength of saturated soil
c_v	consolidation coefficient
d	soil particle size, also water depth
e	void ratio
e_m	void ratio of matrix
f	volume fraction of bubbles
f_c	value of f at which q_y falls to zero
F	deviator force, also surface tension force
F_t	total surface tension force across a plane
F_v	vertical component of surface tension force
G, K	shear and bulk moduli
G', K', ν'	elastic moduli of soil skeleton within matrix
G_d, K_d	drained shear and bulk moduli of soil
G_m, K_m	undrained shear and bulk moduli of matrix
G_s	specific gravity of soil particles
G_{sat}	shear modulus of saturated soil
G_u, K_u	undrained shear and bulk moduli of soil
G_{ui}, K_{ui}	instantaneous undrained shear and bulk moduli of soil
$G_{u\ell}$, $K_{u\ell}$	long-term undrained shear and bulk moduli of soil
G_u^*	undrained shear modulus with no localised consolidation
G_1, K_1, ν_1	elastic moduli of spherical inclusions
G_2, K_2, ν_2	elastic moduli of matrix

h	half-height of sample
H	solubility coefficient
I_1, I_2, I_3	stress invariants
K_g	bulk modulus of gas
K_g^*	apparent long-term bulk modulus of gas
K_w	bulk modulus of water
L	length of meniscus arc
m_1, m_2	mass of gas within bubbles 1 and 2
p	mean total stress
p'	mean effective stress
p_*, p'_*, q_*	local values of p, p' and q within matrix
p_a	atmospheric pressure
$(p')_{av}$	average value of p' within matrix
p'_{ff}	failure value of p' within matrix following flooding
q	deviator stress
r	distance from nearest bubble centre
R	radius of curvature of menisci, also radius of thick-walled shell
R_a	gas constant
R_c	minimum radius of curvature of menisci
S	degree of saturation
S_c	critical initial degree of saturation correpsonding to $S_f = 1$
t	time
T	surface tension
T_a	absolute temperature
T_v	dimensionless time factor
u	pore pressure
u_g	pore gas pressure
u_w	pore water pressure

V_g	volume of gas
V_g^*	gas volume if all the gas was out of solution
V_w	volume of water
V_1, V_2	volume of bubbles 1 and 2
w	water content
z	coordinate axis, also depth below sea-bed
α	angle defining position of plane, also factor in Green's yield curve
β	angle of section of plane, also factor in Green's yield curve
γ_w	unit weight of water
Γ	intercept of critical state line in $v : \log_e p'$ space
Δ	small increment in any variable
ε_1, ε_3	axial and lateral strain
ε_v	volumetric strain
θ	angle subtended by meniscus arc, also angle in polar coordinate system
κ	slope of swelling line in $v : \log_e p'$ space
λ	slope of critical state line and normal consolidation line in $v : \log_e p'$ space
M	slope of critical state line in $q : p'$ space
N	intercept of normal consolidation line in $v : \log_e p'$ space
σ	total stress
σ'	effective stress
σ_1, σ_3	major and minor principal stresses
σ_r	local radial stress within matrix
σ_t	equivalent tensile stress for surface tension forces
σ_v	vertical stress
σ_y	yield stress of matrix
σ_θ	local hoop stress within matrix
τ	shear stress or shear strength

ϕ'	friction angle
ϕ^b	friction angle with respect to changes in $(u_g - u_w)$
χ	factor in Bishop's effective stress equation

Subscripts

f	conditions at failure
o	conditions at the start of shearing (after consolidation)
y	conditions at yield

CHAPTER 1

INTRODUCTION

1.1 Unsaturated soils

1.2 Gas in marine soils

1.3 Previous work on unsaturated soils

- 1.3.1 Effective stress for unsaturated soils
- 1.3.2 An alternative to the single effective stress approach
- 1.3.3 Laboratory testing

1.4 Work at Oxford on soils containing gas bubbles

1.5 Objectives of the work described in this thesis

CHAPTER 1

INTRODUCTION

1.1 UNSATURATED SOILS

Classical soil mechanics has been concerned chiefly with soil in which the voids are completely filled with water. However there are many examples of real soils that are not fully saturated, the voids being filled partly with water and partly with gas. These soils are referred to as "unsaturated" or "partly saturated". (The former term is preferred in this thesis, because the word "saturated" implies an absolute condition; a soil is either saturated or it is not, it cannot be partly saturated.) The behaviour of unsaturated soils is likely to differ significantly from that of saturated soils.

The relative quantities of water and gas within an unsaturated soil can be specified by the degree of saturation S, which is the fraction of the total void volume that is taken up by water. S varies from zero for a dry soil to 1 for a saturated soil.

During the last 30 years considerable effort has been expended on the study of unsaturated soils, in an attempt to understand their behaviour. However, progress has been hampered by the fact that the basic structure of unsaturated soils varies considerably; each type of structure resulting in a different pattern of soil behaviour. Figure 1.1 shows three broad classifications of unsaturated soil. For soils with a low degree of saturation the gas phase is continuous but the water, forming menisci at the grain contacts, is discontinuous (Figure 1.1(a)). At intermediate saturation levels both water and gas are continuous (Figure 1.1(b)). Finally, at a high degree of saturation the water is continuous but the gas, in the form of discrete bubbles, is discontinuous (Figure 1.1(c)). The three different types of unsaturated soil illustrated in Figure 1.1 are likely to behave very differently (Wroth and Houlsby, 1985).

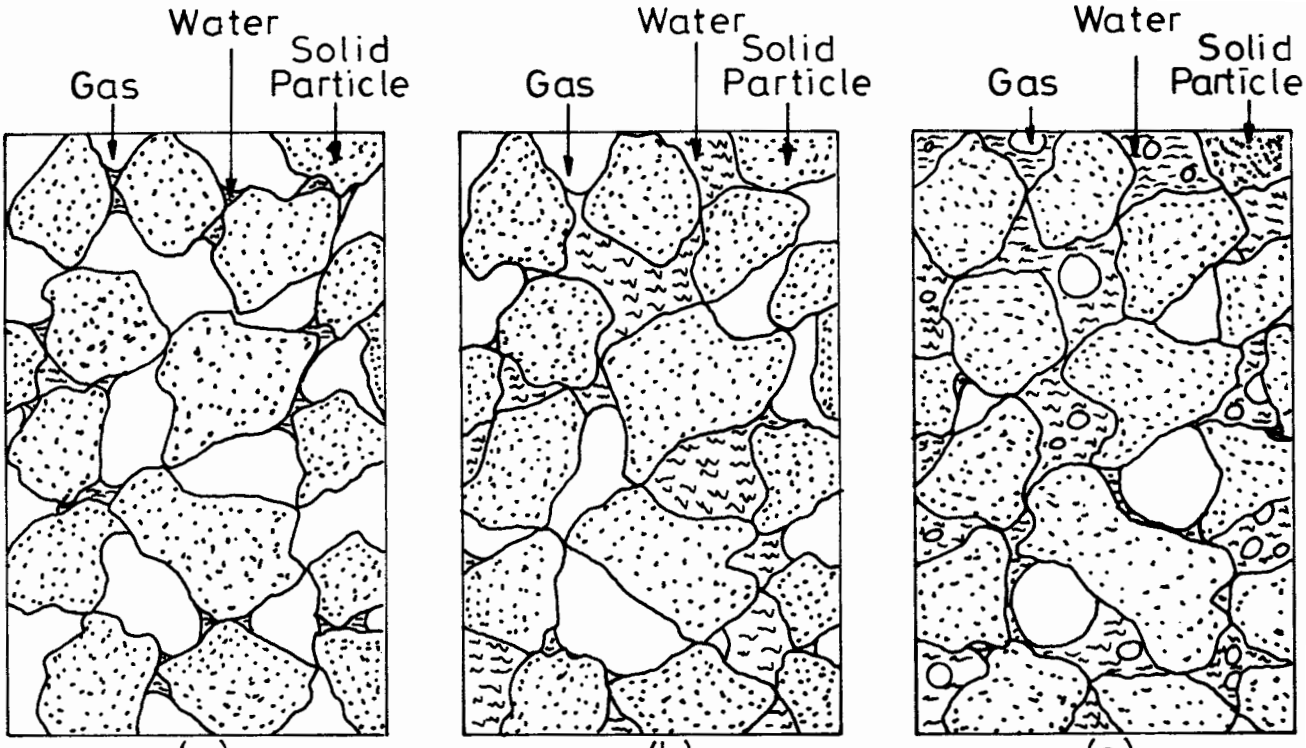

Fig. 1·1. STRUCTURE OF UNSATURATED SOILS.

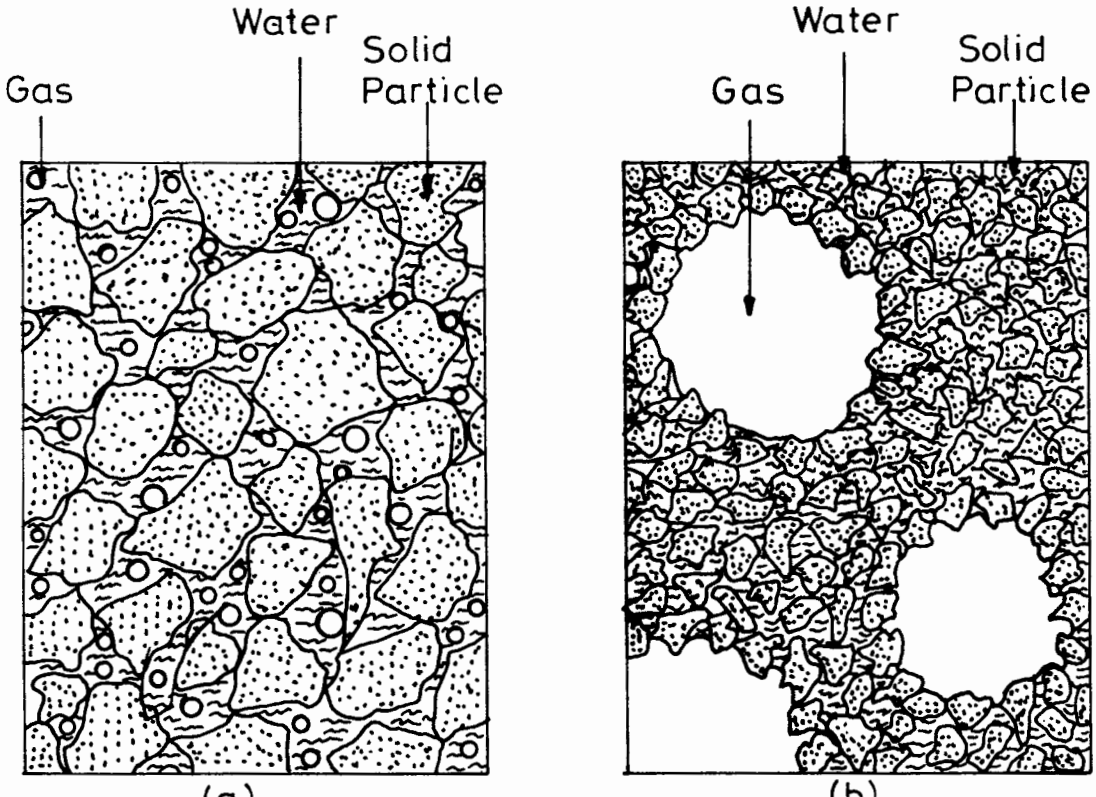

Fig. 1·2. SOILS CONTAINING DISCRETE BUBBLES.

The work presented in this thesis is restricted to unsaturated soils with the gas in the form of discrete bubbles (Figure 1.1(c)). Nageswaran (1983) refers to this class of material as "gassy soil". The gas is likely to take the form of discrete bubbles only if the degree of saturation is high (Barden and Sides, 1970). Sparks (1963) suggests that the critical saturation level is about 0.85, and this suggestion is borne out by the work of Nageswaran (1983). However, the precise value of the critical degree of saturation probably varies slightly for different soils.

A detailed review of previous work on the behaviour of soils containing gas bubbles is given in a separate report which forms an expanded version of Chapter 1 of this thesis (Wheeler, 1986).

The structure of soils containing discrete bubbles can vary considerably, depending on the relative sizes of the bubbles and the soil particles. Terzaghi (1944) was careful to distinguish between small and large bubbles, which he referred to as "gas bubbles" and "gas voids" respectively.

If the gas bubbles are small compared with the particle size, the soil structure is likely to be as illustrated in Figure 1.2(a). The bubbles fit within the normal void spaces without distortion of the soil structure. The radius of curvature of each gas-water interface (which controls the difference between gas pressure and water pressure) is equal to the radius of the bubble.

Figure 1.2(b) illustrates the opposite extreme, with bubbles that are much larger than the normal particle size. In the region of each bubble the soil skeleton is pushed back by the gas, leaving a large gas-filled void. The gas-water interfaces are formed by a large number of small menisci which bridge the gaps between the particles. The radius of curvature of these menisci is not necessarily equal to the bubble radius.

In land-based unsaturated soils the gas may be in the form of discrete bubbles or interconnected voids (Bishop, 1959). However, recent attention

has focussed on the problem of unsaturated soils in the marine environment, where the gas is usually in the form of discrete bubbles.

1.2 GAS IN MARINE SOILS

Offshore investigations in a variety of locations have indicated the presence of undissolved gas in the sediments forming the seabed (Whelan et al, 1975; Esrig and Kirby, 1977). The gas is typically methane, nitrogen or carbon dioxide produced by the decomposition of organic matter. This is known as biogenic gas. Nageswaran (1983) gives a brief description of the formation process, while Claypool and Kaplan (1974), Martens and Berner (1974) and Mechalas (1974) provide a more detailed analysis. Alternative sources for the gas include thermal cracking of complex organic and inorganic compounds at great depth (thermogenic gas) and submarine volcanic or geothermal processes (vulcanogenic gas).

The preservation of sedimentary organic matter is an important requirement for the formation of biogenic gas. Conditions are most favourable when the sediment has a considerable organic content and the rate of deposition is high. The ideal environment is most likely to occur near the mouth of a large river, the Mississippi Delta being a prime example (Whelan et al, 1976). Numerous authors, including Esrig and Kirby (1977) and Whelan and Lester (1980) have reported the presence of gas-bearing soils in the Mississippi Delta and other areas within the Gulf of Mexico. Marine soils containing gas have also been recorded in many other parts of the world, such as British Columbia (McCartney and Bary, 1975), New Zealand (Duncan and Pantin, 1969), the North Sea (Fannin, 1979), the Thames Estuary (Grindley, 1955) and the Bristol Channel (Kirby and Parker, 1980).

Unsaturated marine soils normally occur with a degree of saturation in excess of 0.9 (Esrig and Kirby, 1977), because the gas is compressed by the

head of seawater above. This high level of saturation means that the gas is usually in the form of discrete bubbles. The size of the bubbles varies quite widely, but they are typically much larger than the soil particles (Anderson and Hampton, 1980). Therefore the soil structure is likely to be as illustrated in Figure 1.2(b).

The presence of gas bubbles is likely to have a significant effect on the engineering properties of a marine soil. Because of their high compressibility the bubbles obviously affect the volume change behaviour of the soils (Nageswaran, 1983). However, a number of authors have also reported unusually low values of shear strength in areas where gas is present (Bea and Arnold, 1973; Whelan et al, 1977). Indeed, Coleman and Prior (1978) and Prior and Suhayda (1979) suggest that the presence of undissolved gas may be partly responsible for submarine landslides on very low angle slopes in the Mississippi Delta area.

The low measured values of shear strength may not indicate that soils containing gas bubbles are intrinsically weaker than saturated soils. The suggestion has been made that the low strengths are caused by incomplete dissipation of excess pore water pressures. In regions of gas-bearing soils, water pressures permanently above the hydrostatic level have been recorded by many authors (Esrig and Kirby, 1977; Bennett, 1977; Hirst and Richards, 1977). These excess water pressures could be caused directly by the process of gas generation or they could be due to the gas bubbles reducing the soil permeability, which would hinder the dissipation of pore pressures set up during deposition of the soil. However, work by Nageswaran (1983) has cast some doubt on the accuracy of these measurements of high water pressures. He showed that gas diffusing into the piezometer could artificially elevate the reading of pore water pressure.

One other point to bear in mind is that the shear strengths measured on recovered samples are probably lower than those that occur in-situ, because

of sample disturbance. As a core is brought to the surface from the seabed the sample undergoes very large reductions in total stress and pore water pressure. The gas bubbles expand with the reduction in pressure, while the dissolved gas present in the pore water reappears and adds to the total gas volume. Samples are observed to grow out of the core liners (Esrig and Kirby, 1977) and the escape of gas bubbles has been noted in many instances. Because of these effects, sample disturbance is likely to be far more severe than is the case with saturated soils.

The presence of gas bubbles in marine sediments can be detected by methods other than direct observation of the gas in recovered samples. Acoustic measurements form one of the most useful techniques. Anderson and Hampton (1980) studied the effect of gas bubbles on the acoustic properties of soil in some detail. Gas bubbles result in a dramatic attentuation of acoustic signals, so that regions of gas-bearing sediment stand out as acoustically inpenetrable or "turbid" (Schubel, 1974; Whelan et al, 1977). Extensive areas of acoustical attenuation in the Mississippi Delta region are reported by Sieck (1973).

Detecting the presence of gas in marine soils is relatively easy, but measuring the actual quantity of gas (the degree of saturation) is much more difficult. Currently there are no methods available for direct in-situ measurement of the gas content. Measurements of the degree of saturation are made on recovered samples and these are then converted to in-situ values by using Boyle's Law and Henry's Law (Esrig and Kirby, 1977). There are two major sources of error in this method. The first is the escape of gas during the recovery process. The second source of error is inadequate knowledge of the gas pressure in the recovered sample and in-situ. Both of these gas pressures are required for use with Boyle's Law and Henry's Law, but neither of them is known precisely, because the pore gas pressure is not necessarily equal to the pore water pressure. Errors associated with both gas escape and inadequate knowledge of gas pressures can be avoided by

using pressurised core samplers and an isobaric chamber to keep the recovered samples permanently at the in-situ pressure level. However, this technique is very expensive and used only infrequently.

Obviously a simple technique for measuring the degree of saturation in-situ would have great advantages. It may be possible to measure the degree of saturation by using the speed of sound in the soil (Anderson and Hampton, 1980), and work at Oxford is currently focussing on the possible development of an acoustic probe for use in the marine environment. This would be a major improvement on existing techniques for measuring the degree of saturation.

1.3 PREVIOUS WORK ON UNSATURATED SOILS

The intention in this section is to provide a review of the previous work in the field of unsaturated soils. The work is not necessarily restricted to the case of soils with the gas in the form of discrete bubbles.

Wood (1979) provides a detailed review of published work on unsaturated soils up to 1979.

1.3.1 Effective Stress for Unsaturated Soils

Terzaghi (1923) was the first to put forward the effective stress equation for saturated soils and dry soils:

$$\sigma' = \sigma - u \qquad 1.1$$

The effective stress σ' is equal to the difference between the total stress σ and the pressure in the pore fluid u. For a dry soil u is equal to the pore air pressure u_g, and for a saturated soil u is equal to the pore water pressure u_w. The important concept behind Equation 1.1 is than an effective stress can be defined such that "...all the measurable effects of a change in stress, such as compression, distortion and a change in shearing resistance are exclusively due to changes in the effective stress" (Terzaghi, 1936).

Obviously the analysis of unsaturated soils would be greatly facilitated if the concept of an effective stress could be extended to cover soils containing more than one pore fluid. Bishop (1959) proposed a modification to Equation 1.1 for use with unsaturated soils:

$$\sigma' = \sigma - u_g + \chi(u_g - u_w) \qquad 1.2$$

u_g and u_w are the gas and water pressures respectively, which are not necessarily equal, because of the effect of surface tension. χ is a factor between zero and unity. Bishop stated that χ depends solely on the degree of saturation S, being zero when the saturation is 0.0 and unity at a saturation of 1.0. Equation 1.2 therefore agrees with Equation 1.1 for the two limiting cases of a dry soil and a saturated soil. Bishop's derivation of Equation 1.2 was based on the fact that the water pressure acts on a reduced area of soil grains when part of the pore fluid is gas.

Skempton (1960) and Jennings (1960) also derived Equation 1.2 on the basis of the areas over which the gas and water pressures act. In the aftermath of the 1960 Conference on "Pore Pressure and Suction in Soils" there was general agreement on the form of Equation 1.2 (Aitchison and Bishop, 1960).

The implicaton of Equation 1.2 is that an unsaturated soil consolidated to a particular effective stress, as defined by the equation, will have a void ratio equal to that of a saturated soil consolidated to the same effective stress (defined in the normal way by Equation 1.1). Similarly, the shear strength of an unsaturated soil will be equal to that of a saturated soil at the same effective stress.

Bishop and Donald (1961) used strength measurements from drained triaxial tests to calculate experimental values for the factor χ. This was done by back-calculating from Equation 1.2, using the fact that the effective stress σ_3' in an unsaturated soil must by definition be equal to the value of

$(\sigma_3 - u_w)$ in a saturated soil which has the same shear strength. Similar procedures were used to calculate independent values of χ from undrained triaxial tests and consolidation tests. The values of χ from the three different types of test were plotted against the degree of saturation S (Figure 1.3). The agreement was excellent, and Bishop and Donald took this as confirmation of the uniqueness of the relationship between χ and S for a given soil. The experimental results also fitted very closely to some earlier theoretical expressions for χ produced by Donald (1960).

Jennings and Burland (1962) were amongst the first authors to question the concept of a single effective stress for unsaturated soils. They carried out oedometer tests on compacted silts to examine qualitatively the validity of Equation 1.2 for volume change behaviour. Samples of unsaturated silt were prepared with the air voids at atmospheric pressure and the pore water at a negative pressure (due to surface tension effects). The initial effective stress, given by Equation 1.2, was therefore greater than the total stress σ. With the total stress held constant the samples were then saturated, by soaking with water. In the final saturated state the pore water pressure was zero, so that the effective stress, given by Equation 1.1, was equal to σ. The effective stress therefore decreased during the saturation process, suggesting an increase in the void ratio of the soil. However this was in direct contrast with the observed behaviour, which in every case showed a decrease in soil volume.

Jennings and Burland (1962) concluded that the concept of a single effective stress was not always valid for the volume change behaviour of unsaturated soils. The unique relationship between χ and S indicated by Bishop and Donald's earlier work appeared to be simply a fortuitous result of the type of test used to calculate χ.

Bishop and Blight (1963) re-examined Equation 1.2 with a series of drained triaxial tests on clays, using different stress paths. They found

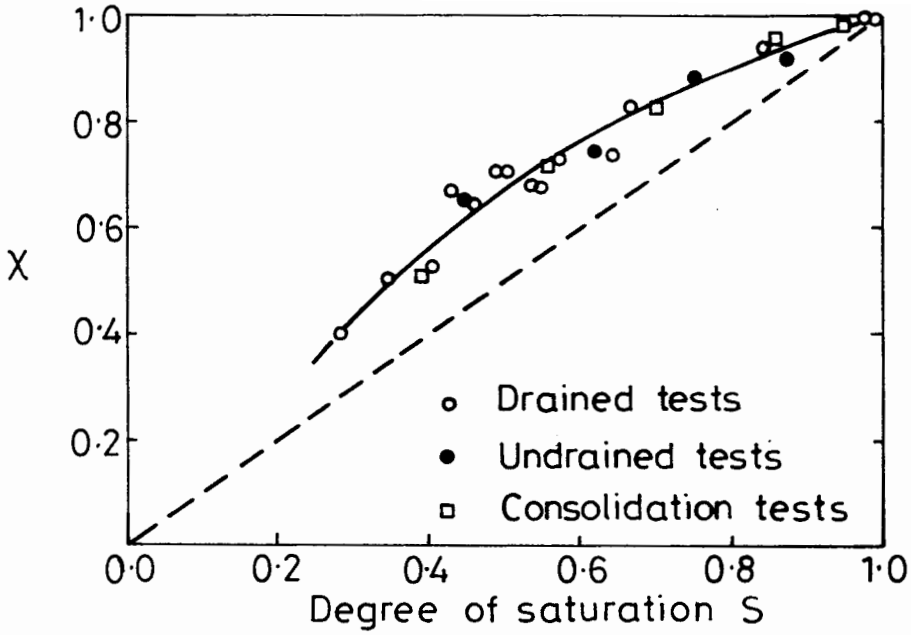

Fig. 1·3. EXPERIMENTAL VALUES OF χ FOR BRAEHEAD SILT. (Bishop and Donald, 1961)

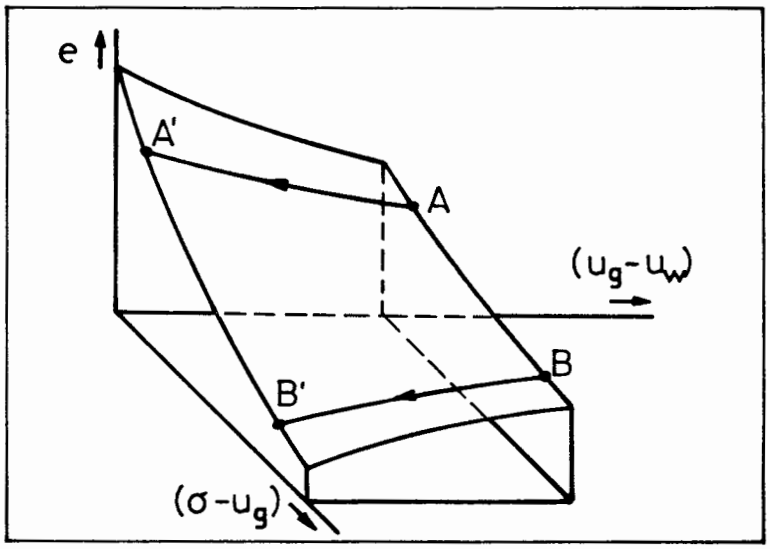

Fig. 1·4. STATE SURFACE FOR VOID RATIO.

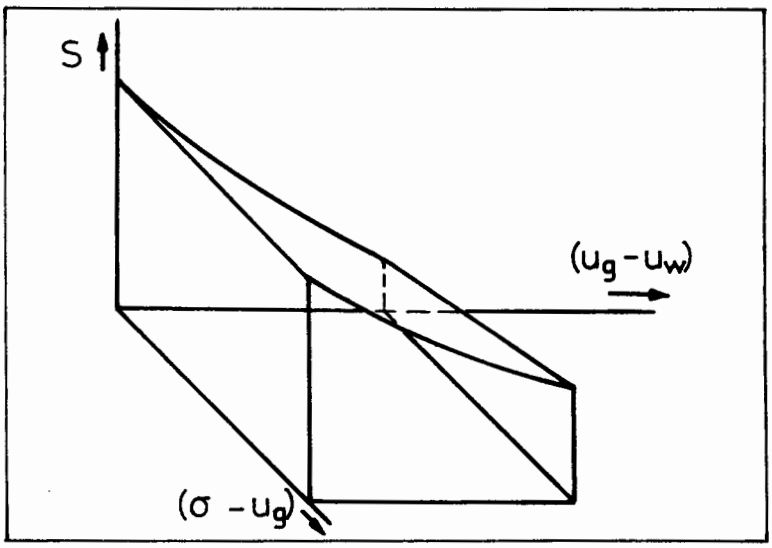

Fig. 1·5. STATE SURFACE FOR DEGREE OF SATURATION

that the parameter χ was path dependent, seeming to be a function of $(u_g - u_w)$ as well as S. They suggested that, for volume change behaviour, Equation 1.2 could be modified to:

$$\sigma' = \sigma - u_g + f(u_g - u_w) \qquad 1.3$$

Burland (1964) reanalysed Bishop and Blight's experimental results to demonstrate once more that the effective stress concept is invalid for the volume change behaviour of unsaturated soils. His line of analysis followed that used by Jennings and Burland (1962).

1.3.2 An Alternative to the Single Effective Stress Approach

By the mid-1960s considerable evidence had been amassed to show that the principle of a single effective stress was invalid for unsaturated soils, at least as far as volume change behaviour was concerned. It was clear that an alternative approach was required.

When Bishop and Blight (1963) concluded that the χ factor was path dependent, they suggested Equation 1.3 as a definition for the effective stress. This led to the idea of two independent stress variables, $(\sigma - u_g)$ and $(u_g - u_w)$, instead of a single effective stress σ'. Bishop and Blight suggested that the volume change behaviour could be plotted as a surface, relating the void ratio e to the stress variables $(\sigma - u_g)$ and $(u_g - u_w)$, as shown in Figure 1.4. Similarly, the variation of shear strength could be plotted as a surface relating $(\sigma_1 - \sigma_3)/2$ to $((\sigma_1 + \sigma_3)/2 - u_g)$ and $(u_g - u_w)$.

Matyas and Radhakrishna (1968) considered that the stress state of an unsaturated soil could be defined by three parameters:

$$\left.\begin{aligned} p' &= \tfrac{1}{3}(\sigma_1 + 2\sigma_3) - u_g \quad \text{(mean normal stress)} \\ q &= \sigma_1 - \sigma_3 \quad \text{(deviatoric stress)} \\ u_c &= u_g - u_w \quad \text{(suction pressure)} \end{aligned}\right\} \qquad 1.4$$

This was consistent with the ideas put forward earlier by Bishop and Blight.

Matyas and Radhakrishna examined the validity of their approach with a series of compression tests, on compacted samples of kaolin-flint, following a wide variety of stress paths. They found that for isotropic compression there appeared to be a unique surface relating the void ratio e to the stress variables $(\sigma - u_g)$ and $(u_g - u_w)$, as shown in Figure 1.4. A second unique surface related the degree of saturation S to the stress variables (Figure 1.5). One-dimensional compression gave a second pair of surfaces relating e and S to $(\sigma - u_g)$ and $(u_g - u_w)$. These results provided strong evidence to support the validity of the stress variables given in Equation 1.4.

It is interesting to note the shape of the $e : (\sigma - u_g) : (u_g - u_w)$ surface shown in Figure 1.4. The surface is warped. At a constant value of $(\sigma - u_g)$, e increases with decreasing $(u_g - u_w)$ if $(\sigma - u_g)$ is low (swelling behaviour, shown by A-A' in the figure) but e decreases with decreasing $(u_g - u_w)$ if $(\sigma - u_g)$ is high (collapse behaviour, B-B'). It was the collapse behaviour at high values of $(\sigma - u_g)$ which disproved the principle of a single effective stress (Jennings and Burland, 1962).

Matyas and Radhakrishna found that the results of a few tests did not lie on the unique surfaces for e and S. These tests all corresponded to stress paths where the saturation was decreasing or the soil was swelling. In all these cases the void ratio e fell below the normal surface. These test paths are analogous to unloading tests on a saturated soil, which give swelling lines that lie below the virgin consolidation line.

Fredlund and Morgenstern (1976) analysed unsaturated soil as a four phase material, the fourth phase being a "contractile skin" forming the air-water interface. They concluded that the stress state could be fully specified by any two of three variables $(\sigma - u_g)$, $(\sigma - u_w)$ and $(u_g - u_w)$. They recommended the use of $(\sigma - u_g)$ and $(u_g - u_w)$, consistent with the work of Bishop and Blight, and Matyas and Radhakrishna.

Fredlund and Morgenstern (1976) verified experimentally the uniqueness of the $e : (\sigma - u_g) : (u_g - u_w)$ surface with a series of tests under isotropic and one-dimensional conditions. In the same series of tests Fredlund and Morgenstern also investigated the uniqueness of the surface relating water content w to $(\sigma - u_g)$ and $(u_g - u_w)$. This would imply a unique surface for the saturation, because S is defined by the void ratio and the water content:

$$S = wG_s/e \qquad 1.5$$

(G_s is the specific gravity of the soil grains.) The correlation was not as good as for the void ratio surface. This was attributed to the experimental difficulties of measuring the small quantities of water flowing from the sample.

In a subsequent paper Fredlund and Morgenstern (1977) described in more detail the analysis of unsaturated soil as a four phase material. They also described a series of null tests $(\Delta\sigma = \Delta u_g = \Delta u_w)$ to check the validity of the stress state variables $(\sigma - u_g)$ and $(u_g - u_w)$. The test results showed no change in either void ratio or saturation, within the accuracy of the measuring systems. Fredlund and Morgenstern took this as confirmation of the stress state variables.

Fredlund, Morgenstern and Widger (1978) considered the relationship between the shear strength of an unsaturated soil τ and the stress state variables. They proposed the following expression:

$$\tau = c' + (\sigma - u_g)\tan\phi' + (u_g - u_w)\tan\phi^b \qquad 1.6$$

c' and ϕ' are the cohesion intercept and angle of friction measured on a saturated sample and ϕ^b is the friction angle with respect to changes in $(u_g - u_w)$. Fredlund, Morgenstern and Widger analysed the experimental results of various previous authors, concluding that there was reasonable agreement with Equation 1.6. Values of ϕ^b varied from about 4^o less than ϕ' to about 2^o more than ϕ'.

Fredlund (1979) attempted to provide mathematical expressions defining the volume change behaviour, to correspond to Equation 1.6 for the shear strength. He suggested the following expression for the surface relating void ratio to $(\sigma - u_g)$ and $(u_g - u_w)$:

$$e = e_o - C_t \log (\sigma - u_g) - C_m \log (u_g - u_w) \qquad 1.7$$

C_t and C_m are compression indices, while e_o is the void ratio when both stress variables are unity. Fredlund gave a similar expression for the water content surface:

$$w = w_o - D_t \log (\sigma - u_g) - D_m \log (u_g - u_w) \qquad 1.8$$

D_t and D_m are water content indices and w_o is the water content when both stress variables are unity.

By considering the limiting case of a saturated soil, and the relationship between e and w given in Equation 1.5, Fredlund showed that the indices C_t and D_t are not independent:

$$D_t = C_t/G_s \qquad 1.9$$

The four indices in Equations 1.7 and 1.8 were therefore reduced to three. These would all apply to the virgin loading surface, and another set of three indices would be required for the unloading (swelling) surfaces.

Equations 1.7 and 1.8 are not entirely consistent with the experimental results of Bishop and Blight (1963) and Matyas and Radhakrishna (1968). Equation 1.7 suggests a planar surface, when the stress variables are plotted on a log scale, while the experimental evidence indicates that the surface relating e to $(\sigma - u_g)$ and $(u_g - u_w)$ is warped (figure 1.4). Lloret and Alonso (1985) proposed expressions for e and S which are more complicated than Equations 1.7 and 1.8, but which take account of the warped nature of the surfaces.

Fredlund (1979) concluded with some ideas on how the relations for the τ, e and S surfaces (Equations 1.6, 1.7 and 1.8) could be used for solving practical engineering problems involving unsaturated soils. He considered problems of earth pressure, slope stability, bearing capacity and settlement. These ideas were developed further in a later paper by the same author (Fredlund, 1985).

1.3.3 Laboratory Testing

The intention in this section is to describe some of the special problems involved with laboratory testing of unsaturated soils, together with the apparatus and techniques developed by previous workers to solve these problems.

Research workers at Imperial College have performed quite extensive testing on unsaturated soils, covering the volume change behaviour under isotropic conditions and drained and undrained triaxial tests (Bishop, 1960; Bishop and Donald, 1961; Bishop and Blight, 1963). The modified triaxial apparatus used for these tests is described by Bishop and Donald (1961) and Bishop and Henkel (1962).

In an unsaturated soil compression of the gas can result in volume changes in addition to those due to drainage. For example an undrained test is no longer a constant volume test. This means that if a triaxial cell is to be used for the testing of unsaturated samples, one of the most important modifications that is required is a means of measuring the volume change independently of the flow from the sample. The solution to this problem adopted at Imperial College was to surround the sample with mercury and measure the vertical displacement of the mercury surface by using a cathetometer sighting on a stainless steel ball floating in the mercury (Bishop and Donald, 1961). The mercury was enclosed in an internal jacket (see Figure 1.6), with the cell pressure applied to both sides of the jacket. This arrangement meant that any variation of the cell volume, caused by changes of cell pressure, had no effect on the level of the mercury surface.

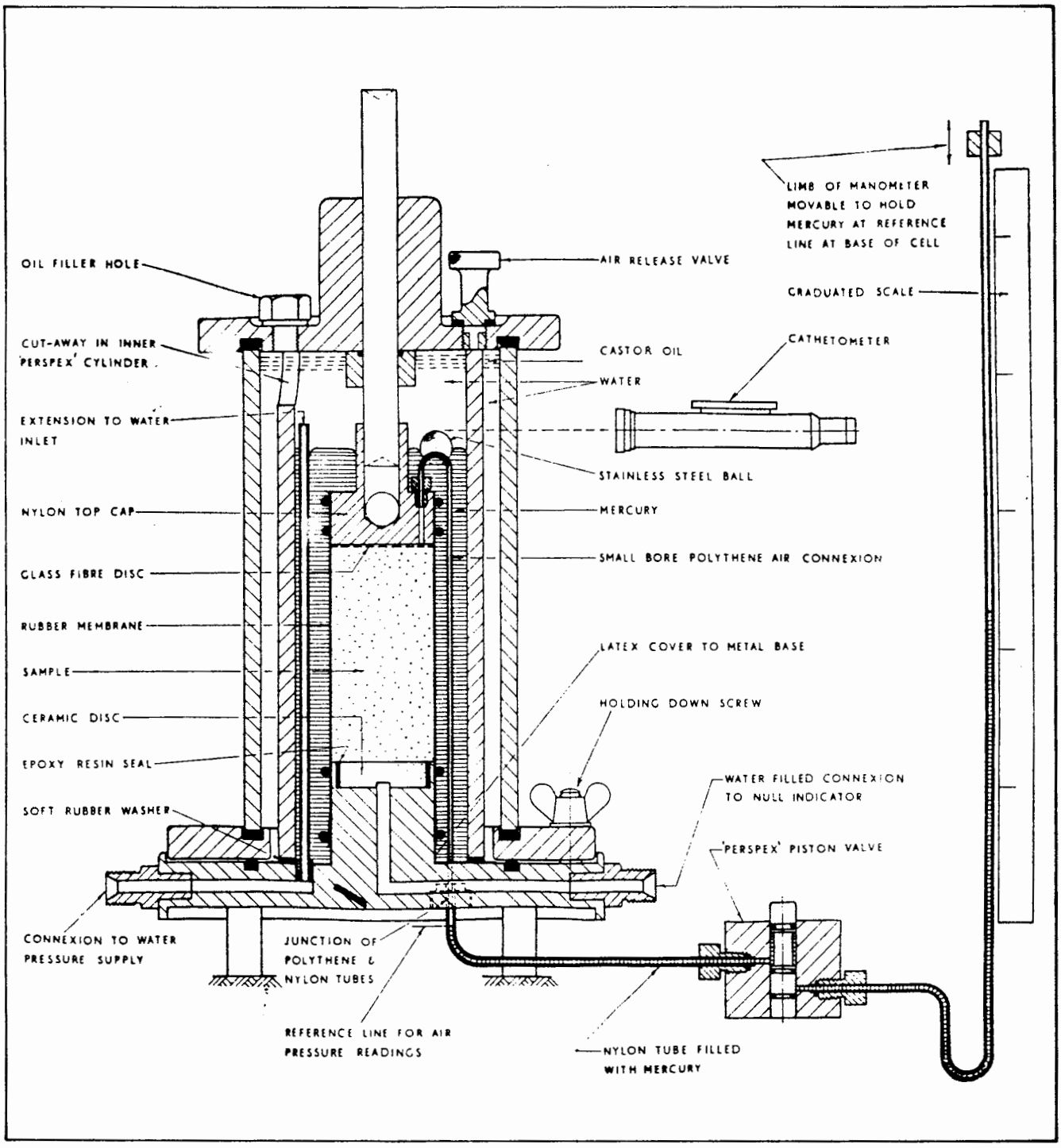

Fig. 1·6. MODIFIED TRIAXIAL APPARATUS FOR TESTING UNSATURATED SOILS (Bishop and Donald, 1961)

Most of the other research workers who have used triaxial cells to study unsaturated soils have used the same basic principle as Bishop and Donald (1961) for measuring the sample volume change. An alternative means of measuring the volume change would be to measure the lateral and vertical strains of the sample.

For drained tests, in either an oedometer or a triaxial cell, in addition to measuring the volume change of the sample it is necessary to measure the volumes of water and gas draining from the soil. Bishop and Donald (1961) describe a bubble pump and air trap which can be used to separate the gas and water leaving the sample.

Measurement of the pore pressures u_g and u_w can be a problem in the testing of unsaturated soils. Bishop (1960) described the technique that has become widely accepted. High air entry porous filters (usually made of a ceramic) are used for measuring the water pressure, while low air entry filters (typically woven glass fibre) are used for the gas pressure. These same types of filter have also been used for applying either the water pressure or the gas pressure during drained tests.

The use of high and low air entry filters for measuring u_w and u_g is probably successful when both water and gas phases are continuous. However, with a soil containing discrete bubbles it is very unlikely that a reading taken at the boundary of the sample will give a realistic measurement of the gas pressure in a typical bubble within the sample (Barden and Sides, 1970). Similarly if the water phase is discontinuous, correct measurement of the water pressure is likely to be difficult.

Use of a high air entry filter for the measurement of u_w will prevent the passage of gas bubbles, but dissolved gas will still diffuse through. This gas may come out of solution after passing through the filter, causing a build up of gas in the measuring system. This could affect the measurement of both pore water pressure (Nageswaran, 1983) and degree of saturation

(Fredlund, 1975). Bishop and Donald (1961) and Fredlund (1975) describe methods for flushing this gas from the system and measuring the quantity of dissolved gas.

Bishop and Donald (1961) investigated another problem which may occur during triaxial testing of unsaturated soils: diffusion of gas through the membrane. Bishop and Donald (1961), Matyas and Radhakrishna (1968) and Barden and Sides (1970) prevented this diffusion by surrounding the sample with mercury, a liquid in which most gases have a very low solubility. Fredlund and Morgenstern (1977) used a different technique. They improved the quality of the membrane, by using two layers of rubber separated by aluminium foil and vacuum grease.

1.4 WORK AT OXFORD ON SOILS CONTAINING GAS BUBBLES

In 1978 Dr G.C. Sills began to study the behaviour of marine soils containing gas bubbles, as a natural extension of her existing interest in soft sediments in marine or estuarine environments.

The work of the research team at Oxford, on soils containing gas bubbles, started with a series of field measurements designed to indicate the presence of gas bubbles and the effect of these bubbles on the compressibility of the soil and the generation of pore pressures. Tests were conducted in Bridgwater Bay (in the Bristol Channel) and Holyhead Harbour (North Wales). Gas was believed to exist in both areas from a study of seismic records.

Measurements were taken, over a number of tidal cycles, of the difference between the pore water pressure in the seabed and the hydrostatic pressure due to the head of seawater. For a saturated soil these pressures are always identical; the increase in total stress due to a rising tide being carried entirely as an increase in the pore pressure. However for an unsaturated soil, the increment of total stress is partly transferred to the soil skeleton, because of the compressibility of the gas bubbles, and the increase in pore

water pressure is less than theincrease in hydrostatic pressure. Over a tidal cycle a roughly sinusoidal variation in the pressure difference would be expected, as shown in Figure 1.7 (Sills and Austin, 1982).

The measurements of pressure difference were taken with a differential piezometer designed and built at Oxford. Descriptions of two versions of the piezometer are provided by Nageswaran (1983). The results, at both Bridgewater Bay and Holyhead Harbour, showed the expected cyclic variation, confirming the presence of gas bubbles in the seabed (Sills and Austin, 1982).

The field measurements with the differential piezometer indicated that gas bubbles could have a significant effect on the behaviour of marine soils, and a programme of laboratory tests on soils containing gas bubbles was instigated. However, the difficulties associated with testing natural undisturbed gassy soil samples in the laboratory were formidable, because of the severe problems of sample disturbance mentioned in Section 1.2. To circumvent these difficulties a technique was developed at Oxford for producing reconstituted soil samples containing a uniform, repeatable distribution of gas bubbles. This "zeolite molecular sieve technique" is described in detail by Nageswaran (1983) and Sills and Nageswaran (in preparation). Brief details are provided in Section 3.1 of this thesis.

Sills and Nageswaran (1984) describe a laboratory simulation of a gas-bearing seabed subjected to a varying tidal head (corresponding to the earlier field study). The seabed consisted of a clayey silt taken from an estuarine site, reconstituted in the laboratory with a controlled distribution of methane bubbles. Measurements were taken, during a number of tidal cycles, of the excess pore water pressure (above hydrostatic) at the bottom of the seabed and the vertical displacement of the soil surface. The results were analysed using Boyle's Law (on the assumption that gas and water pressures were equal) to calculate the variation in the degree of saturation during a tidal cycle. The calculated values of saturation were consistent with independent measurements of the water content.

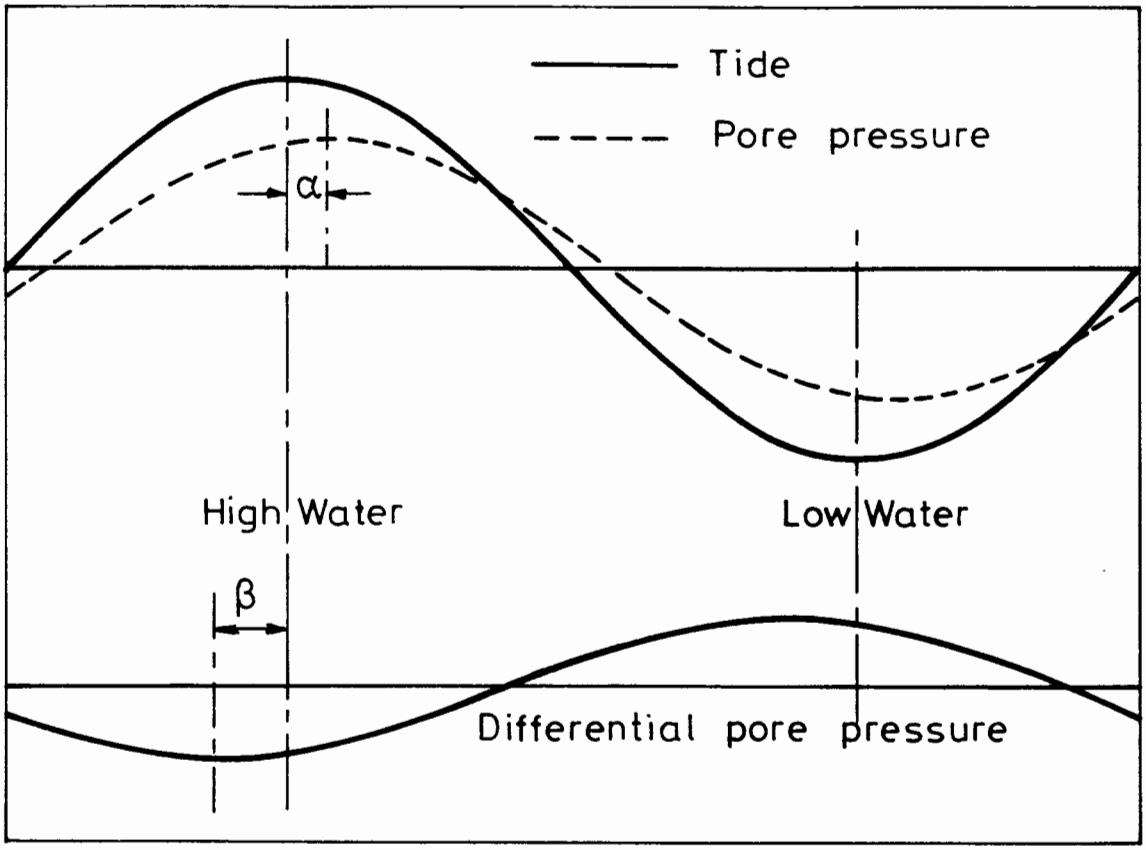

Fig. 1·7. CYCLIC VARIATION OF DIFFERENTIAL PORE PRESSURE IN AN UNSATURATED SEA-BED (Sills and Austin)

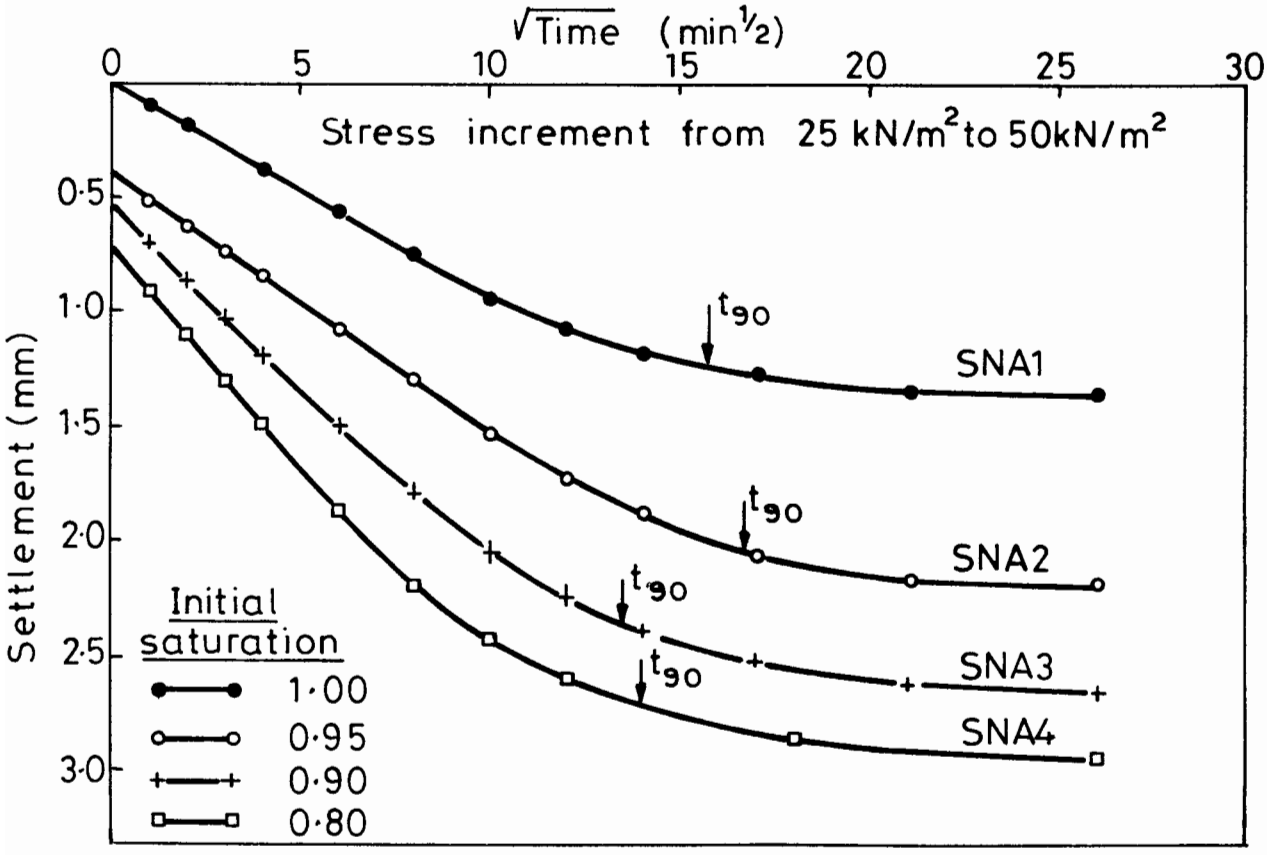

Fig. 1·8. TYPICAL SETTLEMENT-TIME PLOTS FOR ONE-DIMENSIONAL CONSOLIDATION. (Nageswaran)

The same analysis was then applied to the field measurements at Bridgwater Bay and Holyhead Harbour, as well as the results from a third series of field tests at Port Talbot (South Wales). In each case the amplitude of the excess pore water pressure variation indicated a degree of saturation varying between about 0.97 at low water and 0.98 at high water. Sills and Nageswaran assumed a layer of gas-bearing soil 5 m thick, and calculated that this would result in about 40 mm of vertical movement of the seabed surface.

Nageswaran (1983) conducted a detailed series of one-dimensional consolidation tests on reconstituted samples containing methane bubbles. He used a modified oedometer, which allowed separate measurement of the quantities of water and gas draining from the samples. Careful attention was given to the design of the housing for the transducer measuring pore water pressure, to ensure that gas diffusing through the high air entry filter did not affect the reading. No attempt was made to measure the gas pressure u_g as this was considered to be impossible in a soil containing discrete bubbles. Tests were conducted on samples with saturation levels ranging from 0.7 to 1.0.

Figure 1.8 shows the settlement-time plots for one load increment from a typical series of tests. The figure clearly illustrates the immediate undrained compression that occurs if the saturation is less than 1.0 and the fact that the final settlement increases with increasing gas content. Figure 1.8 also indicates that the time to reach 90% of the final settlement is apparently independent of the degree of saturation.

Figure 1.9 shows the void ratio e plotted against the stress $(\sigma - u_w)$ for another typical series of tests. The results do not follow a unique line (as would be the case with saturated samples). For tests SNB1 to SNB4, corresponding to initial saturation levels between 1.0 and 0.85, there is a clear trend; the lower the initial degree of saturation the greater the void ratio at a given stress level. However, this trend does not appear to continue

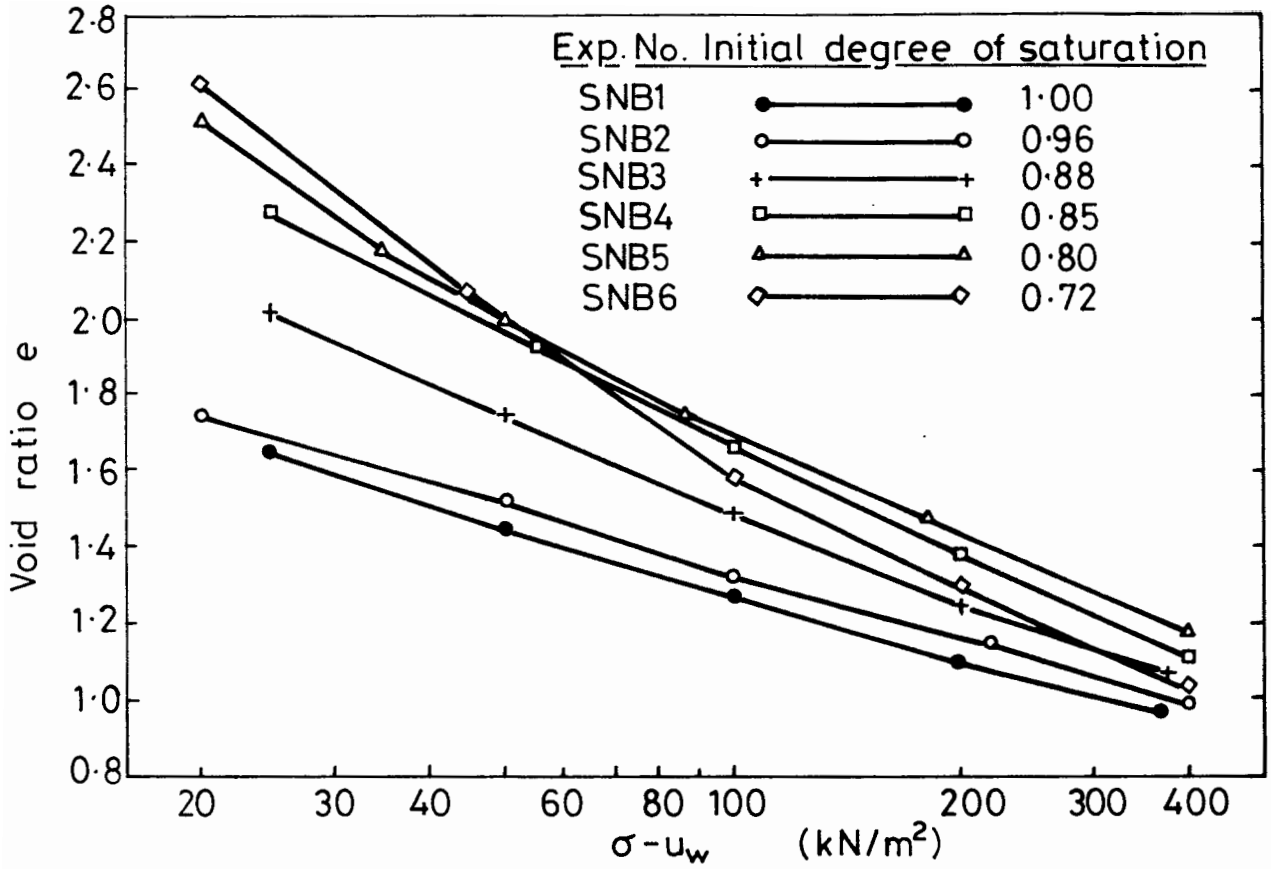

Fig. 1·9. VARIATION OF VOID RATIO DURING ONE-DIMENSIONAL CONSOLIDATION (Nageswaran)

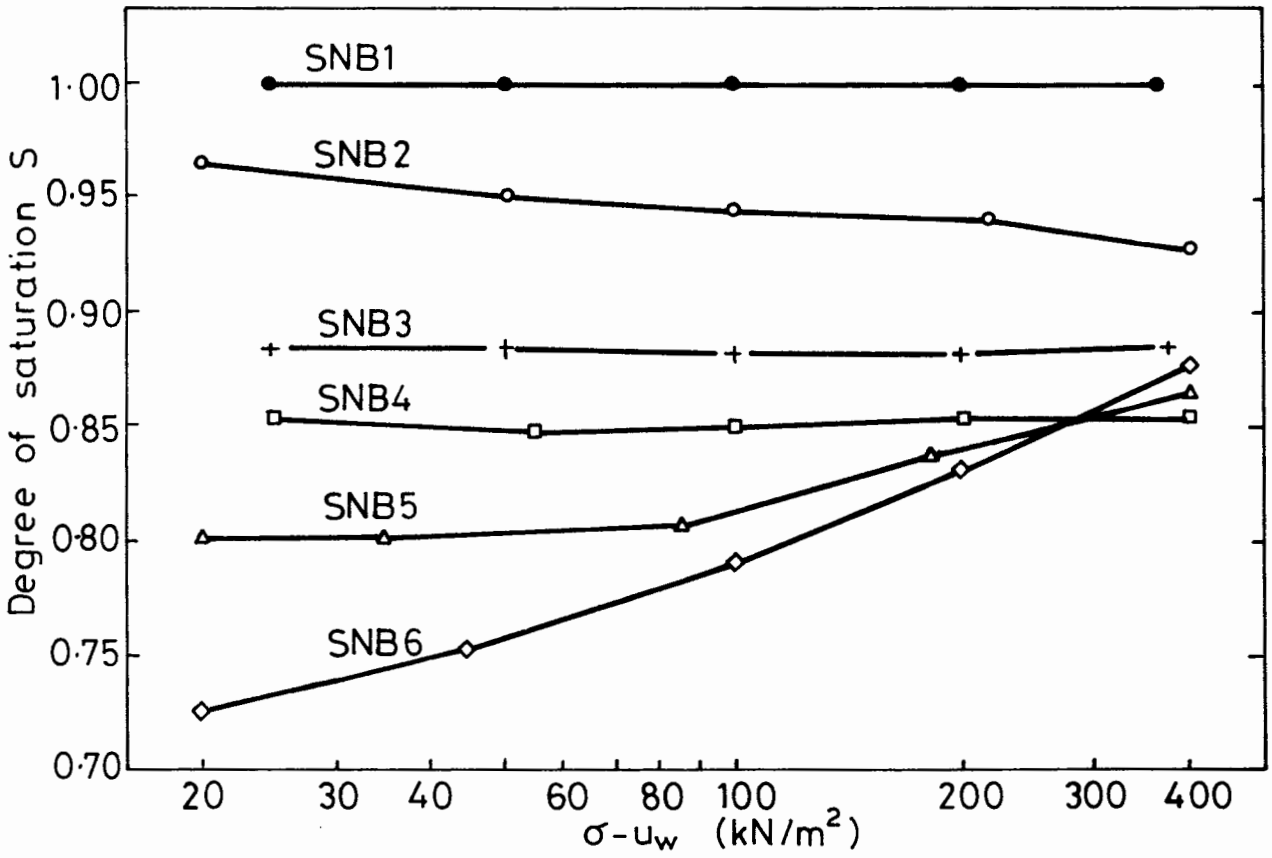

Fig. 1·10. VARIATION OF DEGREE OF SATURATION DURING ONE-DIMENSIONAL CONSOLIDATION (Nageswaran)

for Tests SNB5 and SNB6 (initial saturations of 0.80 and 0.72 respectively). The reason for this difference in behaviour is clear from Figure 1.10, which shows the variation in the degree of saturation for the same series of tests. For Tests SNB1 to SNB4 the saturation remained almost constant during each test, but during Tests SNB5 and SNB6 the saturation increased dramatically. This suggests that for initial saturation values above about 0.85 the methane is in the form of discrete bubbles, resulting in a limited flow of gas, but for lower saturation levels the gas phase is continuous and methane flows freely and rapidly from the sample. This is in agreement with the work of Sparks (1963), who states that the critical saturation level, separating continuous gas from discrete bubbles, is about 0.85.

Nageswaran's results clearly illustrate the inapplicability of an effective stress approach for soils containing gas bubbles. Figure 1.11 shows the $e : (\sigma - u_w)$ curves for Tests SNB1 and SNB3. For Test SNB3, when $(\sigma - u_w)$ is 200 kN/m^2 the void ratio is approximately 1.25. In Test SNB1, on the saturated sample, the void ratio is 1.25 when $(\sigma - u_w)$ is about 100 kN/m^2. This means that, in Test SNB3, when $(\sigma - u_w)$ is 200 kN/m^2 the effective stress is actually 100 kN/m^2. But, rearranging Bishop's effective stress relationship (Equation 1.2):

$$\sigma' = \sigma - u_w - (1 - \chi)(u_g - u_w) \qquad 1.10$$

This means that for Test SNB3:

$$(1 - \chi)(u_g - u_w) = 100 \text{ kN/m}^2 \qquad 1.11$$

But the factor χ is approximately equal to S (see Figure 1.3), so that the term $(1 - \chi)$ had a value of about 0.1 in Test SNB3. Therefore, Equation 1.11 suggests that the pressure difference $(u_g - u_w)$ was about 1000 kN/m^2 in Test SNB3. This is clearly most unlikely, and can actually be shown to be impossible by considering the minimum possible radius of curvature of the menisci forming the interface between gas and water (see Chapter 5). Even if $(1 - \chi)$ was as high as 0.2 or 0.3, Equation 1.11 would imply a value of 300 to 500 kN/m^2 for $(u_g - u_w)$, which is still impossibly high.

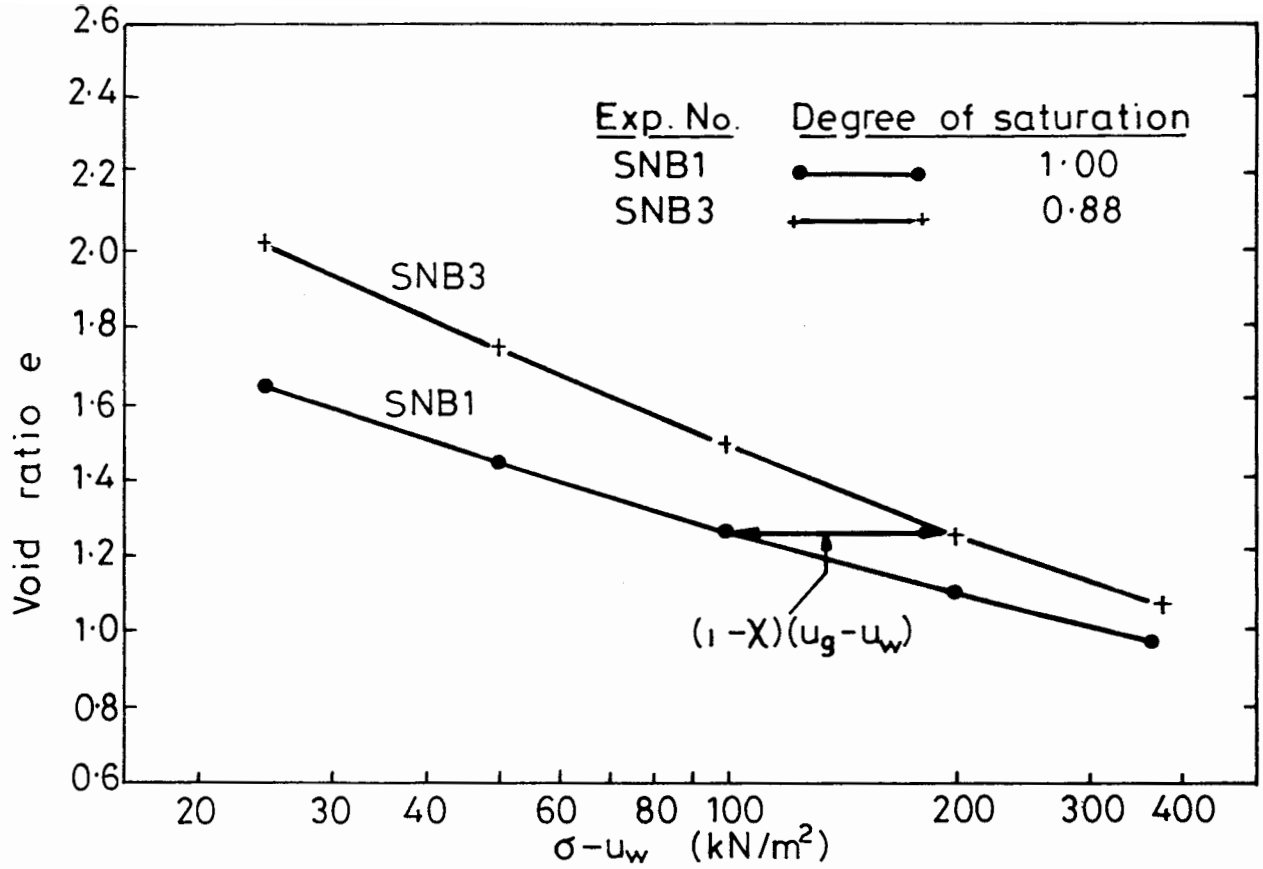

Fig.1·11. APPLICATION OF BISHOP'S EFFECTIVE STRESS LAW TO ONE-DIMENSIONAL CONSOLIDATION RESULTS. (Data from Nageswaran)

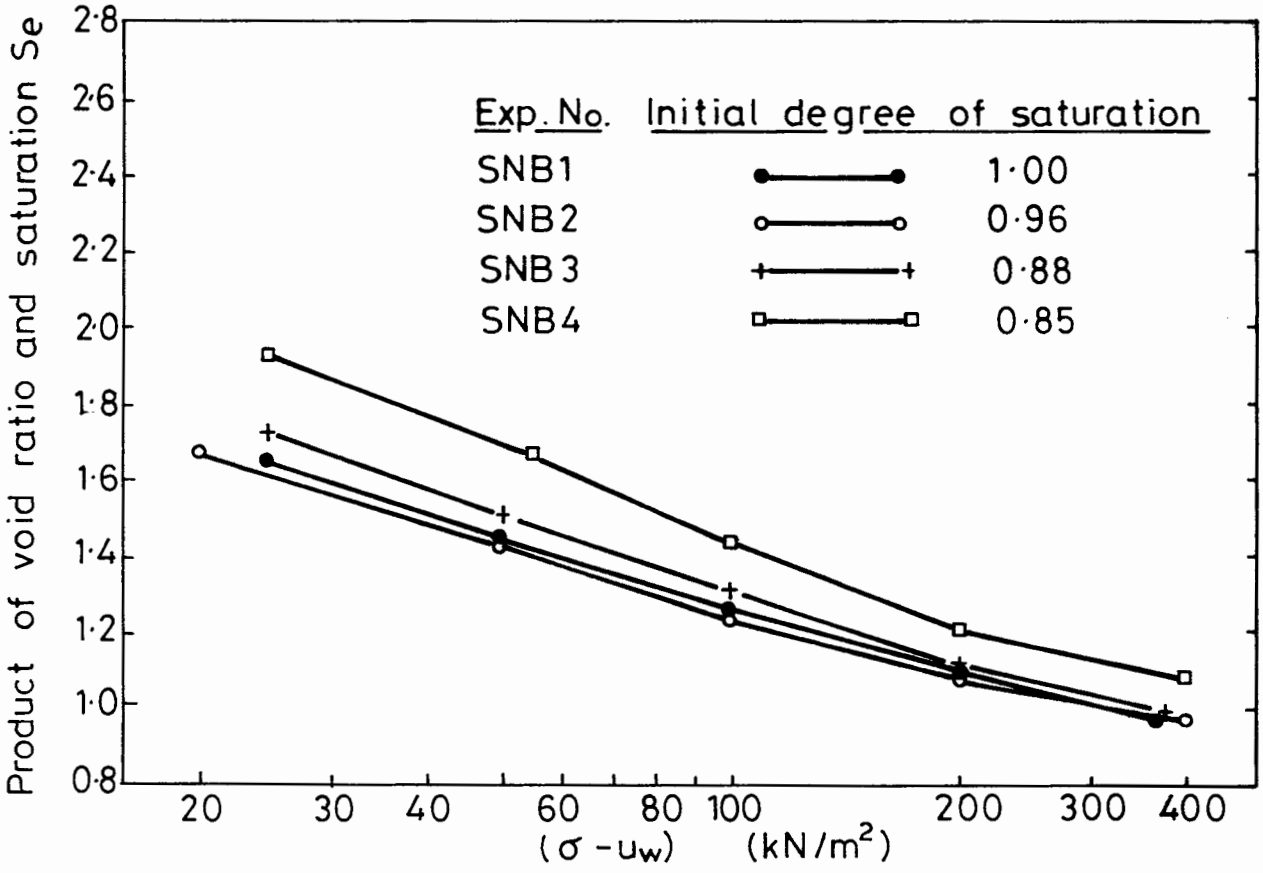

Fig. 1·12. PRODUCT OF VOID RATIO AND SATURATION DURING ONE - DIMENSIONAL CONSOLIDATION (Nageswaran)

With the obvious failure of the single effective stress approach, Nageswaran looked for an alternative way of interpreting the results. Because of the difficulty of measuring u_g there was no possibility of plotting the volume behaviour in terms of the stress variables $(\sigma - u_g)$ and $(u_g - u_w)$, as described in Section 1.3.2. Some theoretical developments by the author, presented in Chapter 7, suggested that the results of consolidation tests might show better correlation if the product of saturation and void ratio (Se) was plotted against $(\sigma - u_w)$ (instead of plotting e against $(\sigma - u_w)$). Figure 1.12 shows Nageswaran's results presented in this fashion (only tests on samples containing discrete bubbles are included). The figure shows that plotting the results in this way brings them much closer to a unique line. However, there is still some scatter and a noticeable trend of increasing (Se) with increasing gas content. Nageswaran finally tried plotting $(1 + e)S$ against $(\sigma - u_w)$, as shown in Figure 1.13. This purely empirical relationship gave results very close to a unique line.

Nageswaran (1983) used the results of his laboratory tests in the development of a theoretical model for the one-dimensional consolidation of soils containing gas bubbles. He used a large strain continuity expression, similar to that given by Gibson, England and Hussey (1967). Nageswaran assumed that the gas and water acted as a single compressible pore fluid and, on the basis of his laboratory test results, he related void ratio and stress by a unique curve of (Se) plotted against $(\sigma - u_w)$ (this appeared to have greater theoretical justification than a unique relationship between $(1 + e)S$ and $(\sigma - u_w)$, which empirically fitted rather better). His model was therefore a slightly hybrid affair, as the continuity expression was based on a single pore fluid, which is probably only realistic for small, occluded bubbles (Figure 1.2(a)), while the assumption of a unique (Se) : $(\sigma - u_w)$ curve is certainly not the constitutive relationship that would be expected from such a structure. Nageswaran completed his model by assuming a constant permeability

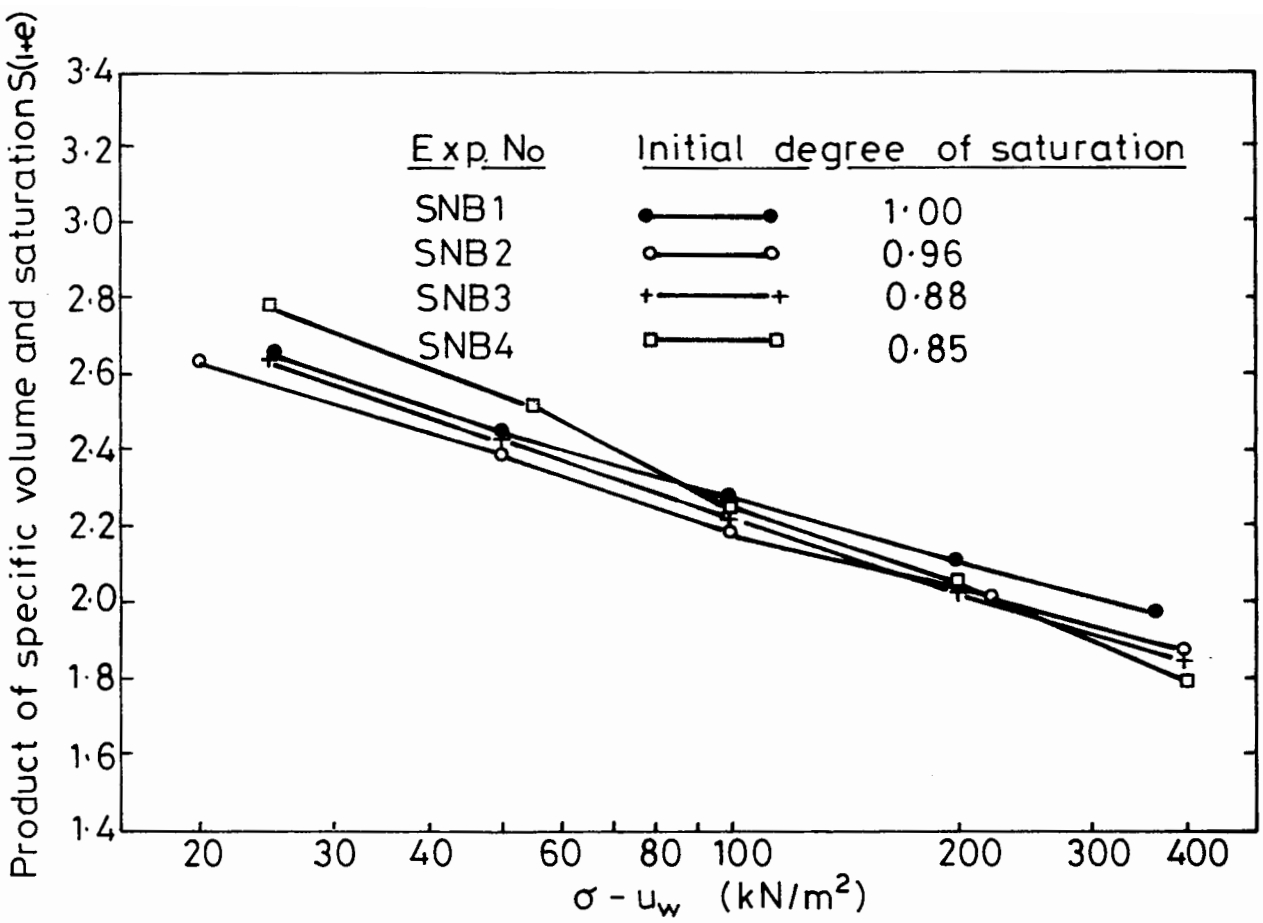

Fig. 1·13. PRODUCT OF SPECIFIC VOLUME AND SATURATION DURING ONE-DIMENSIONAL CONSOLIDATION (Nageswaran)

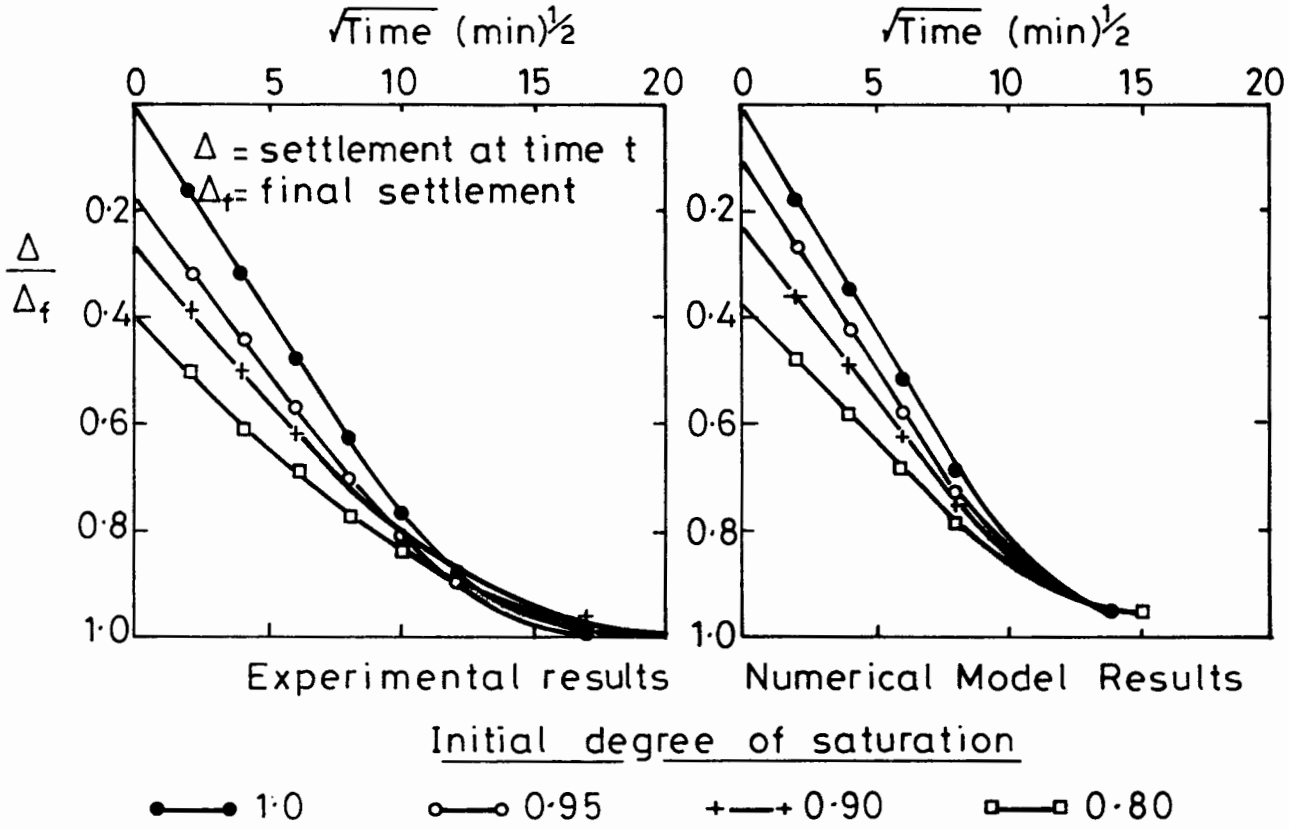

Fig. 1·14. PERFORMANCE OF NAGESWARAN'S NUMERICAL MODEL FOR ONE — DIMENSIONAL CONSOLIDATION.

k and an expression for the pore fluid compressibility β_f which allowed for the solubility H, but not for any difference butween u_g and u_w.

Nageswaran used a finite difference method to solve the equations set up in his model. He presented results for standard one-dimensional consolidation which were in close agreement with the laboratory tests. As the experimental data were used to provide the relationship between (Se) and $(\sigma - u_w)$ it is hardly surprising that the values of the final settlement showed good agreement. However, the modelling was also very successful for both the initial undrained settlement and the time dependent part of the response (Figure 1.14).

As a second demonstration of the consolidation model, Nageswaran derived numerical results for a cyclic variation in total stress, corresponding to a tidal effect. Again, good agreement between theoretical and experimental results was achieved.

Nageswaran completed his work with a very brief experimental study of the undrained shear strength of reconstituted gassy samples. A series of vane tests indicated that the presence of gas bubbles caused a reduction in the undrained strength. Three undrained triaxial tests provided confirmation of this result.

1.5 OBJECTIVES OF THE WORK DESCRIBED IN THIS THESIS

The subsequent chapters of this thesis describe further experimental and theoretical developments in the field of unsaturated soils. The programme of work was planned with the intention of improving the present level of understanding of the behaviour of soils containing discrete gas bubbles. Such developments are of particular significance to the offshore construction industry, if platforms, pipelines and other structures are to be built in areas of gas-bearing sediments. If these structures are to be designed safely and accurately, considerably more knowledge is required of the effect

of gas bubbles on the engineering properties of marine soils. The work is also of relevance to coastal engineering works (harbours, sea defences and dredging of navigation channels) which could also be affected by the presence of gas bubbles.

One question of particular importance to the designers of offshore structures is the effect of gas bubbles on the shear strength of a marine soil. The experimental work described in this thesis consists of a series of undrained triaxial tests designed to answer this question. These tests should directly complement Nageswaran's work on the one-dimensional consolidation of soils containing gas bubbles.

The series of triaxial tests was designed to show the effect of different variables on the undrained shear strength of gas-bearing soils. However, the test series also provides useful information on the stress-strain behaviour prior to failure, the generation of pore pressures during shearing, the elastic moduli and the isotropic consolidation behaviour.

The theoretical developments described in this thesis are an attempt to provide a model for the behaviour of soils containing gas bubbles. The hope was that, by restricting the analysis to those soils containing gas in the form of discrete bubbles, more progress could be made than by attempting to derive a single model relevant to all unsaturated soils. However, it was hoped that the same conceptual model could be used to cover all aspects of soil behaviour, including consolidation, shear strength and elastic properties. This would have considerable advantages over a series of disconnected concepts each modelling a different aspect of soil behaviour.

CHAPTER 2

A MODIFIED TRIAXIAL APPARATUS

2.1 Sample size

2.2 Measurement of volume change

- 2.2.1 Method of measurement
- 2.2.2 Prevention of leakage from cell
- 2.2.3 Change of cell volume with pressure and temperature
- 2.2.4 Water absorption by the perspex cylinder
- 2.2.5 Accuracy of volume change measurement

2.3 Measurement of cell pressure and pore pressure

2.4 Measurement of axial displacement and axial load

2.5 Diffusion of gas through the membrane

CHAPTER 2

A MODIFIED TRIAXIAL APPARATUS

Figure 2.1 shows a general view of the modified triaxial cell designed and built at Oxford for the testing of unsaturated soil samples. Two of these cells were used in the series of undrained triaxial tests. The design was based on the cell used by Bishop and Donald (1961), but a number of important modifications were incorporated. The modifications, and the reasons for them, are described in this chapter.

2.1 SAMPLE SIZE

At an early stage in the design of the cell the sample size was fixed at 38 mm diameter. This small size was chosen so that consolidation and testing could take place relatively quickly, allowing a large number of tests to be conducted in the limited time available. Also, earlier work at Oxford, by Dr G. Austin, had suggested that preparation of larger reconstituted samples containing gas bubbles could be difficult. In fact this latter worry proved to be groundless, but the argument of speed continued to apply. Samples with a diameter much greater than 38 mm would also have resulted in a correspondingly larger and heavier cell. This would have caused additional handling problems, as the de-airing procedure required that the partly-assembled cell be lifted bodily from a water bath into the loading frame (see Section 3.2 of the next chapter).

The small size of the samples did not cause problems of non-homogeneity, as might have been feared, because the sample dimensions were still considerably greater than those of a typical bubble (0.1 mm to 1 mm diameter).

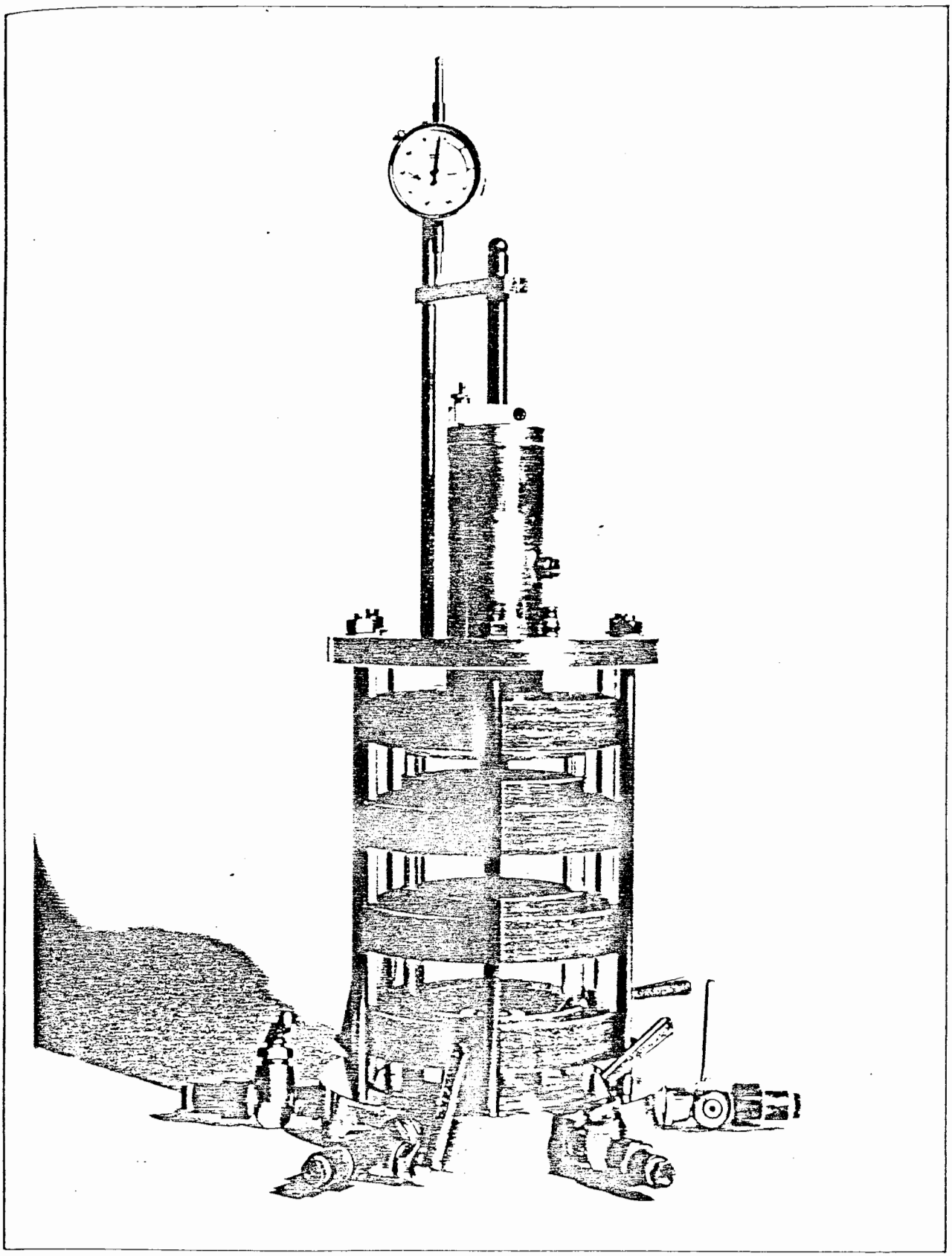

Fig. 2·1. THE MODIFIED TRIAXIAL CELL.

2.2 MEASUREMENT OF VOLUME CHANGE

The most significant changes to the triaxial cell were all associated with the need to measure the volume change independently of the flow from the sample. As explained in Section 1.3.4 of Chapter 1, this need arose because compression of the gas resulted in volume changes in addition to those due to drainage. If the state of the sample was to be known at all times during a test, these volume changes had to be monitored.

2.2.1 Method of Measurement

The method chosen for measuring sample volume change used the same principle as employed by Bishop and Donald (1961) of monitoring the effect on the surrounding cell fluid. However, instead of partly filling the cell with mercury and then measuring the displacement of the mercury surface, the cell was completely filled with water and the flow into the cell was measured with a burette (see Figure 2.2). This avoided the need for two cell fluids, as a fluid interface was no longer required. The change of design also improved the accuracy of measurement, as the displacement of the meniscus in the burette was considerably greater than that of the mercury surface in Bishop and Donald's apparatus (because the cross-sectional area of the burette was much less than that of the cell). Finally, the new method was less cumbersome than Bishop and Donald's technique, because it avoided the use of a cathetometer (an instrument which was likely to be very sensitive to disturbance during a test lasting several days or weeks).

An alternative means of measuring sample volume change would have been to measure separately the axial and lateral strains of the sample. The lateral strain could have been measured with a variety of devices. These included a mechanical caliper arrangement (Bishop and Henkel, 1962), strain-gauged feelers (Matyas and Radhakrishna, 1968) and proximity

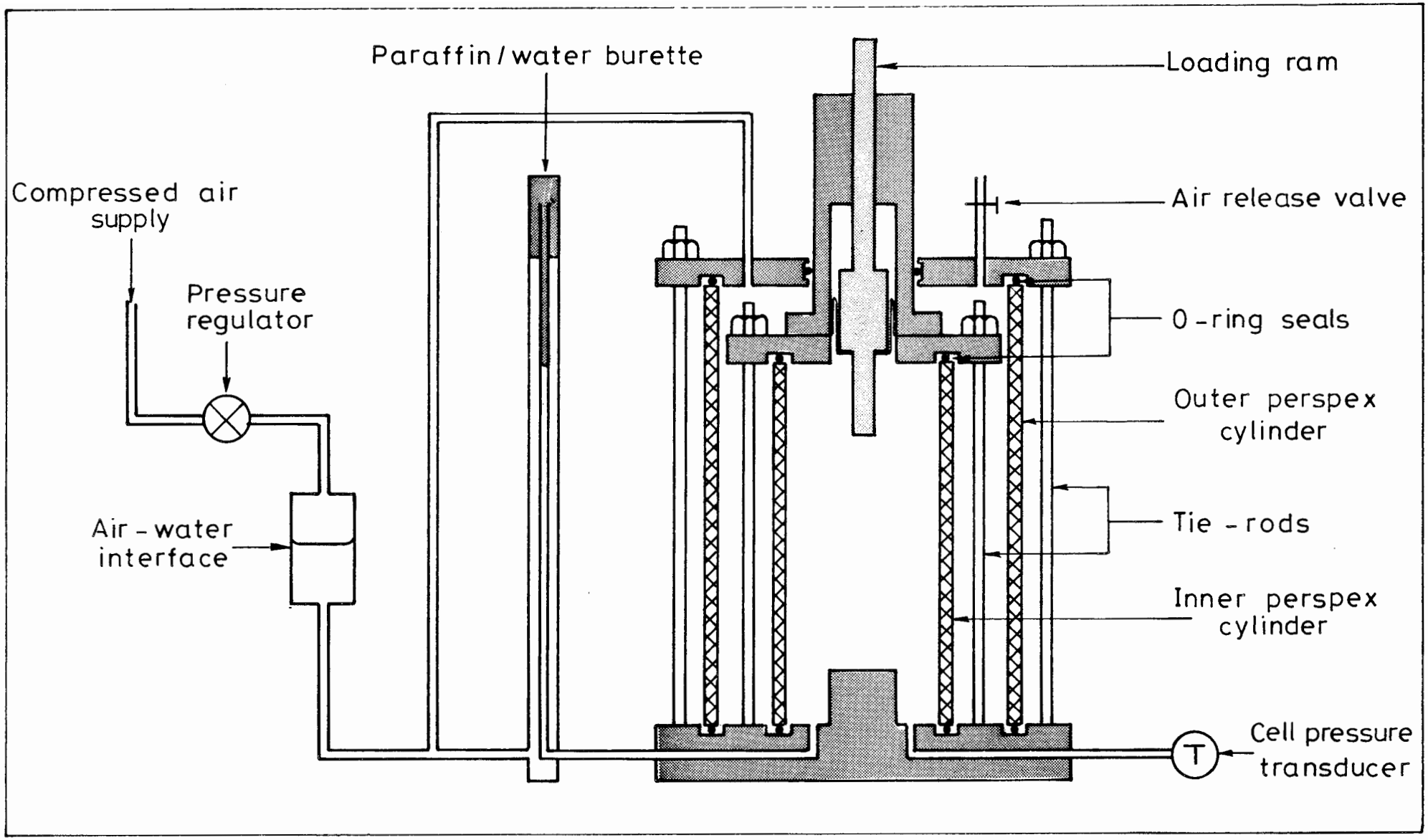

Fig. 2·2 MODIFIED TRIAXIAL APPARATUS.

transducers sensing the distance between the transducer and aluminium foil targets on the sample (Cole, 1978). Various methods of measuring axial strain were available, such as the electrolytic level gauges described by Burland and Symes (1982). The displacement of the loading ram would not have been an adequate measure of axial strain, as this could have been used for only the shear testing stage and not during the initial consolidation stage and the final swell-back stage.

The chosen method of measuring sample volume change was selected over the alternative approach for two reasons. Firstly, the reading that was required was the volume change of the whole sample, rather than just that of a specific gauge length, because the reading had to be combined with measurements of sample weight and volume taken at the end of the test. The chosen method was ideally suited to this requirement, while the alternative was not, particularly if the sample deformed non-uniformly. The second reason was that experimental difficulties were foreseen with the alternative method, in trying to attach the various gauges to a sample only 38 mm in diameter.

2.2.2 Prevention of Leakage from Cell

Having decided to measure volume changes by recording the flow into the cell, all leakage of cell fluid had to be avoided. Leakage around the top and bottom of the perspex cylinder forming the cell wall was prevented by seating the cylinder in grooves within the cell base and top plate. O-rings within these grooves were compressed to form pressure-tight seals by the tension in three tie-rods spanning between the top plate and the cell base (see Figure 2.2).

The main source of fluid leakage from a normal triaxial cell is around the loading ram, where the standard bushing provides an imperfect seal. A layer of oil floating on the water within the cell reduces the

leakage but does not prevent it completely. In the modified cell this problem was solved by the use of a rolling diaphragm seal on the loading ram. The arrangement is illustrated in Figures 2.3 and 2.4. The 12.7 mm ($\frac{1}{2}$") diameter stainless steel shaft forming the loading ram moved within a cylinder bolted to the top plate of the cell. Friction-free alignment of the ram was provided by a pair of linear bearings seated in the upper half of the cylinder. In the lower half of the cylinder was the rolling diaphragm seal, with the "convolution" of the seal lying between the cylinder and the loading ram (which was of increased diameter at this section). The outer flange of the diaphragm was clamped between the cylinder and the top plate of the cell, and the inner flange was clamped between two sections of the loading ram. As the ram moved vertically the convolution of the diaphragm rolled or unrolled. Maximum stroke of the ram was about 65 mm.

To keep the convolution of the diaphragm properly inflated and free from wrinkles, a minimal pressure difference was required across the diaphragm. When the cell was at atmospheric pressure this pressure difference was maintained by connecting the interior of the cylinder to a vacuum line. During shear testing, when the cell pressure was normally well above atmospheric, the cylinder was vented to the atmosphere, to prevent pressure fluctuations on the vacuum line affecting the force on the ram.

Each cell was calibrated for the volume displaced by movement of the ram. Provided that a pressure difference was maintained across the diaphragm, the relationship between volume displaced and ram movement was remarkably linear. Over the entire 65 mm stroke the calibration curves deviated by less than $\pm$ 0.05 cm^3 from a straight line, and for the stroke of 10 to 15 mm required for a typical test the deviation was less than 0.02 cm^3. The slope of the calibration curve (the effective area of the ram) was 13.99 cm^2 for the first cell and 13.95 cm^2 for the second.

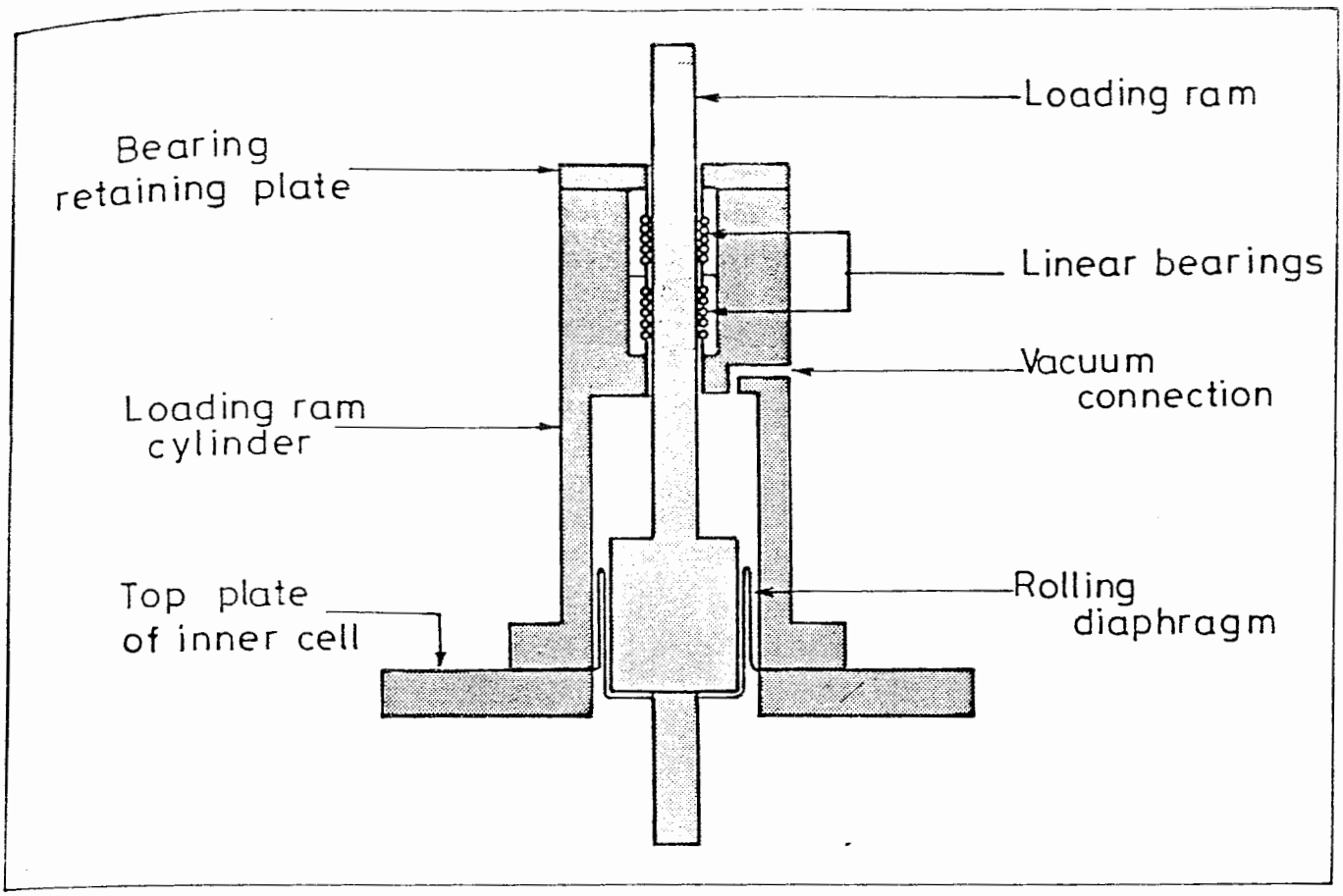

Fig. 2-3. LOADING RAM AND CYLINDER ASSEMBLY.

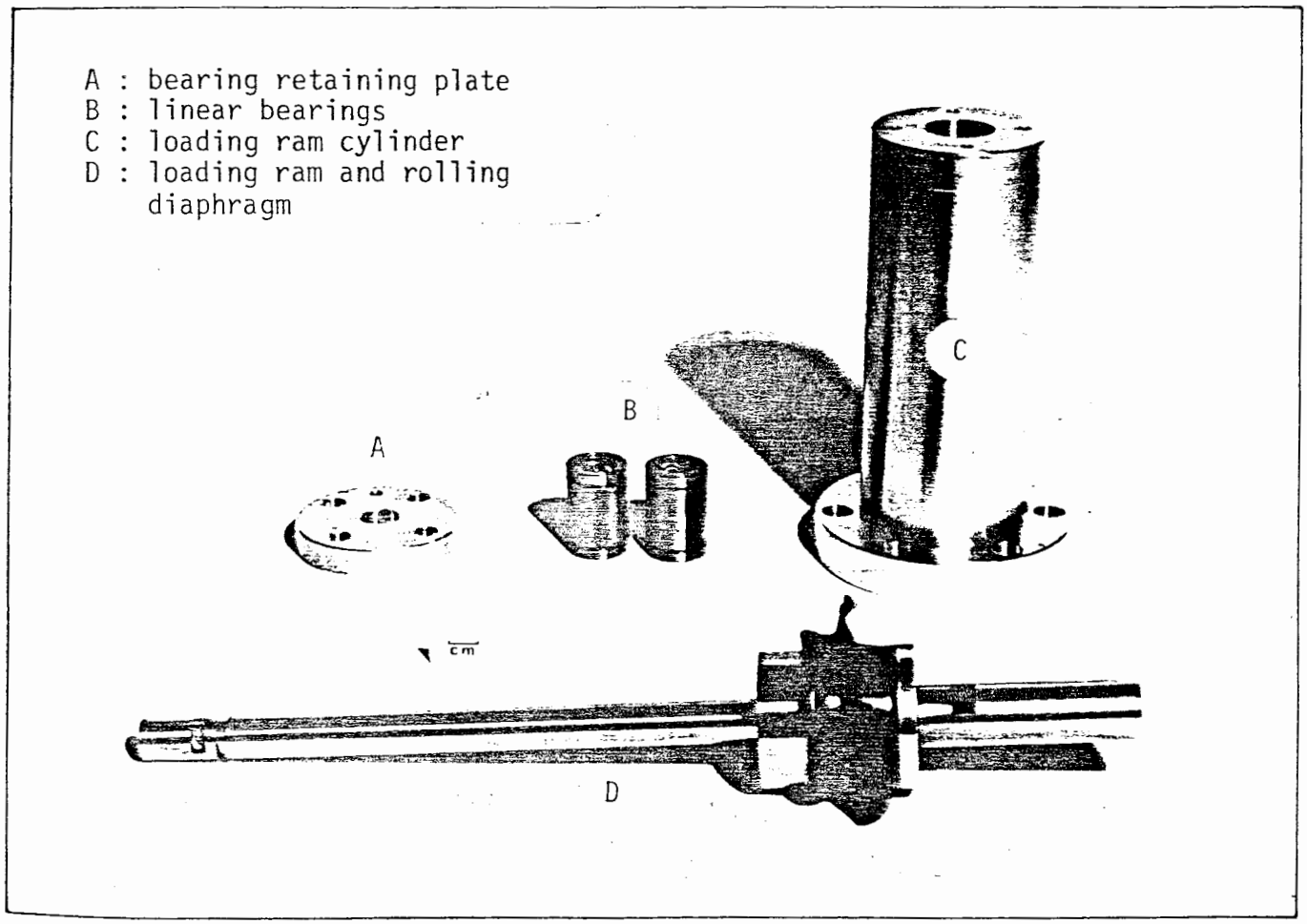

Fig. 2-4. COMPONENTS OF LOADING RAM AND CYLINDER.

To avoid entrapment of air in the diaphragm convolution during filling of the cell, assembly of the apparatus took place under water. The procedure is described in Section 3.2 of Chapter 3.

2.2.3 Change of Cell Volume with Pressure and Temperature

To avoid the problems of cell volume changing with cell pressure, a double-walled construction was used, as shown in Figure 2.1. The annulus between the inner and outer cell walls was always maintained at the same pressure as the inner cell, by the simple method of connecting them to the same pressure supply (Figure 2.2). The pressure connections were arranged so that the burette only measured the flow into the inner cell. With no pressure difference across the inner cell wall there should have been no tendency for any volume change of the inner cell. Bishop and Donald used this same idea for the internal jacket surrounding the mercury in their cell.

Figures 2.5 and 2.1 illustrate the double-walled arrangement. Figure 2.5 shows the basic inner cell, with the cell base, perspex cell wall and the loading ram cylinder bolted to the top plate. The banded perspex cylinder forming the cell wall was from a standard commercial triaxial cell for testing 38 mm or 50 mm samples. Figure 2.1 shows the complete cell. The outer cell wall was seated in O-ring grooves within the cell base and the top plate of the outer cell. The top plate was assembled by sliding it into position down the loading ram cylinder, another O-ring forming the seal on the sliding surface (see Figure 2.2). Six tie-rods spanning between the cell base and the top plate of the outer cell withstood the force exerted by the cell pressure. The banded perspex cylinder forming the outer cell wall was from a commercial triaxial cell for testing samples up to 70 mm diameter.

Fig. 2·5.
INNER CELL.

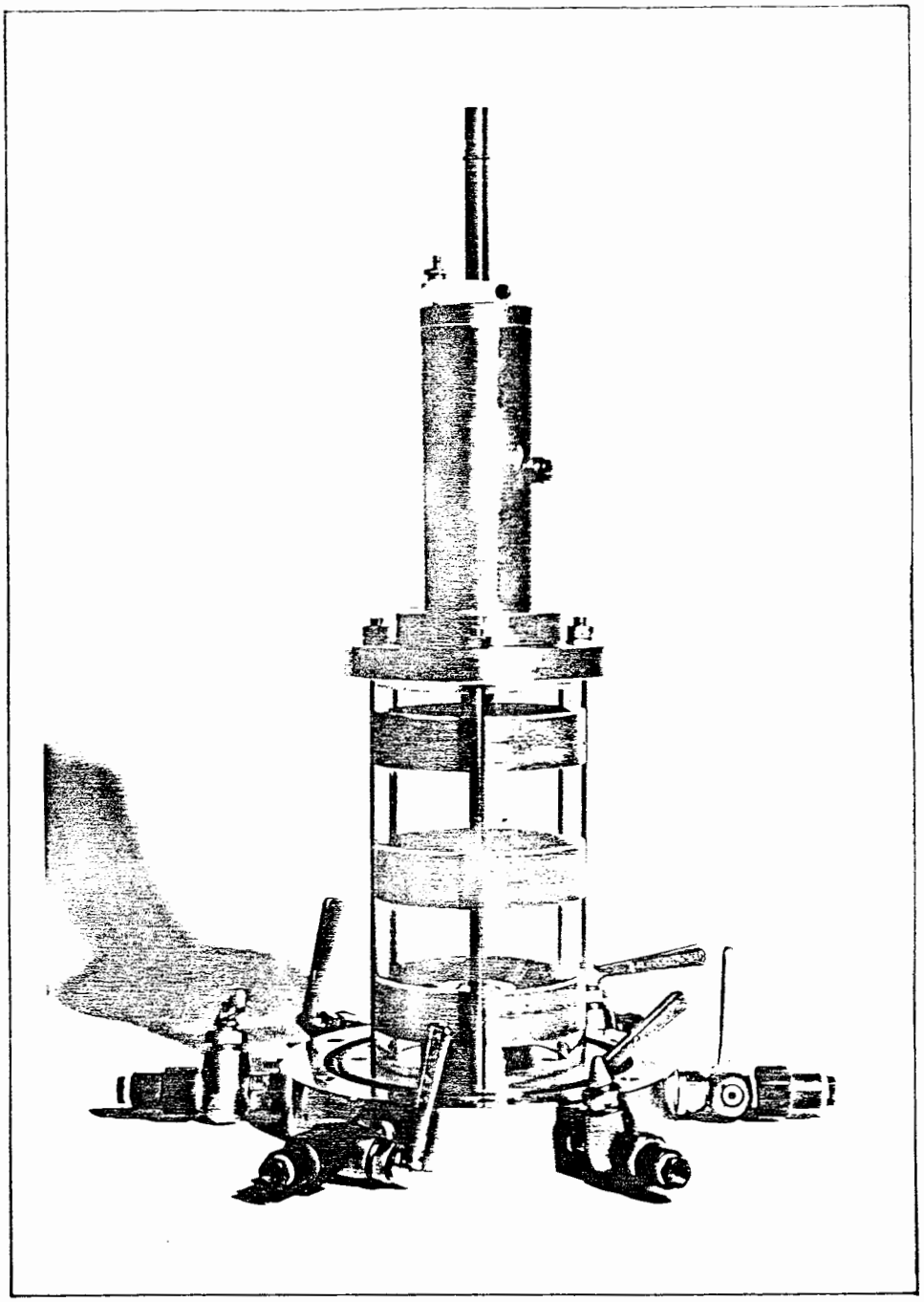

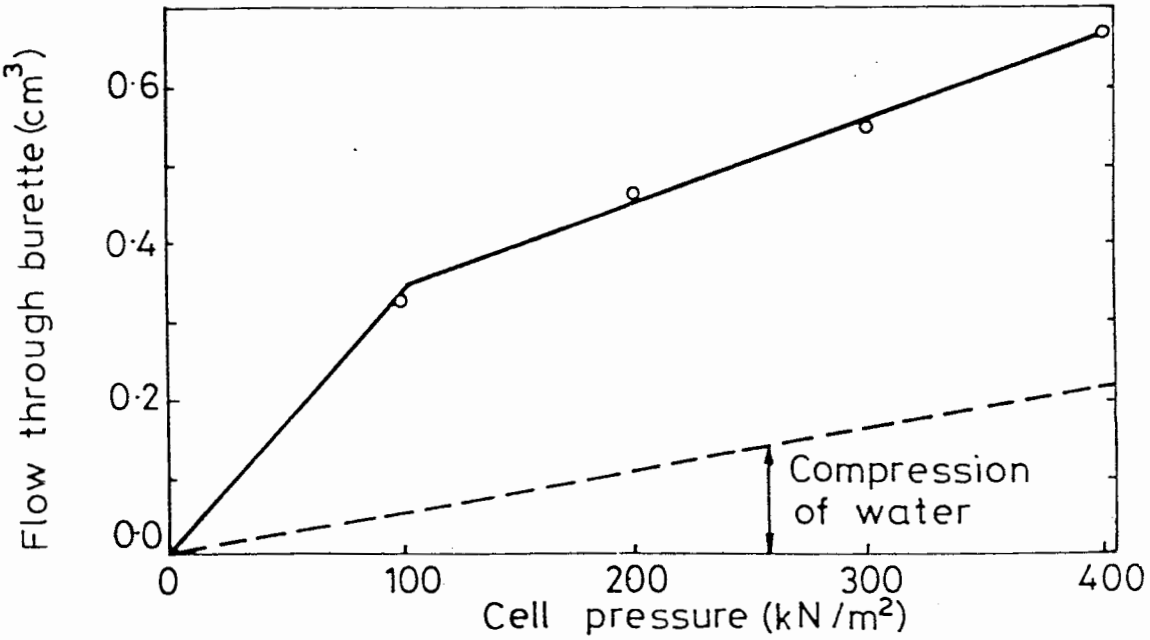

Fig. 2·6. TYPICAL CELL PRESSURE CALIBRATION.

Originally it was hoped that the complication of a double-walled arrangement could be avoided by simply calibrating for the change of cell volume with pressure. Unfortunately this was found to be impossible, because the stress-strain curve for the perspex cylinder showed marked hysteresis, considerable creep effects and very poor repeatability. These problems could have been avoided by replacing the perspex cylinder with one made from a simple, elastic material, such as brass or stainless steel. However, this solution was not adopted, because of the disadvantage of being unable to see the sample during a test.

An interesting problem came to light with a prototype version of the cell. On this prototype, the normal fibreglass reinforcing bands were omitted from the inner perspex cylinder, on the grounds that there should have been no pressure difference across the cylinder. However, it was found that an increment of cell pressure created a transient pressure difference across the inner cell wall. This pressure difference was caused by the fact that the pressures in the inner cell and the annulus took time to respond to a pressure increment applied at the air-water interface and the response times of the two were not the same. The flexure of the unreinforced perspex cylinder due to the transient pressure difference was sufficient to cause considerable volume change of the inner cell. This volume change was not repeatable, being critically dependent on the speed with which the pressure increment was applied. The problem was solved by using reinforcing bands on the inner cell wall. These bands increased the stiffness of the inner cell by a factor of several hundred, which was sufficient to prevent the adverse effects caused by transient pressure differences.

Despite the double-walled arrangement it was still necessary to calibrate each cell for apparent volume change with pressure. The remaining small volume changes were due to three different effects:

compression of the water in the cell; expansion of the short lengths of connecting tube and the valves on the cell outlets; and slight flexure of the top plate of the inner cell. The last effect occurred because the inner cell was not totally enclosed by the outer cell (where the loading ram cylinder passed through). Flexure of the top plate should have been fairly repeatable, as the tie-rods were always tightened to the same torque.

Figure 2.6 shows the pressure calibration curve for one of the cells. The initial non-linearity occurred on both cells and was probably caused by slackness in the valves and tube fittings, which was taken up by the first increment of cell pressure. The compression of the water, calculated from the bulk modulus, accounted for about one third of the total volume change. It was difficult to separate the remaining effects, but not particularly important. All that really mattered was the overall calibration. It was important to remember that the calibration referred not only to the cell but also to the connecting tubing, and a new calibration was required every time the tubing was modified. The accuracy of each calibration was considered to be about $\pm$ 0.05 cm^3.

Temperature variations would have caused major inaccuracies in the measurements of sample volume change, because of thermal expansion of the cell components and the water within the cell. These problems were avoided by controlling the laboratory temperature to within 1^oC. The period of the temperature fluctuations in the laboratory was considerably shorter than the time required to heat up the large volume of water in the cell, so the variation in the temperature of the cell and its contents was probably much less than 1^oC.

2.2.4 Water Absorption by the Perspex Cylinder

Before being used to test soil samples, the first cell was filled with water and extensively tested and calibrated. The testing brought to light an unexpected problem: the perspex cell walls were absorbing water. This absorption caused swelling of the inner cylinder, so that the internal volume increased. The result was a flow of water into the cell, to replace the water absorbed by the perspex and to take up the extra volume created by the swelling. Unfortunately, this aspect of perspex behaviour was not appreciated at the time (although it was documented by the manufacturer, ICI) and a period of two months was spent in trying to track down a non-existent leak from the cell.

The rate of water absorption depended upon the cell pressure and the water content of the perspex. For a particular cell pressure there was an equilibrium water content for the perspex, and absorption slowed as this water content was approached. However, the time taken to reach 95% of the full absorption was about nine months. The manufacturer's data for water absorption at atmospheric pressure are presented in Figure 2.7. The figure shows curves for total immersion in water and also for absorption in air at various relative humidities (when the equilibrium water contents are correspondingly lower). It was obvious that even if the cell were left for nine months, until water absorption had effectively ceased, absorption would begin again as soon as the cell pressure was changed. This meant that some alternative method of preventing absorption, or calibrating for the effect, had to be found.

Attempts were made to prevent the water absorption by coating the inner cylinder with a waterproofing spray or a polyurethane varnish (the latter tentatively recommended by the perspex manufacturer). Neither was successful. The manufacturer was also contacted for advice on a suitable cell fluid that would not be absorbed by the perspex; again without success.

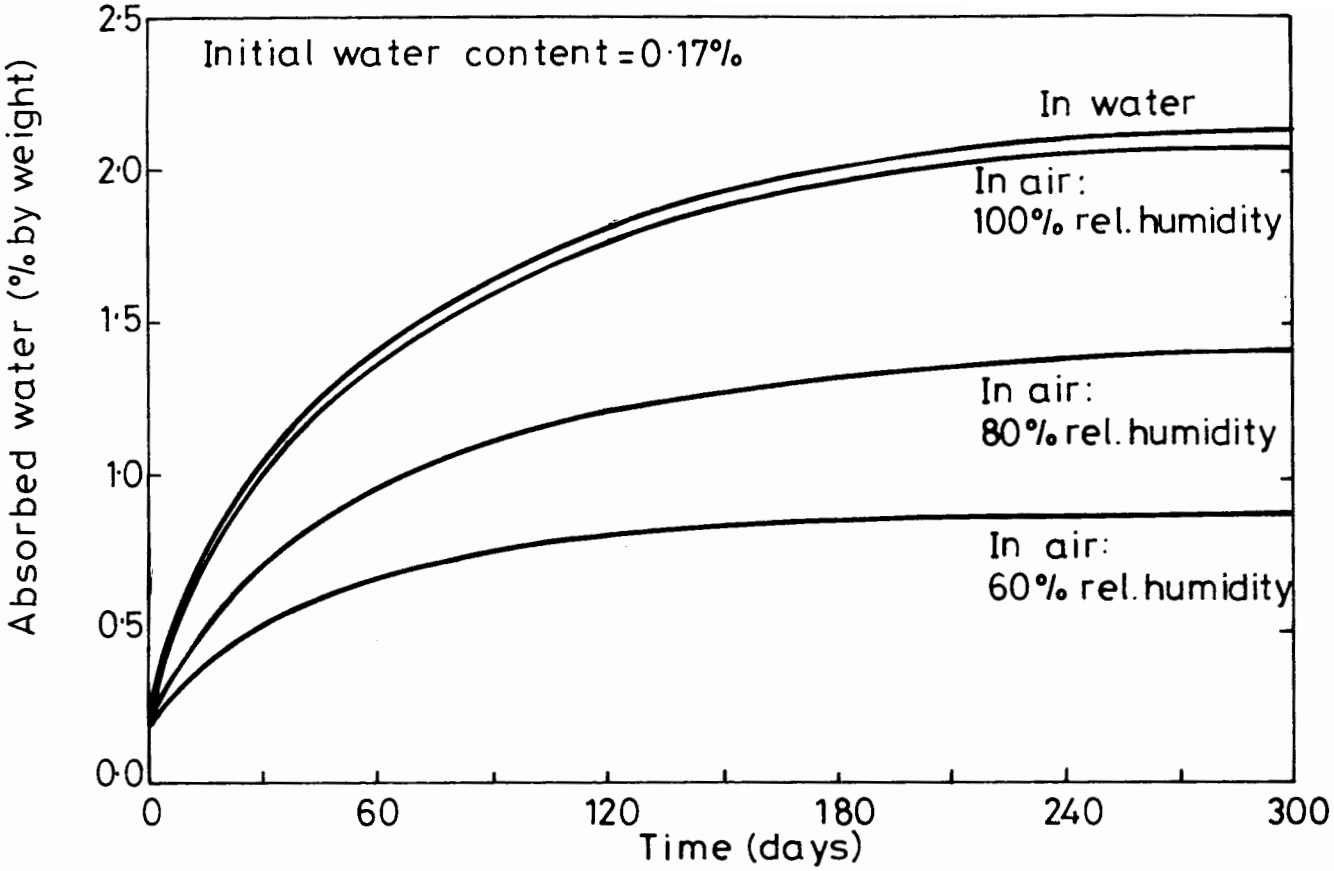

Fig. 2·7. WATER ABSORPTION BY PERSPEX AT ATMOSPHERIC. PRESSURE.

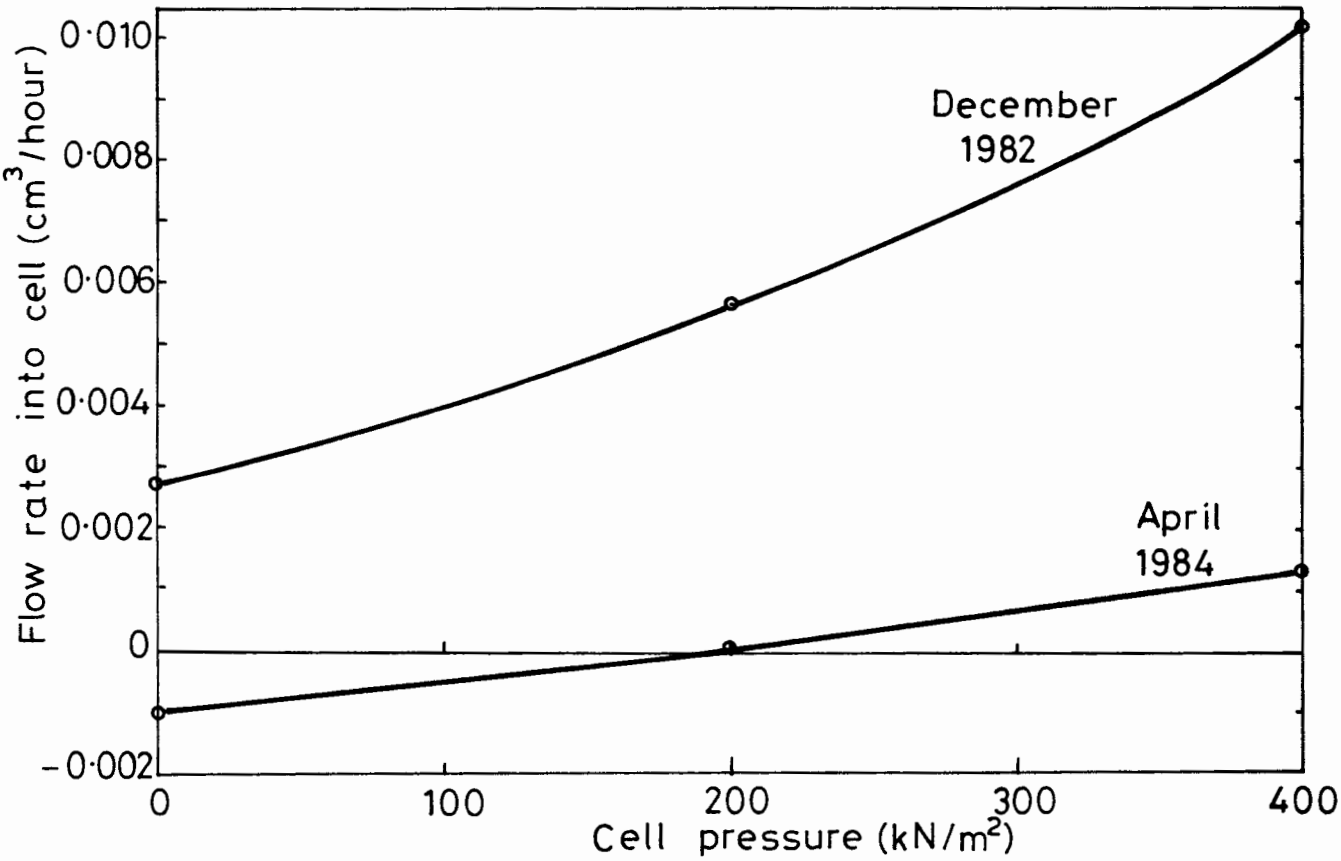

Fig. 2·8. TYPICAL CALIBRATIONS FOR WATER ABSORBTION.

Once more the possibility of replacing the perspex with another material was considered. However, the transparency of perspex still counted strongly in its favour (a glass cylinder was temporarily considered, but this idea was abandoned on the advice of other research workers who had attempted to use glass for similar purposes).

Finally, the decision was taken that calibration for the absorption effect would be acceptable, provided that two precautions were taken. The first precaution was to store the inner cylinder under water, even when no test was in progress, because this kept the water content of the perspex high and the rate of absorption down. The second precaution was to recalibrate the cell frequently, to allow for the changing water content of the perspex.

Calibration curves were made by recording the flow into the cell at various pressures, over a period of several days. Figure 2.8 shows two calibration curves for the same cell. In December 1982, at the start of triaxial testing, the rate of absorption was quite high: about 0.01 cm^3/hour at a cell pressure of 400 kN/m^2. Absorption at this rate had a noticeable effect on the measurements of volume change. By April 1984, towards the end of the series of tests, the rate of absorption had fallen considerably, down to about 0.001 cm^3/hour at 400 kN/m^2, because of permanently storing the perspex under water. Absorption at this rate was hardly significant for the measurements of volume change. The rate of change of the calibration curve also slowed considerably, so that while recalibration was done monthly for the first six months, it was only done every two months from then on.

The calibration for the water absorption effect was probably accurate to about 0.0005 cm^3/hour. Over the 10 to 12 hours required for shear testing, this would provide an accuracy better than $\pm$ 0.01 cm^3.

2.2.5 Accuracy of Volume Change Measurement

The burette used for measuring the flow into the inner cell had a range of 25 cm^3 (without reversing the direction of flow), and could be read to an accuracy of 0.01 cm^3. For a brief trial period the burette was replaced with an automatic volume change transducer manufactured by Imperial College. This device had a range of 50 cm^3, an accuracy of 0.01 cm^3 and the added advantage that measurements of volume change could be logged automatically. However, the transducer was found to be more susceptible to errors caused by gas bubbles than the traditional burette. This was because the gas collected within the transducer, whereas in a burette the bubbles floated to the top where they had no effect on the reading. This problem was of particular significance because of the unsaturated nature of the samples being tested. Gas was obviously present within the sample and it was always difficult to be totally sure that gas had not diffused into other parts of the system. The problem was exacerbated by the fact that the interior of the transducer was invisible, because of the metal construction, so it was never possible to check for the presence of any gas. This resulted in a lack of confidence in the readings, even when the device was working properly. The decision was therefore taken to revert to a traditional burette.

With the burette reading to 0.01 cm^3; the calibration for the effect of loading ram displacement accurate to 0.02 cm^3; and the correction for water absorption accurate to 0.01 cm^3, the overall accuracy for the measurement of sample volume change was about $\pm$ 0.04 cm^3. This figure referred to the 10 to 12 hour period required for shear testing, provided that no change in cell pressure took place. For the entire test procedure, including initial consolidation and final swell-back, the accuracy was rather lower: about $\pm$ 0.16 cm^3. The difference was due to the accuracy of the calibration for cell pressure and the longer time available for water absorption.

The accuracy quoted above was not applicable for the first few hours after the cell was assembled. During this period two separate effects caused additional errors. Firstly, the de-aired water filling the cell was normally at an initial temperature different to that of the laboratory, because the water was stored in a tank outside the temperature controlled area. Expansion or contraction of the water, as the temperature adjusted to that of the laboratory, produced an error in the volume change measurement. Secondly, small bubbles of air were sometimes trapped inthe cell during assembly, and solution of these in the de-aired water caused an apparent volume change. However, the reduced accuracy during the first few hours of operation had no effect on the overall accuracy of volume change measurement. This was because the changes of sample volume were all related to conditions at the end of the test, when the sample weight and volume were measured, and the volume of the sample at the start of the test was not important.

For a typical 38 mm sample,the total void volume was about 40 cm^3. This meant that the accuracy of 0.04 cm^3 achieved during the shear stage corresponded to an error of about $\pm$ 0.001 in the degree of saturation ($\pm$ 0.1% if the saturation was expressed as a percentage). This is illustrated by Figure 2.9 which shows the measured variation in saturation during an early test on a sample which was initially very close to saturated. The degree of saturation increased noticeably during the first part of the test, as the small quantity of gas compressed and went into solution. At an axial strain of about 3% the sample reached full saturation and the plot remained horizontal until the end of the test. The scatter of less than $\pm$ 0.001 on the latter part of the curve confirmed the accuracy of the measurement technique.

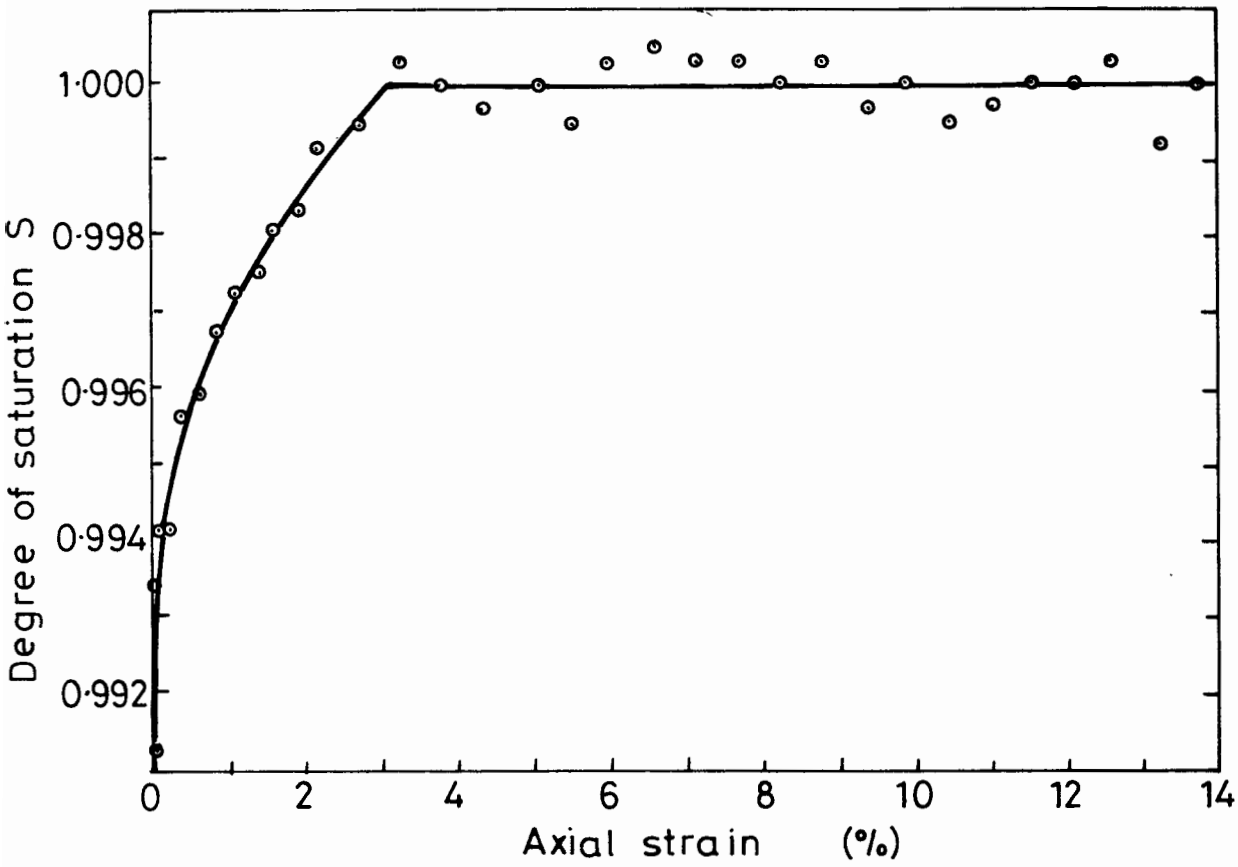

Fig. 2·9. VARIATION IN DEGREE OF SATURATION: TEST No.11

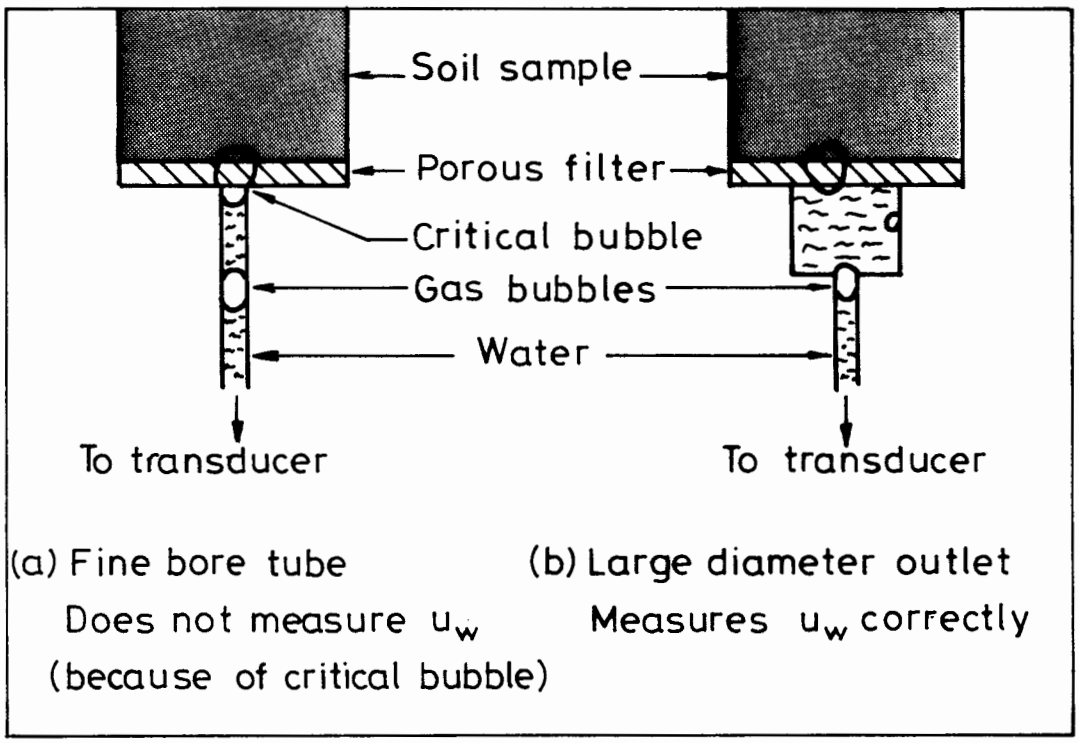

Fig. 2·10. EFFECT OF DIFFUSED GAS ON MEASUREMENT OF PORE WATER PRESSURE (Nageswaran, 1983)

2.3 MEASUREMENT OF CELL PRESSURE AND PORE PRESSURE

The cell pressure was measured with a standard pressure transducer. The connection between the cell and the transducer was entirely separate from the tube connecting the cell to the burette and the pressure supply (Figure 2.2). The pressure recorded by the transducer was thus unaffected by any pressure drop along the fine-bore tube carrying the flow to the cell. The electrical output of the transducer could be read to whatever accuracy was desired, depending solely upon the accuracy of the voltmeter. However the stability of the transducer was such that the true accuracy of the measurement was probably about $\pm$ 1 kN/m^2.

The pore water pressure u_w was measured at the base of the sample with a pressure transducer connected to the cell by a very short length of fine-bore tube (to minimise the compliance of the system). Again, the accuracy of the transducer was probably about $\pm$ 1 kN/m^2. Careful attention was given to the design of the measuring system, to ensure that gas diffusing through the high air entry filter did not affect the pressure reading. This was achieved by using a large diameter channel immediately behind the filter, as described by Nageswaran (1983) and illustrated in Figure 2.10. Two separate connections were provided to the base of the sample, so that bubbles of diffused gas trapped below the filter could be flushed from the cell and measured (see Section 3.3). During the consolidation and swell-back stages these same connections were used for drainage of the sample.

From an early stage in the development of the cell, it seemed likely that measurement of the gas pressure u_g would prove to be impossible, because the gas was in the form of discrete bubbles (see Section 1.3.4, Chapter 1). A brief attempt was made to measure u_g, using an idea put forward by Nageswaran (1983). He found that a fine-bore tube connected to a high air entry filter gave an elevated reading of pore pressure, which he attributed to a bubble of diffused gas blocking the tube and

extending back through the filter into the soil (Figure 2.10). He suggested that this elevated reading of pore pressure might in some way be representative of the gas pressure within the soil. This idea was examined in the first triaxial tests, by using a fine-bore outlet on one of the two connections to the base of the sample. This did indeed give pore pressure readings that were sometimes higher than those from the large diameter outlet, confirming the effect reported by Nageswaran. However, the measurements were highly unrepeatable, suggesting that the measured pressure did not represent the gas pressure within the soil, and the idea was not pursued further.

No facilities were provided for drainage or pore pressure measurement at the top of the sample. This would have been more difficult than with saturated samples, as two separate connections would have been required, so that diffused gas could be flushed away.

With the pore water pressure measured at the base, the speed at which undrained tests could be conducted was determined by the equalization of pore pressure throughout the sample (Bishop and Henkel, 1962). During the developemnt of the cell, the possibility of using lubricated end plattens was considered. These would have produced more uniform conditions throughout the sample, allowing a faster strain rate to be used. The lubricated ends would also have prevented concentrations of stress and volume change which might affect the stress-strain behaviour (Rowe and Barden, 1964). However, a decision was finally made against the use of lubricated ends, because of the experimental complications involved. It was considered unlikely that the effects of end restraint would be markedly different for saturated and unsaturated samples, so that comparisons between different tests would still be quite valid without the use of lubricated ends.

2.4 MEASUREMENT OF AXIAL DISPLACEMENT AND AXIAL LOAD

The axial displacement of the loading ram was measured with a dial gauge mounted on the top plate of the outer cell; the dial gauge plunger resting on an arm attached to the loading ram (Figure 2.1). The dial gauge reading of ram displacement was used to calculate the axial strain of the sample. As well as being easier than measuring the strain directly on the sample, this method was more consistent with the measurement of sample volume change, because it gave the average axial strain of the complete sample, rather than the strain of some reduced gauge length. The dial gauge was used instead of an LVDT or some other automatic device, because it was already necessary to record the burette reading manually, so no real advantage could be gained by automatic logging of the loading ram displacement. The reading of the dial gauge was accurate to $\pm$ 0.01 mm. This was equivalent to an axial strain of just over 0.01%.

A clamp mounted on the top of the loading ram cylinder (Figure 2.1) was used to prevent movement of the ram when the sample was not being loaded. During the consolidation and swell-back stages the ram was clamped at the top of its stroke, well clear of the sample (see Chapter 3).

The axial load was measured outside the cell, with a proving ring reading to an accuracy of $\pm$ 0.2 N. An internal load cell was not required, because the friction on the loading ram was very low and, more importantly, very constant. In fact, there was no detectable variation of the friction, within the accuracy of the proving ring. This was a consequence of separating the two functions normally fulfilled by the bushing: sealing the cell and aligning the ram. In the modified cell the seal was provided by the rolling diaphragm, and the ram alignment by the linear bearings. This idea, of separating the two functions of the bushing, could be very useful for all triaxial cells as a means of avoiding the complication and expense of internal load cells.

When measuring the axial load it was important to remember to disconnect the vacuum line from the loading ram cylinder, leaving it open to the atmosphere. Otherwise fluctuations of pressure on the vacuum line affected the reading on the proving ring. A neat innovation was included on the second of the two cells to be built, to avoid the possibility of inadvertantly leaving the vacuum line connected. The clamp on the loading ram also acted as a seal to the cylinder, so that as soon as the clamp was released, to allow the ram to move, the cylinder was automatically vented to the atmosphere.

2.5 DIFFUSION OF GAS THROUGH THE MEMBRANE

No special precautions were taken against the diffusion of gas through the membrane, as the evidence indicated that no significant diffusion was taking place. Measurements taken during the consolidation stage showed that volume change was effectively complete after four days, for both saturated and unsaturated samples. The unsaturated samples still contained a considerable quantity of gas at this point, and if movement across the membrane was taking place this gas would have been expected to diffuse through into the de-aired water filling the cell. However, there was no evidence whatsoever of this taking place, as the volume of the samples remained almost constant after the four day period. This behaviour contrasted with the experience of Bishop and Donald (1961), who found considerable gas diffusion. Perhaps the difference was due to the fact that Bishop and Donald tested samples containing continuous gas voids, rather than discrete bubbles.

In the absence of any evidence for gas diffusion through the membrane, there was obviously no reason to follow Bishop and Donald's example of using mercury as the cell fluid. This had considerable advantages. Mercury would have been unpleasant to work with, and the very high density would have caused significant variation in the lateral stress over the height of the sample.

CHAPTER 3

TRIAXIAL TESTING PROCEDURE

3.1 Sample preparation

3.2 Setting up in the triaxial cell

3.3 Isotropic consolidation in the cell

3.4 Shear testing

3.5 Saturation stage

3.6 Swell-back stage

3.7 Measurement of wet and dry weights

3.8 Processing of the results

3.9 The programme of tests

CHAPTER 3

TRIAXIAL TESTING PROCEDURE

This chapter describes the experimental procedure that was used for the series of undrained tests in the modified triaxial apparatus.

3.1 SAMPLE PREPARATION

The soil used for the series of tests was a clayey silt from the estuary of the River Parett at Combwich in Somerset. Samples were tested in a reconstituted form, rather than in a natural state. Combwich Mud was chosen for two reasons. Firstly, it was a real, natural material from the sort of environment where gas-bearing sediments might be found. Secondly, Nageswaran's one-dimensional consolidation tests were on this material, and it was considered important that the series of triaxial tests should complement his work. To balance these favourable points, the Combwich Mud did have a number of disadvantages when compared with a material such as Kaolin, which is commonly used in laboratory tests. Firstly, the properties of the Combwich Mud probably varied considerably more than those of Kaolin (which is prepared commercially in very large quantities). Secondly, the coefficient of consolidation of the Combwich Mud was only one tenth that of Kaolin, so tests took 10 times as long; and finally, the salt content of the Combwich Mud caused corrosion of any metal components in contact with the sample.

The liquid and plastic limits of the Combwich Mud were about 55% and 27% respectively. The coefficient of consolidation, from Nageswaran's tests, was about 5×10^{-8} m^2/s. The specific gravity of the soil grains was 2.64 and the particle size distribution is shown in Figure 3.1. Occasional large items, including worms and vegetable matter, were removed by wet sieving through a standard 63 μm mesh. This left only the clay and silt sized particles, which in the natural state formed more than 98% of the solid volume. Tap-water was used for the wet sieving process, bringing the salinity down from the natural level of 11 parts per thousand to about 3 parts per thousand.

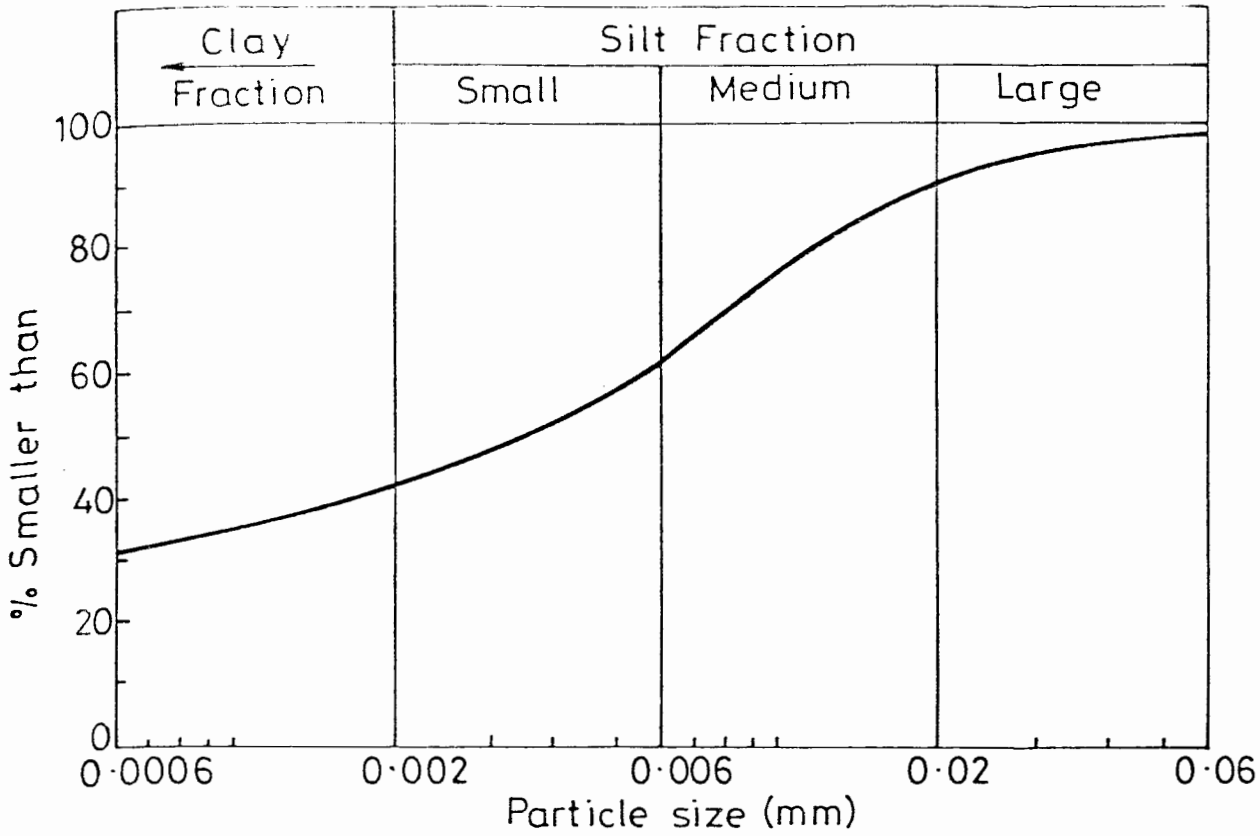

Fig. 3·1. PARTICLE SIZE DISTRIBUTION OF COMBWICH MUD.

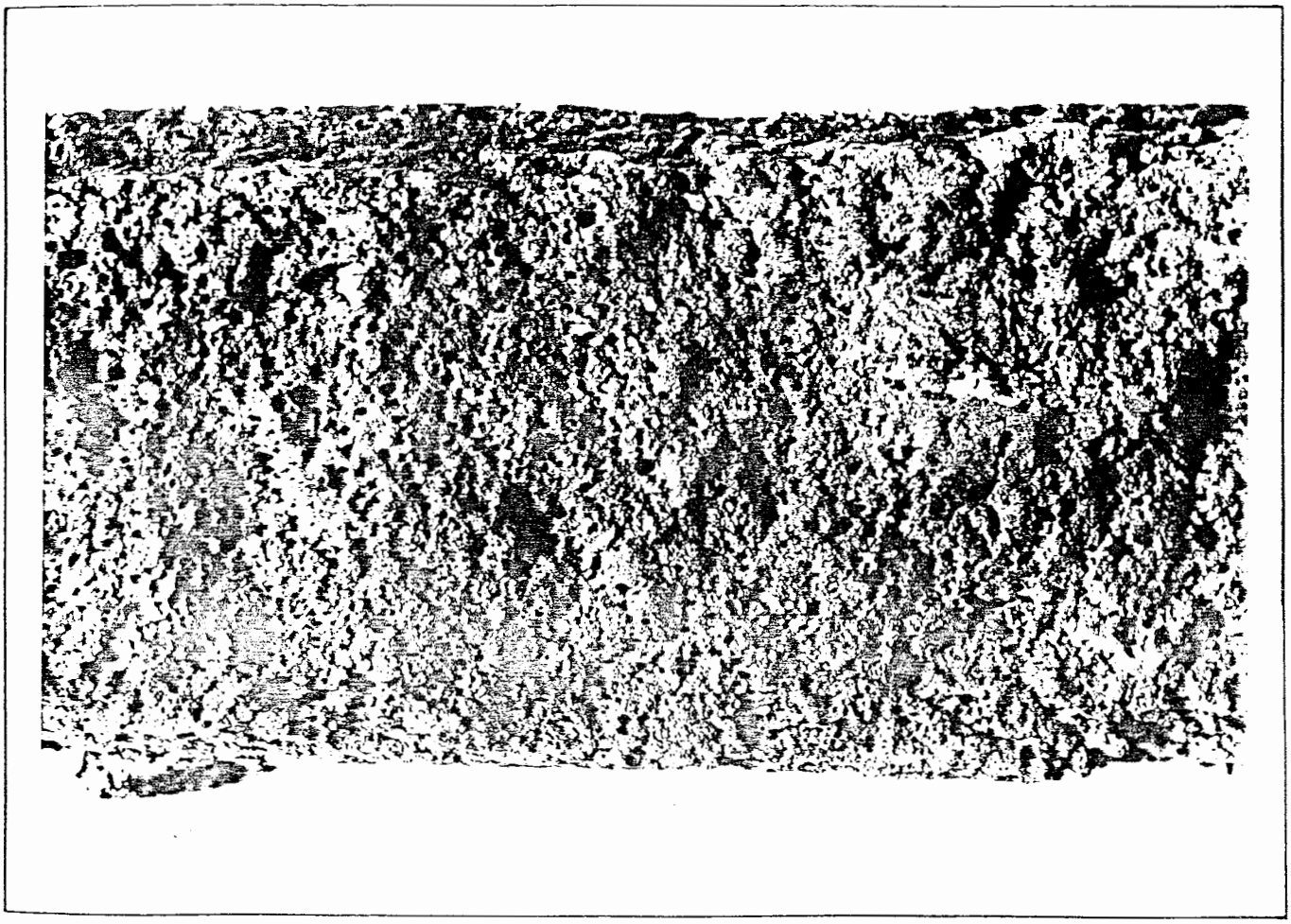

Fig. 3·2. APPEARANCE OF GASSY SOIL. MAGNIFIED X 6.
Degree of Saturation=0·8. 1-D Consolidation to 35kN/m^2
(Nageswaran 1983)

A controlled distribution of methane bubbles was introduced in the laboratory. Methane was selected by Nageswaran as being the gas most commonly found in marine sediments.

The bubbles of gas were produced by using the "zeolite molecular sieve technique", described in detail by Nageswaran (1983) and Sills and Nageswaran. The zeolites are a group of inert chemicals with a very strong affinity for polar molecules such as water. They have the important property that if the water of hydration is removed by heating, the crystal structure remains intact, and other molecules of a suitable size can be taken into the zeolite crystal (Breck, 1974). If a dried zeolite is impregnated with gas and then mixed with a soil slurry, the zeolite will take up the water from the slurry in preference to the gas, which is released to form bubbles.

Various types of natural and synthetic zeolite are commercially available. The choice of zeolite was made by comparing the molecular diameter of methane, which is 4.0 Ångstrom, with the pore size available in the different zeolite crystals. Zeolite Type 5A ($Ca_{4.5}Na_3(AlO_2)_{12}30H_2O$), which has a pore diameter of 5.0 Ångstrom, was chosen as the most suitable (Fieser and Fieser, 1967). This zeolite was also available in powder form, with a particle size of less than 6 μm - very similar to that of Combwich Mud. The specific gravity of zeolite 5A is 2.42.

The zeolite was dried for 24 hours in an oven, at a temperature of 105°C, to remove the water of hydration. After this it was placed in an evacuated chamber, at -70 to -80 kN/m^2, for 24 hours to remove most of the air from the crystals, leaving the largest possible pore volume available for the methane. The zeolite was then impregnated with methane, at a pressure of 200 kN/m^2, for 24 hours. This should have ensured that the maximum possible quantity of methane was taken up, as Nageswaran (1983) found that a pressure of 100 kN/m^2 and an absorbtion time of 10 hours was sufficient to fill the entire available pore space.

The methane saturated zeolite was mixed with a slurry of Combwich Mud, to form a soil-zeolite slurry at a void ratio of 4.0. This high void ratio (corresponding to a water content of about 150%) ensured that the zeolite powder mixed evenly with the slurry.

Because the physical properties of the soil and the zeolite were not identical (Nageswaran, 1983), it was important that the different samples, with different gas contents, all contained the same volume of zeolite particles. The decision was taken that 20% of the volume of solids would be zeolite, the remaining 80% being soil particles. After adding the desired quantity of methane saturated zeolite, the remainder of the zeolite volume was made up with water saturated zeolite, prepared as a slurry at a void ratio of 4.0. It was important that the water saturated zeolite did not contain any air. This was ensured by stirring the zeolite slurry for 24 hours in an orbital shaker, before it was mixed with the soil slurry and the methane saturated zeolite.

With zeolite forming 20% of the solid content, the average specific gravity of the particles was reduced to about 2.60.

The final mixing of the various constituents was conducted as fast as possible, to minimise the amount of methane that escaped from the soil. Nageswaran (1983) conducted tests to study the speed at which methane was released from the zeolite, and on the basis of his results it appeared that the quantity of methane lost during mixing and transfer to the consolidation apparatus would be very small.

The slurry was poured into 38 mm diameter moulds for initial one-dimensional consolidation, and the first load was applied immediately, using a hanger and weights. This contrasted with the procedure used by Nageswaran. He waited 24 hours, for the release of all the gas, before applying any stress. However, it was found that a more uniform distribution of gas bubbles was produced if the load was applied immediately, so that the soil was already consolidating as the gas was released.

The samples were drained at both ends, to increase the speed of consolidation, and the load was applied in two increments, to avoid high pore pressure gradients while the soil was still very soft. Most of the samples were consolidated with an applied load of 50 kN/m^2, although the stress on the sample was probably rather lower, because of friction on the walls of the tube. This was the lowest stress at which gas-bearing samples could be extruded and set up in the triaxial cell. Figure 3.2 shows the type of soil structure present at about this stress level. The photograph shows one of Nageswaran's samples consolidated one-dimensionally to a stress of 35 kN/m^2. The sample shown in the figure contained a considerable quantity of gas (the degree of saturation was about 0.8) and the bubbles are clearly visible.

Some thought was given to the idea of consolidating the samples from a slurry directly on to the base of the triaxial cell, using a split-former arrangement (Loudon, 1967). This would have avoided the sample disturbance due to extrusion from the mould and transfer to the triaxial cell. However, it was decided that the effects of this disturbance were not particularly severe, as the sample was re-consolidated to a higher stress level in the cell. Consolidation directly on to the cell base would have resulted in a slower rate of testing, because the cell would have been occupied for several extra days during the initial one-dimensional consolidation stage. Therefore the idea was dropped.

The gas bubbles produced by the zeolite molecular sieve technique were typically 0.1 mm to 1 mm in diameter. Comparison with the particle size distribution in Figure 3.1 shows clearly that the bubbles were considerably larger than the size of a typical soil particle. This was considered to be representative of the situation that would normally occur in marine sediments (Anderson and Hampton, 1980).

3.2 SETTING UP IN THE TRIAXIAL CELL

About three days after applying the last load increment, the one-dimensional consolidation was complete, and the sample was ready for transfer to the triaxial cell.

The first step in the procedure of setting up the sample was to de-air the valves on the cell and the various connections within the cell base, by flushing with de-aired water. There were a total of five connections: two to the inner cell (one from the burette, the other from the pressure transducer); one to the outer cell; and two to the base of the sample. The two drainage lines to the base of the sample ran through the cell base to a perspex pedestal on which the sample was to be mounted (Figure 3.3). A porous filter was glued to the top of the pedestal. Below the filter were the wide diameter outlets of the two drainage lines, linked by an annular groove, to allow flushing from one line to the other. The pedestal was secured to the cell base by four small bolts, with O-rings providing seals on the two drainage lines. As the perspex pedestal was transparent, it was easy to check that the drainage connections were completely de-aired.

The sample was trimmed to the correct length, and then extruded from the mould on to the pedestal. A perspex loading cap was placed on top (Figure 3.3), and a rubber membrane was slipped over the sample, using a membrane stretcher (Bishop and Henkel, 1962). After removing any air trapped between the membrane and the sample, rubber O-rings were used to secure the membrane at the top and bottom. A slight negative back pressure was applied to the base of the sample, by sucking gently on one of the drainage connections, to stabilise the sample on the pedestal. Finally, a stainless steel ball was placed in the seat within the loading cap.

The next stage of the setting up procedure was the assembly of the inner cell, the components of which are shown in Figure 3.4. To ensure that

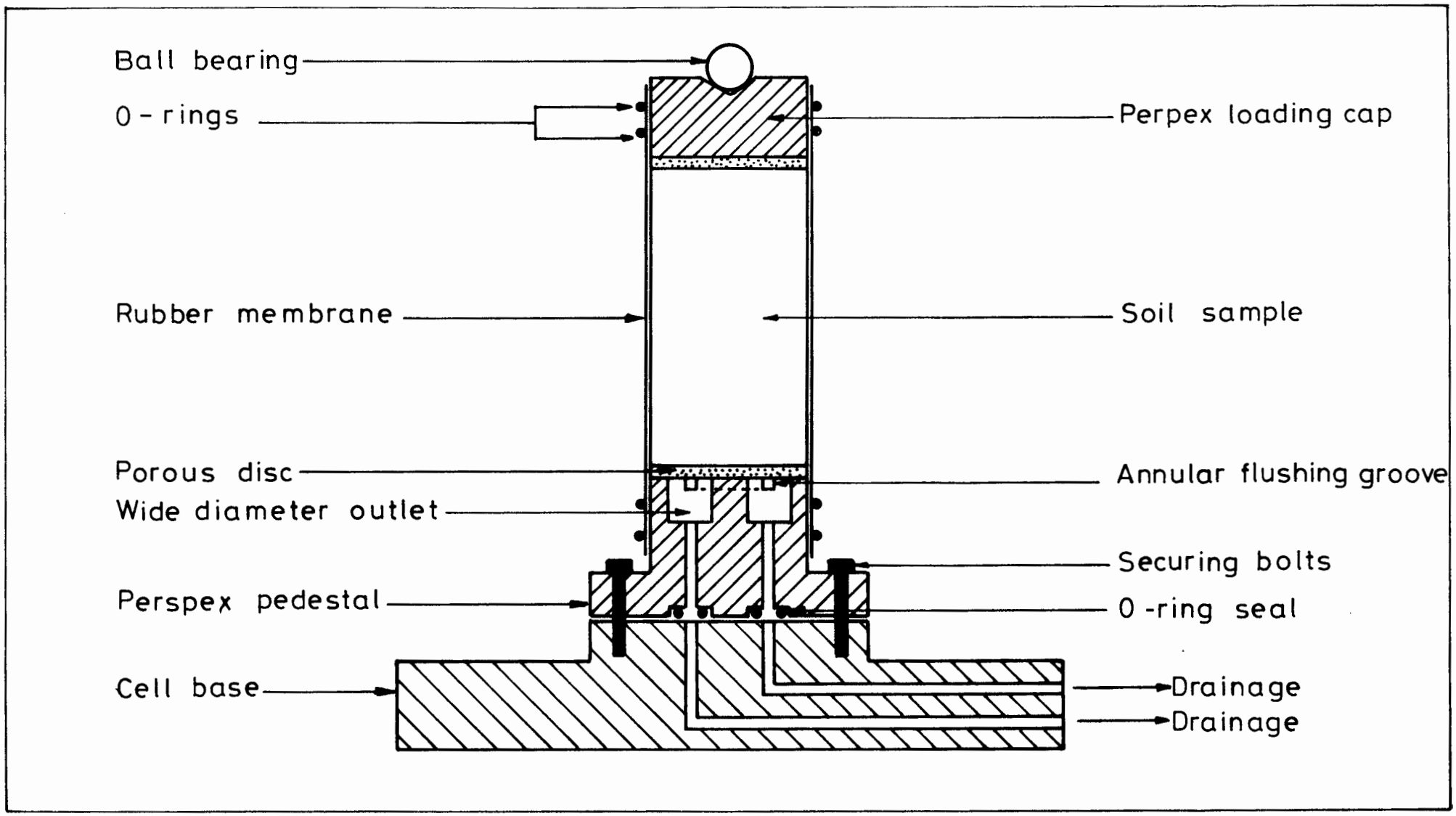

Fig. 3·3. PERSPEX PEDESTAL AND SOIL SAMPLE.

the convolution of the rolling diaphragm was properly de-aired, the assembly took place under water. The cell base, complete with the sample, was transferred to a large glass tank, which was then filled with de-aired water from the piped supply available in the laboratory. The tank was large enough to take both cells simultaneously, so that two samples could be set up at the same time.

While the tank was filling with water, the convolution of the rolling diaphragm was de-aired. After connecting a vacuum line to the rolling diaphragm cylinder, to inflate the convolution, the entire top plate assembly was turned upside down. The convolution was then filled with de-aired water, using a syringe and hypodermic. This operation was performed most satisfactorily with the loading ram clamped in a mid-stroke position. After filling the convolution the ram was moved to the top of its stroke and clamped again, so that it would not foul the sample as the cell was assembled. The top plate assembly was then lifted into the tank, still upside down. Finally, the perspex cell wall was removed from underwater storage and placed in the tank with the other components of the inner cell.

When the tank was full, the perspex cell wall was placed over the sample and located in position within the O-ring groove in the cell base. Keeping the rolling diaphragm permanently under water, the top plate assembly was inverted and placed on top of the cell wall, the perspex cylinder fitting within the O-ring groove. After opening the valve on one of the cell outlets (to avoid pressurising the cell), the three tie-rods were inserted and tightened to a carefully controlled torque. The valve was then closed and the assembled cell was lifted from the tank into the loading frame of the compression machine.

The next stage was the assembly of the outer cell, the components of which are shown in Figure 3.5. The perspex cylinder forming the outer cell

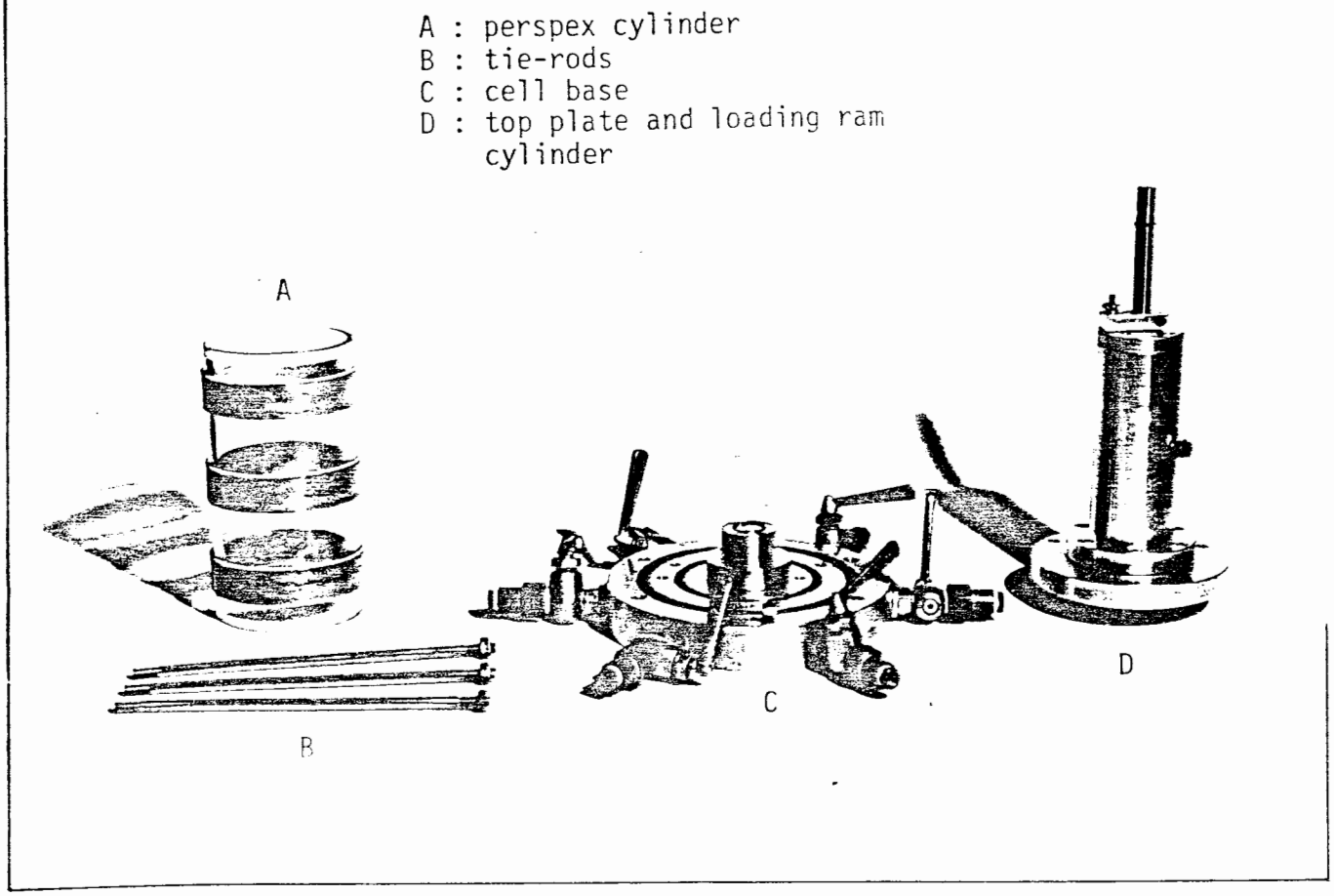

Fig. 3·4. COMPONENTS OF INNER CELL.

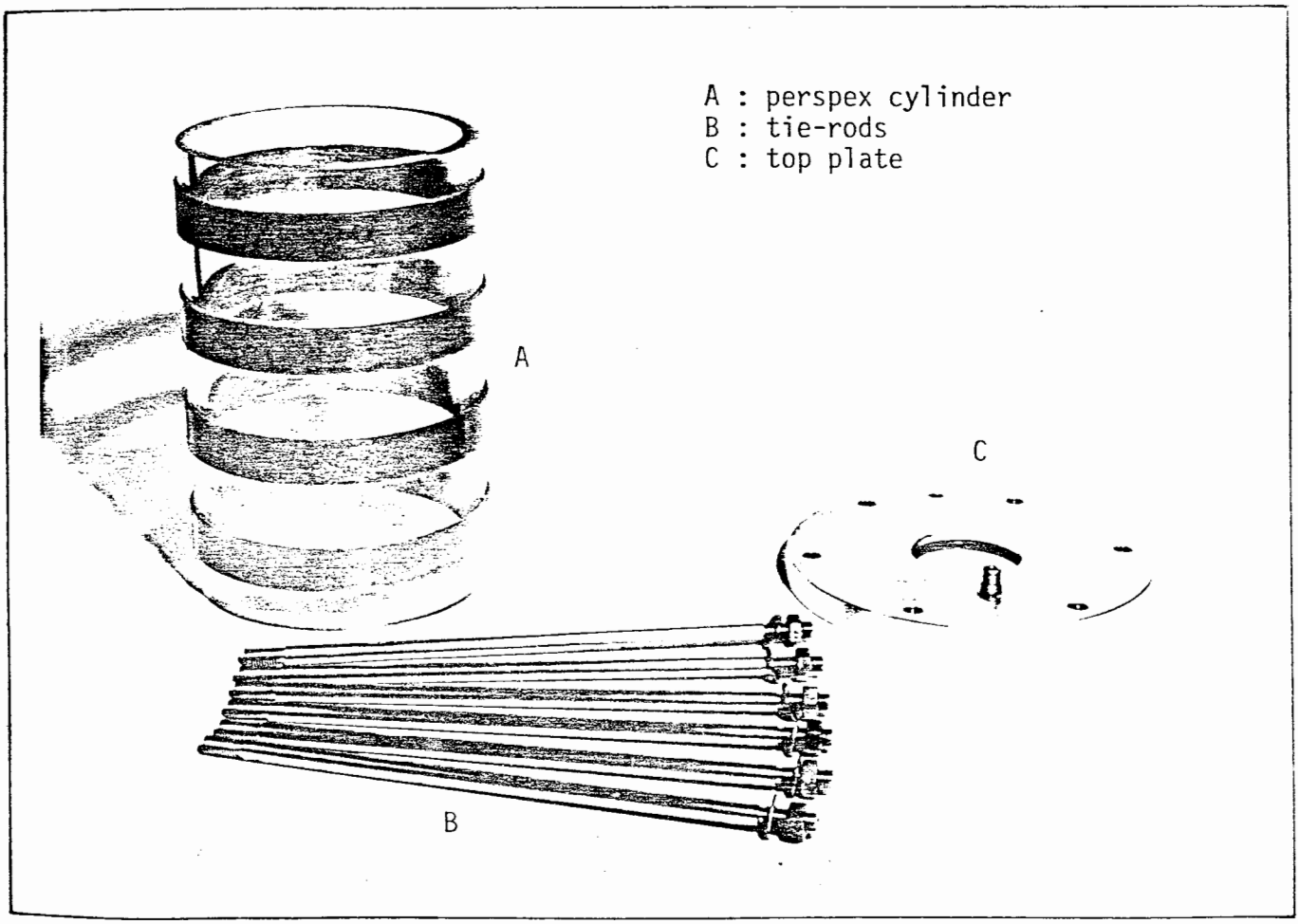

Fig. 3·5. COMPONENTS OF OUTER CELL.

wall was placed over the inner cell and the top plate was moved into position by sliding it down the loading ram cylinder (the vacuum line had to be temporarily disconnected for this operation). After locating the perspex cell wall in the O-ring grooves within the cell base and top plate, the six tie-rods were inserted and tightened to seal the cell. The outer cell was then filled with water from a large air-water interface, the air being vented from the cell through an outlet in the top plate.

After assembling and filling the cell, the dial gauge for measuring axial displacement and the proving ring for measuring axial load were mounted in position (Figure 3.6). Finally, the various connecting tubes were attached to the cell, as shown in Figure 3.7. It was important to keep all the tubes completely de-aired while the connections were made.

3.3 ISOTROPIC CONSOLIDATION IN THE CELL

After mounting the sample in the cell, it was consolidated isotropically, to remove the effects of the one-dimensional stress history. Loudon (1967) reported that, for saturated samples, an isotropic stress level three times the previous vertical stress was required to erase totally the one-dimensional effects. The critical ratio could be even higher for unsaturated samples, which are likely to be more dependent on stress history. This point is illustrated by Figure 3.8, a photograph of a gassy soil consolidated to 560 kN/m^2 in one of Nageswaran's tests, which clearly shows the flattened gas bubbles produced by one-dimensional loading. In the series of triaxial tests, the samples were consolidated isotropically to stress levels ranging from 100 kN/m^2 to 400 kN/m^2. This meant that the ratio of the isotropic stress to the previous vertical stress varied between 2 and 8, and for some of the tests the effects of the one-dimensional loading were probably not totally erased. Unfortunately it was impossible to avoid this, because 50 kN/m^2 was the lowest stress that could be used for one-dimensional

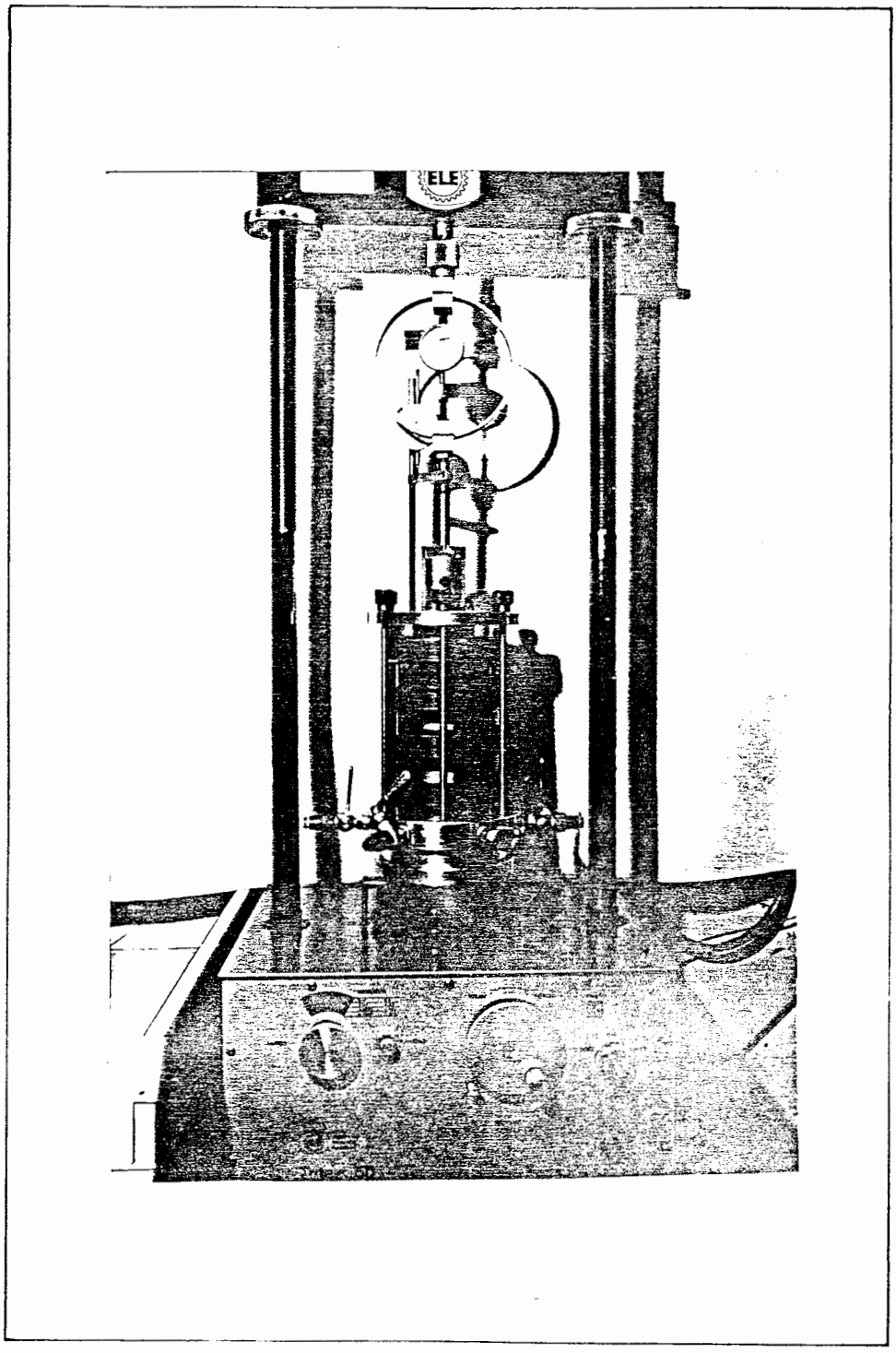

Fig. 3·6. SAMPLE SET UP IN CELL.

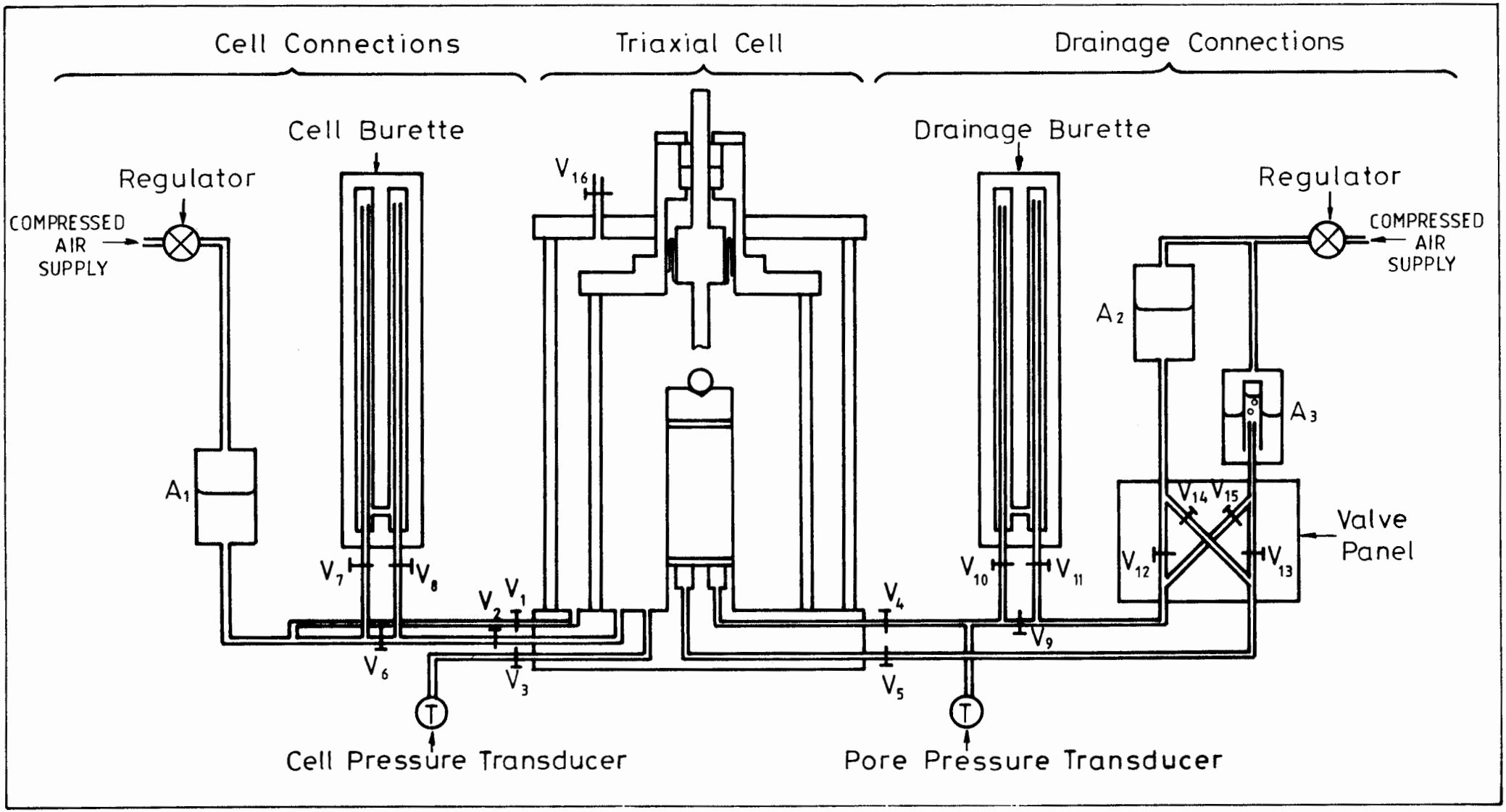

Fig. 3-7. EXPERIMENTAL APPARATUS.

pre-consolidation (Section 3.1) and isotropic stress levels down to 100 kN/m^2 were required (Section 3.9).

The fact that the ratio of the isotropic stress to the previous vertical stress was not the same in all the tests (varying from 2 to 8) could have had some influence on the test results. To investigate this point, one of the samples was consolidated one-dimensionally to a stress of 100 kN/m^2 (instead of the standard 50 kN/m^2) before being consolidated isotropically to 400 kN/m^2.

The isotropic consolidation could have been done in stages or in a single load increment. Although a series of load increments would have given more information on the isotropic consolidation behaviour, this would have taken considerably longer and many fewer tests would have been completed in the limited time available. The decision was therefore taken to consolidate with a single stress increment, because the main priority of the test series was the measurement of undrained shear strengths, rather than a study of consolidation behaviour.

At the start of the isotropic consolidation stage, the regulator on the cell pressure supply line was set to atmospheric pressure, and the valves to the inner and outer cells, V_1, V_2 and V_3, were then opened (Figure 3.7). Any flow into the inner cell was diverted through the cell burette, by closing valve V_6 and opening valves V_7 and V_8. Drainage from the sample was prevented by closing valves V_5, V_9, V_{10} and V_{11}, but valve V_4 was opened so that the pore water pressure in the sample was measured by the transducer. The initial state of the sample was recorded by taking readings from the cell pressure transducer, the pore pressure transducer and the cell burette.

The cell was pressurised to the desired level (σ_3) by adjusting the regulator on the cell pressure supply line, and new readings were then taken

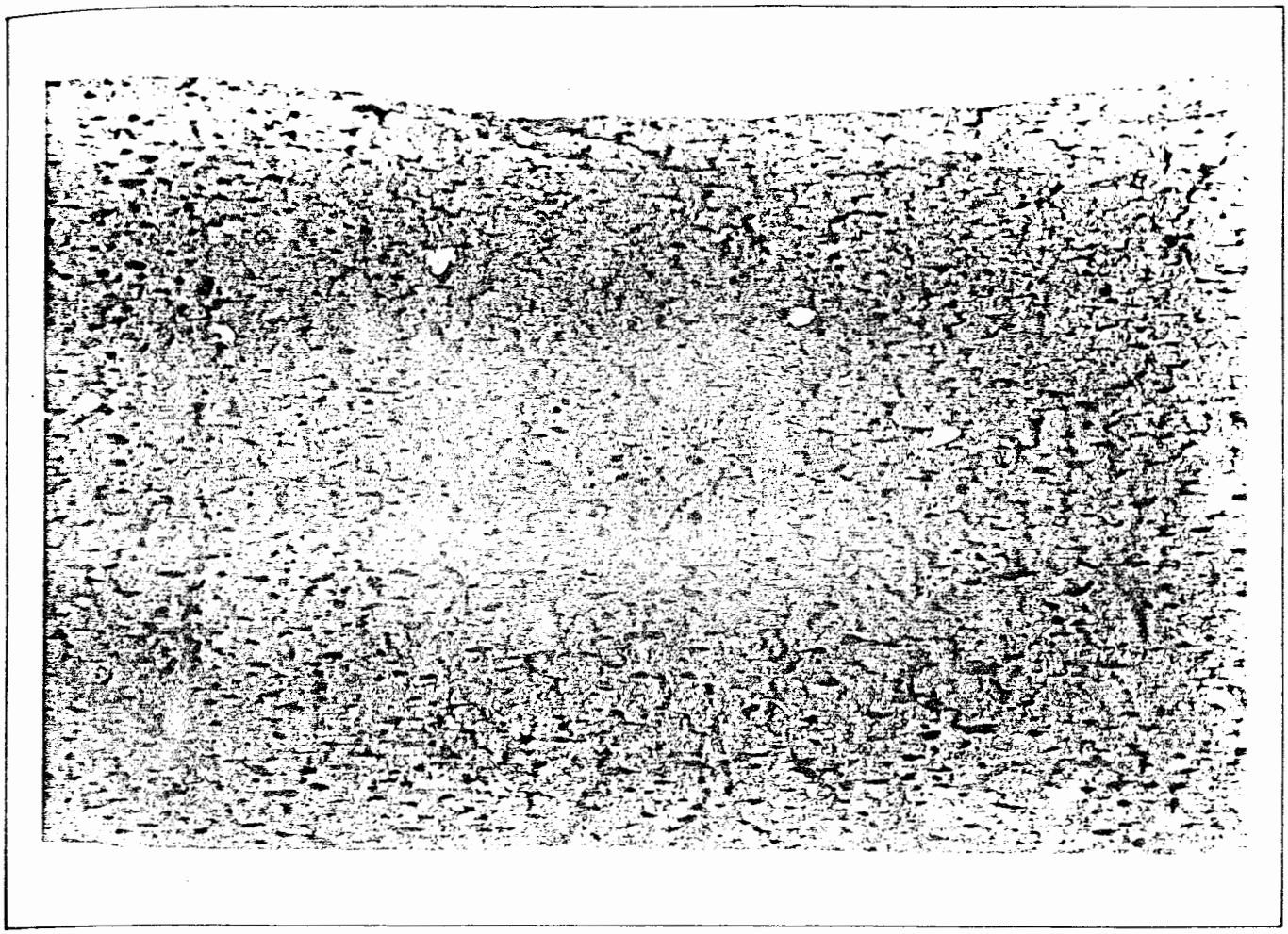

Fig. 3·8. APPEARANCE OF GASSY SOIL MAGNIFIED BY 6
Degree of Saturation = 0·8. 1-D Consolidation to 560 kN/m^2
(Nageswaran, 1983)

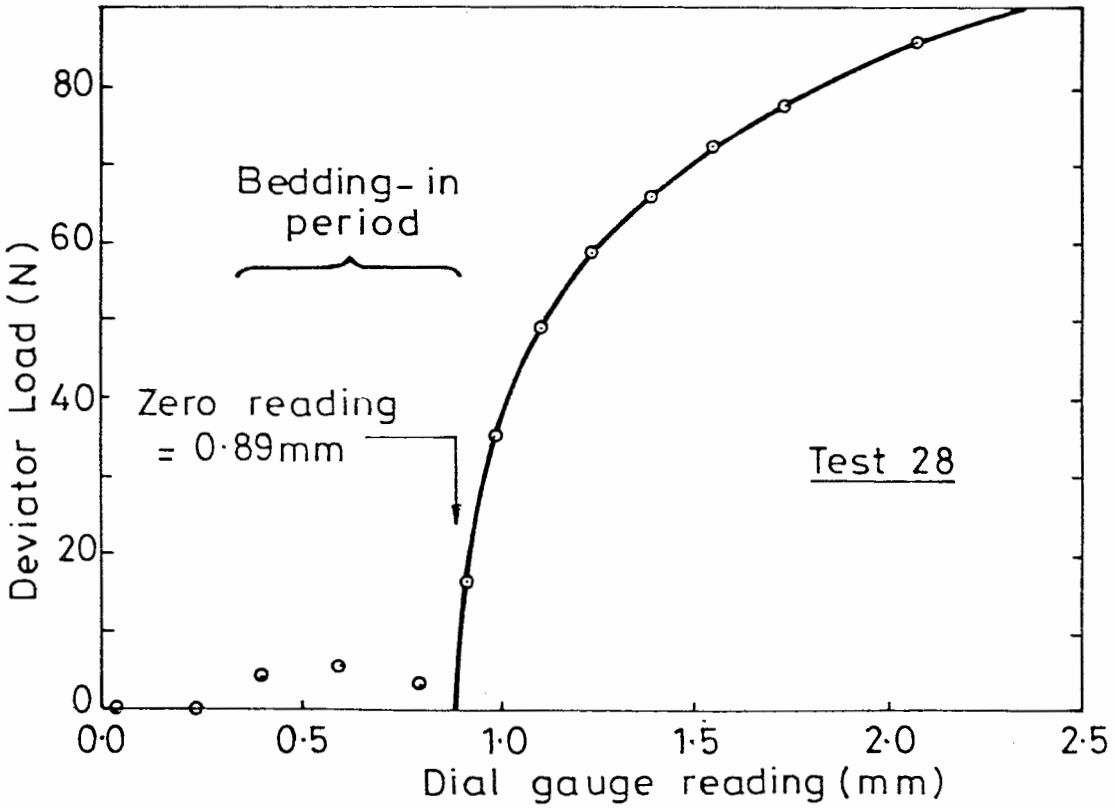

Fig. 3·9. INITIAL BEDDING-IN PERIOD.

from the pore pressure transducer and the cell burette. These readings were only approximate, because they were taken just a few minutes after the cell was pressurised, whereas the sample volume and the pore water pressure would have taken some hours to stabilise, because of the movement of gas into solution. As soon as the cell was pressurised the vacuum line was disconneced from the loading ram cylinder, as this was no longer required to keep the rolling diaphragm convolution inflated.

The back pressure for the consolidation stage (u_{wo}) was set by closing the pore pressure valve on the cell, V_4, opening the valves from the back pressure supply, V_9 and V_{12}, and adjusting the regulator on the supply line until the pore pressure transducer read the desired value. Finally, consolidation was started by opening the drainage valve V_4.

Readings from the cell burette were taken at regular intervals during consolidation. These readings were then adjusted for the absorption of water by the perspex cell, to give the change in sample volume. The measurements were also adjusted for any slight axial displacement of the ram, recorded by the dial gauge. The small displacements were caused by slight deformation of the loading ram clamp as the cell was pressurised.

The measurements of the change in sample volume, from the cell burette, were the sole means of monitoring the progress of consolidation. The drainage burette was not used to record the flow from the sample (valve V_9 was open and valves V_{10} and V_{11} were closed). If the flow had been diverted through the drainage burette, the top of the burette would have filled with gas draining from the sample.

Consolidation was effectively complete within three to four days, confirming the c_v value of about 5×10^{-8} m^2/s calculated from Nageswaran's results.

At the end of consolidation all gas bubbles were flushed from the drainage line and from beneath the porous filter, by opening valves V_5 and V_{13} so that water flowed through the drainage lines between the two air-water interfaces A_2 and A_3 (Figure 3.7). The flow was generated by a head difference of about 50 cm (5 kN/m^2) between A_2 and A_3. Interface A_2 was held about 25 cm above the level used during consolidation, with interface A_3 about 25 cm below the consolidation level, so that the average pressure at the sample remained unchanged. The direction of flow through the drainage lines was reversed several times, until no further gas appeared in interface A_3. Flow reversal was controlled by the valve panel: the flow was in one direction with valves V_{12} and V_{13} open, and in the other direction with valves V_{14} and V_{15} open (Figure 3.7). When flushing was complete, all the drainage valves were closed, except valve V_4 which was left open so that the transducer recorded the pore water pressure.

3.4 SHEAR TESTING

Before the first shear test began, a displacement rate had to be selected. The maximum allowable rate was controlled largely by the time required for equalisation of the pore pressures at the middle and ends of the sample. This equalisation was necessary if the pore water pressure measured at the base was to be truly representative of conditions throughout the sample. Bishop and Henkel (1962) give a theoretical relationship, attributed to Gibson, for the degree of equalisation during a test in which the sample is sheared between fixed ends. For 95% equalisation the time factor T_v is given by:

$$T_v = \frac{c_v t}{h^2} = 1.67 \qquad 3.1$$

c_v is the coefficient of consolidation, t is the time, and h is the half-height of the sample. Insertion of the c_v value of 5 x 10^{-8} m^2/s in Equation 3.1, together with a sample half-height of 38 mm, gave a time of about 13 hours

for 95% equalisation. The time could have been drastically reduced by employing radial drainage, but this was considered undesirable, because of the non-homogeneities that would have been produced (Nageswaran and Houlsby, 1982).

After some consideration, a displacement rate of 0.02 mm/min was selected, corresponding to a time to failure of 10 to 12 hours. This meant that tests were conducted in a single day, and that the pore water pressures reached almost 95% equalisation at the time of failure. However, pore pressure measurements taken during the early part of each test were invalid, because there was insufficient time for equalisation. The choice of displacement rate was made on the grounds that the chief aim of the test series was the measurement of the undrained shear strengths and the conditions at failure, rather than a detailed study of the stress paths to failure. A slower rate of testing would have resulted in less accurate measurements of the failure conditions, for two reasons. Firstly, if a test lasted several days there was a danger that failure would occur during the night, when nobody would be on hand to record the cell burette reading. Secondly, the longer a test lasted, the greater would be the inaccuracies due to water absorption by the perspex.

In retrospect, the choice of displacement rate was probably a bad decision. Better information on the generation of pore water pressures during shearing would have been very useful, and the penalties of a slower rate of testing would not have been as severe as originally feared (because the stress-strain curves all showed very flat maxima, so it would not have mattered if the precise failure point was missed, and because the calibrations for water absorption proved to be very accurate). However, by the time these points became clear it was too late. By then a significant number of tests had been conducted with a deformation rate of 0.02 mm/min, and it was considered unwise to change the speed, because this would have brought in the complication of strain rate effects.

The shearing stage of each test began with the measurement of the zero reading for the axial load. The loading ram was unclamped and moved down with the manual control of the compression machine to within a few millimetres of the sample. For this operation the flow from the cell was not diverted through the burette (valve V_6 was opened instead of valves V_7 and V_8), because the large volume of water displaced by the considerable movement of the ram would have over-ranged the burette. The ram was then set in motion at the standard displacement rate of 0.02 mm/min. After a few minutes the proving ring reading stabilized, and this was recorded as the force required to drive the ram against the cell pressure.

The ram was moved down manually again, until it was just about to touch the sample. After diverting the flow back through the cell burette (by closing valve V_6 and opening valves V_7 and V_8), the ram was set in motion at 0.02 mm/min. The point at which loading of the sample began was calculated by plotting the deviator load (the axial load in excess of that required to drive the ram against the cell pressure) against the axial displacement. The procedure is illustrated in Figure 3.9, which is a plot from a typical test. The figure shows an initial bedding-in period, caused by the loading ram sliding down the stainless steel ball on the sample. As the ram seated properly on the steel ball, loading of the sample began and the force increased dramatically. The axial displacement corresponding to zero strain was calculated by extrapolating the curve back to zero load.

The initial height of the sample was computed from the dial gauge reading corresponding to zero strain and an earlier reading taken with the loading ram at the top of its stroke. The height of each cell had previously been calibrated by using a dummy perspex sample of known height. The repeatability of the calibrations was very good, because the tie-rods on the inner cell were always tightened to the same torque, so the height of the cell remained constant. The accuracy of the measurement of sample height was about $\pm$ 0.1 mm.

Readings from the dial gauge, the proving ring, the cell burette and the pore water pressure transducer were recorded at frequent intervals during the shear test (every10 minutes for the first hour or two, and then every 20 or 30 minutes). The cell pressure transducer was also monitored and the regulator was adjusted as necessary to keep the pressure constant (movement of the meniscus in the burette caused slight pressure variation, because of the difference between the densities of water and paraffin). While the test was in progress, a programmable calculator was used to compute the axial strain, the deviator load, the pore water pressure and the change in sample volume.

Each test was terminated at a strain of 15% or 2% higher than the failure strain, whichever was the greater. Because the maxima of the stress-strain curves were very flat, failure was defined as a point where no measurable increase in stress occurred for a 2% strain increment.

At the end of the shearing stage, the ram was stopped and the sample was unloaded by winding up the ram with the manual control. The ram was finally clamped in position about 10 mm above the sample.

3.5 SATURATION STAGE

To calculate the volume of methane in each sample, and hence the degree of saturation, a method was developed which involved saturating the sample at some point in the test, by forcing all the gas into solution. During some tests the results of the shearing stage clearly indicated that full saturation had been reached (see Figure 2.9 in the previous chapter). If this was not the case an additional stage was necessary, specifically to saturate the sample.

Saturation was achieved by increasing the cell pressure by 200 kN/m^2. The change in sample volume was monitored as the methane first compressed

and then moved into solution. After approximately 24 hours no further change in volume occurred, indicating that the quantity of gas in solution had reached an equilibrium value. To confirm that the sample was fully saturated, the cell pressure was increased by another 100 kN/m^2. Any remaining undissolved methane would have caused an immediate volume change, due to compression of the gas. If the sample volume remained unchanged, this was a clear indication that full saturation had been achieved.

The volume of gas in the sample at any point during the shearing stage could be calculated from the change in sample volume between that point and a time when the sample was saturated. If full saturation occurred during the shear stage, the measurement of methane volume was accurate to $\pm$ 0.04 cm^3, as described in Section 2.2.5. If a separate saturation stage was required, the measurement of methane volume was accurate to $\pm$ 0.10 cm^3 (an accuracy of 0.04 cm^3 during the shear stage; 0.05 cm^3 for the accuracy of the cell pressure calibration; and 0.01 cm^3 for inaccuracies due to water absorbtion during the saturation stage).

Unfortunately the technique of measuring the methane volume by forcibly saturating the sample at some point in the test was not developed until two thirds of the triaxial tests had been completed. The technique used until then involved measuring the sample volume at the end of the test and then using the measurements of the change in volume to calculate the sample volume at all points in the test. The variation of methane volume was calculated by subtracting the volumes of solids and water (measured at the end of the test) from the total volume. This method of measuring the methane volume was considerably less accurate (about $\pm$ 0.4 cm^3), because there were many more stages involved and because the final measurement of the sample volume was quite inaccurate (see Section 3.7). For some of these earlier tests the results clearly indicated that the sample became fully saturated during the shear stage and it was therefore possible to re-analyse the results using

the new technique. However, for the remainder of the earlier tests there was no way of improving the accuracy.

3.6 SWELL-BACK STAGE

After the shearing and saturation stages, the sample was allowed to swell back to a state where both cell pressure and back pressure were zero. The swell-back was necessary to prevent the sample sucking in an unmeasurable quantity of fluid as it was removed from the cell. During swell-back, the flow into the sample and the change in sample volume were measured with the drainage burette and the cell burette respectively.

Reduction of the cell pressure to atmospheric in a single decrement would have caused large negative pore water pressures, which might have resulted in cavitation effects. This problem was avoided by reducing the cell pressure and the back pressure in two stages. For the first stage the cell pressure was reduced by only 100 kN/m^2, and the back pressure was set at the same level. For the second stage the cell pressure and the back pressure were both reduced to zero.

Before reducing the cell pressure to atmospheric, for the second stage of swell-back, a vacuum line was connected to the rolling diaphragm cylinder, to keep the diaphragm convolution properly inflated.

Swell-back was normally completed in three to four days. Any methane bubbles trapped in the drainage line or beneath the porous filter were then flushed from the system by using the head difference between the air-water interfaces A_2 and A_3, as described in Section 3.3. The quantity of methane flushed from the system was measured in the manner suggested by Fredlund (1975), by using a calibrated cylinder inverted over the drainage outlet in interface A_3 (Figure 3.7). The gas volume was measured to an accuracy of $\pm$ 0.01 cm^3. After the flushing was complete both drainage outlets on the cell (valves V_4 and V_5) were closed.

The gas draining from the sample during swell-back affected the measurement of the flow of water into the sample during the same period, because the volume of gas collecting in the drainage line replaced an identical volume of water. Therefore the total flow of water into the sample during the swell-back stage was calculated by adding the volume of gas flushed from the drainage line to the flow measured through the burette during swell-back. The total inflow was calculated to an accuracy of about $\pm$ 0.02 cm^3.

3.7 MEASUREMENT OF WET AND DRY WEIGHTS

Following the swell-back stage the inner and outer cells were emptied of water and the apparatus was dismantled, leaving the sample standing on the cell base. The wet and dry weights of the sample were then measured.

Special precautions were necessary when measuring the wet weight. Because the sample underwent considerable deformation during consolidation and shearing, the surrounding membrane often formed wrinkles. During swell-back the membrane was no longer pressed firmly against the sample, because the back pressure and cell pressure were equal, and therefore the wrinkles filled with methane and water. The weight of water held in the wrinkles had to be included in the wet weight of the sample. To achieve this, the wet weight was measured with the sample still sealed in the membrane. The perspex pedestal on which the sample was mounted was detached from the cell base, by removing the four securing bolts (Figure 3.3). After allowing the drainage lines in the pedestal to empty, two small rubber bungs were inserted in the outlets at the base of the pedestal, to prevent any further loss of water from the sample. The entire assembly, including pedestal, sample, loading cap, membrane, O-rings and rubber bungs, was then weighed. The weights of the pedestal, loading cap, etc, were subtracted to give the wet weight of the sample alone.

The accuracy of measurement for both the wet weight and the dry weight was ± 0.02 g (both were calculated from the difference of two readings, each of which was accurate to ± 0.01 g).

During the early tests, as well as recording the wet and dry weights after swell-back, the sample volume was also measured. This was before the development of the improved technique for measuring the gas volume (by forcibly saturating the soil). The sample volume was measured with a pycnometer jar, to an accuracy of about ± 0.2 cm^3. The sample was placed in the pycnometer while still sealed with the membrane (complete with pedestal, loading cap, O-rings and rubber bungs), so that the volume of water and methane within the wrinkles was included. In fact it was during these early tests that the problem of the fluid within the wrinkles became apparent. For the first few tests the membrane was removed before the sample was placed in the pycnometer. It was immediately obvious that something was wrong, because the calculated values of the degree of saturation during the shear stage were often well in excess of 1.0. After some time this was correctly attributed to the fact that the fluid within the wrinkles was not being included in the measurement.

3.8. PROCESSING OF THE RESULTS

The volumes of solids and water in the sample after swell-back were calculated from the wet and dry weights and the specific gravity of the soil grains. By correcting for the flow of water into the sample during swell-back, the volume of water in the sample during the undrained shear stage was calculated. The variations of the void ratio e and the degree of saturation S throughout the shear test were computed from the following relationships:

$$e = \frac{\text{volume of water + volume of methane}}{\text{volume of solids}} \qquad 3.2$$

$$S = \frac{\text{volume of water}}{\text{volume of water + volume of methane}} \qquad 3.3$$

The variation of the methane volume during shear testing had already been calculated from the results of the saturation stage.

The accuracy achieved for the measurement of S was $\pm$ 0.001 if the sample became saturated during the shear stage and $\pm$ 0.0025 if a separate saturation stage was required. For the earlier tests, before the development of the improved technique for measuring the gas volume, the accuracy was about $\pm$ 0.01. The accuracy achieved for the void ratio e varied between $\pm$ 0.004 and $\pm$ 0.015, depending upon the method used for measuring the gas volume.

The values of e and S at the beginning of the shear stage (e_o and S_o) provided useful information on the isotropic consolidation behaviour, while the values at the end of the shear stage (e_f and S_f) provided information on the failure conditions.

Having calculated the volume of the sample at the start of the shear stage, the processing of the shear test results could continue. The initial cross-sectional area of the sample A_o was calculated from the initial volume and height; and the variation of the volumetric strain ε_v was computed from the measurements of the change in sample volume. The deviator stress q was then calculated from the deviator load F and the initial cross-sectional areas A_o:

$$q = \frac{F(1 - \varepsilon_1)}{A_o(1 - \varepsilon_v)} \qquad 3.4$$

Equation 3.4 includes the effects of the axial strain ε_1 and volumetric strain ε_v on the cross-sectional area (Bishop and Henkel, 1962). The values of q were accurate to about $\pm$ 1 kN/m^2.

The deviator stress was corrected for the strength of the rubber membrane, using the formula presented by Bishop and Henkel (1962). This formula is strictly only applicable to tests where the sample volume remains constant. However, the membrane correction was always quite small and the errors introduced by using this simplified formula were probably insignificant (Bishop and Henkel found that the formula was quite acceptable for drained tests on saturated samples). The membranes were about 0.3 mm thick, with an extension modulus of 0.4 kN/m. The correction to the deviator stress was typically about 6 kN/m^2 at a strain of 15%.

A stress-strain curve was produced for each test, with the deviator stress plotted against the axial strain. This was used to calculate the value of the undrained shear strength C_u (half the maximum deviator stress). The value of C_u was accurate to about $\pm$ 0.5 kN/m^2.

The readings from the pore water pressure transducer were used to plot the development of the water pressure u_w during the test. The results for the early part of each test were probably very inaccurate, because there was insufficient time for the equalisation of pore pressure throughout the sample.

The variation in the pore gas pressure was calculated from the change in saturation, using Boyle's Law and Henry's Law. Boyle's Law relates the gas pressure at any point in the test, u_g, to the initial gas pressure, u_{go}:

$$\frac{(u_g + p_a)}{(u_{go} + p_a)} = \frac{V^*_{go}}{V^*_g} \qquad 3.5$$

p_a is atmospheric pressure, V^*_g is the gas volume if all the gas was out of solution at a pressure u_g, and V^*_{go} is the initial value of V^*_g.

V_g^* consists of two components: the actual volume of undissolved gas, and the volume that the dissolved gas would take up if it was out of solution. The volume of undissolved gas is equal to $V_w(1 - S)/S$, where V_w is the volume of water in the sample. The volume that the dissolved gas would take up if it was out of solution is given by Henry's Law as HV_w, where H is the solubility coefficient. This assumes that the tests were conducted sufficiently slowly, so that the quantity of dissolved gas was always at an equilibrium value. Provided that this was the case:

$$V_g^* = \left(\frac{1 - S}{S} + H\right)V_w \qquad 3.6$$

Similarly, V_{go}^* can be expressed in terms of the saturation at the start of the test, S_o:

$$V_{go}^* = \left(\frac{1 - S_o}{S_o} + H\right)V_w \qquad 3.7$$

The water volume is the same in Equations 3.6 and 3.7, because the tests were undrained. Inserting Equations 3.6 and 3.7 in Equation 3.5 and rearranging:

$$u_g = \frac{\{(1 - S_o)/S_o + H\}(u_{go} + p_a)}{\{(1 - S)/S + H\}} - p_a \qquad 3.8$$

Equation 3.8 was used to calculate the variation of gas pressure throughout each test. To do this it was necessary to assume a value for the gas pressure at the start of the test, u_{go}. Various different assumptions were made, to see what the effect was. The solubility coefficient H for methane in water was taken as 0.034 (Yamamoto et al, 1976).

The variation in the mean total stress p was calculated from the cell pressure σ_3 and the deviator stress q:

$$p = \sigma_3 + q/3 \qquad 3.9$$

A stress path was then produced for each test, by plotting q against $(p - u_w)$. For a saturated soil this would be termed the effective stress path (Atkinson and Bransby, 1978), but for a sample containing gas bubbles the stress $(p - u_w)$ is no longer an effective stress (see Chapter 1).

The stress-strain behaviour during the early part of each shear test was used to calculate the undrained shear modulus G_u and the undrained bulk modulus K_u. The definitions of the elastic moduli are given by Atkinson and Bransby (1978), for axisymmetric conditions:

$$G_u = \frac{\Delta q}{2(\Delta\varepsilon_1 - \Delta\varepsilon_3)} \qquad 3.10$$

$$K_u = \frac{\Delta p}{\Delta\varepsilon_v} \qquad 3.11$$

$\Delta\varepsilon_1$, $\Delta\varepsilon_3$ and $\Delta\varepsilon_v$ are the increments of axial, lateral and volumetric strain produced by the stress increments Δq and Δp. If the lateral stress σ_3 is held constant, Equations 3.10 and 3.11 can be expressed solely in terms of the axial stress increment $\Delta\sigma_1$:

$$G_u = \frac{\Delta\sigma_1}{3\Delta\varepsilon_1 - \Delta\varepsilon_v} \qquad 3.12$$

$$K_u = \frac{\Delta\sigma_1}{3\Delta\varepsilon_v} \qquad 3.13$$

The lateral strain increment has been eliminated from Equation 3.12 by expressing $\Delta\varepsilon_3$ in terms of $\Delta\varepsilon_1$ and $\Delta\varepsilon_v$.

The deviator stress was plotted against $(3\varepsilon_1 - \varepsilon_v)$ to calculate the undrained shear modulus, and against $3\varepsilon_v$ to calculate the bulk modulus (see Equations 3.12 and 3.13). In each case a secant modulus was computed, at a deviator stress of half the failure value (see Figure 3.10). The elastic behaviour would probably have been better represented by the slope of an

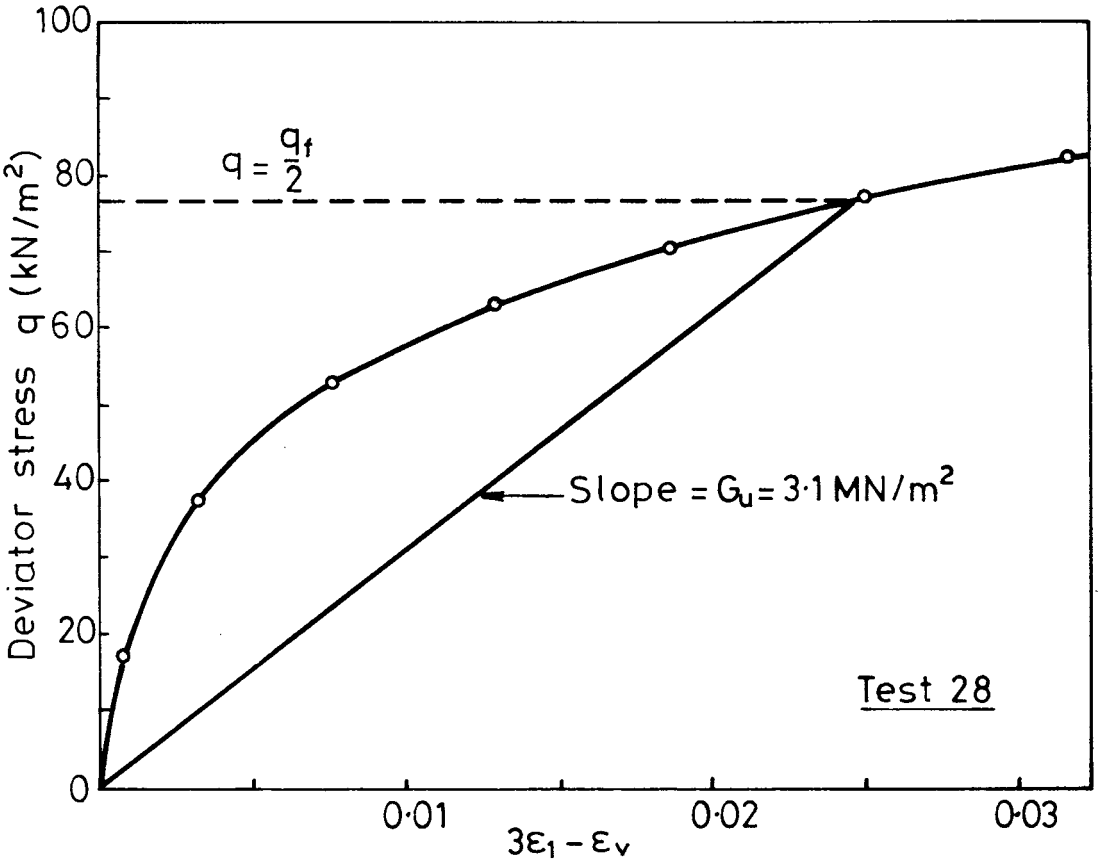

(a) Shear Modulus

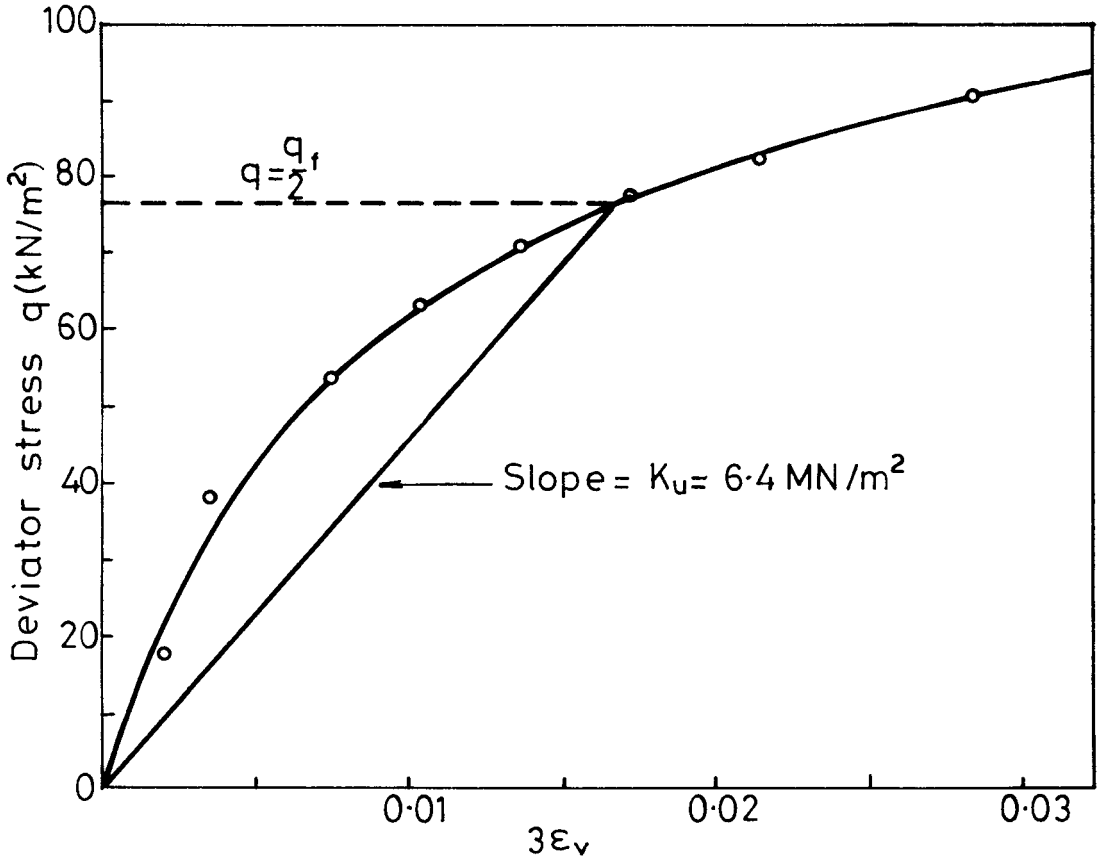

(b) Bulk Modulus

Fig. 3·10. PROCEDURE FOR CALCULATING ELASTIC MODULI

unload-reload curve. However, unloading and reloading would have affected the undrained shear strength, because the behaviour of soils containing gas bubbles appears to be very dependent on the stress history.

3.9 THE PROGRAMME OF TESTS

Table 3.1 shows the timetable for two typical tests, illustrating the way in which each sample was prepared while the previous sample was being tested. By using this procedure, the time taken per test was reduced to about 10 days. Recalibration of the cell for the water absorbtion effect was done every month or every two months, and this also took about 10 days. As a result, the maximum rate of testing, with two cells in operation, was about four tests per month (two in each cell). However this rate was only achieved during the last six months of the test programme, after the second cell was commissioned and all the various teething problems had been solved.

A total of 50 samples was tested. The first four were tested in a standard triaxial apparatus, before the modified cells were built. These initial experiments were conducted to test the sample preparation technique and to gain some insight into the effect of gas bubbles on the undrained shear strength. Tests 5 to 10 were the earliest tests in a modified triaxial cell, when various teething problems were eliminated (mainly the effect of the fluid in the membrane wrinkles). These tests did not provide any usable results. Table 3.2 gives brief details of the remaining 40 tests. Three tests (Nos. 17, 27 and 30) were aborted before completion, because of experimental difficulties, leaving 37 tests which provided useful data.

Table 3.2 shows, for each sample, the degree of saturation at the start of shearing (after isotropic consolidation in the cell). The initial saturation varied between 0.9 and 1.0. This ensured that the methane was in the form of discrete bubbles (Sparks, 1963; Nageswaran, 1983) and was also representative of the saturation levels likely to occur in marine

Table 3.1 Timetable for Two Typical Tests

Day	Test A	Test B
1	Finish 1-D consolidation Set up sample in cell Start consolidation stage	
2	Consolidation	
3	Consolidation	
4	Consolidation	Dry zeolite in oven
5	Finish consolidation Conduct shear test Start saturation stage	Place zeolite in vacuum chamber
6	Finish saturation stage Start swell-back stage	Impregnate zeolite with methane Mix water saturated zeolite
7	Swell-back	Mix soil-zeolite slurry Start 1-D consolidation
8	Swell-back	1-D consolidation
9	Swell-back	1-D consolidation
10	Finish swell-back stage Dismantle cell Measure wet weight	1-D consolidation
11	Measure dry weight	Finish 1-D consolidation Set up sample in cell Start consolidation stage

Table 3.2 Details of Test Programme

Test No.	Cell No.	% of zeolite sat. with methane	Initial saturation S_o	Consol. pressure (σ_3-u_{wo}) (kN/m^2)	Back pressure u_{wo} (kN/m^2)	Accuracy of S	Comments
11	1	0%	0.991	200	0	±0.001	
12	1	50%	0.907	200	0	±0.01	
13	1	50%	0.980	200	100	±0.001	
14	1	0%	1.000	200	100	±0.001	
15	1	70%	0.982	200	100	±0.001	
16	1	70%	0.974	200	100	±0.001	
17	1	50%		Test	aborted		Air in drainage line
18	1	50%	0.950	400	0	±0.01	
19	1	0%	0.987	400	0	±0.001	
20	1	50%	0.914	200	0	±0.01	
21	1	25%	0.978	200	0	±0.001	
22	2	25%	0.953	200	0	±0.01	
23	2	50%	0.984	200	100	±0.001	
24	1	50%	0.969	200	100	±0.001	
25	1	70%	0.947	400	0	±0.01	
26	1	25%	0.974	200	0	±0.001	
27	2	50%		Test	aborted		Sample damaged
28	1	50%	0.916	200	0	±0.01	
29	1	50%	0.906	400	0	±0.01	
30	2	50%		Test	aborted		Hole in membrane
31	1	50%	0.906	400	0	±0.01	
32	2	50%	0.911	400	0	±0.01	
33	1	30%	0.938	400	0	±0.01	
34	2	30%	0.947	400	0	±0.01	
35	1	50%	0.931	400	0	±0.01	
36	2	50%	0.933	400	0	±0.01	
37	2	30%	0.958	400	0	±0.01	
38	1	30%	0.945	400	0	±0.001	
39	2	70%	0.905	200	0	±0.01	
40	1	70%	0.941	400	0	±0.001	
41	2	0%	0.980	400	0	±0.001	
42	1	0%	0.980	200	0	±0.001	
43	2	50%	0.898	200	0	±0.0025	Disturbance test
44	1	50%	0.903	100	0	±0.0025	
45	2	25%	0.985	100	0	±0.001	
46	1	25%	0.986	200	0	±0.001	Disturbance test
47	2	40%	0.919	100	0	±0.0025	
48	1	70%	0.933	400	0	±0.0025	
49	2	0%	0.997	100	0	±0.001	
50	1	50%	0.975	400	0	±0.001	1-D Stress = 100 kN/m^2

sediments (Esrig and Kirby, 1977). The table also shows, for each test, the value of the consolidation pressure i.e. the cell pressure (σ_3) minus the back pressure (u_{wo}) during consolidation. Three different values were used, covering a suitable range of conditions, (100, 200 and 400 kN/m^2). Two different values of back pressure (u_{wo}) were employed for the consolidation stage: zero and 100 kN/m^2. The higher back pressure was only used with a consolidation stress of 200 kN/m^2. These two values of back pressure were probably too low to be truly representative of typical seabed conditions. However, there were experimental difficulties in producing gas-bearing soils at higher back pressures (see Section 4.1 of the next chapter).

The penultimate column of Table 3.2 shows which of the various procedures for measuring the methane volume was used for each test. For Tests 41 to 50 the gas volume was measured by saturating the sample at some point during the test; either during the shear stage (giving an accuracy of ± 0.001 for the saturation) or in a separate saturation stage (an accuracy of ± 0.0025). For Tests 11 to 40 the gas volume was originally calculated by measuring the sample volume at the end of the test, giving an accuracy of ± 0.01. However, for about half of these earlier tests the sample clearly became saturated during the shear stage, and the results were later re-analysed using the new technique.

Test 50 was non-standard, because a one-dimensional pre-consolidation stress of 100 kN/m^2 was used, instead of the normal value of 50 kN/m^2. The idea was to see whether the shear behaviour was affected by the pre-consolidation stress.

Tests 43 and 46 were designed to model the effects of the disturbance that occurs when samples are recovered from the seabed. After consolidating each sample under a cell pressure of 200 kN/m^2, the drainage line was closed and the cell pressure was reduced to atmospheric. This was meant to

represent the stress relief that occurs when a sample is brought to the surface. The drainage line was closed on the assumption that a real sample would be sealed immediately after recovery, before sufficient time had elapsed for significant drainage. After 24 hours the cell pressure was increased to 200 kN/m^2 and the drainage line was opened again, to model the effect of setting up the recovered sample in a triaxial cell. When any renewed consolidation was complete, the shear test was conducted in the normal fashion. The main aim of these two tests was to see if the effects of disturbance were markedly different on saturated and unsaturated samples. Therefore Test 43 was on a sample with an initial degree of saturation of about 0.9, while Test 46 was on a sample that was almost saturated.

CHAPTER 4

EXPERIMENTAL RESULTS

4.1 Sample preparation technique

4.2 Isotropic consolidation

4.3 Behaviour during shearing

4.4 Undrained shear strength

4.5 Axial strain at failure

4.6 Degree of saturation and void ratio at failure

4.7 Pore water pressure

4.8 Pore gas pressure

4.9 Stress paths and failure conditions

4.10 Undrained shear modulus

4.11 Undrained bulk modulus

4.12 Influence of one-dimensional consolidation

4.13 Sample disturbance tests

CHAPTER 4

EXPERIMENTAL RESULTS

The results from the series of triaxial tests are presented in this chapter. However, discussion of the results is delayed until Chapter 9, so that the experimental observations can be compared with the predictions of the theoretical model developed in Chapters 5 to 8.

The experimental results are summarised in Table 4.1.

4.1 SAMPLE PREPARATION TECHNIQUE

Figure 4.1 illustrates the success of the zeolite molecular sieve technique for producing soil samples containing gas bubbles. The figure shows the degree of saturation after isotropic consolidation S_o plotted against the percentage of zeolite impregnated with methane, for each of the different combinations of consolidation pressure $(\sigma_3 - u_{wo})$ and back pressure u_{wo}. There is considerable scatter of the results, but it is clear that an increase in the quantity of methane saturated zeolite generally results in a lower degree of saturation.

The scatter in the results is probably caused by variation in the quantity of gas escaping from the samples during the initial one-dimensional consolidation stage. This would seem a likely explanation, as the conditions during one-dimensional consolidation probably varied from sample to sample, because of changes in the friction between the cylindrical mould and the seal on the loading piston.

The four separate curves of Figure 4.1 are all plotted on the same set of axes in Figure 4.2, which shows more clearly the influence of the consolidation pressure and the back pressure on the sample preparation technique.

Table 4.1 Summary of Results

Test No.	% of zeolite saturated with methane	Consolidation pressure $(\sigma_3 - u_{wo})$ kN/m²	Back pressure (u_{wo}) kN/m²	Initial degree of saturation (S_o)	Initial void ratio (e_o)	Undrained shear strength (c_u) kN/m²	Axial strain at failure (ε_{1f}) %	Degree of saturation at failure (S_f)	Pore water pressure at failure (u_{wf}) kN/m²	Δu_w during last 2% strain kN/m²	Undrained shear modulus (G_u) MN/m²	Undrained bulk modulus (K_u) MN/m²
11	0%	200	0	0.991	1.180	76.5	13	1.000	146	0	17.8	18.2
12	50%	200	0	0.907	1.223	78.5	14	0.961	132	3	5.7	4.8
13	50%	200	100	0.980	1.198	69.5	13	1.000	246	2	7.3	15.8
14	0%	200	100	1.000	1.164	76.5	13	1.000	250	0	7.1	∞
15	70%	200	100	0.982	1.192	72.0	11	1.000	247	0	7.7	10.3
16	70%	200	100	0.974	1.166	72.0	10	1.000	246	2	9.2	12.2
18	50%	400	0	0.950	1.058	168.0	13	1.000	260	5	9.0	9.2
19	0%	400	0	0.987	1.039	144.5	13	1.000	293	1	18.8	66.0
20	50%	200	0	0.914	1.230	79.5	16	0.972	119	5	4.1	7.0
21	25%	200	0	0.978	1.228	75.0	13	1.000	141	3	9.3	10.9
22	25%	200	0	0.953	1.175	71.0	10	0.992	103	14	4.9	13.9
23	50%	200	100	0.984	1.201	64.5	12	1.000	245	1	8.3	15.4
24	50%	200	100	0.969	1.259	61.0	13	1.000	248	5	5.5	9.0
25	70%	400	0	0.947	1.136	173.0	12	1.000	243	7	11.0	8.3
26	25%	200	0	0.974	1.200	76.0	12	1.000	133	1	7.6	13.1
28	50%	200	0	0.916	1.226	76.5	16	0.985	110	11	3.1	6.4
29	50%	400	0	0.906	1.156	195.0	23	1.000	154	17	5.1	6.4
31	50%	400	0	0.906	1.130	183.0	25	0.996	175	15	5.0	7.9
32	50%	400	0	0.911	1.102	177.5	24	1.000	171	11	4.5	7.4
33	30%	400	0	0.938	1.109	170.5	17	1.000	224	16	10.7	11.8
34	30%	400	0	0.947	1.063	172.5	17	1.000	213	16	8.6	15.7
35	50%	400	0	0.931	1.121	170.0	16	1.000	232	10	6.8	9.9
36	50%	400	0	0.933	1.076	157.0	15	0.995	236	13	7.3	15.2
37	30%	400	0	0.958	1.041	161.5	13	1.000	252	9	10.0	14.4
38	30%	400	0	0.945	1.013	169.0	15	1.000	245	10	12.8	18.2
39	70%	200	0	0.905	1.249	69.0	13	0.953	119	8	5.4	8.4
40	70%	400	0	0.941	1.092	169.0	16	1.000	229	11	7.4	12.1
41	0%	400	0	0.980	1.023	192.5	9	1.000	283	2	14.0	40.0
42	0%	200	0	0.980	1.153	75.0	16	1.000	-	-	8.3	54.0
43*	50%	200	0	0.898	1.204	85.5	15	0.961	121	5	4.7	7.8
44	50%	100	0	0.903	1.383	31.8	14	0.955	-	-	3.1	10.2
45	25%	100	0	0.985	1.292	39.4	11	1.000	77	0	7.5	12.3
46*	25%	200	0	0.986	1.134	76.0	13	1.000	-	-	12.9	23.0
47	40%	100	0	0.919	1.358	35.6	11	0.945	70	2	4.9	10.1
48	70%	400	0	0.933	1.041	160.5	13	0.987	-	-	9.8	11.9
49	0%	100	0	0.997	1.244	38.8	9	1.000	73	1	5.8	41.0
50**	50%	400	0	0.975	1.020	136.0	16	1.000	-	-	13.5	21.0

* Sample disturbance tests

** One-dimensional consolidation stress = 100 kN/m²

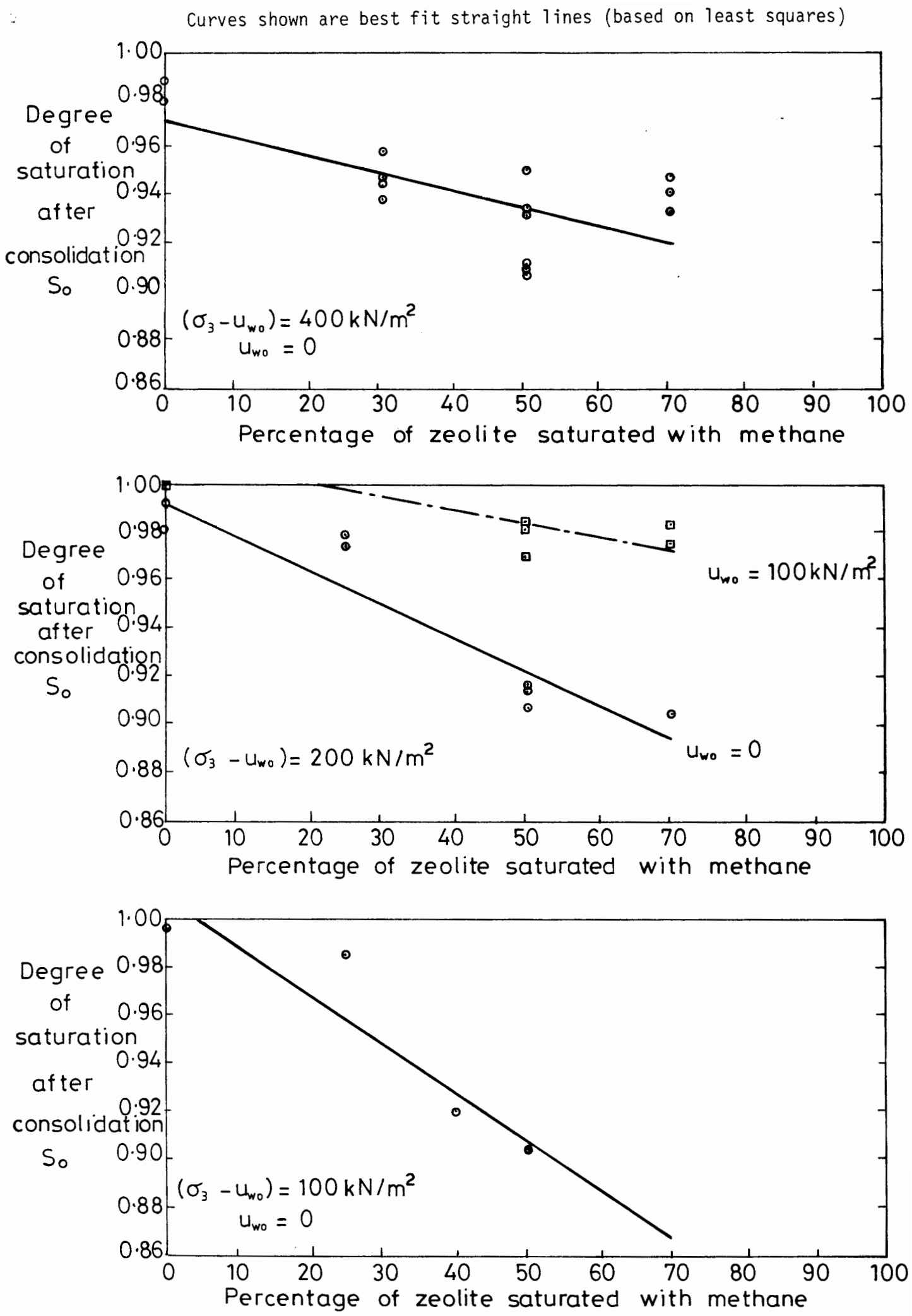

Fig. 4·1. SAMPLE PREPARATION TECHNIQUE.

With a back pressure of zero, samples can be produced with saturation levels ranging from about 0.99 down to about 0.90. It is very difficult to produce completely saturated samples without applying a back pressure, because of the small quantities of air trapped within the samples during preparation and setting up. Figure 4.2 shows that this problem appears increasingly severe as the consolidation pressure is increased. It is also very difficult to produce saturation levels below about 0.90, because if more than 70% of the zeolite is filled with methane, the gas forms interconnected voids (rather than discrete bubbles) during the initial one-dimensional consolidation, and most of the methane then drains from the sample during consolidation. This means that the last 30% of the zeolite can never actually be used for producing gas bubbles, and it could be replaced with soil. However by the time this point was appreciated a considerable number of tests had been completed and it was considered unwise to change the proportion of zeolite within the samples, because of the different physical properties of the zeolite and the soil.

With a back pressure of 100 kN/m^2, saturation levels ranging from 1.00 down to about 0.97 can be achieved (Figure 4.2). Because of the elevated back pressure there is no problem in producing completely saturated samples. In fact a significant proportion of the zeolite has to be saturated with methane before enough gas is released to produce unsaturated samples. Insufficient tests were conducted to indicate properly this critical proportion of the zeolite, and in Figures 4.1 and 4.2 it is shown rather arbitrarily as 20% of the zeolite volume. The minimum saturation level that can be produced with a back pressure of 100 kN/m^2 is about 0.97. It is not possible to achieve lower saturation levels simply by filling more of the zeolite with methane, because the gas then forms interconnected voids during the initial one-dimensional consolidation, when the back pressure is zero.

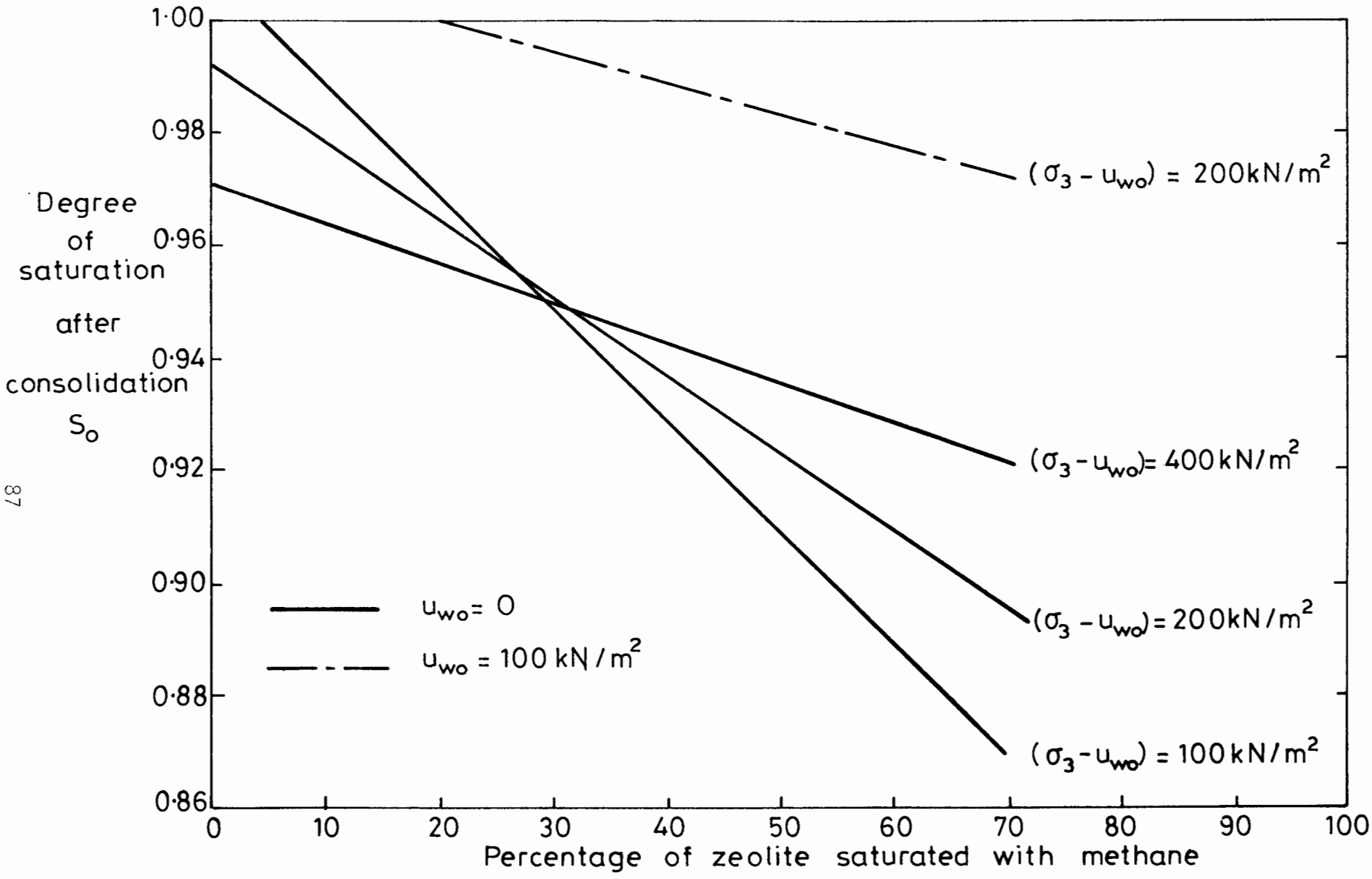

Fig. 4·2. SAMPLE PREPARATION TECHNIQUE.

With back pressures above 100 kN/m^2, the range of saturation levels that could be achieved would presumably be even more restricted. This is an obvious limitation of the sample preparation technique, which appears to be unsuitable for producing gassy samples at high back pressures.

4.2 ISOTROPIC CONSOLIDATION

Figure 4.3 illustrates the state of the samples produced by isotropic consolidation. The figure shows the void ratio of the soil after consolidation e_o plotted against the degree of saturation after consolidation S_o, for the three different values of consolidation pressure $(\sigma_3 - u_{wo})$. There is considerable scatter of the results, but for each value of consolidation pressure there appears to be a definite trend, with the void ratio rising as the saturation falls. The central graph also appears to indicate that the variation of e_o with S_o is independent of the back pressure (although the results are not conclusive on this point, because the scatter is particularly severe on this plot).

If there is a unique relationship between the void ratio and the consolidation pressure (which would be termed the "effective stress" in a saturated soil), then the three curves in Figure 4.3 would all be horizontal. Clearly this is not the case, and it appears that the void ratio is a function of the degree of saturation as well as the consolidation pressure.

Section 1.4 of Chapter 1 described how Nageswaran, on the advice of the author, tried plotting his one-dimensional consolidation results in terms of the parameter Se, instead of the void ratio e. The results of the isotropic consolidation tests can be presented in the same fashion. Figure 4.4 shows the data of Figure 4.3 replotted in terms of the parameter Se. For reasons described in the next chapter this parameter is referred to as the "matrix void ratio". Despite the scatter of the results, Figure 4.4 shows that $S_o e_o$ is almost independent of the degree of saturation for

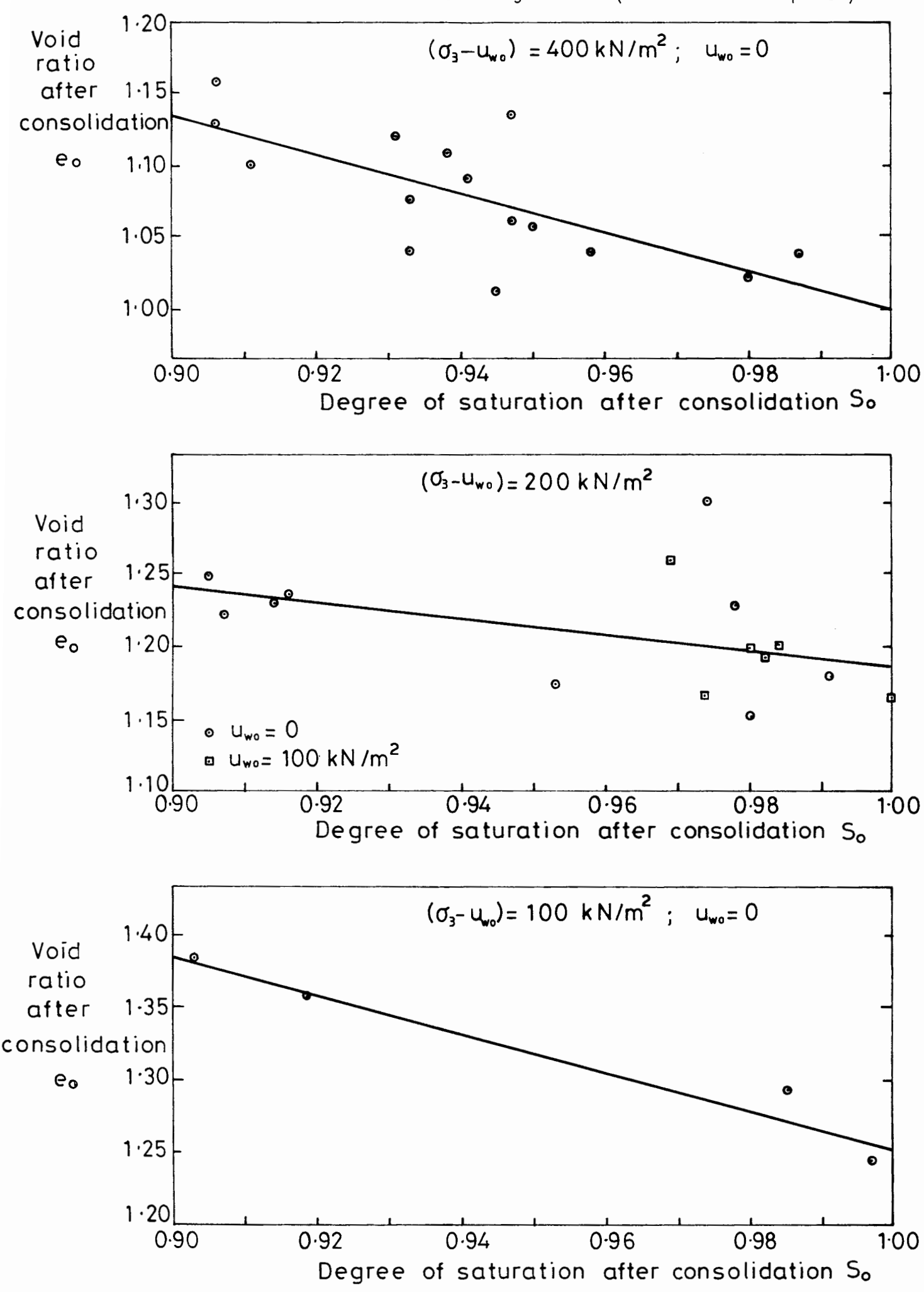

Fig. 4·3. VOID RATIO AFTER CONSOLIDATION.

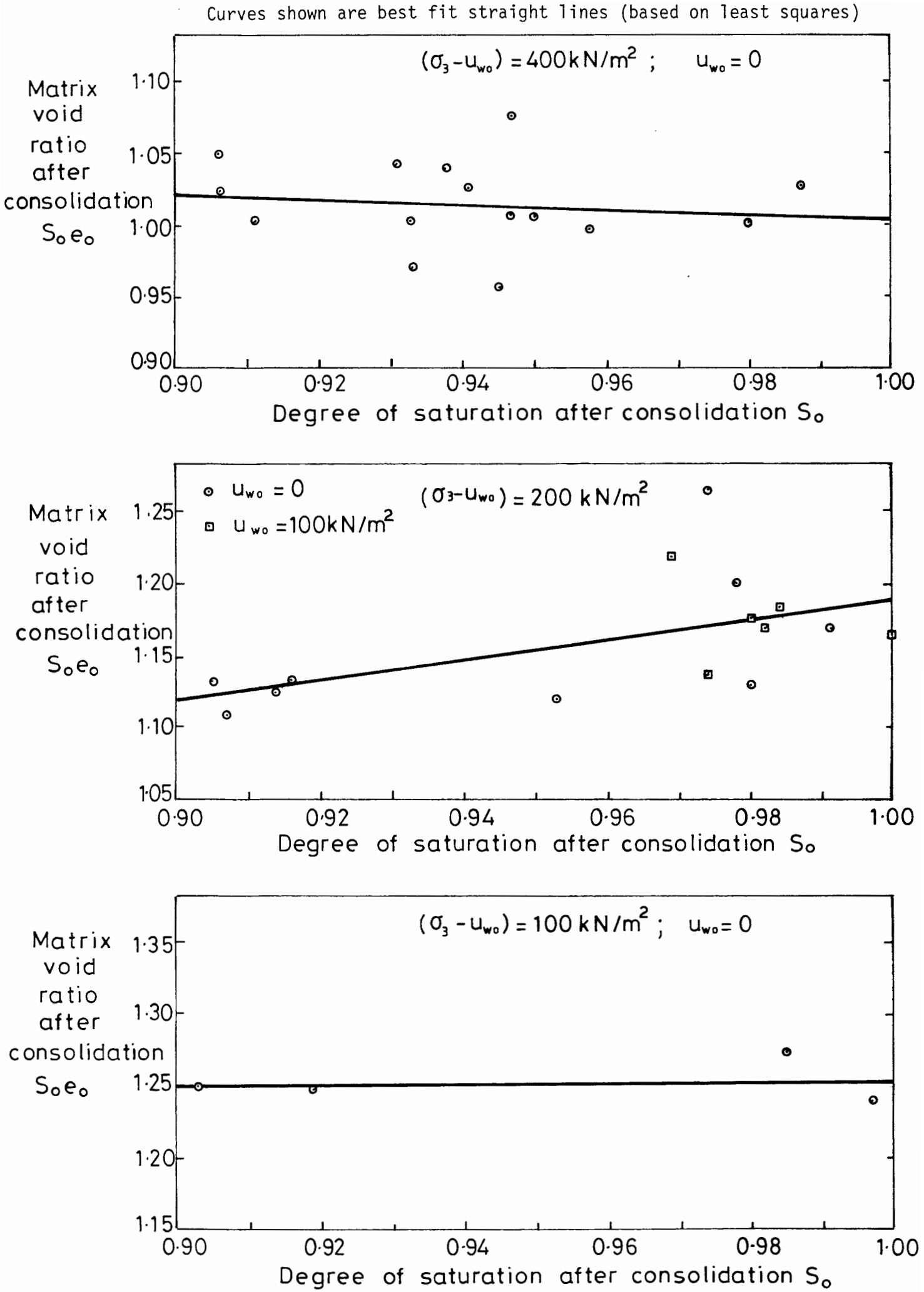

Fig. 4.4. MATRIX VOID RATIO AFTER CONSOLIDATION.

each value of consolidation pressure (a horizontal line can be drawn through the points). The central graph (consolidation pressure = 200 kN/m^2) appears to be a slight exception to this rule, but this may be due simply to the greater scatter of the data in this plot.

Figure 4.5 summarizes the information on the preceding two figures. The upper graph shows three curves (each for a different saturation level) relating the overall void ratio after consolidation e_o to the consolidation pressure $(\sigma_3 - u_{wo})$. The lower graph shows a unique line relating the matrix void ratio after consolidation $S_o e_o$ to the consolidation pressure, independent of the degree of saturation. The individual data points shown in Figure 4.5 correspond to the "best-fit" lines in Figure 4.4. The single curve of the lower plot in Figure 4.5 can be produced directly form the three curves of the upper graph.

The unique line in the lower graph of Figure 4.5 has the following equation:

$$(1 + S_o e_o) = 3.062 - 0.174 \log_e (\sigma_3 - u_{wo}) \qquad 4.1$$

Therefore, the critical state parameters λ and N, which define the normal consolidation line for saturated samples, have the following values:

$$\lambda = 0.174 \quad , \quad N = 3.062 \qquad 4.2$$

It is interesting to compare Figure 4.5 with the results from Nageswaran's one-dimensional consolidation tests, presented in Chapter 1 (Figures 1. 9 and 1.12). Although the replotting of Nageswaran's results in terms of the parameter Se brings the different curves much closer, they are still some way from a unique line, and there still appears to be a definite trend, with Se rising as the saturation falls. In contrast, the isotropic consolidation behaviour illustrated in Figure 4.5 shows a unique line relating Se to the consolidation pressure.

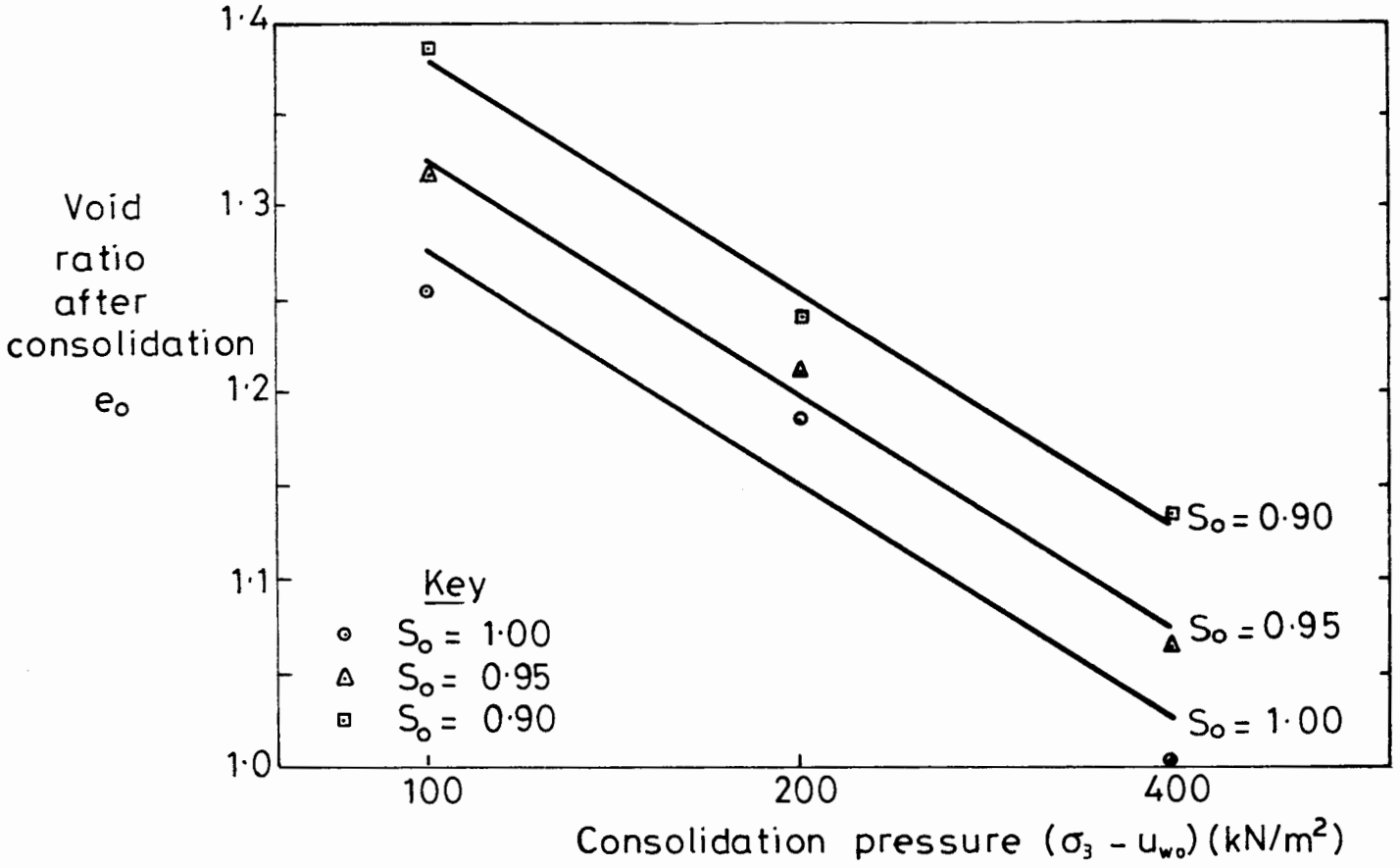

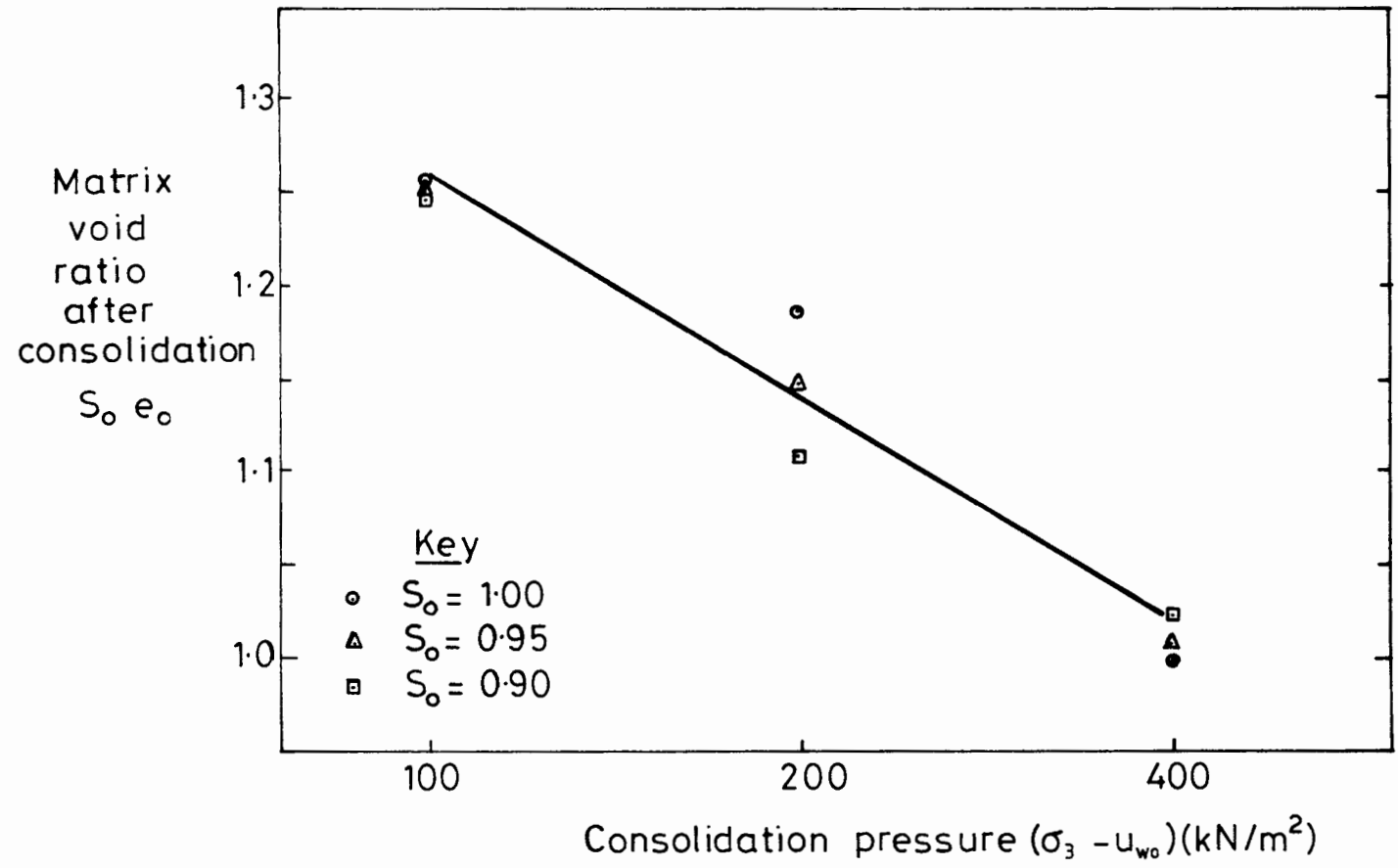

Fig. 4·5. ISOTROPIC CONSOLIDATION.

Theoretical analyses of both the isotropicand the one-dimensional consolidation behaviour are presented in Chapter 7, and the experimental observations recorded in this chapter are compared with the theoretical predictions in Chapter 9.

4.3 BEHAVIOUR DURING SHEARING

Figure 4.6 illustrates the results from the undrained shear stage of a typical test. For the test shown in the figure (Test 18) the consolidation pressure was 400 kN/m^2, the back pressure was zero and the degree of saturation at the start of shearing S_o was 0.950. This test was fairly typical, because the value of S_o was in the middle of the full range of experimental values (0.90 to 1.00).

The top graph in Figure 4.6 shows the deviator stress q plotted against the axial strain ε_1. The curve shows a very flat maximum, and the sample finally failed at a deviator stress of 336 kN/m^2. All the tests produced stress-strain curves with flat maxima. Therefore the presence of gas bubbles has no apparent effect on the overall shape of the stress-strain curves, because saturated samples of normally consolidated clay would also exhibit flat maxima. This suggests that the general mode of failure is unaffected by the gas bubbles and this point is borne out by the fact that both saturated and unsaturated samples appeared to fail by plastic flow (deforming to definite "barrel" shapes) rather than by rupturing on specific shear surfaces.

The central graph in Figure 4.6 shows the pore water pressure u_w plotted against the axial strain ε_1 for Test 18. When studying this curve, it should be remembered that the measurements of pore water pressure were rather suspect, particularly during the early part of each test, because the tests were conducted too fast to allow full equalization of pressure throughout the samples (see Section 3.4, Chapter 3).

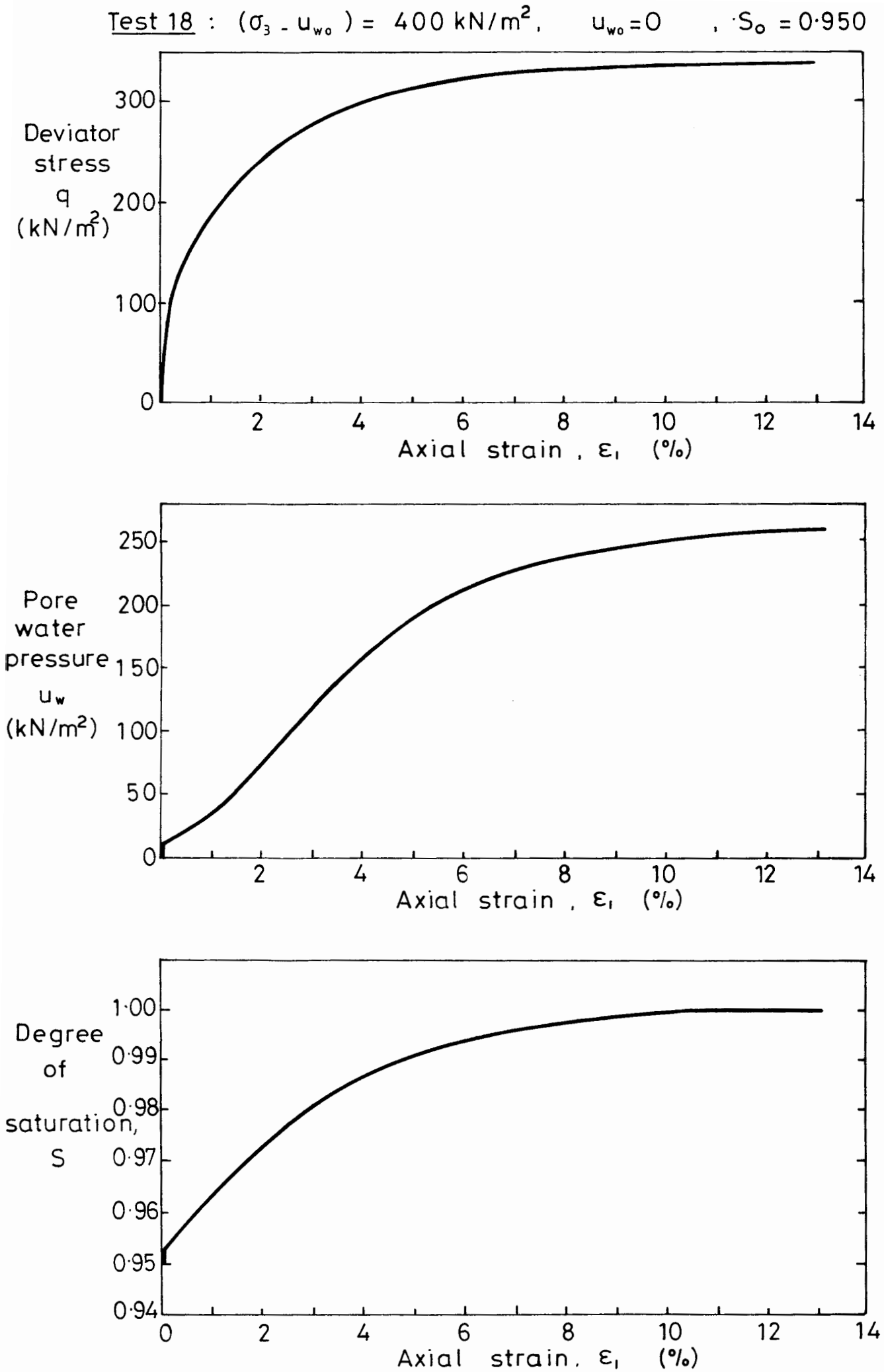

Fig. 4·6. TYPICAL BEHAVIOUR DURING SHEARING.

At the beginning of Test 18 the pore water pressure was zero (unchanged from the back pressure during the consolidation stage). The apparent discontinuity at the start of the test, with u_w rising immediately to 12 kN/m^2, was caused by the pore water pressure generated during the bedding-in period. During this period, before the loading ram was properly seated, the sample experienced a small fluctuating value of deviator stress, which produced a slight increase in the pore water pressure.

After the bedding-in period, the slope of the pore water pressure curve increases steadily, reaching a maximum at an axial strain of about 2%. This appears to confirm that the test was conducted too fast for full equalisation in the early stages, because during an undrained test on a normally consolidated clay the pore pressure would usually be generated most rapidly at the very start of the test. The increasing slope of the curve suggests that the pore water pressure measured at the boundary of the sample was lower than the pore pressure at the centre of the sample, because the increasing slope represents the high pore pressures at the centre dissipating through to the boundary after a period of time. The suggestion of high pore water pressure at the sample centre is in agreement with the behaviour reported by Bishop and Henkel (1962) for undrained tests on normally consolidated saturated clays.

The final pore water pressure recorded in Test 18 was 260 kN/m^2, but Figure 4.6 shows clearly that the measured pore water pressure was still rising at the end of the test (by 5 kN/m^2 in the last 2% strain). This indicates that full equalisation was not even achieved during the later stages of the test, because the pore pressure measured at the boundary continued to increase, despite the fact that failure had already occurred. This apparent increase in u_w after failure is further confirmation that the pore water pressure was higher at the centre of the sample than at the boundary.

The bottom graph of Figure 4.6 shows how the degree of saturation S varied during Test 18. The curve shows a slight discontinuity at the start

of the test (similar to the plot of pore water pressure), because the pore gas pressure generated during the bedding-in period caused slight compression of the bubbles. After the bedding-in period, the saturation increased steadily until the sample reached a fully saturated condition at a strain of about 10.5%. Not all the samples reached a fully saturated state. Full saturation was most likely to occur if the initial degree of saturation S_o was high. This point is discussed in more detail in Section 4.6.

4.4 UNDRAINED SHEAR STRENGTH

The measurements of undrained shear strength were considered the primary objective of the experimental tests.

Figure 4.7 shows the undrained shear strength C_u plotted against the degree of saturation at the start of shearing S_o for each of the different combinations of consolidation pressure and back pressure. The four curves show markedly different trends: the presence of gas bubbles increasing the shear strength in the top curve but reducing the shear strength in two of the remaining curves. It is clear that the effect of gas bubbles on the undrained shear strength is influenced greatly by the consolidation pressure and the back pressure.

The information presented in Figure 4.7 is summarized in Figure 4.8. The values of undrained shear strength C_u have been normalised by dividing by the consolidation pressure $(\sigma_3 - u_{wo})$.

In Figure 4.8, three of the four curves show $C_u/(\sigma_3 - u_{wo})$ tending to almost a common value as S_o approaches 1.0 (as would be expected). However the final curve (consolidation pressure = 400 kN/m^2, back pressure = 0) is slightly offset. A possible explanation for this is that a small portion of the initial gas volume was probably large air voids trapped during sample preparation, rather than discrete methane bubbles released from the zeolite. The influence of these air voids on the soil behaviour would probably differ

7 Curves shown are best fit straight lines (based on least squares)

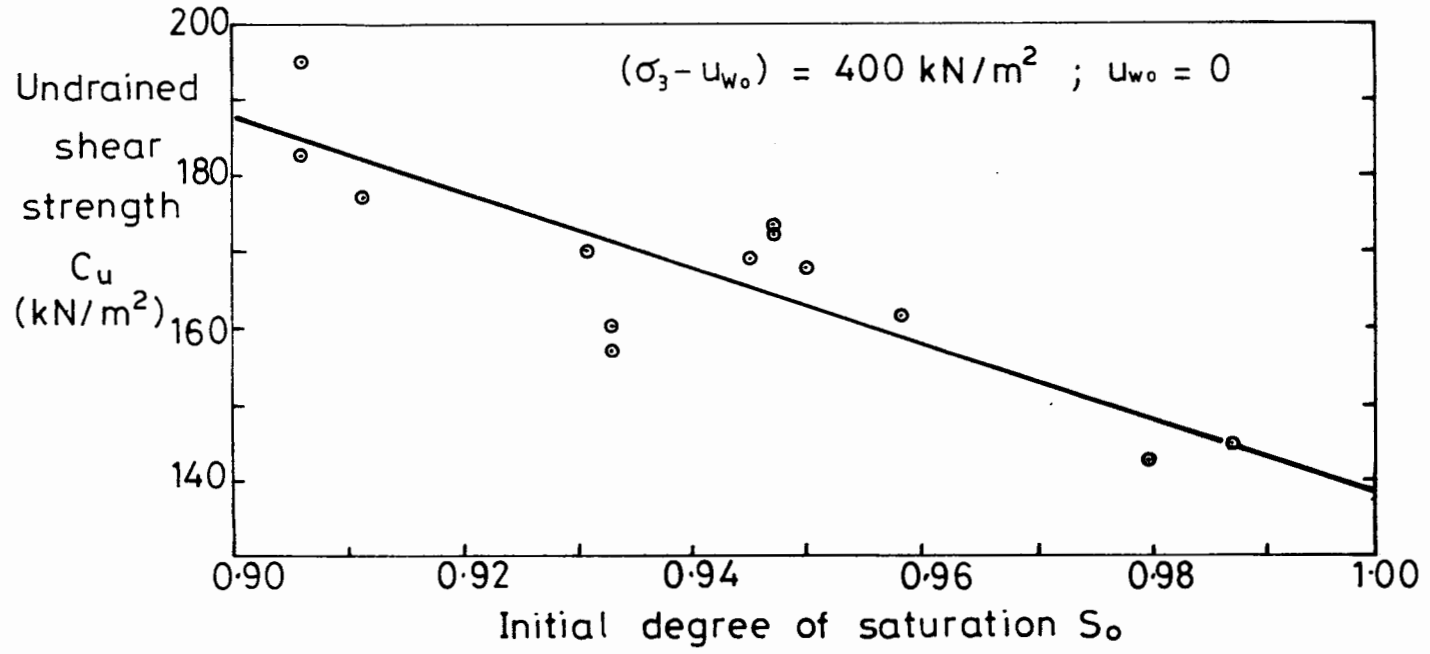

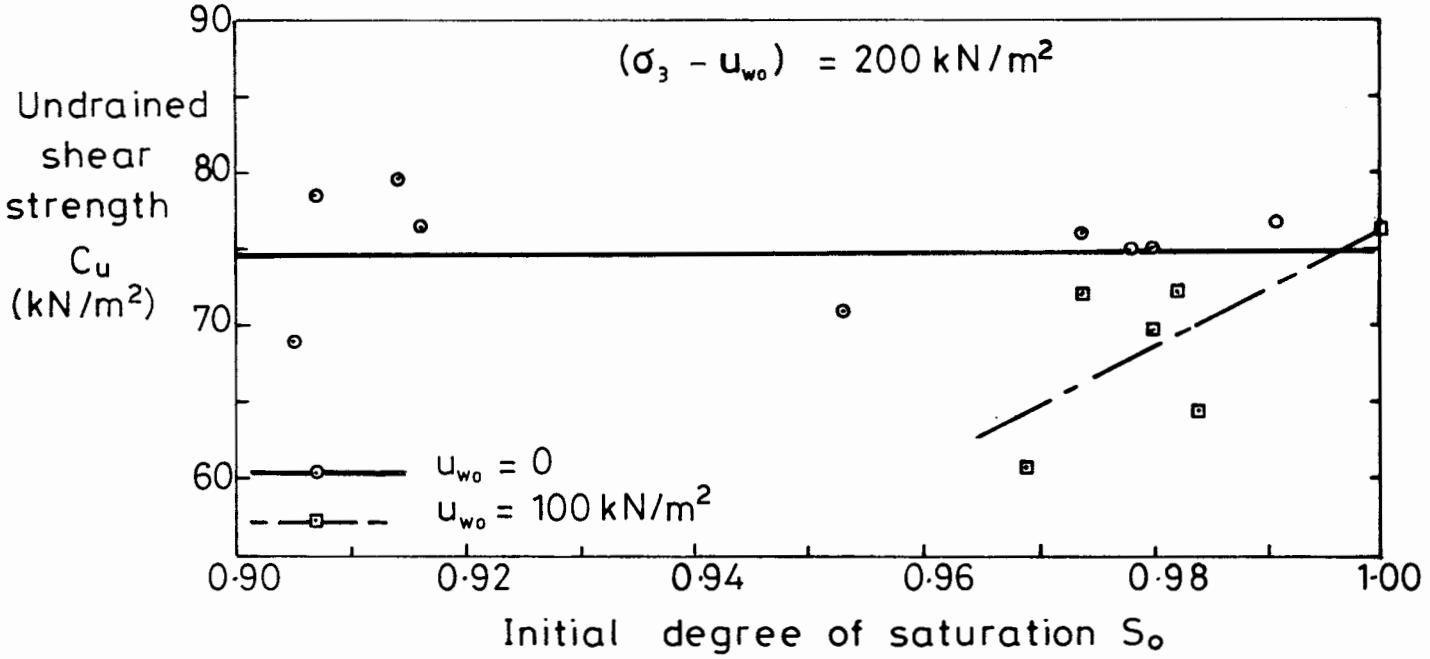

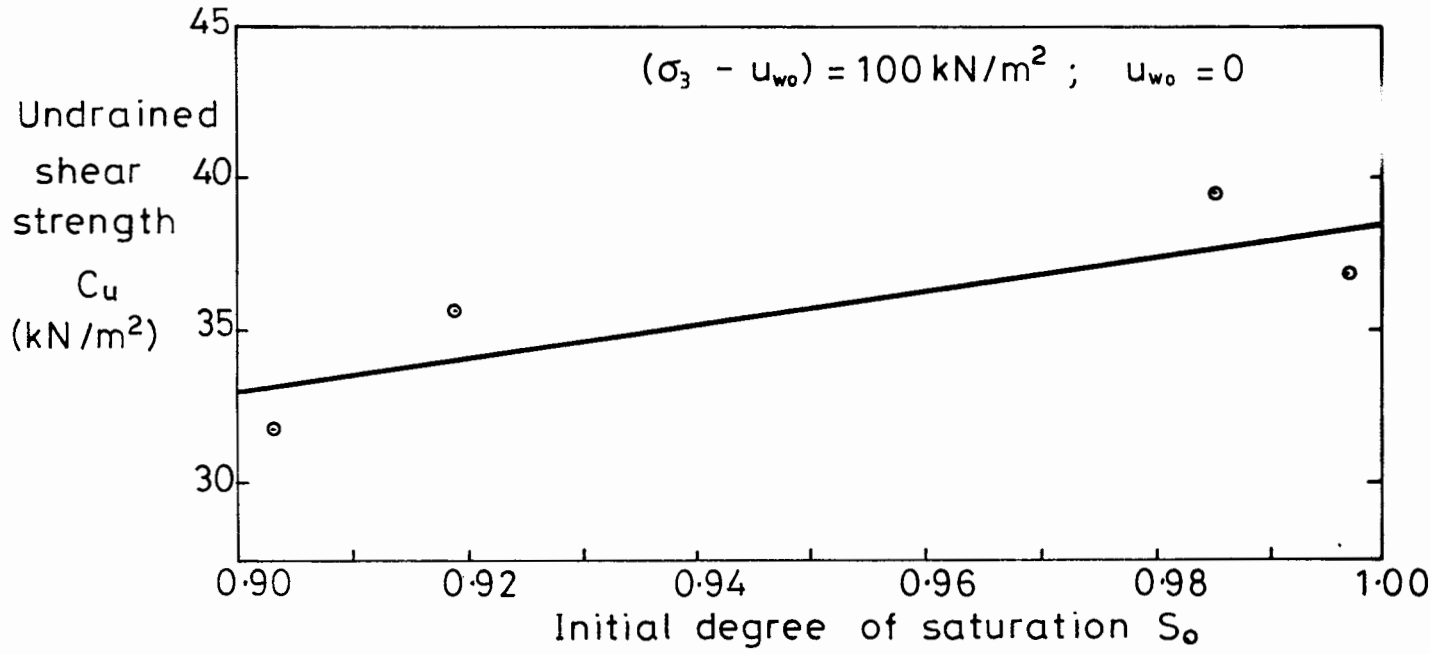

Fig. 4·7. UNDRAINED SHEAR STRENGTH.

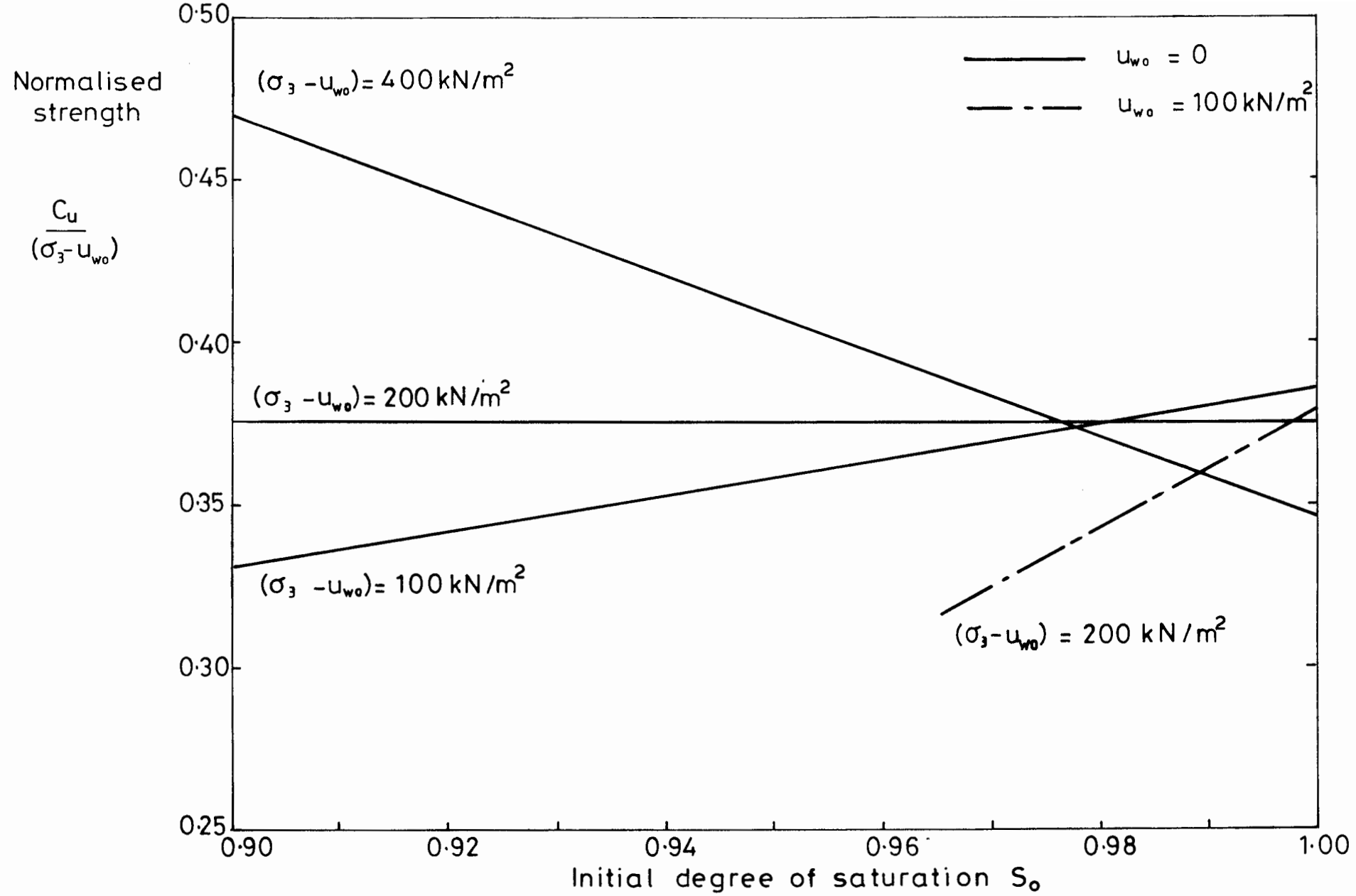

Fig. 4·8. NORMALISED UNDRAINED SHEAR STRENGTH.

from the effect of the methane bubbles, producing a slight offset in the curve. The series of tests with a consolidation pressure of 400 kN/m^2 would have been most susceptible to this phenomenon, because this was the series of tests for which it was hardest to produce satured samples (see Section 4.1).

The different slopes of the four curves in Figure 4.8 clearly indicate how the effect of the gas bubbles on the undrained shear strength is influenced by the consolidation pressure and the back pressure. As the consolidation pressure is reduced or the back pressure is increased, the effect of the gas bubbles becomes increasingly detrimental.

A theoretical analysis of the undrained shear strength of soils containing gas bubbles is presented in Chapter 8, and the experimental observations are compared with the theoretical predictions in Chapter 9.

4.5 AXIAL STRAIN AT FAILURE

Because the maxima of the stress-strain curves were very flat, it was always hard to identify a precise failure strain. To ensure that a consistent criterion was used for all the tests, failure was defined as the point where no measurable increase in deviator stress occurred for a 2% strain increment.

Figure 4.9 shows the axial strain at failure ε_{1f} plotted against the initial degree of saturation S_o for each of the different combinations of consolidation pressure and back pressure. In Figure 4.10 the different curves are all plotted on the same set of axes. The failure strains for saturated samples are about 10% to 12%, and the failure strain increases as S_o is reduced, typically reaching 13% to 15% when S_o is 0.90. The exception to this pattern is the series of tests with a consolidation pressure of 400 kN/m^2, which shows considerably higher failure strains at low values of S_o (exceeding 25% when S_o is 0.90).

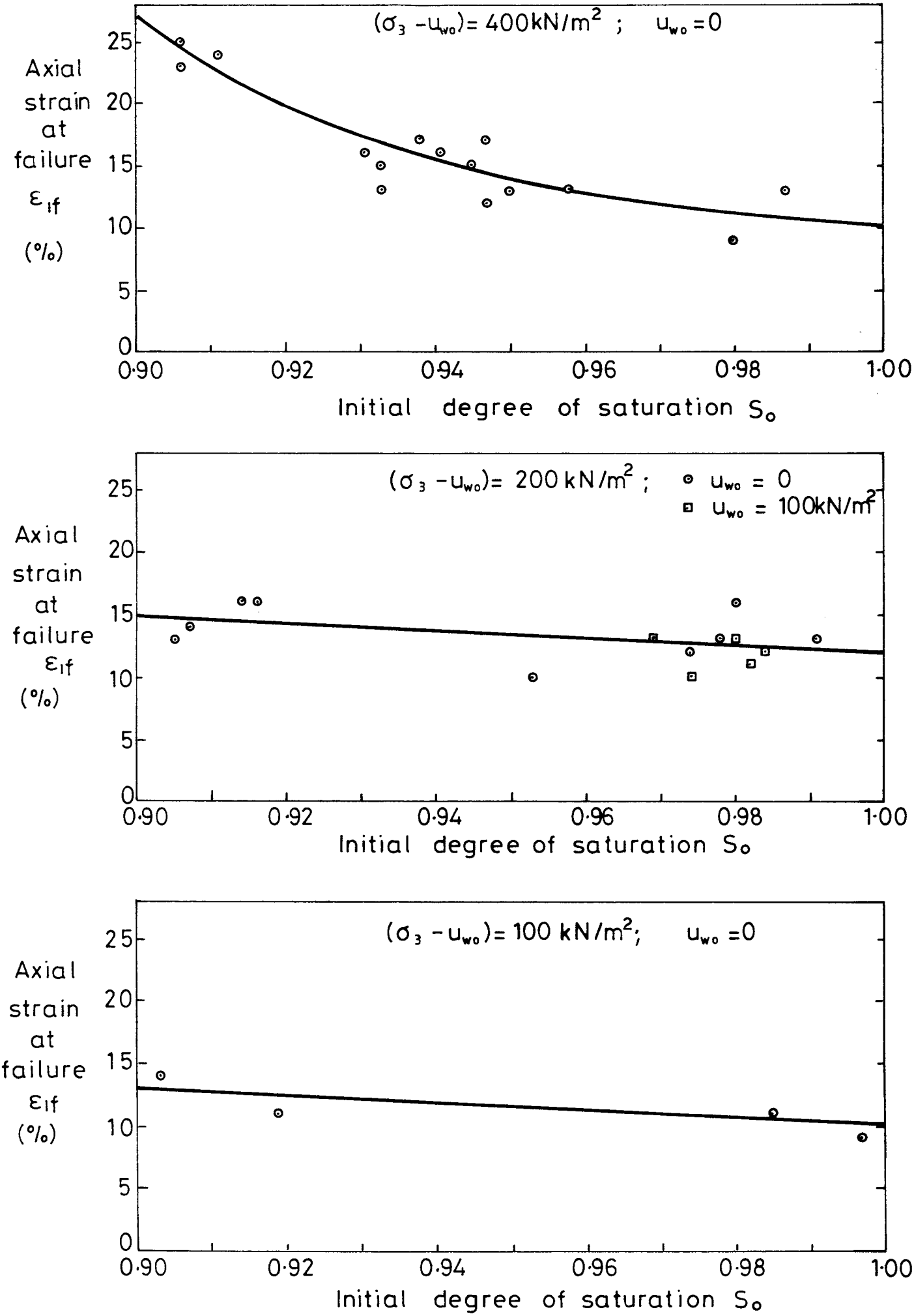

Fig. 4·9. AXIAL STRAIN AT FAILURE.

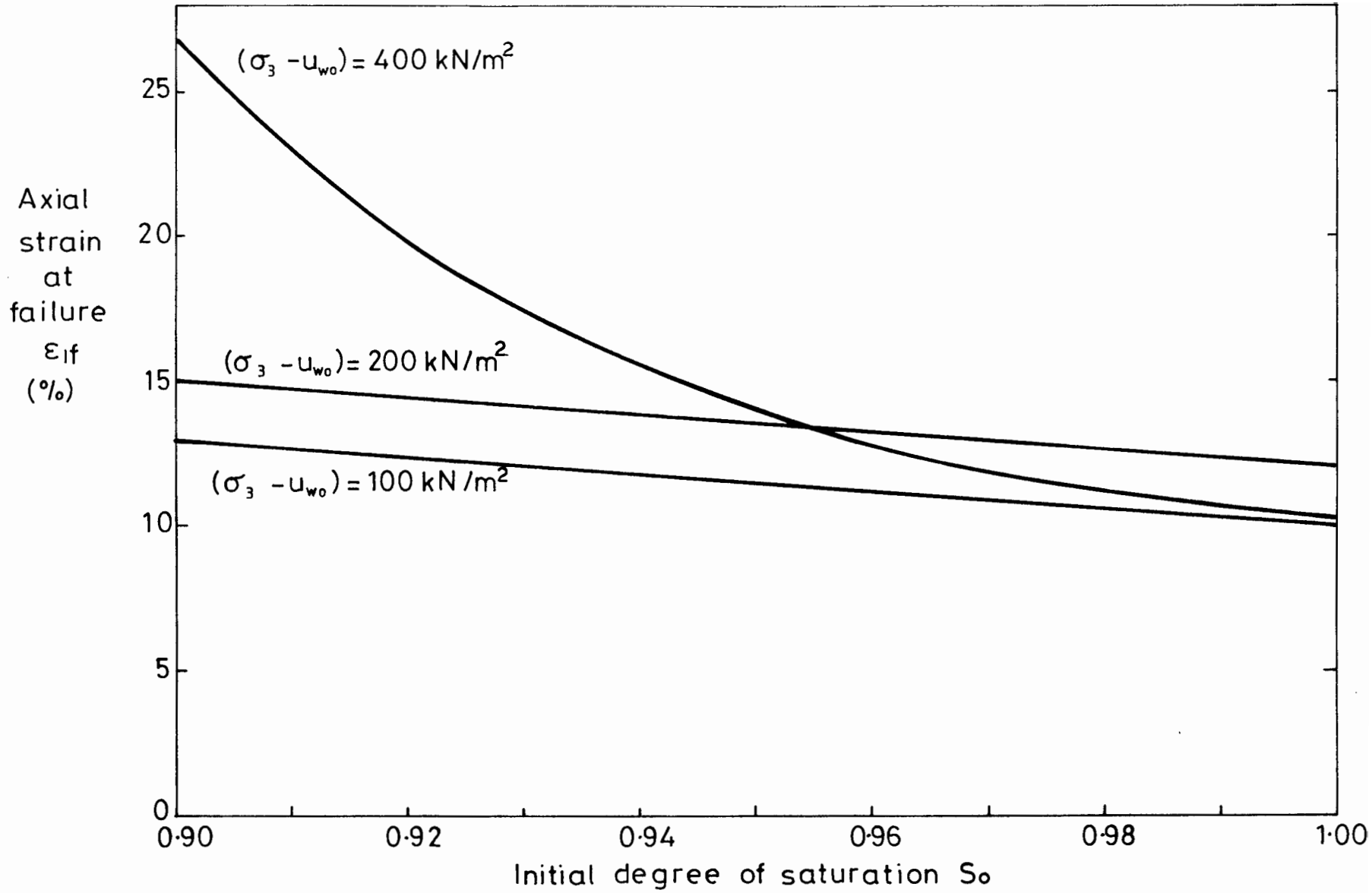

Fig. 4·10. AXIAL STRAIN AT FAILURE.

4.6 DEGREE OF SATURATION AND VOID RATIO AT FAILURE

Figure 4.11 shows the degree of saturation at failure S_f plotted against the initial degree of saturation S_o for the various values of consolidation pressure. In the top graph the scatter of the results at low values of S_o is quite severe and the curve has been drawn rather arbitrarily. Similarly, in the bottom graph there are only four data points and the curve has been drawn through these points by following the pattern observed in the two upper curves. All the curves indicate that if the initial saturation S_o is above a certain critical value S_c the soil reaches full saturation during the shear test. If S_o is below S_c the saturation increases during shearing, but the soil does not reach a fully saturated state.

The three curves of Figure 4.11 are all plotted on the same axes in Figure 4.12. This figure clearly indicates the effect of the consolidation pressure on the value of the critical saturation S_c. As the consolidation pressure increases, with the back pressure held at zero, S_c falls from about 0.96 at a consolidation pressure of 100 kN/m^2 to about 0.91 at 400 kN/m^2. With a back pressure of 100 kN/m^2 all the samples tested reached full saturation, because the minimum value of S_o was only about 0.97. Unfortunately this means that the results provide no information on the effect of the back pressure on the value of S_c.

Figure 4.13 shows the void ratio at failure e_f plotted against S_o, for the various values of consolidation pressure. The curves in this figure were calculated directly from those in Figures 4.4 and 4.12, by using the fact that the parameter Se must remain constant during an undrained test (Se is the volume of water in a volume of soil containing unit volume of solids). Therefore:

$$S_f e_f = S_o e_o \qquad 4.3$$

Rearranging:

$$e_f = \frac{S_o e_o}{S_f} \qquad 4.4$$

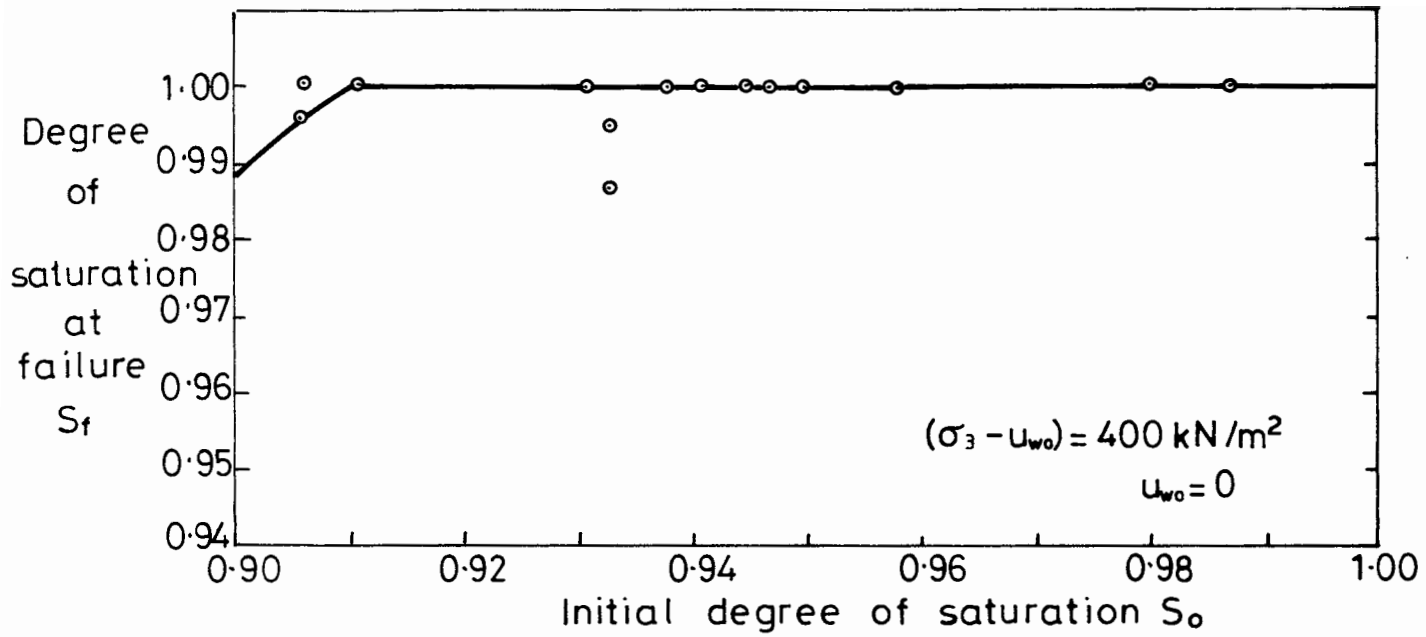

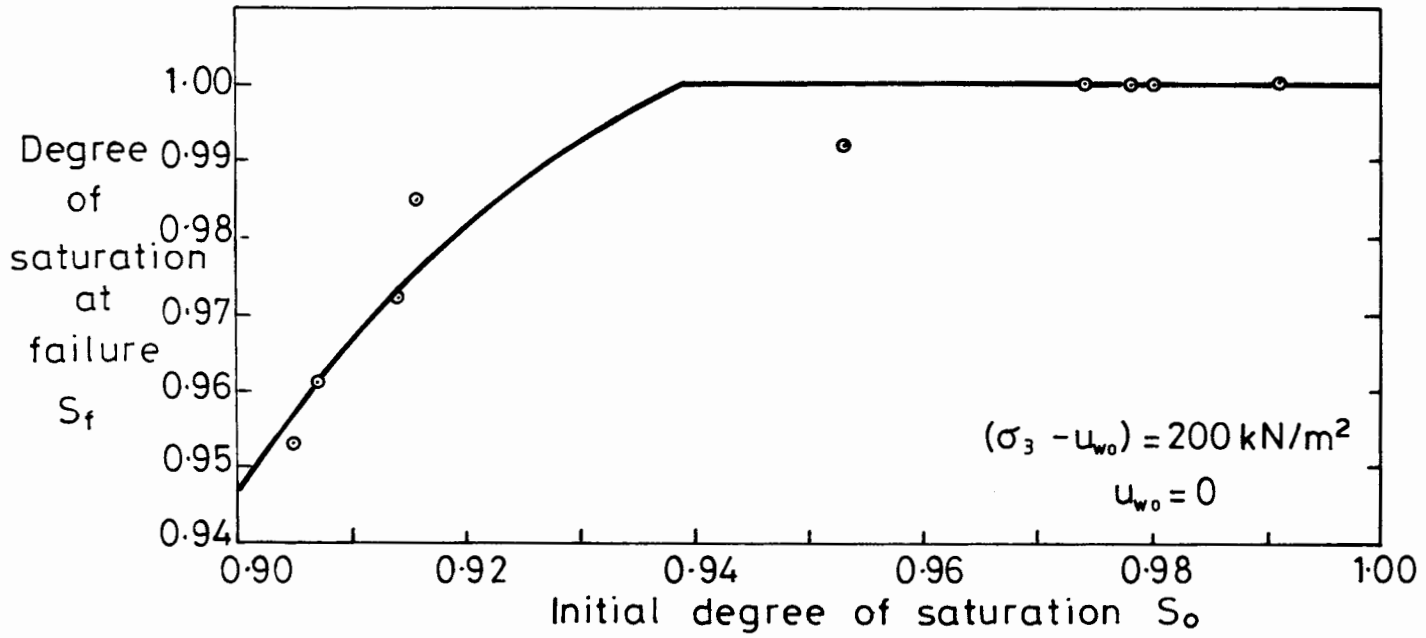

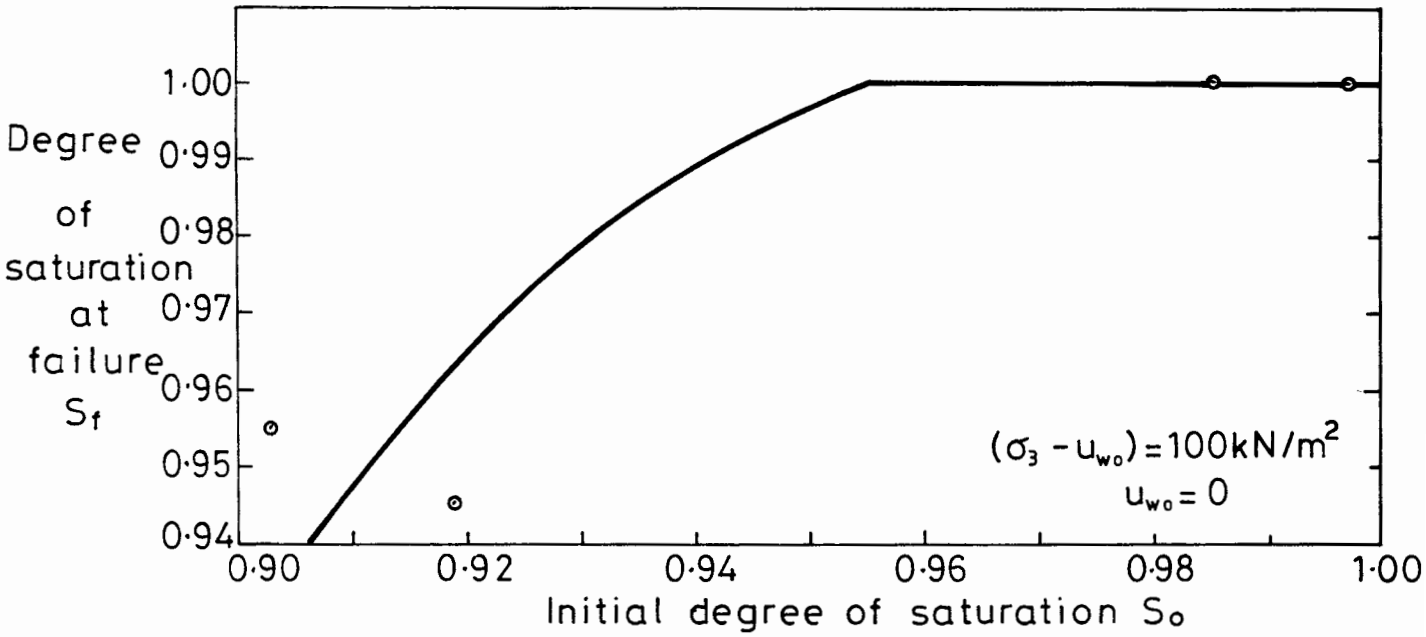

Fig. 4·11. DEGREE OF SATURATION AT FAILURE.

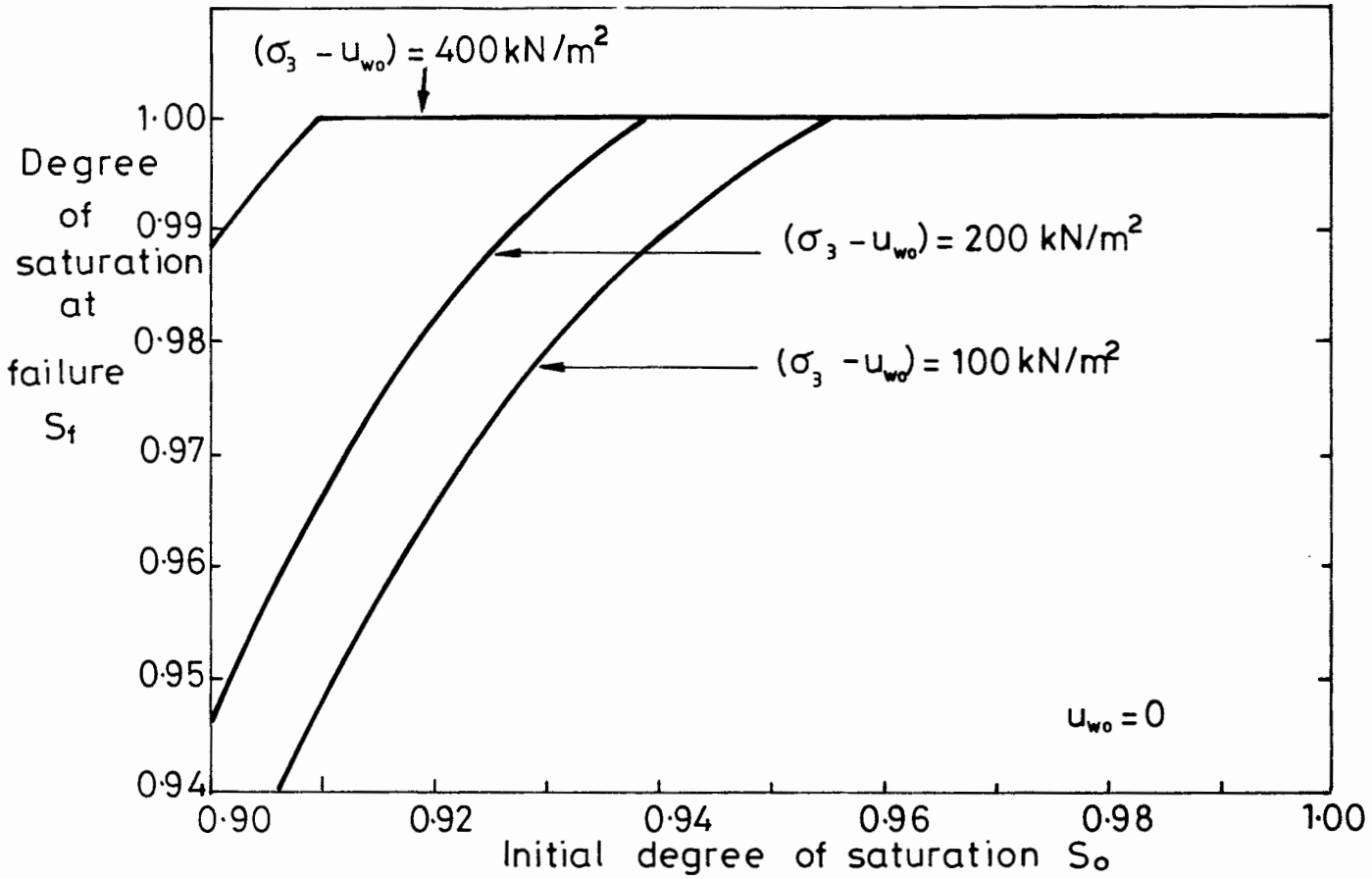

Fig. 4·12. DEGREE OF SATURATION AT FAILURE.

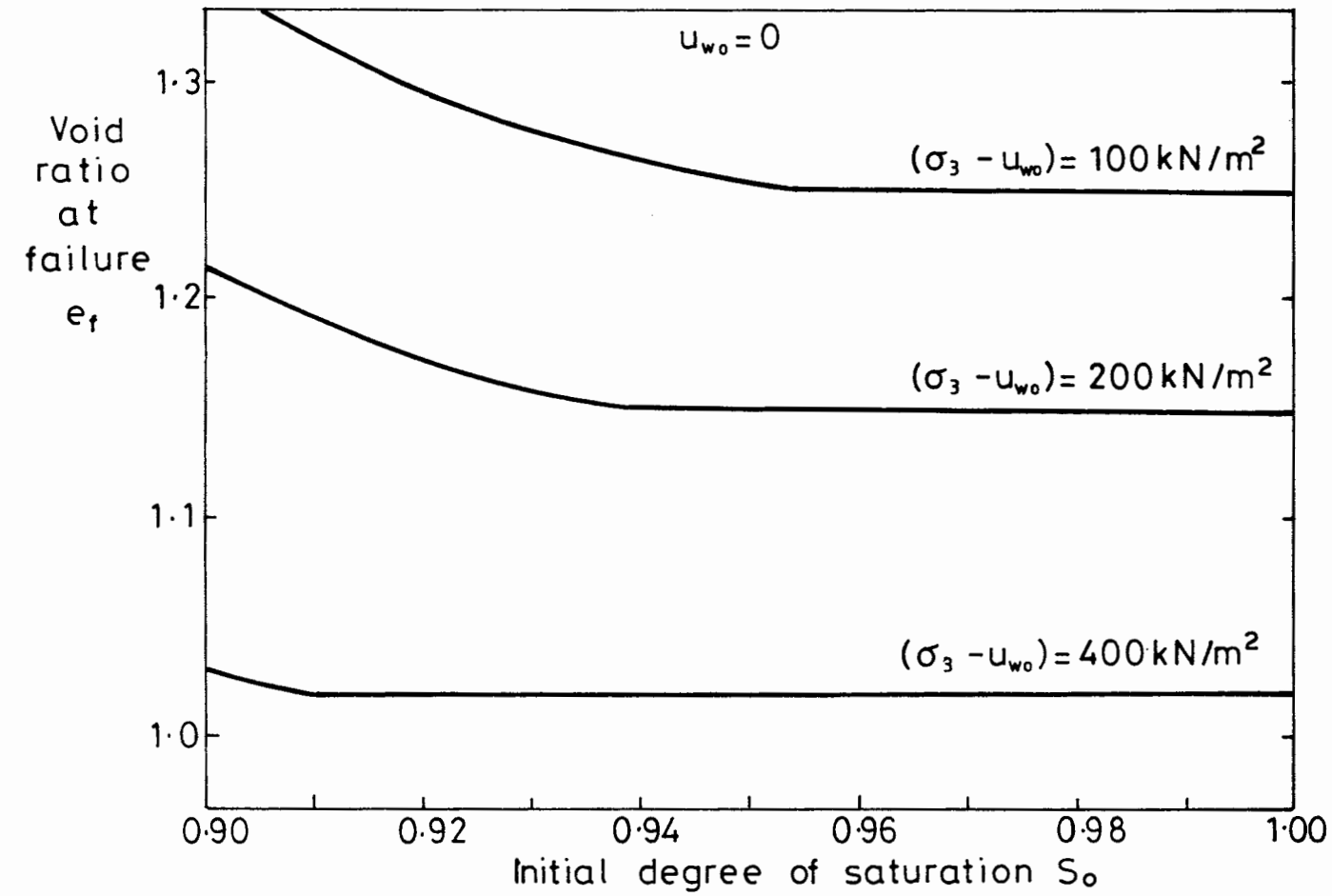

Fig. 4·13. VOID RATIO AT FAILURE.

If S_o is above S_c, so that the soil is in a fully saturated state at failure, Equation 4.4 reduces to:

$$e_f = S_o e_o \qquad 4.5$$

However, Section 4.2 described how the values of $S_o e_o$ produced by isotropic consolidation are uniquely related to the consolidation pressure. Therefore the horizontal lines in Figure 4.13 at high values of S_o are simply a consequence of the consolidation behaviour.

It is interesting to consider two different tests, one on a sample that is saturated right from the start, and the other on a sample that becomes saturated during the test. If both these samples fail in a saturated condition at the same void ratio, it might be expected that they would have the same undrained shear strength. However this is not the case. Figure 4.8 indicates that C_u varies with S_o (for a given consolidation pressure), despite the fact that e_f is independent of S_o for those samples that fail in a saturated state (Figure 4.13). It is clear that even if a sample reaches full saturation before failure, its behaviour is still affected by the fact that it has previously contained gas bubbles. This suggests that the structure of the soil is permanently affected by the earlier presence of the bubbles. This point is discussed in more detail in Chapter 9.

4.7 PORE WATER PRESSURE

Figure 4.14 shows the pore water pressure generated during shearing plotted against the initial saturation, for the various combinations of consolidation pressure and back pressure. The results are presented as the difference between the pore water pressure at failure u_{wf} and the pore water pressure at the start of shearing u_{wo}. Unfortunately, during five of the tests towards the end of the series, values of u_{wf} were not recorded, because of problems with a faulty pore water pressure transducer (see Table 4.1).

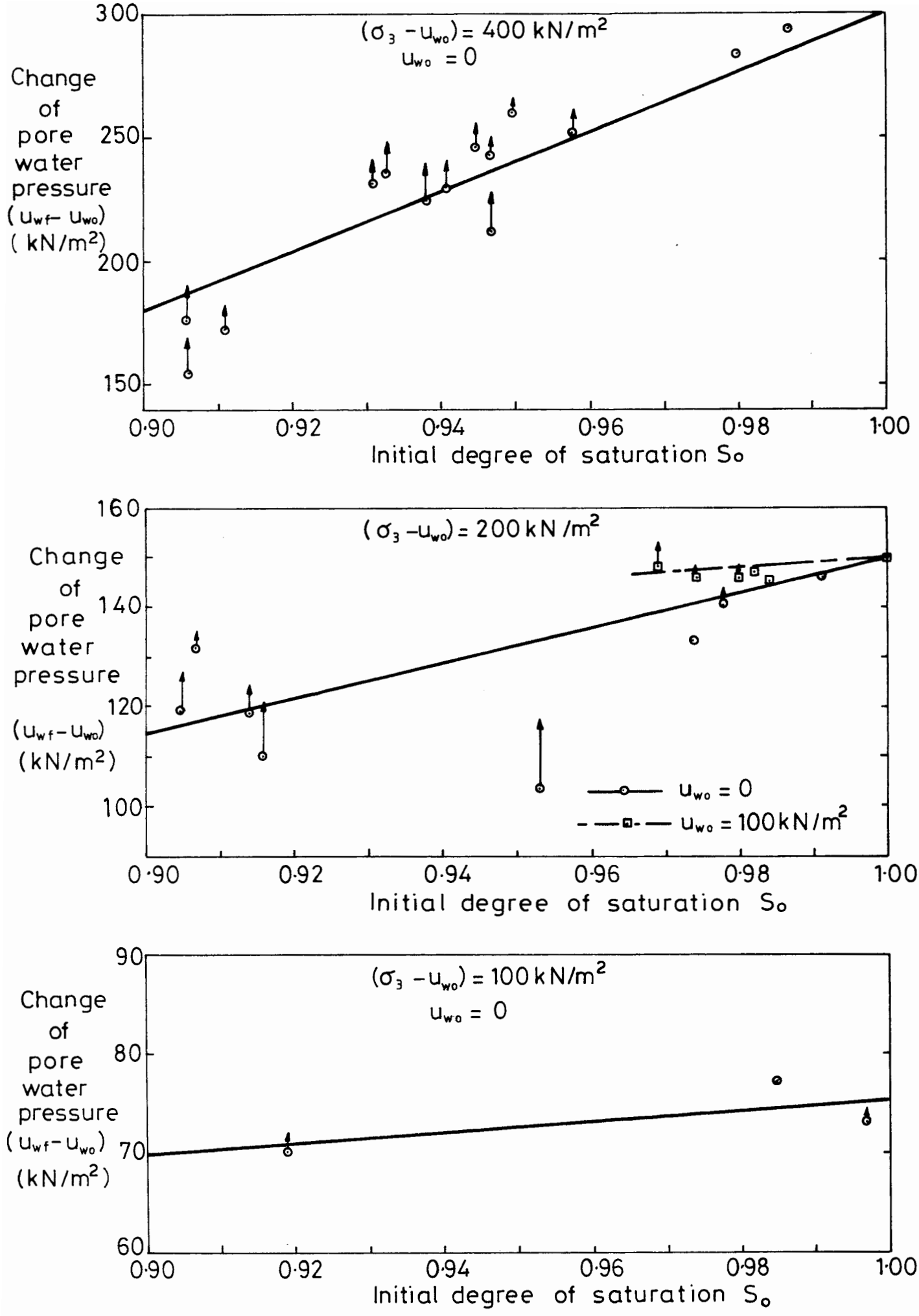

Fig. 4·14. CHANGE OF PORE WATER PRESSURE.

Because the shear tests were conducted too fast to allow full equalisation of pore pressure throughout the samples, there is some doubt about the validity of the measurements of u_{wf}. The arrows attached to each of the data points in Figure 4.14 are an attempt to convey some idea of the degree of uncertainty. The size of each arrow represents the measured change in u_w during the final 2% of axial strain. A large arrow indicates that the measured value of u_w was still rising dramatically at the end of the test and suggests that the true value of u_{wf} may have been considerably higher than the measured value.

The sizes of the arrows in Figure 4.14 seem to show that u_w almost reached equilibrium in those tests where S_o was greater than about 0.97. However, for the tests where S_o was less than 0.97, the measured values of u_w were still changing quite considerably when the tests were terminated. It appears that for saturated or near-saturated samples the rate of testing was sufficiently slow to allow full equalisation, but that samples containing large volumes of gas bubbles required a slower rate of testing. This difference was probably caused by the fact that tests on gas-bearing samples are affected by the time required for the gas to move into solution. Another explanation could be that the presence of the gas bubbles reduces the value of the consolidation coefficient c_v.

The four curves of Figure 4.14 are all plotted on the same set of axes in Figure 4.15. In this figure the results have been normalized by dividing the change in pore water pressure $(u_{wf} - u_{wo})$ by the consolidation pressure $(\sigma_3 - u_{wo})$. It should be remembered that the curves shown in the figure may be very inaccurate, because of errors in the measurements of u_{wf} at low values of S_o. However, despite this caveat, a few tentative conclusions can be drawn from the figure. Firstly, the normalised change in pore water pressure is the same for all saturated samples (as would be expected) and rather less for unsaturated samples. Secondly, the change of pore water

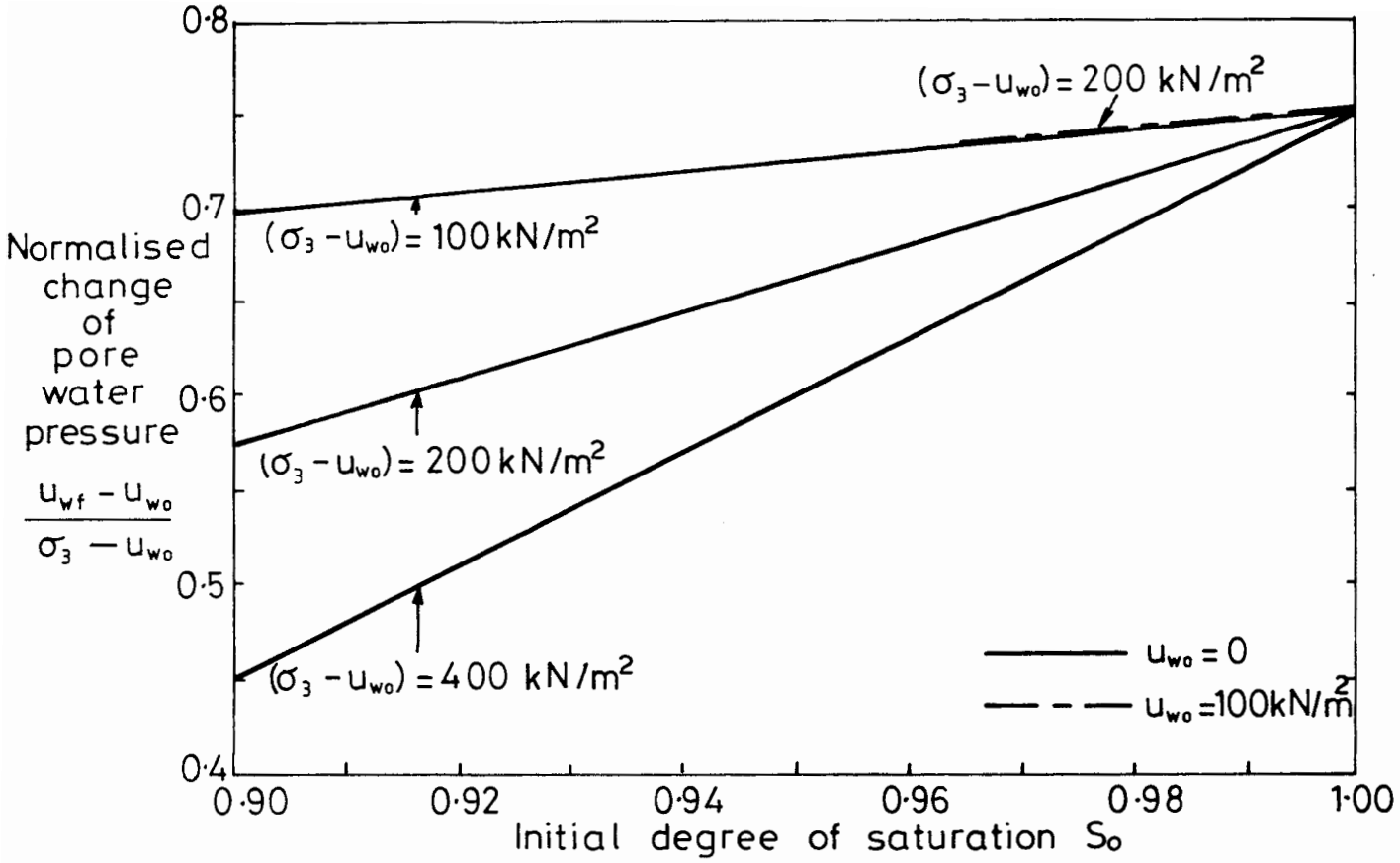

Fig. 4·15. NORMALISED CHANGE OF PORE WATER PRESSURE.

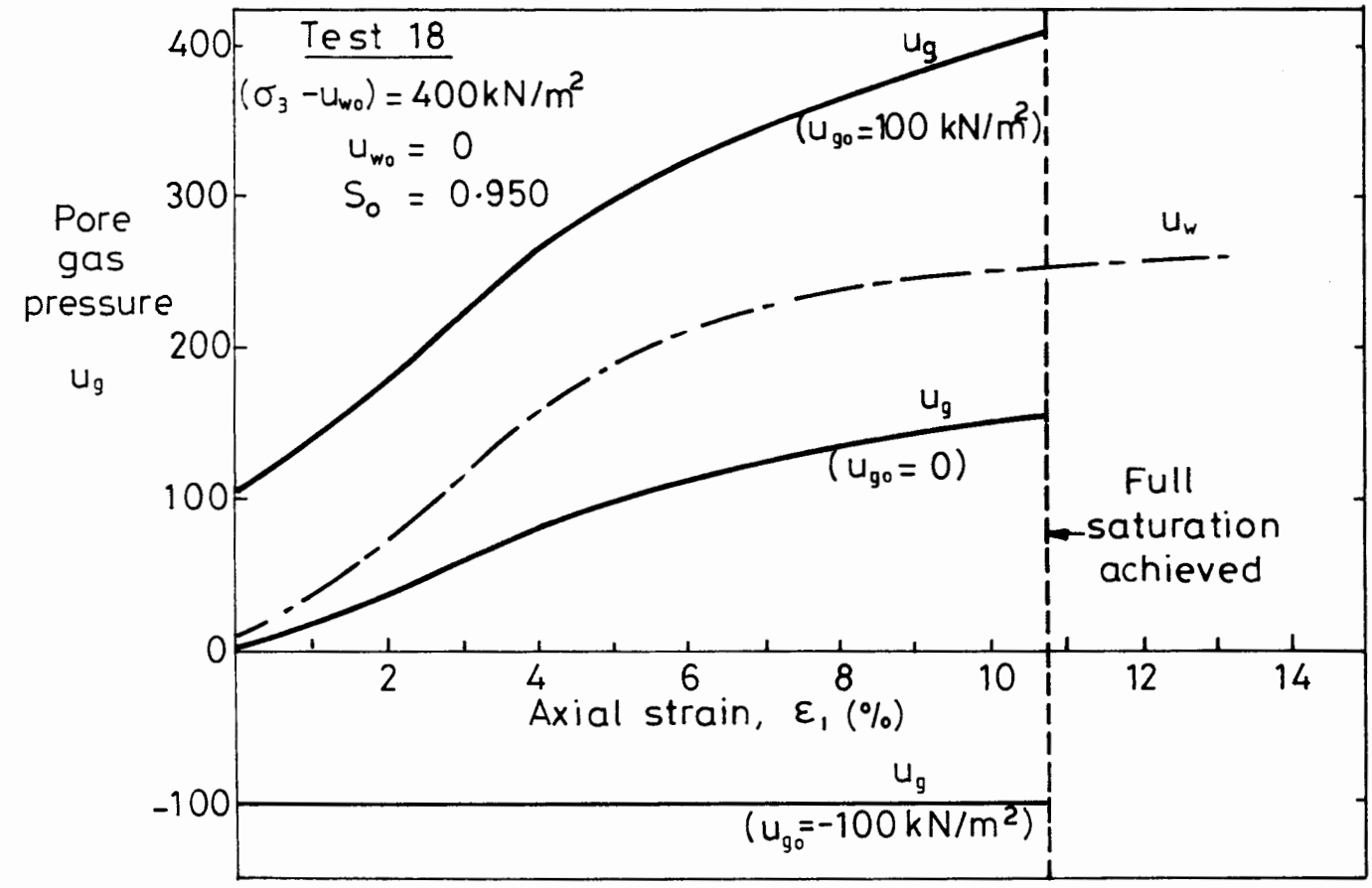

Fig. 4·16. TYPICAL VARIATION OF PORE GAS PRESSURE.

pressure is reduced most dramatically by the gas bubbles when the consolidation pressure is high and the back pressure is low.

4.8 PORE GAS PRESSURE

Section 3.8 of the previous chapter described how the measurements of the degree of saturation could be used to calculate the variation of the pore gas pressure throughout each test. To do this it was necessary to assume a value for the gas pressure at the start of the test u_{go}. The three solid curves in Figure 4.16 show the calculated variation of u_g for a typical test (Test 18) with three different assumptions for the value of u_{go}. For the middle curve the initial gas pressure u_{go} was assumed to be the same as the initial water pressure u_{wo} (which was zero for this particular test). The other two curves show the variation of the pore gas pressure if u_{go} was either 100 kN/m^2 above u_{wo} or 100 kN/m^2 below u_{wo}. The chain-dotted line is the variation of the pore water pressure, which is shown for comparison. It is clear from the figure that the change of gas pressure can not be calculated precisely, because it depends upon the value of u_{go}. At this stage it is difficult to draw any conclusion on the likely value of either u_{go} or the change in gas pressure.

4.9 STRESS PATHS AND FAILURE CONDITIONS

Figure 4.17 shows the stress paths for a typical test (Test 18). The straight line with a slope of 3 is the total stress path, which consists of the deviator stress q plotted against the mean total stress p (Atkinson and Bransby, 1978). The curved line shows q plotted against $(p - u_w)$. For a saturated soil this would be termed the effective stress path, but for a sample containing gas bubbles the stress $(p - u_w)$ is no longer an effective stress (see Chapter 1). The horizontal separation between the two stress paths is the pore water pressure u_w.

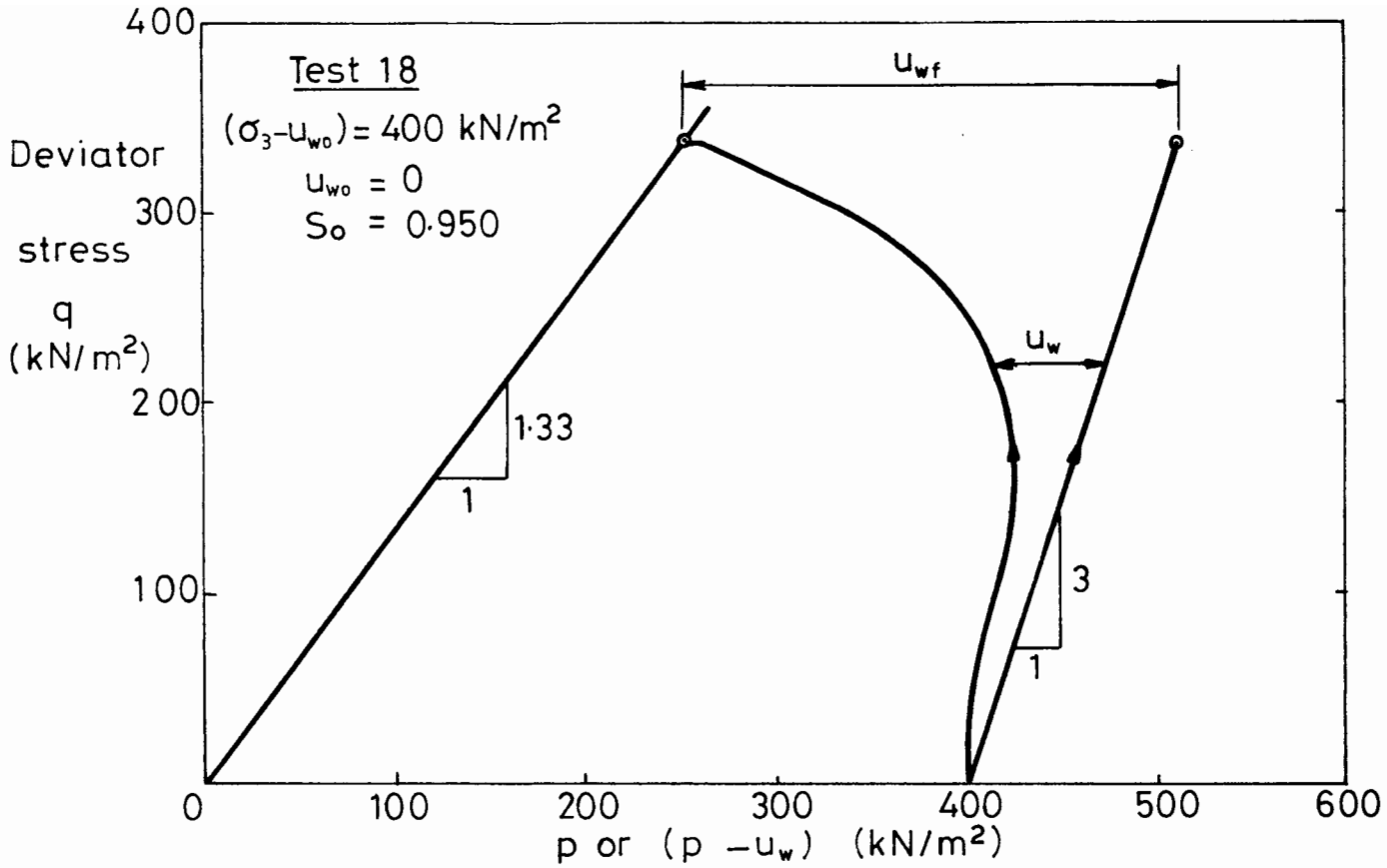

Fig. 4·17. STRESS PATH FOR A TYPICAL TEST.

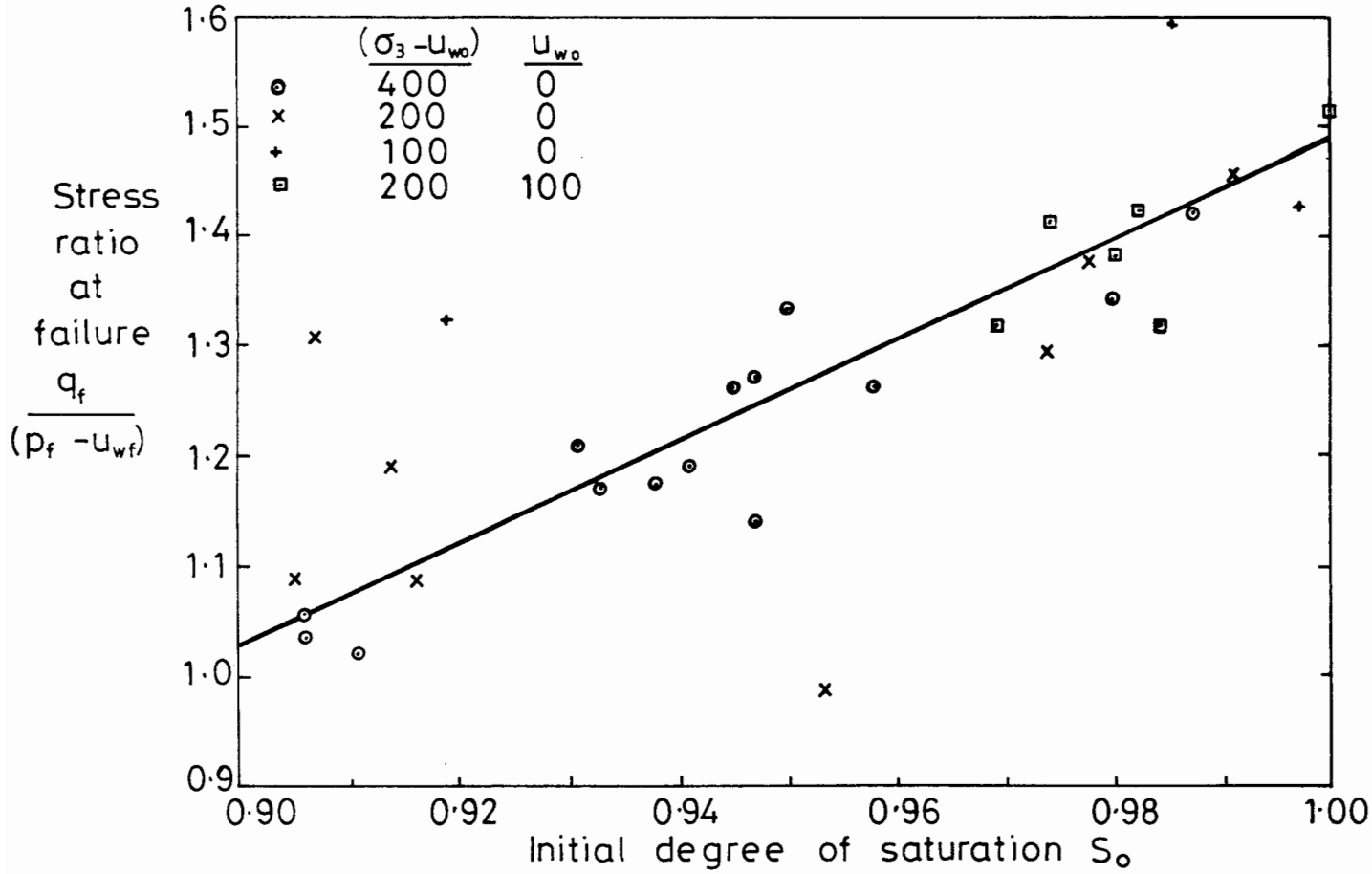

Fig. 4·18. STRESS RATIO AT FAILURE.

The $(p - u_w)$ stress path shown in Figure 4.17 may be very inaccurate, particularly in the early part of the test, because of the errors in the measurements of u_w. In all the tests, even those on saturated samples, the stress path tended to the right in the early stages. This is a further indication that the pore water pressure measured at the base was less than the water pressure generated throughout the rest of the sample. The only other explanation for an increase in $(p - u_w)$ during the early part of an undrained test on a saturated sample would be that the soil was anisotropic, with the vertical stiffness greater than the horizontal stiffness (Graham and Houlsby, 1983). This appears to be very unlikely, because the samples were isotropically consolidated to stress levels that were up to eight times the earlier one-dimensional stress.

Figure 4.17 shows that the ratio of the deviator stress at failure q_f to the value of $(p - u_w)$ at failure was apparently 1.33 for Test 18. However, this value may be quite inaccurate, because of the uncertainty in the measurement of u_{wf}.

Figure 4.18 shows the stress ratio at failure $q_f/(p_f - u_{wf})$ plotted against the initial saturation S_o. The data from all the tests are presented in the figure and the trend in the results appears to be independent of the consolidation pressure and the back pressure. For saturated samples, the stress ratio at failure is given by the critical state parameter M (Atkinson and Bransby, 1978). From the figure:

$$M = 1.49 \qquad 4.6$$

The stress ratio at failure apparently decreases as S_o is reduced, reaching a value of about 1.03 when S_o is 0.90. This would suggest that there is not a unique critical state line in $q : (p - u_w)$ space for soil samples containing gas bubbles. However, Figure 4.18 should be viewed with some caution, because of the inaccuracy of the measurements of u_{wf} in tests for

which S_o was less than about 0.97. If the true values of u_{wf} for these samples were greater than the measured values (as was probably the case), the actual stress ratios at failure would be higher than the values shown in the figure i.e. closer to the saturated value.

Figure 4.19 shows the specific volume at failure $(1 + e_f)$ plotted against the stress parameter $(p_f - u_{wf})$, for the different values of consolidation pressure and initial degree of saturation. The solid line illustrated in Figure 4.19 represents the failure conditions for saturated samples, while the data points show the failure conditions from individual tests. Four different symbols are used in the figure, to give some indication of the initial degree of saturation for each experimental point.

Although Figure 4.19 should be treated rather circumspectly, because of the uncertainty in the values of u_{wf}, it appears to show quite clearly that there is no unique relationship between the specific volume and the stress $(p - u_w)$ at failure. For samples that start out unsaturated, the failure conditions plot as points lying above and to the right of the saturated critical state line. This is true even for samples which reach full saturation prior to failure.

Section 4.6 described how samples failing at the same void ratio e_f did not have the same deviator stress at failure q_f. Therefore, it appears that there is no critical state relationship between any of the three parameters q, $(p - u_w)$ and $(1 + e)$.

The straight line shown in Figure 4.19 is the critical state line for saturated samples. The line has the following equation:

$$(1 + e_f) = 2.946 - 0.174\log_e(p_f - u_{wf}) \qquad 4.7$$

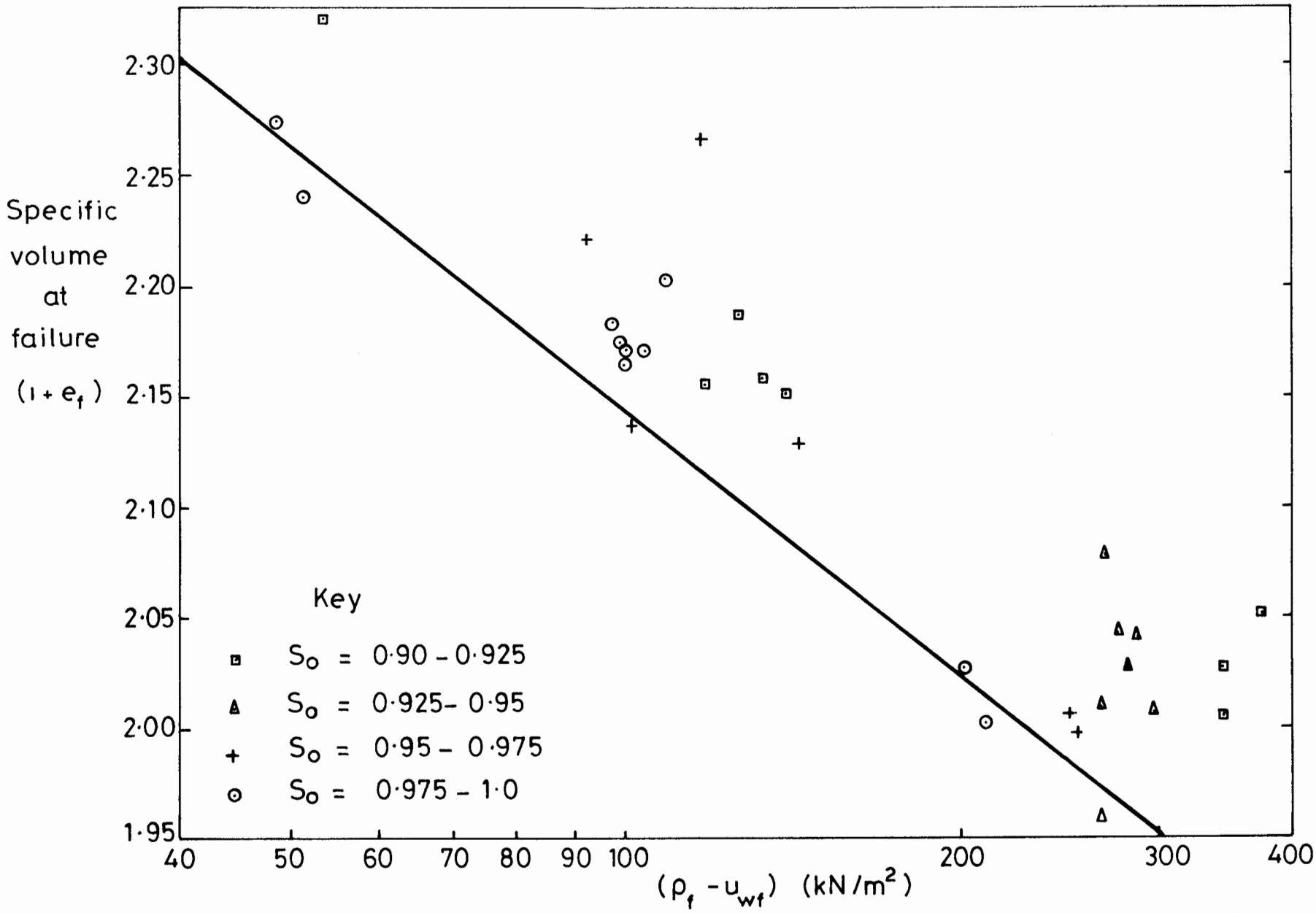

Fig. 4·19. CONDITIONS AT FAILURE.

Therefore, the parameters λ and Γ, which define the critical state line, have the following values:

$$\lambda = 0.174, \qquad \Gamma = 2.946 \qquad 4.8$$

It is reassuring to note that the value of λ calculated from the critical state line is the same as the value calculated from the normal consolidation line (given in Equation 4.2).

From Equations 4.2 and 4.8 the spacing of the normal consolidation line and the critical state line is given by:

$$N - \Gamma = 0.116 \qquad 4.9$$

Equation 4.9 could be used to determine the value of the parameter κ (the slope of a swelling-line), because the spacing of the normal consolidation line and the critical state line is a function of λ and κ. However, the exact expression for this spacing depends upon the particular critical state model that is being employed. For example the original Cam Clay model (Schofield and Wroth, 1968) suggests a spacing of $(\lambda - \kappa)$, while the Modified Cam Clay model (Roscoe and Burland, 1968) involves a slightly different spacing. Irrespective of which model is assumed, the value of κ calculated from Equation 4.9 could be very inaccurate, as it would be very sensitive to small inaccuracies in the measurements of N, Γ and λ. A better method for calculating κ would be to measure the slope of a swelling-line directly, but unfortunately this was not done.

4.10 UNDRAINED SHEAR MODULUS

Figure 4.20 shows the secant values of the undrained shear modulus G_u plotted against the initial degree of saturation S_o, for the various combinations of consolidation pressure and back pressure. There is considerable scatter of the results, but the three graphs all show a clear trend, with G_u decreasing as the saturation is reduced. The scatter of the results was

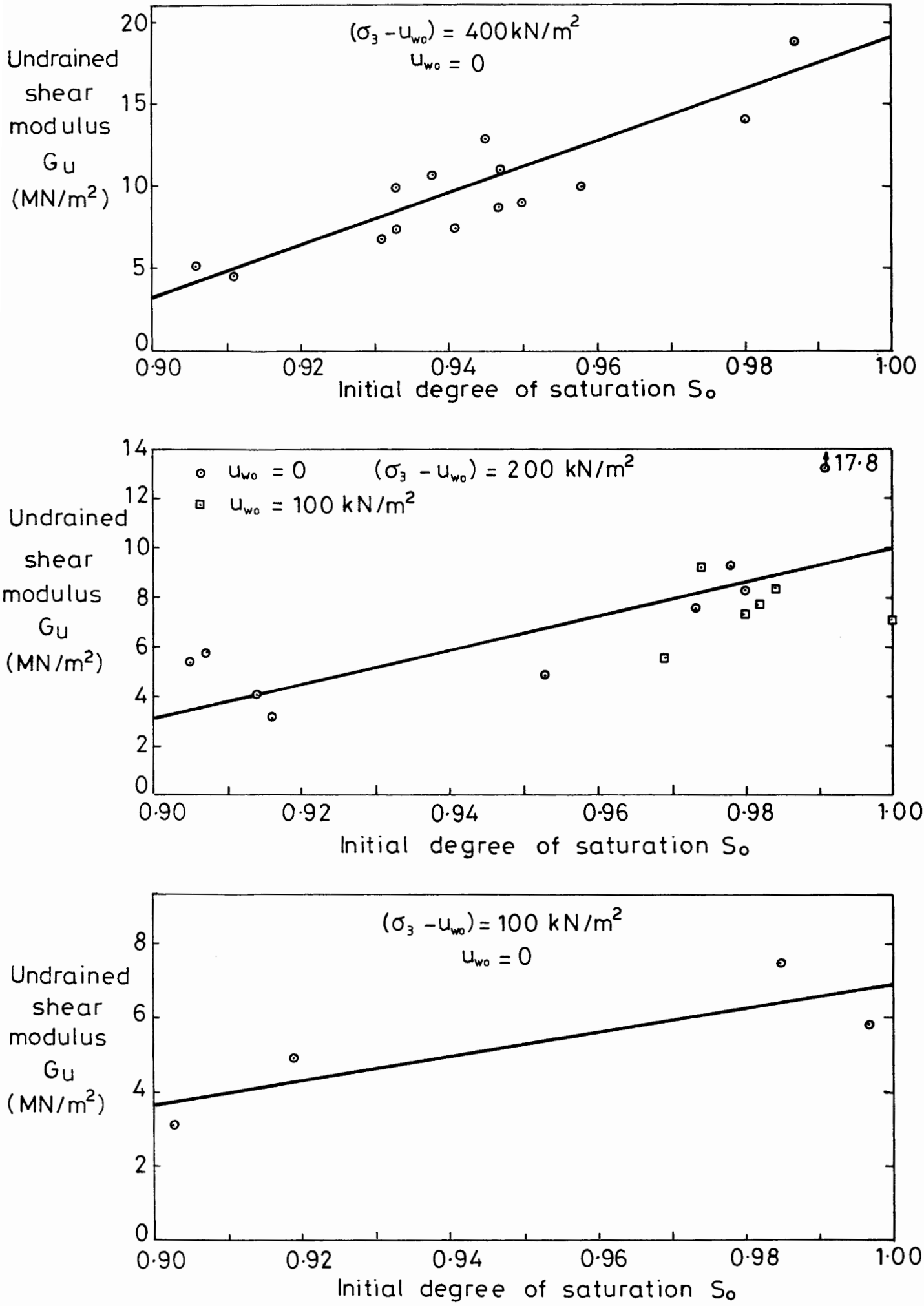

Fig. 4·20. UNDRAINED SHEAR MODULUS.

probably caused, at least partly, by the fact that the experimental apparatus and procedure were designed to suit the primary objective of measuring the undrained shear strength, and were not ideal for studying the conditions prior to failure. In particular the method of axial strain measurement was poorly suited to a study of small strain behaviour (Jardine, Symes and Burland, 1984).

Figure 4.21 shows the three curves of the previous figure all plotted on the same set of axes. The vaues of G_u have been normalised by dividing by G_{sat}, the value of G_u for a saturated sample prepared to the same consolidation pressure. The subscript "u" (referring to undrained conditions) has been dropped from the symbol G_{sat}, because the shear modulus of a saturated soil is independent of the drainage conditions (Atkinson and Bransby, 1978). The values of G_{sat} are 6.9 MN/m^2, 10 MN/m^2 and 19 MN/m^2 for the three different consolidation pressures. These values, which were taken from the curves of Figure 4.20, obey the following approximate relationship:

$$G_{sat} = b(\sigma_3 - u_{wo})^{0.7} \qquad 4.10$$

b is a constant. This is in agreement with accepted behaviour for saturated soils (Wroth et al, 1984).

The effect of the consolidation pressure on the normalised value of G_u is illustrated by Figure 4.21. As the consolidation pressure is increased, with the back pressure held constant, G_u becomes increasingly sensitive to the initial saturation S_o. Unfortunately it is difficult to establish the effect of the back pressure on the values of G_u, because the test series for which the back pressure was 100 kN/m^2 covered such a small band of saturation values.

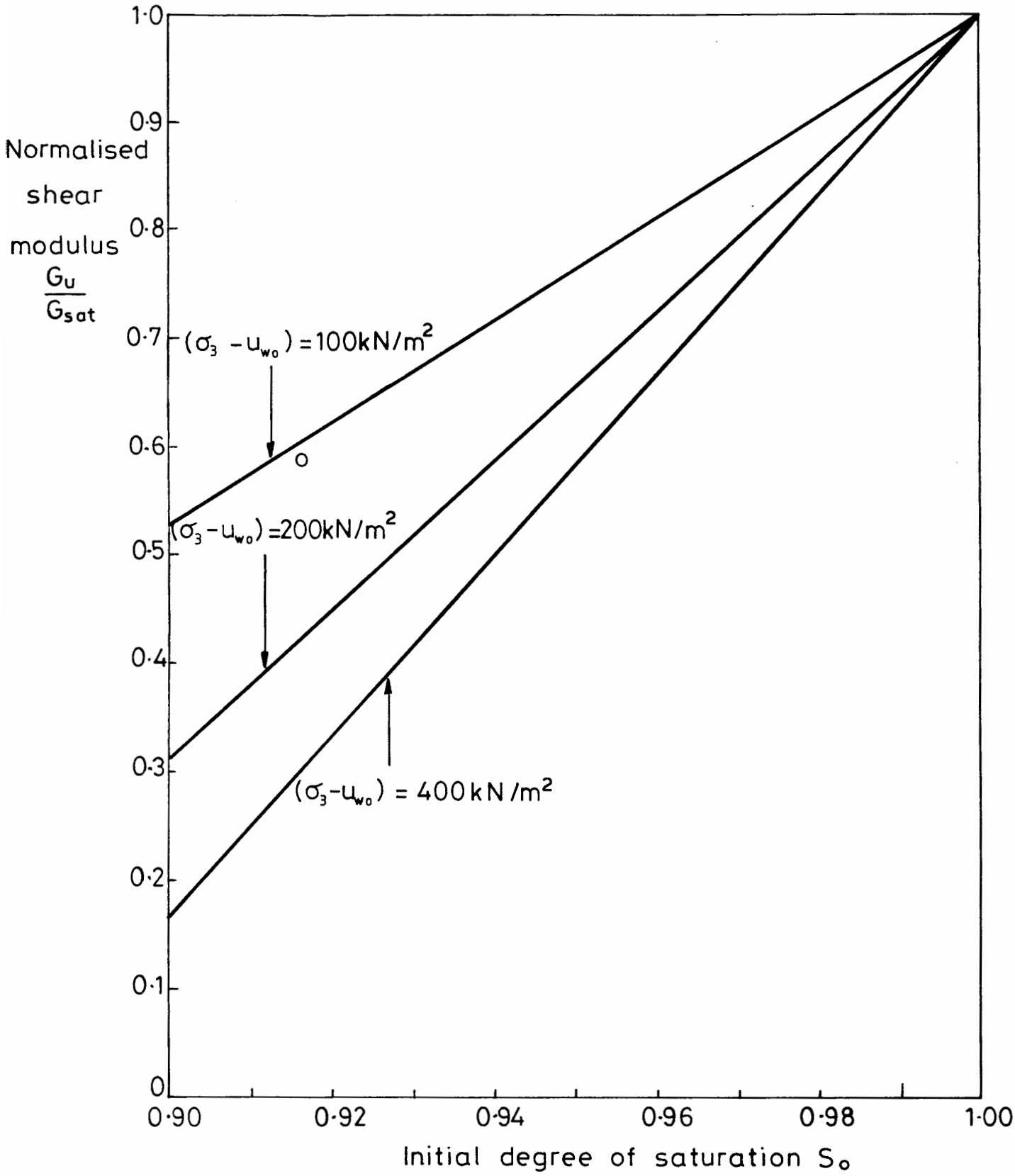

Fig. 4·21. NORMALISED UNDRAINED SHEAR MODULUS.

4.11 UNDRAINED BULK MODULUS

Figure 4.22 shows the secant values of the undrained bulk modulus K_u plotted against the initial degree of saturation S_o, for each of the different combinations of consolidation pressure and back pressure. It is clear that even a small volume of gas bubbles reduces the bulk modulus dramatically.

In Figure 4.23 the values of K_u have been normalised by dividing by the shear modulus of the equivalent saturated soil G_{sat}. This may appear initially a rather strange choice of normalisation, but the theoretical analysis presented in Chapter 6 suggests that it is in fact the most logical form of presentation. The curves shown in Figure 4.23 present a rather complicated picture, in which it is hard to see any coherent pattern. At low values of S_o the normalised shear modulus decreases with increasing consolidation pressure $(\sigma_3 - u_{wo})$, but at higher values of S_o the effect of $(\sigma_3 - u_{wo})$ is less clear.

Theoretical expressions for the elastic moduli of soils containing gas bubbles are derived in Chapter 6. The experimental values of the shear modulus and the bulk modulus recorded in this chapter are compared with the theoretical predictions in Chapter 9.

4.12 INFLUENCE OF ONE-DIMENSIONAL CONSOLIDATION

For the majority of tests, the stress level employed in the initial one-dimensional consolidation was 50 kN/m^2. The samples were then consolidated isotropically to 100 kN/m^2, 200 kN/m^2 or 400 kN/m^2. The ratio of the isotropic consolidation pressure to the previous vertical stress therefore varied between two and eight for the different tests. In Section 3.3 of the previous chapter it was suggested that the change in this ratio might affect the soil behaviour, and Test 50 was designed to investigate this possibility. In Test 50 a stress of 100 kN/m^2 was used for one-dimensional consolidation (followed by isotropic consolidation to 400 kN/m^2).

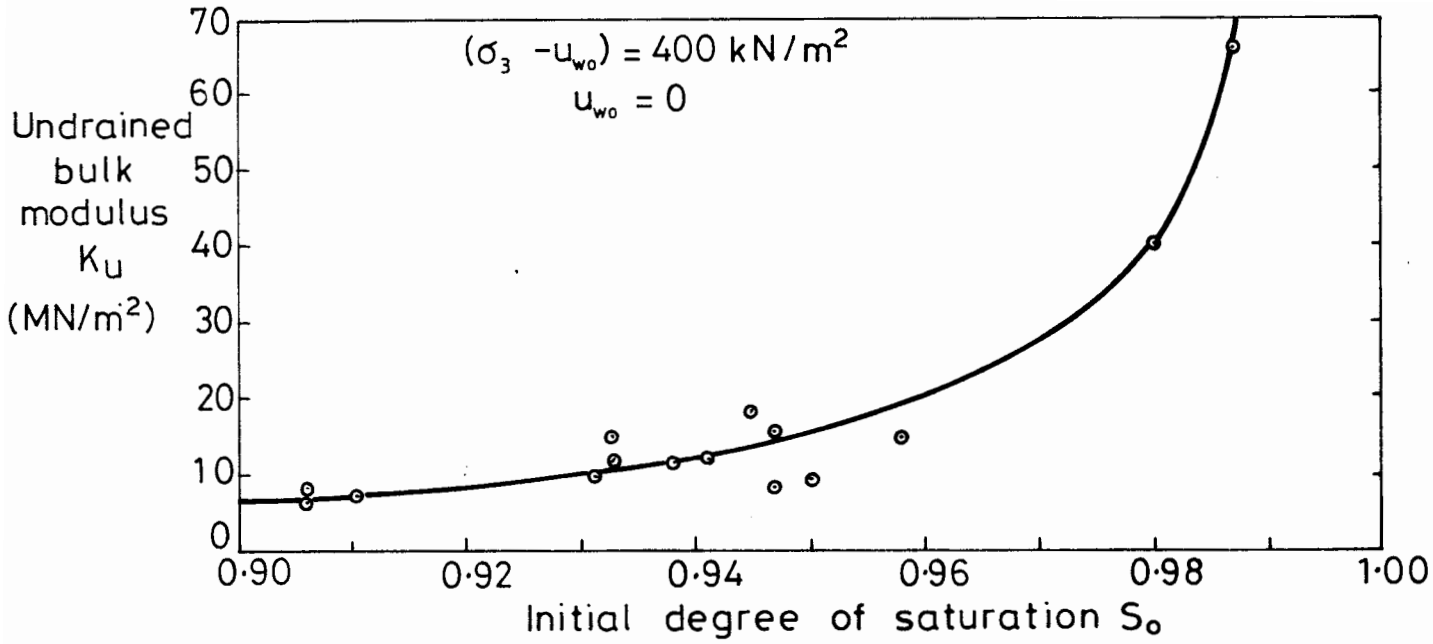

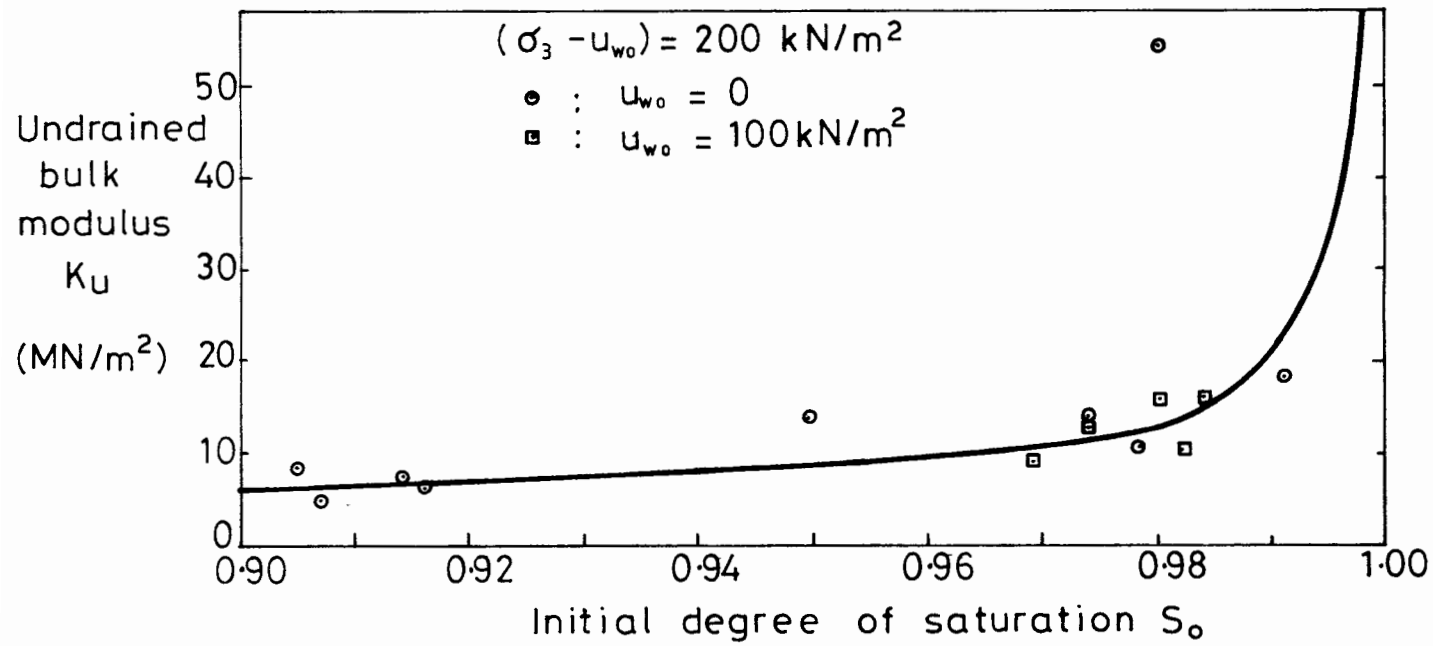

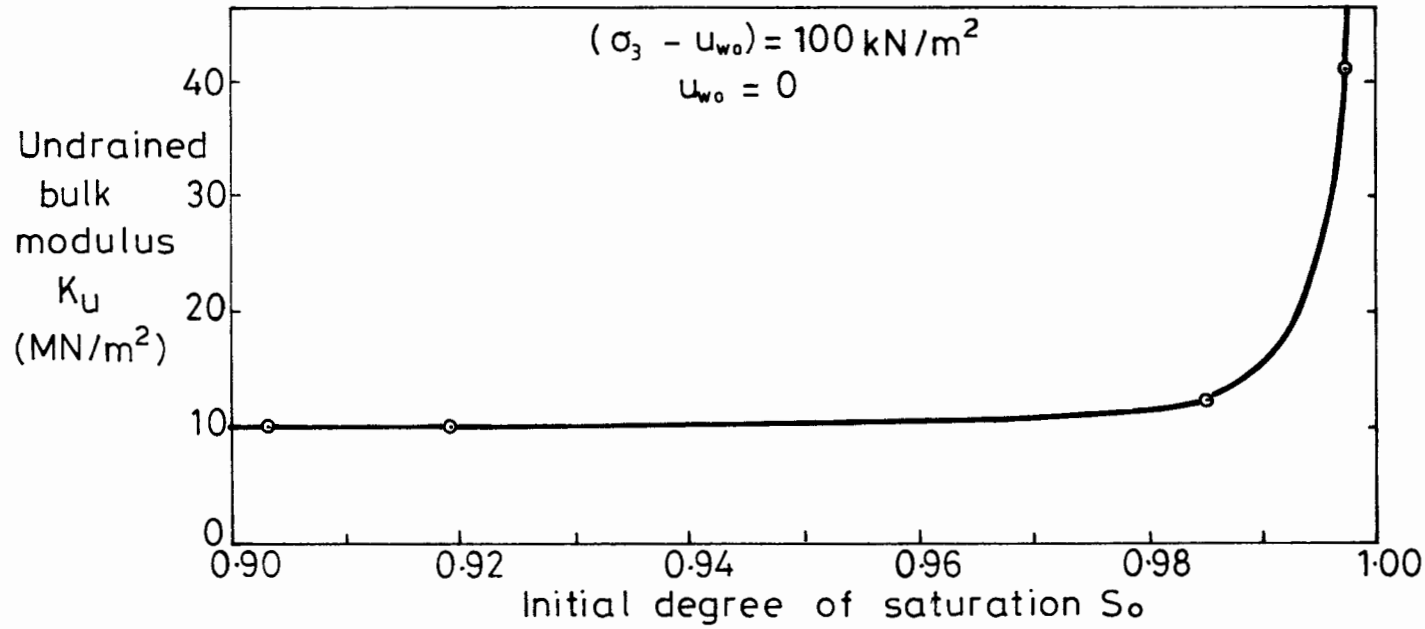

Fig. 4·22. UNDRAINED BULK MODULUS.

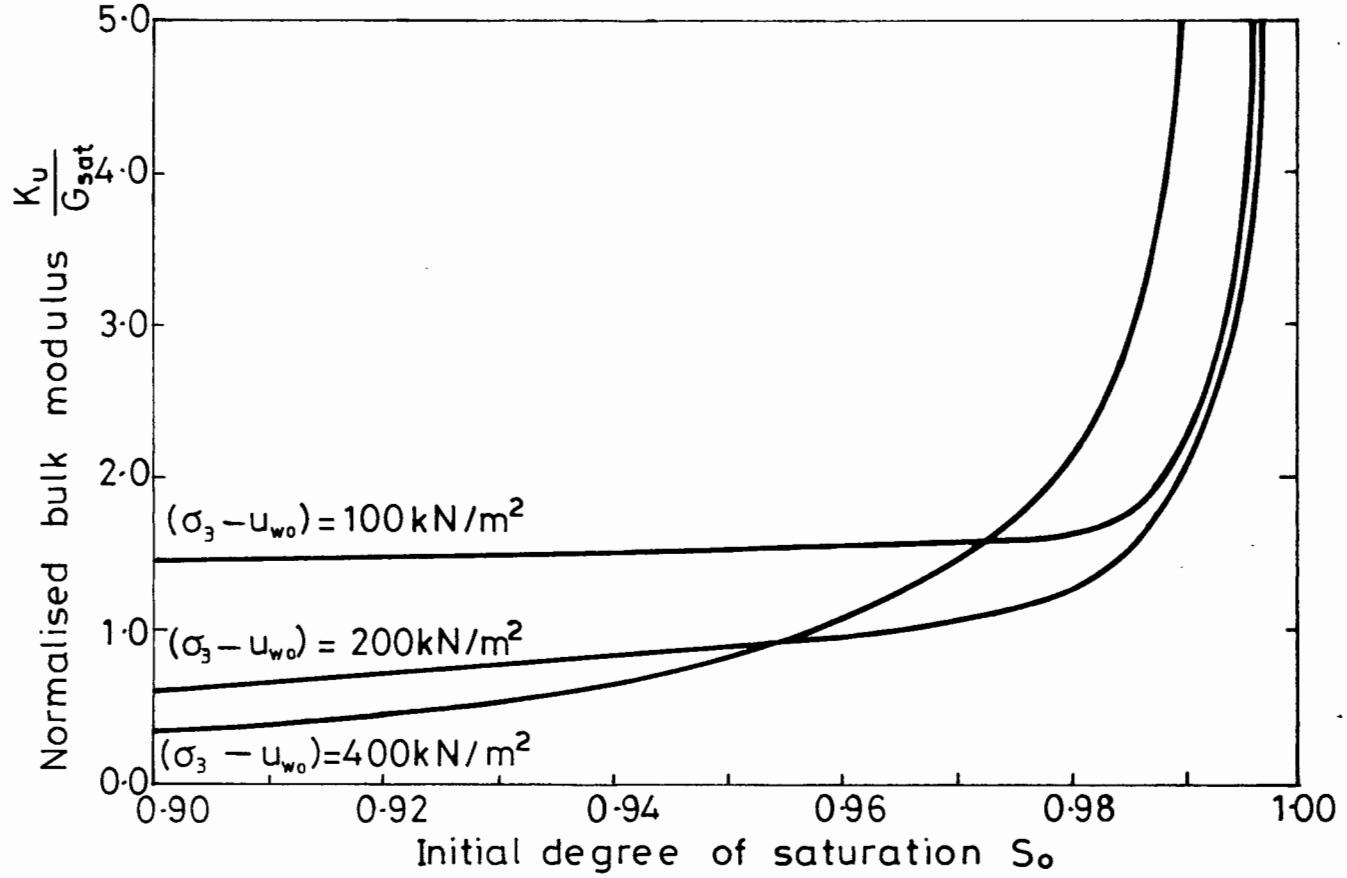

Fig 4·23. NORMALISED UNDRAINED BULK MODULUS.

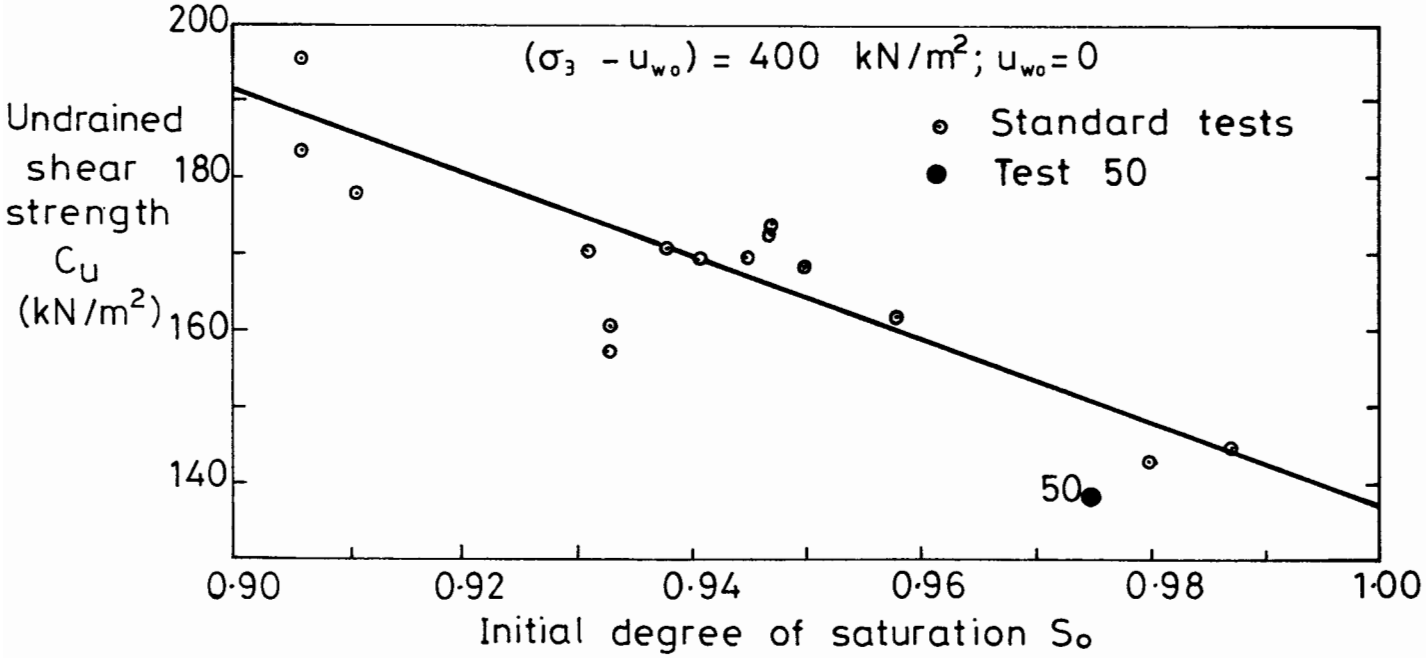

Fig. 4·24. INFLUENCE OF ONE-DIMENSIONAL CONSOLIDATION.

Figure 4.24 shows the undrained shear strength measured in Test 50, together with the results from all the other samples consolidated isotropically to 400 kN/m^2. The value of C_u from Test 50 is slightly lower than the general trend, but is is within the normal scatter of the results. The various other parameters measured in the test (such as failure strain, undrained shear modulus and undrained bulk modulus) also came within the general scatter of results. It therefore appears that the soil behaviour is not severely affected by the ratio of the isotropic consolidation stress to the previous one-dimensional stress (provided that this ratio is above a certain minimum value).

4.13 SAMPLE DISTURBANCE TESTS

Tests 43 and 46 were designed to model the effects of the sample disturbance caused by recovery from the seabed, as described in Section 3.9 of the previous chapter. After preparing each sample under a consolidation pressure of 200 kN/m^2 and zero back pressure the drainage line was closed and the cell pressure was reduced to atmospheric. After 24 hours the cell pressure of 200 kN/m^2 was reapplied and the drainage line was opened again. When any renewed consolidation was complete, the shear test was conducted in the normal manner.

Figure 4.25 shows the main results from the sample disturbance tests, together with the corresponding data from the other samples prepared to the same consolidation pressure and back pressure.

When the cell pressure was reduced in Tests 43 and 46 the sample volume increased as the gas bubbles expanded and additional gas came out of solution. The sample then compressed again as the cell pressure was reapplied, but the final volume after reconsolidation was slightly less than after the initial consolidation. This point is illustrated in the upper graph of Figure 4.25, which shows the void ratio after consolidation e_o. In the figure, Tests 43

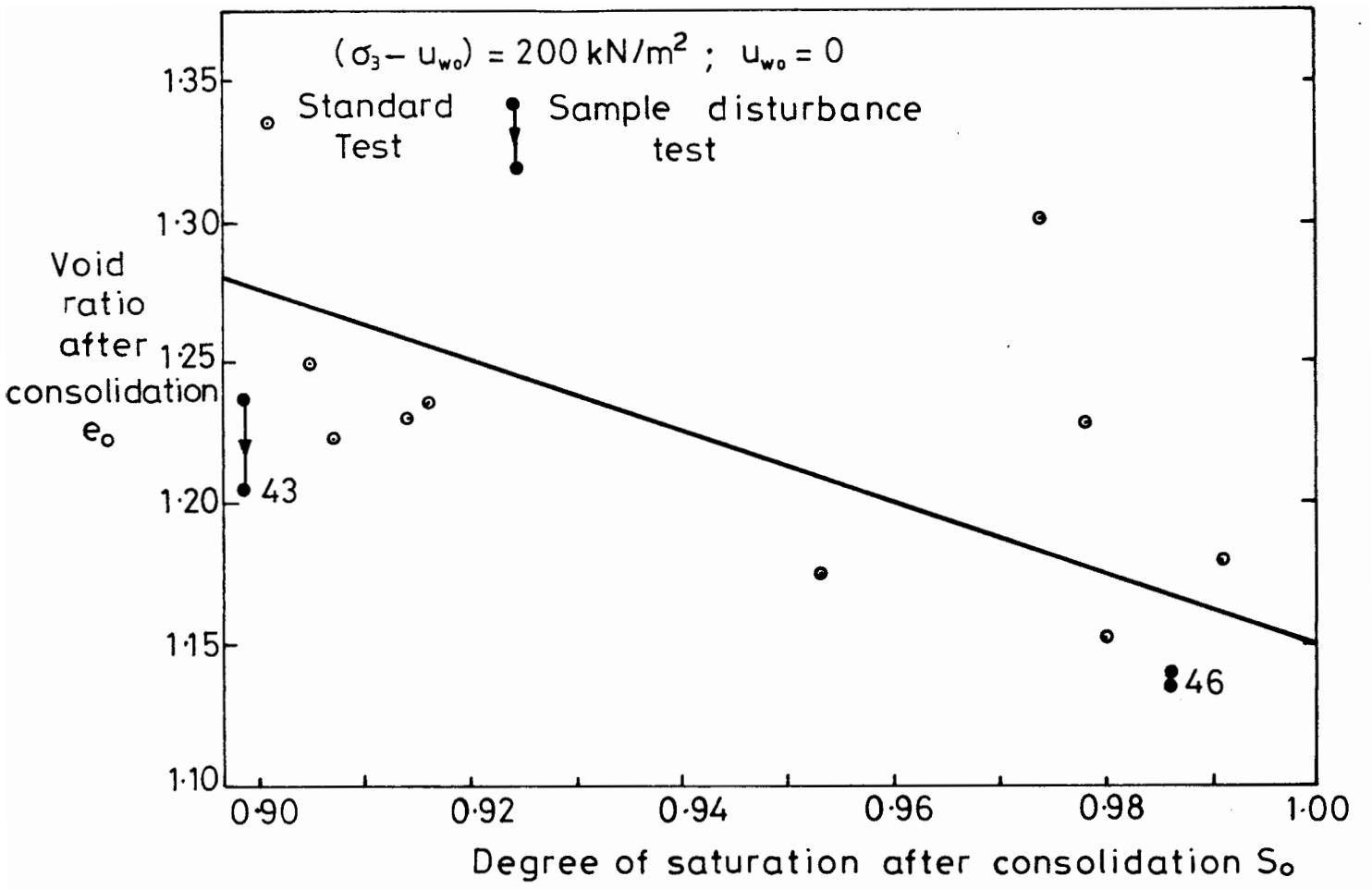

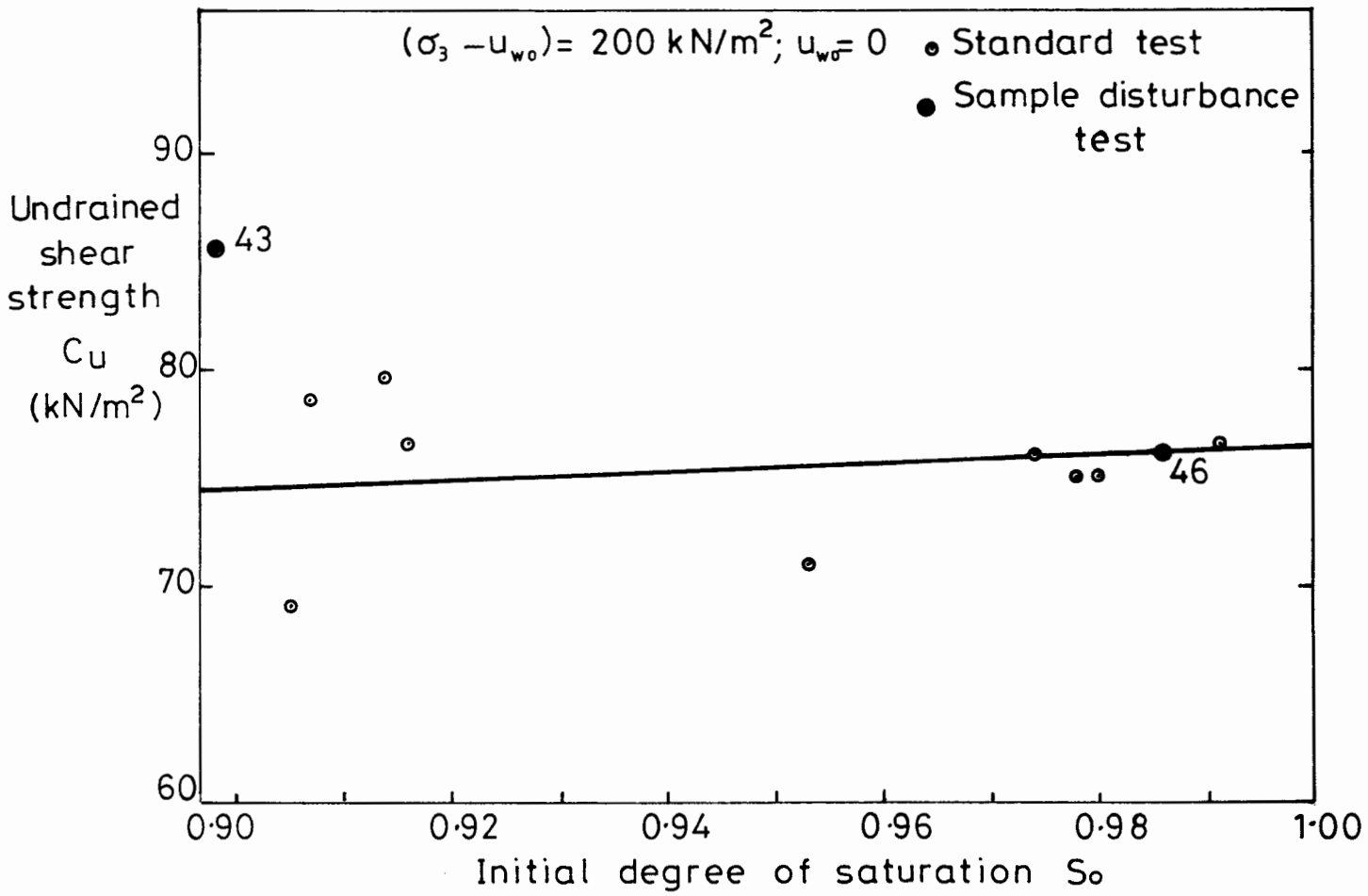

Fig. 4·25. SAMPLE DISTURBANCE TESTS.

and 46 are each represented by two points: the top point corresponding to the void ratio after the initial consolidation and the bottom point referring to conditions after reconsolidation. The change of void ratio is an indication that the soil behaviour is dependent upon the total (as distinct from effective) stress history. This type of behaviour would not be observed with saturated samples, because the reduction of cell pressure under undrained conditions would not change the effective stress.

The upper graph of Figure 4.25 clearly shows that the reduction of void ratio caused by pressure release and reconsolidation was much more significant in Test 43 than in Test 46. This is only to be expected, because the sample in Test 46 was almost saturated.

The lower graph in Figure 4.25 shows the undrained shear strength measured in Tests 43 and 46, together with the results from the other samples prepared to the same consolidation pressure and back pressure. The effect of the reduction in void ratio during the reconsolidation stage of Test 43 is immediately apparent. While the shear strength measured in Test 46 was apparently unaffected by the attempt to model sample disturbance, the strength measured in Test 43 was about 15% higher than the corresponding value from the standard tests. The magnitude of this increase is well outside the normal scatter of the results.

The results from the sample disturbance tests are somewhat unexpected. Although samples containing gas bubbles are more sensitive to disturbance than saturated samples (as had been expected), the disturbance appears to increase the shear strength rather than reduce it. A similar pattern was observed with the other parameters measured in the triaxial tests. For example, there was a slight increase in the elastic moduli measured in Test 43 (although rather confusingly there was also a similar increase in the moduli measured in Test 46).

The results of the disturbance tests must be viewed with caution, and the conclusions cannot be applied directly to samples taken in the field. Two rather arbitrary tests do not constitute a proper study of the problem. It is quite possible that under a different consolidation pressure or back pressure the disturbance would have produced a reduction, rather than an increase, in the strength. For example, if the samples had been prepared under a higher back pressure the expansion of the gas bubbles as the cell pressure was reduced would have been greater, and this might have been sufficient to damage the structure of the soil. More importantly the stress history produced in Tests 43 and 46 was not really representative of the type of disturbance caused in the field. In particular, the samples were free to expand both vertically and laterally, so that no shearing occurred during the expansion. In contrast, a typical sample tube would prevent lateral expansion, constraining the sample to expand in only one direction and thus causing shearing. This could obviously have a detrimental effect on the shear strength measured in a subsequent laboratory test.

CHAPTER 5

A MODEL FOR SOILS CONTAINING GAS BUBBLES

CHAPTER 5

A MODEL FOR SOILS CONTAINING GAS BUBBLES

This chapter covers the development of a theoretical model for soils containing gas bubbles. In Chapters 6 to 8 the model is analysed in greater detail, in order to predict various aspects of the soil behaviour; namely the elastic moduli, the consolidation behaviour and the undrained shear strength. In Chapter 9 the theoretical predictions are compared with the experimental results presented in Chapter 4.

5.1 THE INFLUENCE OF BUBBLE SIZE

In Section 1.1 of Chapter 1 it was noted that the structure of soils containing discrete bubbles of gas could vary considerably, depending on the relative sizes of the bubbles and the soil particles. Figure 5.1 shows the two extreme cases, with the gas bubbles either much smaller or much larger than the size of a typical particle. Bubbles that are much smaller than the soil particles can fit within the normal void spaces without affecting the structure (Figure 5.1(a)). In contrast, very large bubbles have a major effect on the structure, as large gas-filled cavities are formed within the soil skeleton (Figure 5.1(b)).

Most previous authors who have studied the problem of unsaturated soils containing discrete bubbles have assumed, either explicitly or implicitly, that the soil structure is as shown in Figure 5.1(a), with the bubbles small enough to fit within the normal void spaces. A number of such authors are mentioned by Wood (1979), and more recent papers include those by Anderson and Hampton (1980), Chang and Duncan (1983) and Okusa (1985). A soil containing very small gas bubbles is relatively easy to analyse, because the soil obeys the same effective stress law as a saturated soil, and the sole effect of the gas bubbles is to change the compressibility of the pore fluid (Sparks, 1963).

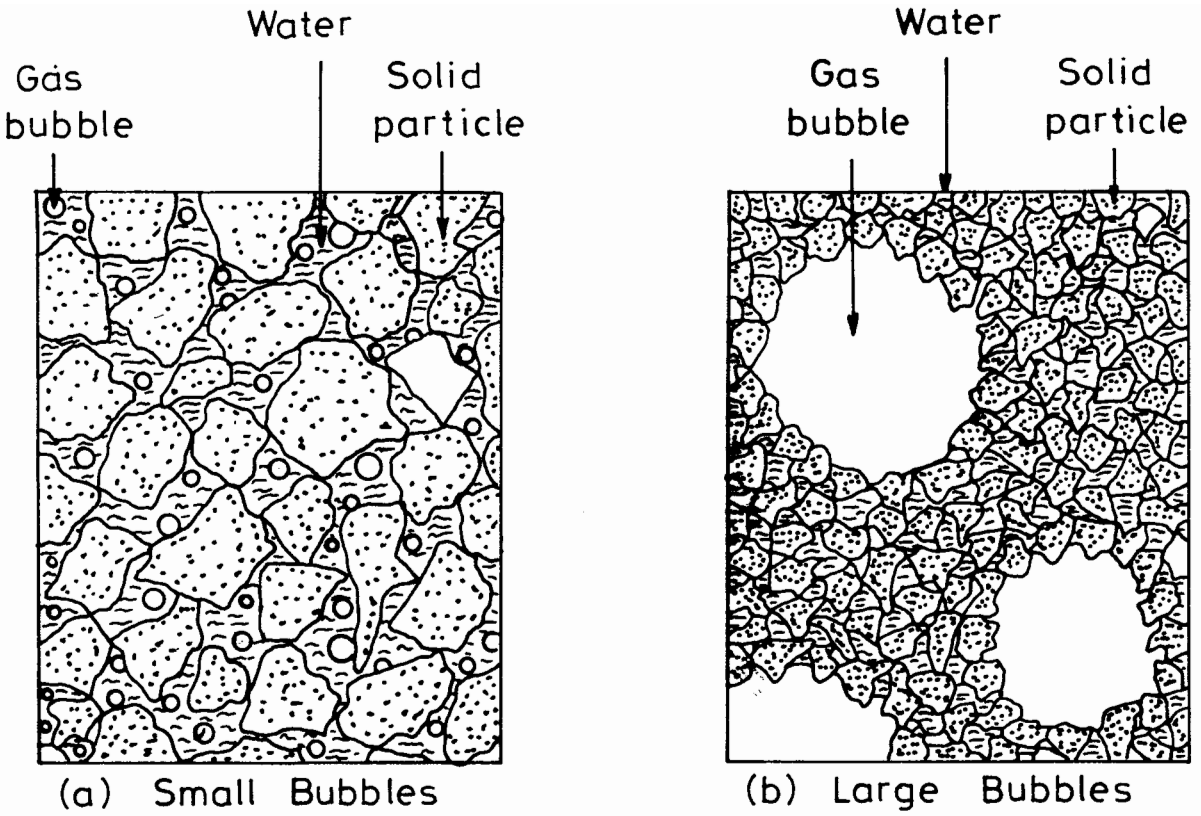

Fig. 5·1. THE STRUCTURE OF SOILS CONTAINING GAS BUBBLES.

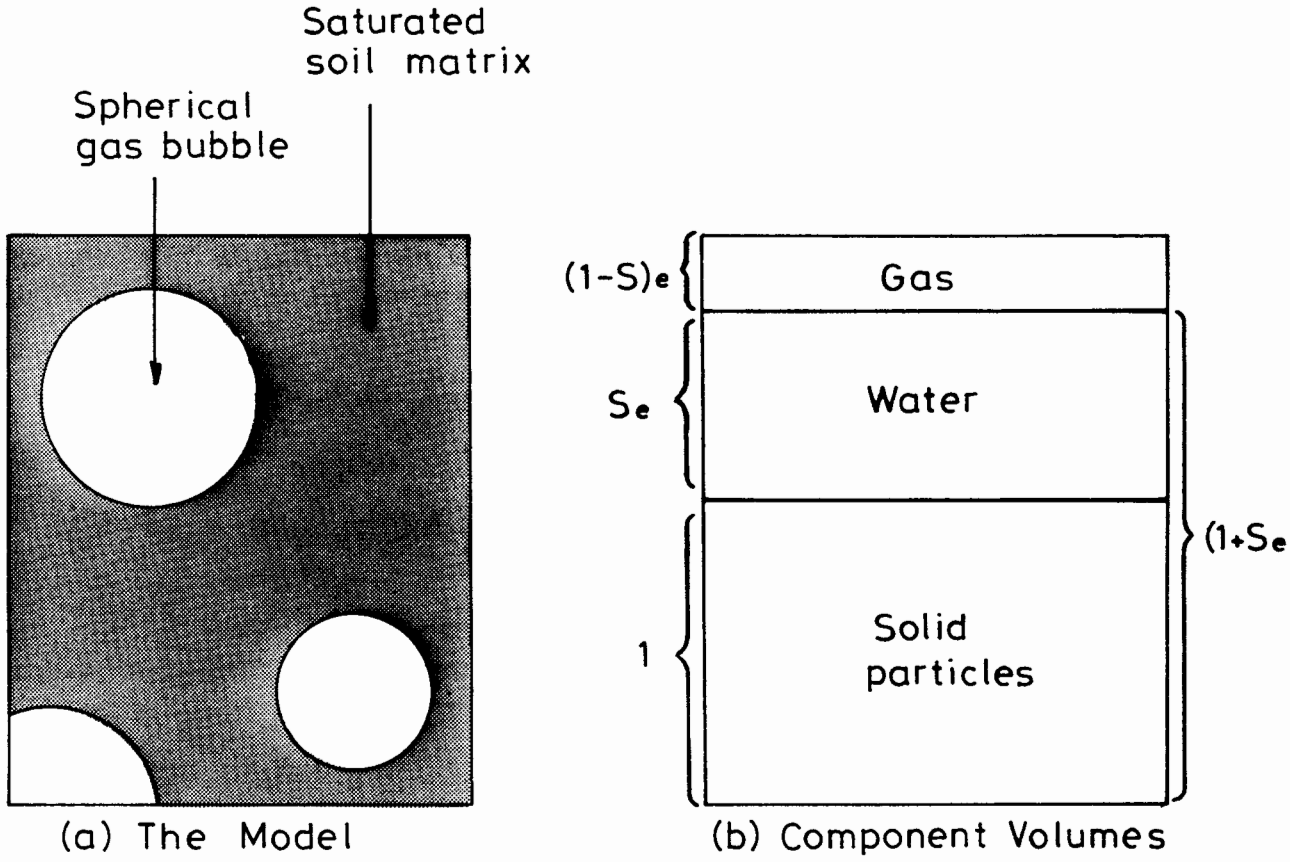

Fig. 5·2. A MODEL FOR SOILS CONTAINING LARGE BUBBLES.

Unfortunately the structure illustrated in Figure 5.1(a), with gas bubbles much smaller than the typical soil particles, is probably totally unrepresentative of the situation that occurs in unsaturated marine sediments. Anderson and Hampton (1980) report that gas bubbles in marine and lacustrine sediments are normally many orders of magnitude larger than the soil particles, and the gas bubbles within the reconstituted samples produced in the laboratory were similarly large (see Section 3.1, Chapter 3).

The conventional approach, of assuming that the bubbles simply change the compressibility of the pore fluid, is probably unsuitable for the study of unsaturated marine soils, because of the size of the gas bubbles. This point was borne out by a detailed analysis of a model for soils containing very small gas bubbles, which failed to explain any of the major features observed in the experimental tests described in Chapters 3 and 4. The theoretical analysis of the small bubble model, covering consolidation behaviour, undrained shear strength and elastic moduli, is covered in a separate report (Wheeler, in preparation).

The structure shown in Figure 5.1(b), with the gas bubbles much larger than the soil particles, is probably a reasonable representation of both real marine sediments and the samples produced in the laboratory. The development of a model for this particular case is therefore of considerable practical significance, and this is the problem that is tackled in the next few chapters. There appears to be no record of any previous attempt to model this type of soil structure.

5.2 THE LARGE BUBBLE MODEL

The soil structure illustrated in Figure 5.1(b) is very different to the conventional idea of small gas bubbles which fit inside the normal void spaces without affecting the soil skeleton. The large gas bubbles shown in the figure form cavities within the skeleton, and each bubble is surrounded

by many soil particles. The interfaces between gas and water are formed by a large number of small menisci which bridge the gaps between the particles at the edge of a bubble. This means that the difference between the gas pressure u_g and the water pressure u_w depends upon the surface tension T (Massey, 1975) and the radius of curvature R of the menisci:

$$u_g = u_w + \frac{2T}{R} \qquad 5.1$$

The value of R may be much smaller than the bubble radius a.

Equation 5.1 does not include the effect of the vapour pressure (the component of pressure within the bubbles which arises from the presence of the water vapour). According to Schuurman (1966) and Teunissen (1982) the vapour pressure is very small.

With the type of structure illustrated in Figure 5.1(b), the logical approach is to combine the solid and water phases to form a single phase of saturated soil. This leads to the concept of large isolated gas bubbles surrounded by a continuum of saturated soil, as shown in Figure 5.2(a).

Figure 5.2(b) shows that a sample containing unit volume of solid particles will contain a volume $(1 - S)e$ of gas bubbles and a volume $(1 + Se)$ of saturated soil matrix. It is apparent that the parameters e and S are rather cumbersome for defining the volumetric state of a soil containing large gas bubbles. An alternative set of parameters, better suited to the model of Figure 5.2(a), would obviously be desirable. The void ratio of the saturated soil matrix e_m and the volume fraction of bubbles f form a suitable pair of parameters.

In terms of the traditional parameters e and S, the void ratio of the matrix is given by:

$$e_m = Se \qquad 5.2$$

The volume fraction of bubbles (the proportion of the total soil volume that is taken up by gas) is given by:

$$f = \frac{(1 - S)e}{1 + e} \qquad 5.3$$

The parameters e_m and f are used in the subsequent chapters for the analysis of the model, in preference to the parameters e and S.

It seems very unlikely that the behaviour of a soil containing large gas bubbles can be expressed in terms of a single effective stress, in contrast to the case of a soil containing small gas bubbles (Wood, 1979). Inspection of the large bubble model illustrated in Figure 5.2(a) suggests that the behaviour of the saturated soil matrix will depend upon the difference between the total stress within the matrix and the pore water pressure, in the normal manner of saturated soil. However, there will be no effective stress relationship for the complete soil.

The analysis of the large bubble model is really a saturated soil problem with a complicated geometry. The saturated soil matrix surrounds large gas-filled cavities. These cavities (the gas bubbles) will produce local stress concentrations in the neighbouring soil matrix, in the same way that a hole in a metal sheet produces stress concentrations (Pascoe, 1978). It is vital that these stress concentrations within the saturated soil matrix are accounted for, by analysing fully the variations of stress throughout the matrix. The problem cannot be solved by simply drawing a "wavy plane" through the matrix and considering some sort of "average" stresses (the approach used by various authors to derive the effective stress expression for saturated soils; Skempton, 1960).

To define properly the model shown in Figure 5.2(a), the boundary conditions at the edge of a bubble must be specified. At the boundary the total stress in the saturated soil matrix, in a direction normal to the bubble wall, must be equal to the gas pressure within the bubble u_g.

Therefore the gas pressure u_g forms a boundary condition on the matrix. However, the bubble behaviour and the matrix response are completely coupled, because the deformation of the matrix in turn affects the gas pressure. Straining of the matrix surrounding a bubble will cause a change in the volume of the bubble itself, with an associated change in u_g (from Boyle's Law). The problem is therefore a complicated one of bubble-matrix interaction.

The total stress applied to the matrix at the internal bubble boundary by the gas pressure, together with any externally applied stress, produces a field of pore water pressures throughout the matrix. The pore water pressure u_w at the bubble boundary is not necessarily equal to the pore gas pressure u_g, and the menisci at the edge of the bubble must be curved to accommodate the pressure difference $(u_g - u_w)$. The required radius of curvature R is given by rearranging Equation 5.1:

$$R = \frac{2T}{u_g - u_w} \qquad 5.4$$

The gas pressure may be higher or lower than the water pressure at the bubble boundary, depending on the stress history. This means that the radius of curvature R of the menisci can be either positive or negative (convex or concave menisci). This is illustrated in Figure 5.3.

The analysis of the model can be simplified considerably if all the gas bubbles are assumed to be spherical in shape. This would appear to be a reasonable assumption for isotropically consolidated samples. For one-dimensionally consolidated samples, the bubbles are approximately spherical at low stress levels (see Figure 3.2, Chapter 3), but are considerably flattened at higher stress levels (Figure 3.8, Chapter 3). Whatever the consolidation history, the bubbles are likely to distort from a spherical shape during a shear test. These flattened bubbles could probably be modelled as ellipsoidal in shape. However, in this thesis the bubbles are

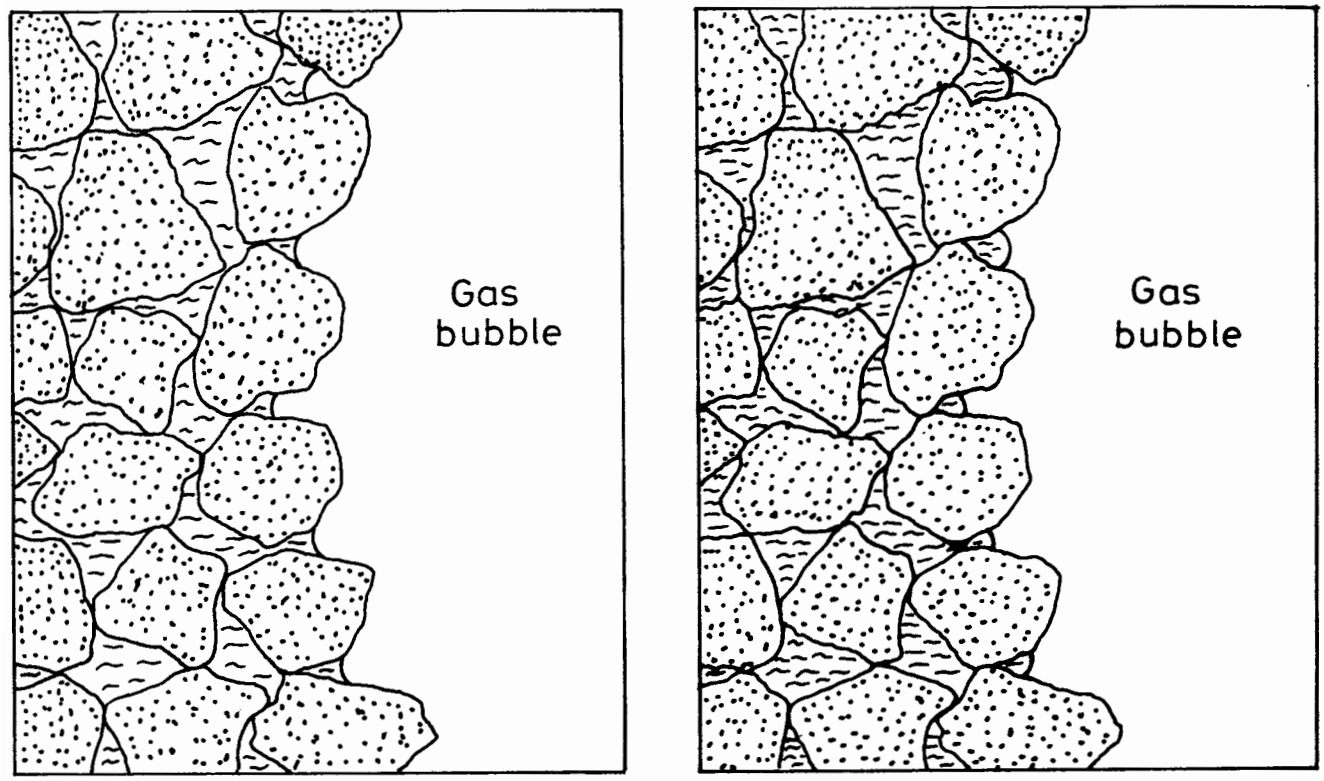

(a) Gas pressure higher than water pressure

(b) Gas pressure lower than water pressure

Fig. 5·3. CURVATURE OF MENISCI.

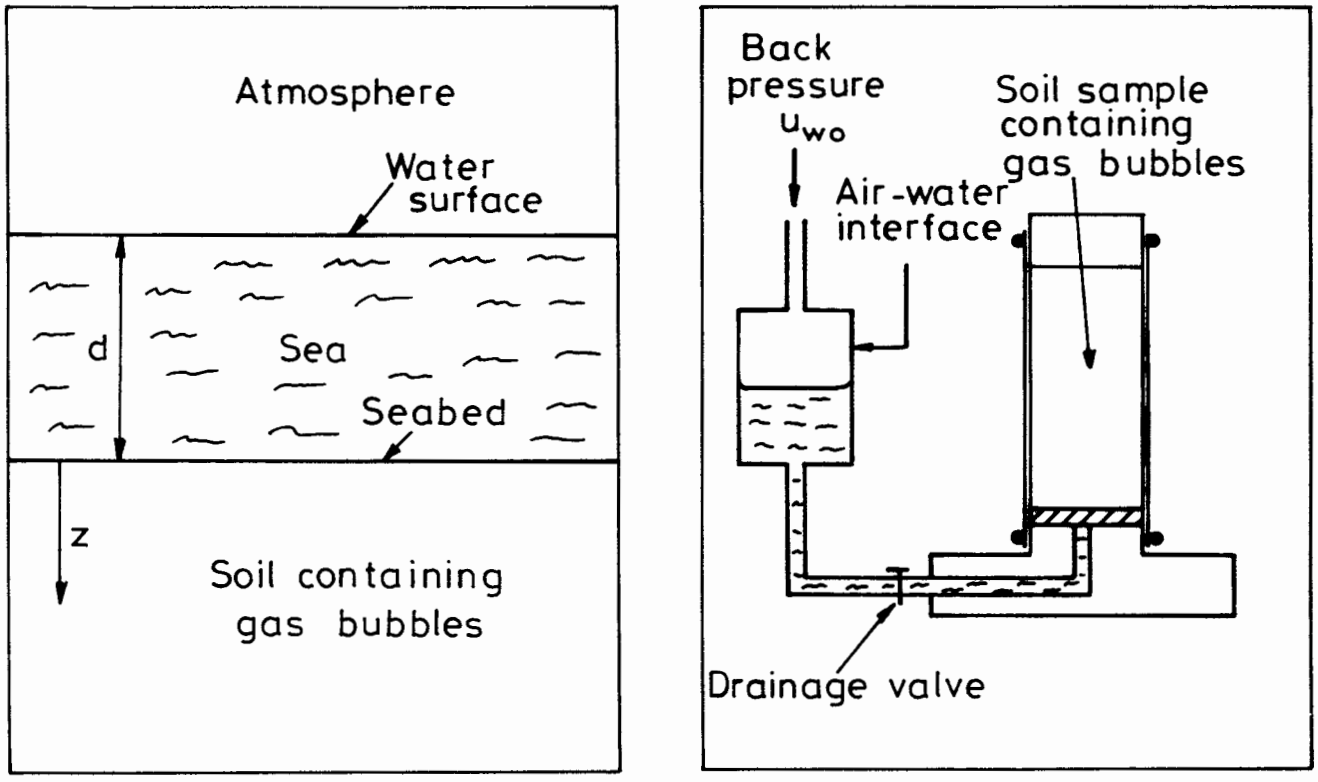

(a) Typical field conditions

(b) Laboratory conditions

Fig. 5 4. DIFFUSION OF GAS TO THE SOIL BOUNDARY.

always assumed to be spherical. Much of the analytical work presented in the next three chapters could be extended to ellipsoidal bubbles at the expense of further complexity.

5.3 MOVEMENT OF DISSOLVED GAS

One of the assumptions implicit in the large bubble model is that the bubble sites are firmly fixed within the soil. This means that gas drainage occurs only by the movement of dissolved gas. Two separate mechanisms exist for the movement of dissolved gas. Firstly, dissolved gas can be carried along by a flow of water through the matrix. Secondly, the gas can move relative to the water, by the process of diffusion, if there is a gradient in the concentration of dissolved gas.

The diffusion process means that gas can move from one bubble to another. Under suitable conditions gas from one bubble dissolves in the pore water and then diffuses through the water to come back out of solution at another bubble.

According to Henry's Law, the concentration of dissolved gas which can exist in equilibrium with a bubble of undissolved gas is dependent on the bubble pressure u_g. The higher the pressure u_g the more gas is forced into solution. If there are two bubbles at different pressures the concentration of dissolved gas within the pore water will be highest around the high pressure bubble. This means that a concentration gradient exists within the pore water, and diffusion of gas will occur from the high pressure bubble to the low pressure bubble. This movement of gas between the bubbles increases the pressure of the low pressure bubble and reduces the pressure of the high pressure bubble; and the process continues until the two bubbles are at the same pressure.

The analysis of the two bubbles can be extended to cover a considerable number of bubbles, suggesting that all the gas bubbles within the soil are at the same pressure (provided that equilibrium conditions have been reached).

The radius of curvature R of the menisci must be the same for all bubbles (Equation 5.4), although the bubble radius a may vary. This point is important, because it means that the theoretical analyses can be carried out in terms of a single gas pressure u_g, which is the actual pressure in all the bubbles, rather than just some average value covering bubbles that are all at different pressures.

If some boundary of the soil is in contact with the atmosphere, or a large volume of air, then diffusion of gas will occur from the bubbles to the boundary, until the bubble pressure u_g is equal to the air pressure at the boundary. The situation is illustrated by Figure 5.4(a), which shows typical field conditions. Gas will diffuse upwards from the bubbles within the soil to the seabed, and then up through the seawater to the atmosphere, until the gas bubbles are at atmospheric pressure. Figure 5.4(b) shows the equivalent arrangement for the laboratory tests described in Chapters 3 and 4. With the drainage valve open, gas diffuses from the bubbles to the air-water interface, until the bubbles are at the interface pressure u_{wo}.

The diffusion of gas from the bubbles to the soil boundary is obviously very significant. For the series of triaxial tests described in Chapters 3 and 4, this diffusion would suggest that the gas pressure after consolidation u_{go} was equal to the back pressure u_{wo}. This is an important conclusion, because there was no experimental method for measuring the gas pressure (see Chapters 3 and 4).

The diffusion of gas between the bubbles and the atmosphere has another very interesting effect if the bubbles are filled with a gas other than air. The diffusion of any type of gas through the pore water depends upon the concentration gradient of that particular gas. Similarly, Henry's Law (which governs the movement of gas into and out of solution) is strictly defined in terms of the partial pressure of each individual gas species. This means that the gas originally filling the bubbles diffuses away to the atmosphere,

to be replaced by air diffusing from the atmosphere to the bubbles. After all diffusion is complete the bubbles should be filled with air at atmospheric pressure. It would be very interesting to check whether this was in fact the case in the laboratory tests i.e. whether the bubbles, which originally contained methane, were filled with air by the end of each test.

In the field the situation may be complicated by the fact that gas generation is still taking place. If this is the case, the bubbles will not necessarily be at atmospheric pressure and will not contain solely air. The rate of gas generation required to maintain a bubble pressure significantly above atmospheric may not be very great, because the rate of diffusion away from the bubbles may be very slow. A slow diffusion rate is caused by a low diffusion coefficient (which may occur in the pore water of soils; Barden and Sides, 1967) or a low concentration gradient (which occurs if the bubbles are some distance below the seabed).

5.4 STIFFNESS OF THE GAS BUBBLES

The apparent stiffness of the gas bubbles depends upon the time period over which the bubble response is measured, because of the effect of gas moving into solution. If a load increment is applied very quickly and the corresponding volume change is measured immediately, there will be no time for any movement of gas into or out of solution. However, if the deformation is measured after a considerable time has elapsed, gas will have moved into solution under the influence of the change in gas pressure. Therefore, there are two separate values for the bubble stiffness: an instantaneous value, giving the immediate response; and a long-term value for the equilibrium response.

The time required for the movement of gas into solution is rather uncertain. For bubbles of air in free water the movement into solution is normally complete in less than one hour (Wyman et. al., 1952; Blanchard

and Woodcock, 1957). However the time scale may be longer in the pore water of a soil (Barden and Sides, 1967).

The instantaneous stiffness of the bubbles is given simply by the bulk modulus of the gas K_g. Under isothermal conditions, which are likely for all situations other than very high frequency acoustic measurements (Anderson and Hampton, 1980), the gas obeys Boyle's Law, and K_g is equal to the absolute value of the gas pressure:

$$K_g = u_g + p_a \qquad 5.5$$

The long-term stiffness of the bubbles K_g^* relates the final change in gas volume (after any movement into solution) to the final change in gas pressure. K_g^* differs from the true gas modulus K_g, because it does not refer to a constant mass of gas (as some of the gas moves into solution). An expression for K_g^* can be derived by considering the "total gas volume" V_g^* which would be taken up if all the gas was out of solution at the gas pressure u_g.

A sample of soil which contains unit volume of matrix will contain a volume $f/(1 - f)$ of gas, and a volume $e_m/(1 + e_m)$ of water. If the quantity of dissolved gas is in equilibrium with the gas pressure u_g, then the relationship between the "total gas volume" V_g^* and the actual undissolved gas volume V_g is given by:

$$V_g^* = V_g + \frac{He_m}{1 + e_m} \qquad 5.6$$

The term $He_m/(1 + e_m)$ represents the volume that the dissolved gas would take up if it was out of solution (by Henry's Law).

As the objective is to calculate the stiffness of the gas bubbles, there must be no drainage of water from the soil. Therefore the matrix void ratio e_m can be considered as constant in Equation 5.6. Differentiating Equation 5.6, the actual change in gas volume ΔV_g (after any movement into solution) is equal to the change in V_g^*:

$$\Delta V_g = \Delta V_g^* \qquad 5.7$$

But the "total gas volume" V_g^* refers to a fixed mass of gas, so ΔV_g^* is related to the change in gas pressure Δu_g by the true gas modulus K_g:

$$\Delta V_g^* = \frac{-V_g^* \, \Delta u_g}{K_g} \qquad 5.8$$

Substituting Equations 5.8 and 5.6 into Equation 5.7, together with the fact that the gas volume V_g is equal to $f/(1 - f)$:

$$\Delta V_g = -\left(\frac{f}{1 - f} + \frac{He_m}{1 + e_m} \right) \frac{\Delta u_g}{K_g} \qquad 5.9$$

But the apparent long-term modulus of the gas K_g^* is defined by:

$$\Delta V_g = -\frac{f}{(1 - f)} \frac{\Delta u_g}{K_g} \qquad 5.10$$

Comparing Equations 5.9 and 5.10:

$$K_g^* = \frac{K_g}{1 + \frac{He_m}{(1 + e_m)} \frac{(1 - f)}{f}} \qquad 5.11$$

5.5 LOCALISED CONSOLIDATION

The time-dependent behaviour of soils containing large gas bubbles is complicated by the process of localised consolidation in the matrix around each bubble. A uniform total stress applied to the boundary of a sample sets up a field of total stress in the matrix. The stress field varies with position, because of the stress concentrations caused by the bubbles. This results in a varying field of pore water pressures in the saturated soil matrix. Given time these pore water pressures tend to equalise, leading to localised consolidation and swelling in the matrix, which affects the deformation of the sample.

It is clear that there are at least three time-dependent effects which influence the behaviour of soils containing large gas bubbles: localised consolidation; the movement of gas into solution; and large scale consolidation (if drainage is permitted). The time scale for the localised consolidation will normally be measured in seconds, because the drainage path lengths are of the order of the bubble diameter. The movement of gas into solution normally occurs in minutes or hours, as described in the previous section. Finally, the large scale consolidation probably takes hours or days in a small laboratory sample, but weeks or even years in a full-scale problem in the field.

5.6 BUBBLE FLOODING AND GAS ENCROACHMENT

There are limits to the validity of the large bubble model. One of these limits occurs when the pressure difference $(u_g - u_w)$ reaches a critical level corresponding to a minimum value for the radius of curvature R of the menisci.

The concept of a minimum radius for the menisci can be understood by referring to Figure 5.5. A single meniscus viewed from inside a bubble is shown in Figure 5.5(a). The meniscus bridges the gap between three soil particles at the bubble boundary. The particles are assumed to be identical spheres of diameter d, arranged in a close-packed formation so that they touch at points X, Y and Z. If the meniscus is to bridge the gap between the particles, it must pass through points X, Y and Z. From the geometry of Figure 5.5(b), these three points are a distance $d/2\sqrt{3}$ from point O, which lies at the centre of the gap. Therefore, the radius of curvature of the meniscus cannot be less than a critical value R_c, which is given by:

$$R_c = \frac{d}{2\sqrt{3}} \qquad 5.12$$

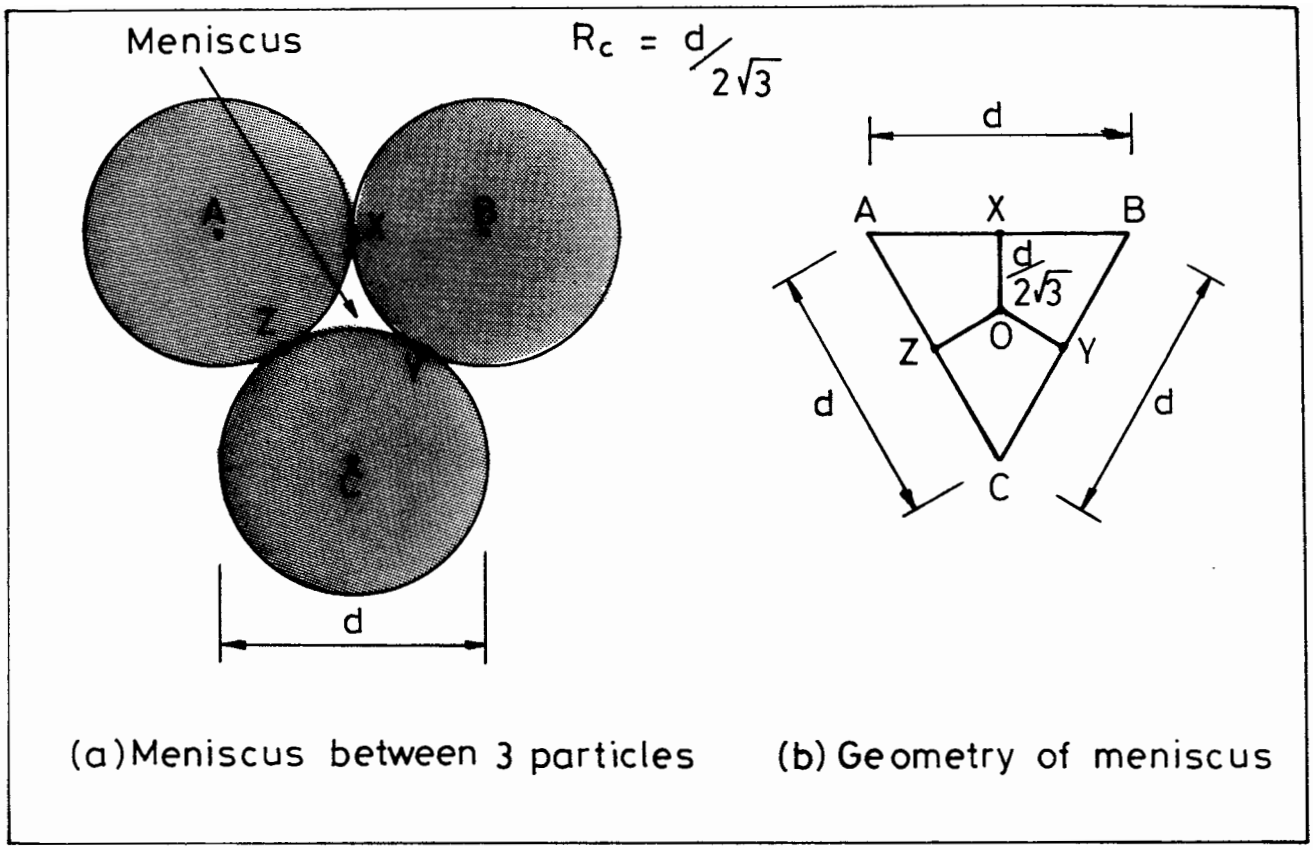

Fig. 5·5. MINIMUM RADIUS OF CURVATURE FOR MENISCI.

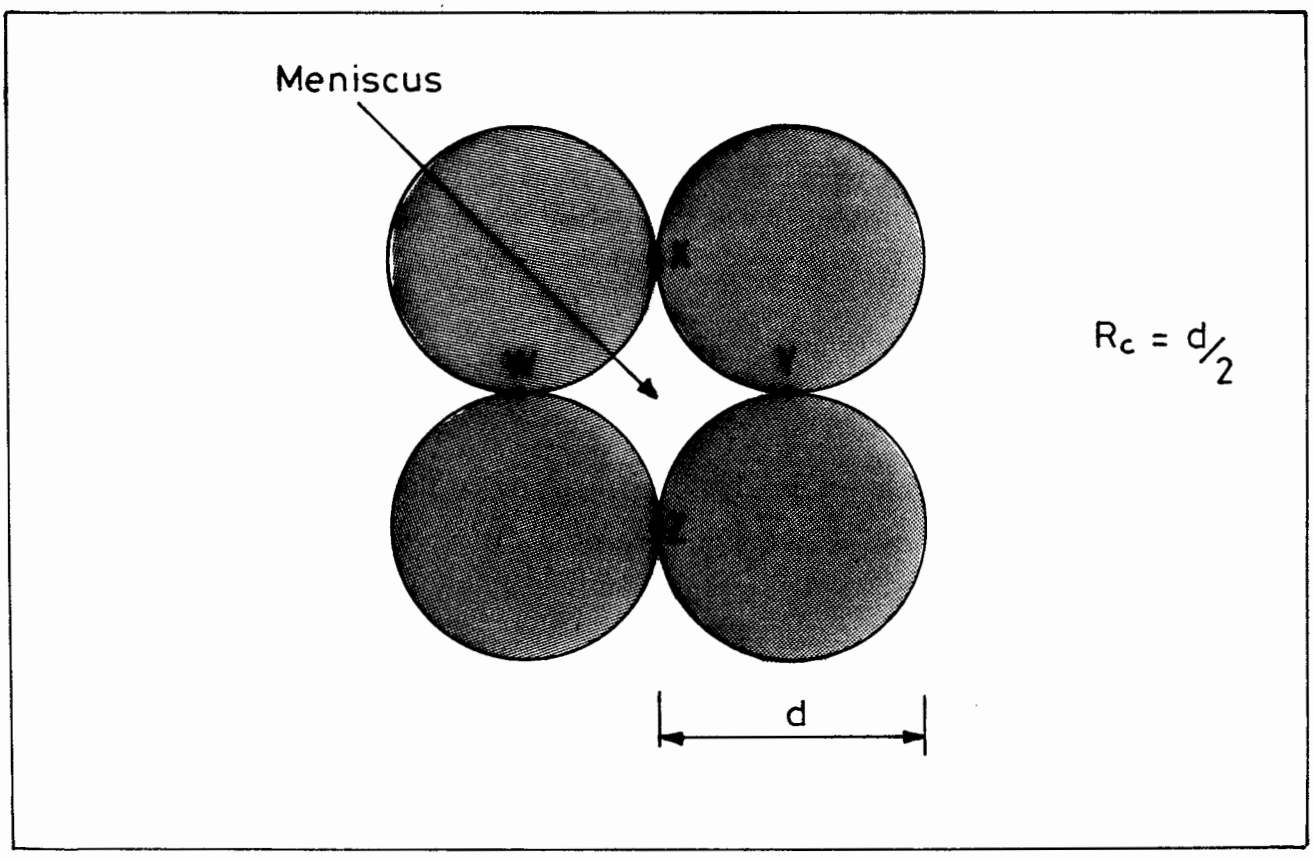

Fig. 5·6. MINIMUM RADIUS OF CURVATURE.
(Alternative Packing Arrangement)

A meniscus with a radius of curvature less than this critical value would be unable to bridge the gap between the three soil particles.

If the particles are less closely-packed than those shown in Figure 5.5, the critical radius of curvature R_c will be greater than the value given in Equation 5.12. For example, if the particles are packed as shown in Figure 5.6, the meniscus must pass through four points (W, X, Y and Z), and the value of R_c is given by:

$$R_c = \frac{d}{2} \qquad 5.13$$

In practice soil particles are not spherical, and a soil contains a variety of different particle sizes and packing arrangements, so there is no precise expression for R_c. The actual value of R_c corresponds to a meniscus which is just able to bridge the largest gap between the particles at the bubble boundary. Obviously R_c is always of the order of the particle size, and is not related to the bubble radius a.

The value of R_c determines a range of possible values for the pressure diference $(u_g - u_w)$:

$$-\frac{2T}{R_c} \leq (u_g - u_w) \leq \frac{2T}{R_c} \qquad 5.14$$

Equation 5.14 indicates that the gas pressure can be either higher or lower than the water pressure (convex or concave menisci).

If the pressure difference $(u_g - u_w)$ reaches the upper limit given in Equation 5.14 the situation will be as illustrated in Figure 5.7. Any tendency for a further increase in $(u_g - u_w)$ results in a sudden encroachment of gas into the surrounding soil skeleton (Figure 5.7(b)). This encroachment reduces the gas pressure (by increasing the gas volume), so that $(u_g - u_w)$ falls back below the critical value. The model described in Section 5.2 (saturated soil surrounding isolated gas bubbles) obviously breaks down once the gas moves into the soil skeleton.

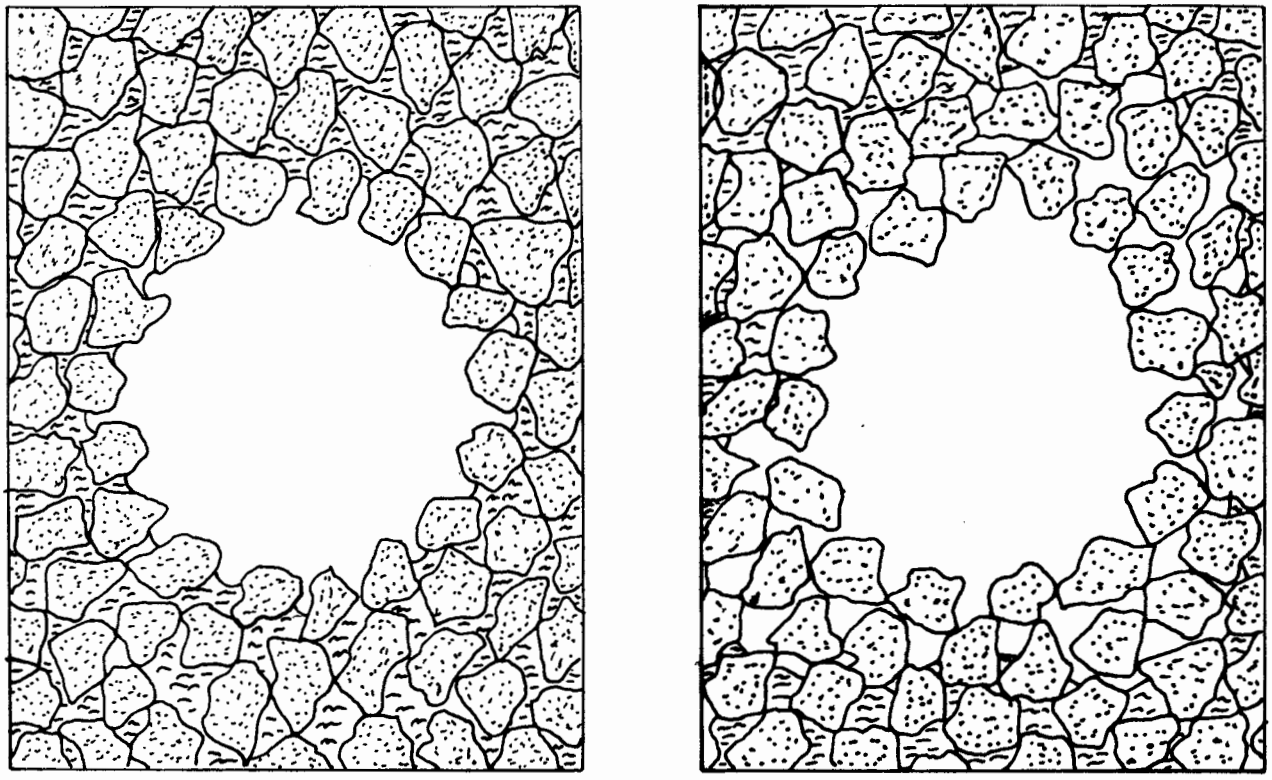

(a) $(u_g - u_w)$ at upper limit (b)Encroachment into skeleton

Fig. 5·7. GAS ENCROACHMENT INTO SOIL SKELETON.

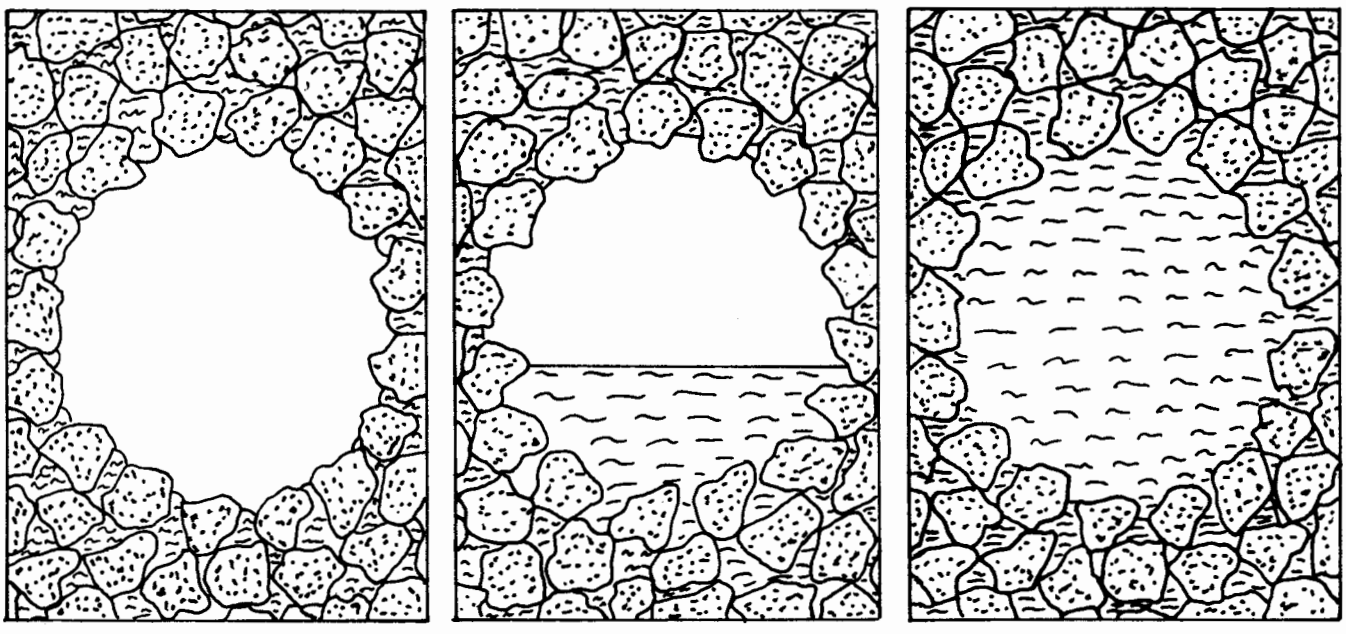

(a) $(u_g - u_w)$ at lower limit (b)Bubble cavity floods (c) Diffusion of gas from cavity.

Fig. 5·8. FLOODING OF BUBBLES.

If the pressure difference $(u_g - u_w)$ reaches the lower limit given in Equation 5.14 the situation will be as illustrated in Figure 5.8. Any tendency for a further decrease in $(u_g - u_w)$ produces a sudden flood of water into the bubble cavity (Figure 5.8(b)). Once a bubble has flooded, the gas pressure within the bubble must be equal to the water pressure, because the interface between the gas and water is a flat surface. This means that the gas pressure within the flooded bubble is greater than the gas pressure within any bubbles that remain unflooded (for which $(u_g - u_w)$ is still negative). This results in the diffusion of gas from the flooded bubble to the other bubbles, until the cavity is entirely filled with water (Figure 5.8(c)). Again, the model defined in Section 5.2 breaks down once this flooding of the bubbles occurs.

If the model analysis suggests that $(u_g - u_w)$ is outside the bounds given by Equation 5.14, this indicates that either gas encroachment into the soil skeleton has occurred or the bubbles have flooded. The model cannot deal with either of these possibilities in a precise fashion. However, it is possible to assess qualitatively the effects of either gas encroachment or bubble flooding (see Chapter 8).

The critical value of the pressure difference $(u_g - u_w)$, given by Equation 5.14, determines the maximum depth beneath the seabed at which the structure of the large bubble model can exist indefinitely. The analysis presented in Section 5.3 indicated that diffusion of gas to the surface would ultimately bring the bubbles to atmospheric pressure. Inserting $u_g = 0$ in Equation 5.14:

$$u_w \leq \frac{2T}{R_c} \qquad 5.15$$

If sufficient time has elapsed, all excess pore water pressures should have dissipated, so that u_w is given simply by the head of overlying water. Inserting this in Equation 5.15:

$$\gamma_w(d + z) \leq \frac{2T}{R_c} \qquad 5.16$$

d is the water depth and z is the distance below the seabed (see Figure 5.4(b)).

Equation 5.16 can be used to estimate the maximum depth at which the large bubble structure can exist on a permanent basis. Bubbles can form at depths greater than this, but once gas generation ceases the bubble pressure starts to drop towards atmospheric and the bubbles flood with water when the critical situation of Equation 5.14 is reached.

5.7 SURFACE TENSION FORCES

The model described in Section 5.2 takes no account of the surface tension forces occuring at the menisci. The model allows for the fact that the gas pressure u_g may be different from the water pressure u_w (which implicitly assumes the presence of surface tension), but does not allow for the direct effect of surface tension forces acting across a plane which intersects a bubble. It is important to consider whether the surface tension forces can be ignored in this way.

Some measure of the importance of the surface tension forces can be achieved by replacing the forces, which act at the perimeter of each bubble with an equivalent tensile stress σ_t acting over the bubble area.

An expression for the equivalent tensile stress σ_t can be derived by considering the bubble illustrated in Figure 5.9. The bubble, of radius a, is intersected by a horizontal plane (Figure 5.9(a)), and the problem is to find the surface tension force acting across the plane. The plane can be considered as a "wavy plane", which passes through the particle contact points within the saturated soil matrix, rather than actually intersecting the particles. If the plane is drawn at random through the soil it will not necessarily pass through the centre of the bubble, so the vertical position of the plane is defined by the angle α.

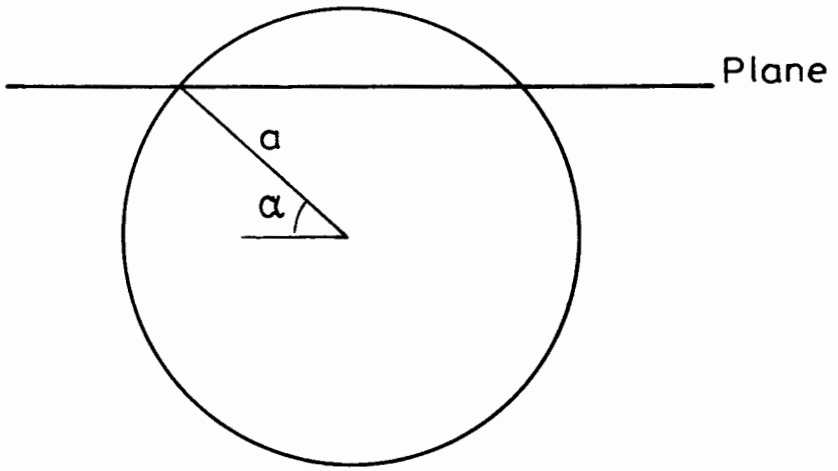

(a) Bubble intersected by plane

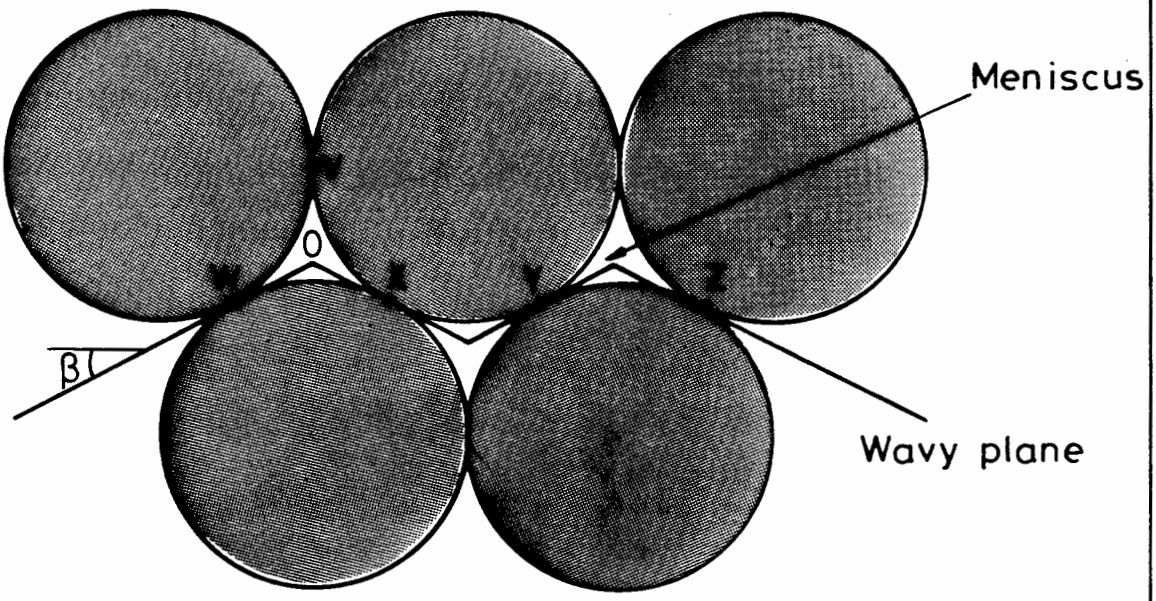

(b) Wavy plane intersecting menisci

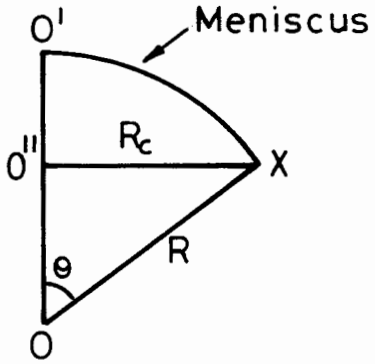

(c) Edge view of meniscus

Fig. 5·9. SURFACE TENSION FORCE ACROSS A PLANE.

Figure 5.9(b) shows a section of the bubble wall, viewed from the centre of the bubble. The soil particles are represented as identical spheres in a close-packed formation, but the analysis presented here is equally applicable to other packing arrangements or particle shapes. The figure shows the wavy plane intersecting three menisci and passing through the particle contact points W, X, Y and Z. Each section of the wavy plane is inclined at an angle β, so that the section passes through a particle contact point (such as X) and the centre of curvature of the meniscus (point O).

Figure 5.9 (c) shows an edge view of one section of the meniscus. The section runs from the particle contact point X to a point O', which is immediately behind the centre of curvature of the meniscus (point O) in the view shown in Figure 5.9(b). A final point O" is also immediately behind point O in Figure 5.9(b), but O" lies in the plane of the three particle contact points V, W and X. The meniscus has a radius of curvature R, and the section XO' subtends an angle θ. The distance XO" is equal to the minimum radius of curvature R_c.

The length L of the section of meniscus XO' is given by:

$$L = R\theta = R\sin^{-1}\left(\frac{R_c}{R}\right) \qquad 5.17$$

Therefore, the surface tension force F across this section is given by:

$$F = TR\sin^{-1}\left(\frac{R_c}{R}\right) \qquad 5.18$$

However, this force does not act in a vertical direction i.e. it does not act normal to the general horizontal orientation of the wavy plane. The vertical component F_v of the force F is given by:

$$F_v = F\cos\alpha\cos\beta = TR\cos\alpha\cos\beta\sin^{-1}\left(\frac{R_c}{R}\right) \qquad 5.19$$

The circumference of the circle forming the line of intersection of the wavy plane and the bubble can be calculated from Figure 5.9(a) as $2\pi a \cos\alpha$. The arc XO' forms a length $R_c\cos\beta$ of this total circumference (Figure 5.9(b)). Therefore the total surface tension force F_t normal to the wavy plane is given by:

$$F_t = F_v \frac{2\pi a \cos\alpha}{R_c \cos\beta} = \frac{2\pi T R a \cos^2\alpha}{R_c} \sin^{-1}\left(\frac{R_c}{R}\right) \qquad 5.20$$

The surface tension force F_t can be converted to an equivalent tensile stress σ_t by dividing by the area of the bubble at the level where it is cut by the wavy plane ($\pi a^2 \cos^2\alpha$):

$$\sigma_t = \frac{2T}{a} \frac{R}{R_c} \sin^{-1}\left(\frac{R_c}{R}\right) \qquad 5.21$$

Equation 5.21 indicates that σ_t does not depend on α, i.e. σ_t is indepentent of the level at which the plane intersects the bubble.

Figure 5.10 shows the term $(R/R_c)\sin^{-1}(R_c/R)$ plotted against R/R_c. When R/R_c is unity (menisci at maximum curvature) $(R/R_c)\sin^{-1}(R_c/R)$ has a value of $\pi/2$, and as R/R_c tends to infinity (flat menisci) the value drops towards 1. Inserting these limits in Equation 5.21 gives upper and lower bounds for the equivalent tensile stress σ_t:

$$\frac{2T}{a} \leq \sigma_t \leq \frac{\pi T}{a} \qquad 5.22$$

At an interface between air and water, the surface tension T is 0.073 N/m (Weast, 1984). The values for methane and other commonly occuring gases are probably very similar. In the series of experimental tests described in Chapters 3 and 4, the smallest gas bubbles were probably about 0.1 mm diameter (a = 0.05 mm). Inserting these values into Equation 5.22, the maximum value of σ_t was probably less than 5 kN/m^2. The typical bubbles in the experimental tests were about 0.5 mm diameter, and for these bubbles σ_t was less than

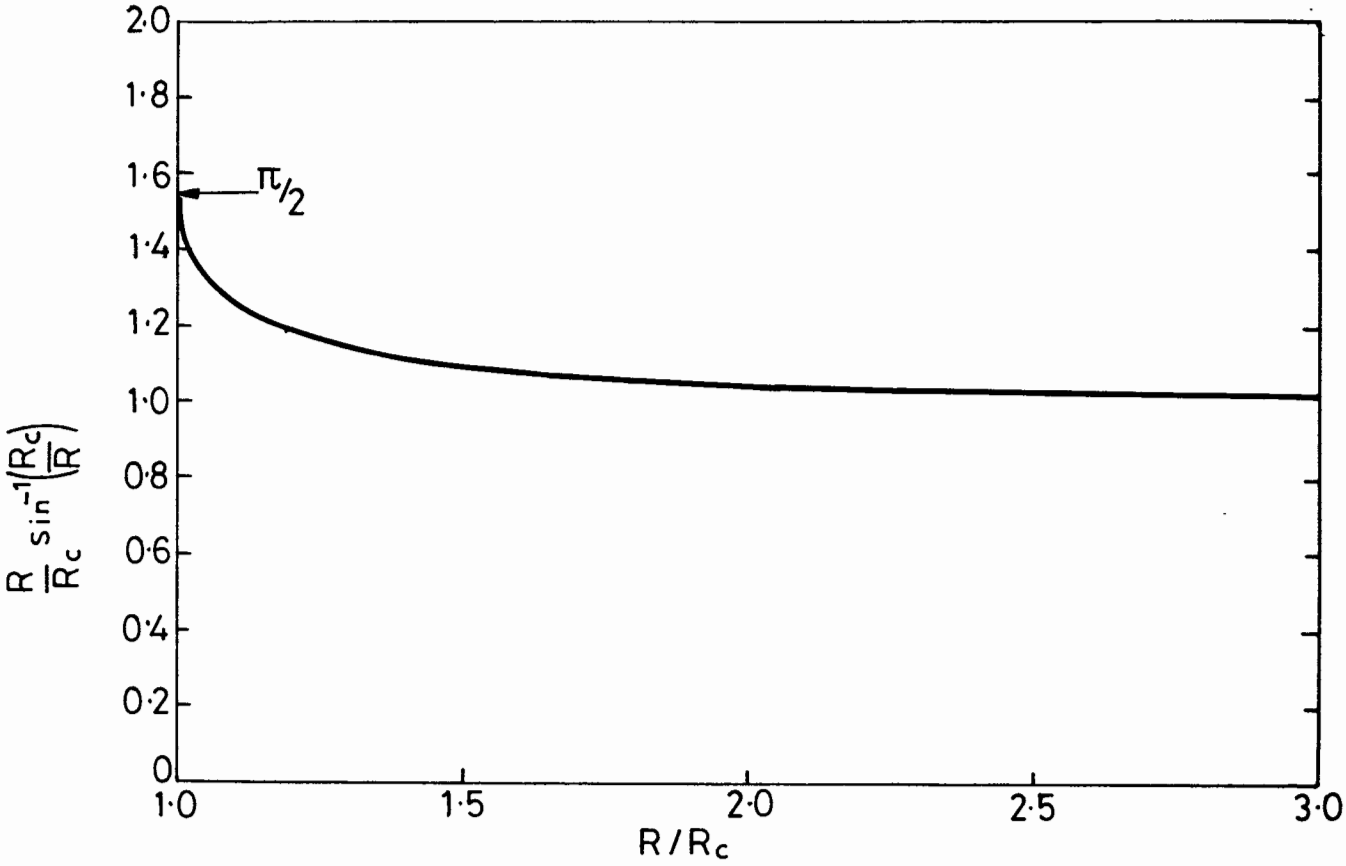

Fig. 5·10. SURFACE TENSION PARAMETER.

1 kN/m^2. Therefore, the values of σ_t were much lower than the other stresses acting in the soil, and the same would be true for any soil containing bubbles larger than 0.1 mm diameter. This suggests that it is probably quite acceptable to ignore the surface tension forces when analysing the behaviour of a soil containing large bubbles.

It must be made clear that although the direct effects of the surface tension forces are insignificant, the pressure difference $(u_g - u_w)$, which is an indirect effect of surface tension (Equation 5.1), cannot be ignored. In the experimental tests the soil particles were a few microns in diameter. Therefore the radius of curvature R of the menisci could have been as low as 10^{-6} m, giving a pressure difference $(u_g - u_w)$ greater than 100 kN/m^2 (see Equation 5.1). A pressure difference of this magnitude could be very significant.

5.8 ANALYSIS OF THE LARGE BUBBLE MODEL

In the following three chapters various aspects of the behaviour of soils containing large gas bubbles are examined by analysing the model developed in this chapter. Chapter 6 covers the elastic moduli; Chapter 7 the consolidation behaviour; and Chapter 8 the undrained shear strength. With the material presented in this order, rigorous analysis of the model becomes increasingly difficult, and additional approximations are required in each chapter.

There appears to be no previous analytical work on the problem of soils containing large gas bubbles. The nearest approach to this subject, within the field of soil mechanics, has been the study of spherical cavity expansion, by authors such as Chadwick (1959) and Vesic (1972). These studies refer to soils containing a single cavity, whereas the large bubble model consists of a saturated soil containing a considerable number of cavities. The large bubble model is further complicated by the fact that the pressure within the

cavities (the gas pressure u_g) is a dependent variable, and not a known boundary condition as is the case in the cavity expansion problem. Despite these differences, the cavity expansion theories are very useful for analysing the compression and consolidation behaviour (Chapter 7).

Outside the field of soil mechanics there is a number of significant references for the large bubble model. Walsh and Brace (1966) considered the elastic behaviour of rocks containing cavities and cracks. Their analysis is relevant to the work on the elastic moduli, presented in Chapter 6. However, the most useful references for the large bubble model are papers on the behaviour of metals containing voids, cavities or inclusions. Goodier (1933), MacKenzie (1950), Eshelby (1957), Budiansky (1965) and Hill (1965) all considered the behaviour of an elastic material containing spherical cavities or inclusions. The work of these authors is relevant to the chapter on the elastic moduli (Chapter 6). Haynes (1971), Green (1972), Needleman (1972), Gurson (1977) and several other authors analysed the problem of a rigid-plastic material containing cavities. Their work is particularly helpful in Chapter 8, which covers the undrained shear strength.

CHAPTER 6

THEORETICAL ANALYSIS : ELASTIC MODULI

CHAPTER 6

THEORETICAL ANALYSIS : ELASTIC MODULI

In this chapter the model described in Chapter 5 is used to predict the elastic moduli of soils containing gas bubbles. Both drained and undrained moduli are considered.

Under undrained conditions the soil response is time-dependent, because of both the movement of gas into solution and the localised consolidation effect. Therefore, two sets of undrained moduli are defined, covering the instantaneous and the long-term behaviour. In contrast, the values of the drained moduli are not time-dependent, because they always refer to the long-time response, when all excess pore pressures have dissipated and all drainage is complete.

6.1 METHOD OF ANALYSIS

Hill (1965) considered the elastic behaviour of a composite material consisting of a volume fraction f of spherical inclusions, with moduli K_1 and G_1, in a matrix with moduli K_2 and G_2. He provided the following equations for K and G, the bulk and shear moduli of the composite:

$$\frac{f}{K - K_2} + \frac{1 - f}{K - K_1} = \frac{\alpha}{K} \qquad 6.1$$

$$\frac{f}{G - G_2} + \frac{1 - f}{G - G_1} = \frac{\beta}{G} \qquad 6.2$$

$$\text{where} \quad \alpha = 3 - 5\beta = \frac{K}{K + 4\,G/3} \qquad 6.3$$

Budiansky (1965) considered the elastic behaviour of a multiphase material. For the case of two phases his results can be rearranged to the same form as those of Hill.

By inserting the relevant values for K_1, G_1, K_2 and G_2 in Equations 6.1 to 6.3, expressions can be derived for the various elastic moduli of the model described in the previous chapter.

6.2 INSTANTANEOUS UNDRAINED MODULI

The instantaneous undrained bulk and shear moduli are given the symbols K_{ui} and G_{ui} respectively. The subscript u refers to the drainage conditions and the subscript i to the timescale.

For the instantaneous undrained behaviour, the moduli of the inclusions and matrix in Hill's equations are:

$$K_1 = K_g, \quad G_1 = 0, \quad K_2 = K_m, \quad G_2 = G_m \tag{6.4}$$

K_g is the bulk modulus of the gas, which can be expressed in terms of the gas pressure (Equation 5.5, Chapter 5). K_m and G_m are the undrained bulk and shear moduli of the matrix.

The undrained bulk modulus of the saturated soil matrix K_m can be expressed in terms of the bulk modulus of the pore water K_w and the bulk modulus of the soil skeleton within the matrix K':

$$K_m = \frac{K_w(1 + e_m)}{e_m} + K' \tag{6.5}$$

e_m is the void ratio of the matrix (see Equation 5.2, Chapter 5). The derivation of Equation 6.5, which is given by Anderson and Hampton (1980), is based on the assumption that the solid particles are incompressible. Normally the compressibility of the pore water can also be ignored and K_m can be considered as infinite.

The undrained shear modulus of the saturated soil matrix G_m is given simply by the shear modulus of the soil skeleton within the matrix G', because the pore water is unable to sustain any shear stresses:

$$G_m = G' \tag{6.6}$$

The elastic moduli of the matrix skeleton K' and G' are treated in this chapter as if they are soil constants. In practice this is not the case, as both K' and G' depend upon the state of the saturated soil forming the matrix. For example, critical state theory suggests that K' is dependent on both the void ratio of the matrix and the mean effective stress in the matrix (Atkinson and Bransby, 1978). This means that when calculating the various moduli of a soil containing gas bubbles it is necessary first to evaluate K' and G' from a knowledge of the state of the matrix.

6.2.1 Instantaneous Undrained Shear Modulus

Hill's expressions (Equations 6.1 to 6.3) can be combined to give a quartic equation for the overall shear modulus G:

$$\frac{fK_1}{K_1 + 4G/3} + \frac{(1 - f)K_2}{K_2 + 4G/3} + \frac{5fG_2}{G - G_2} + \frac{5(1 - f)G_1}{G - G_1} + 2 = 0 \qquad 6.7$$

The parameters given in Equation 6.4 can be substituted into Equation 6.7, to give an expression containing the instantaneous undrained shear modulus G_{ui}:

$$\frac{fK_g}{K_g + 4G_{ui}/3} + \frac{(1 - f)K_m}{K_m + 4G_{ui}/3} + \frac{5fG'}{G_{ui} - G'} + 2 = 0 \qquad 6.8$$

The expression has been reduced to a cubic equation, because G_1 is zero. Equation 6.8 can be solved iteratively for G_{ui}.

Figure 6.1 illustrates how G_{ui} varies with the volume fraction of bubbles. f increases from right to left in the figure, so that the general orientation is consistent with the presentation used for the experimental results presented in Chapter 4 i.e. a saturated soil is represented by the right-hand boundary of the figure.

For the curve shown in Figure 6.1 the parameters K_g/G' and K_m/G' have been taken as zero and infinity respectively. The values of G_{ui} are very insensitive to these two parameters. If K_g/G' is increased from zero

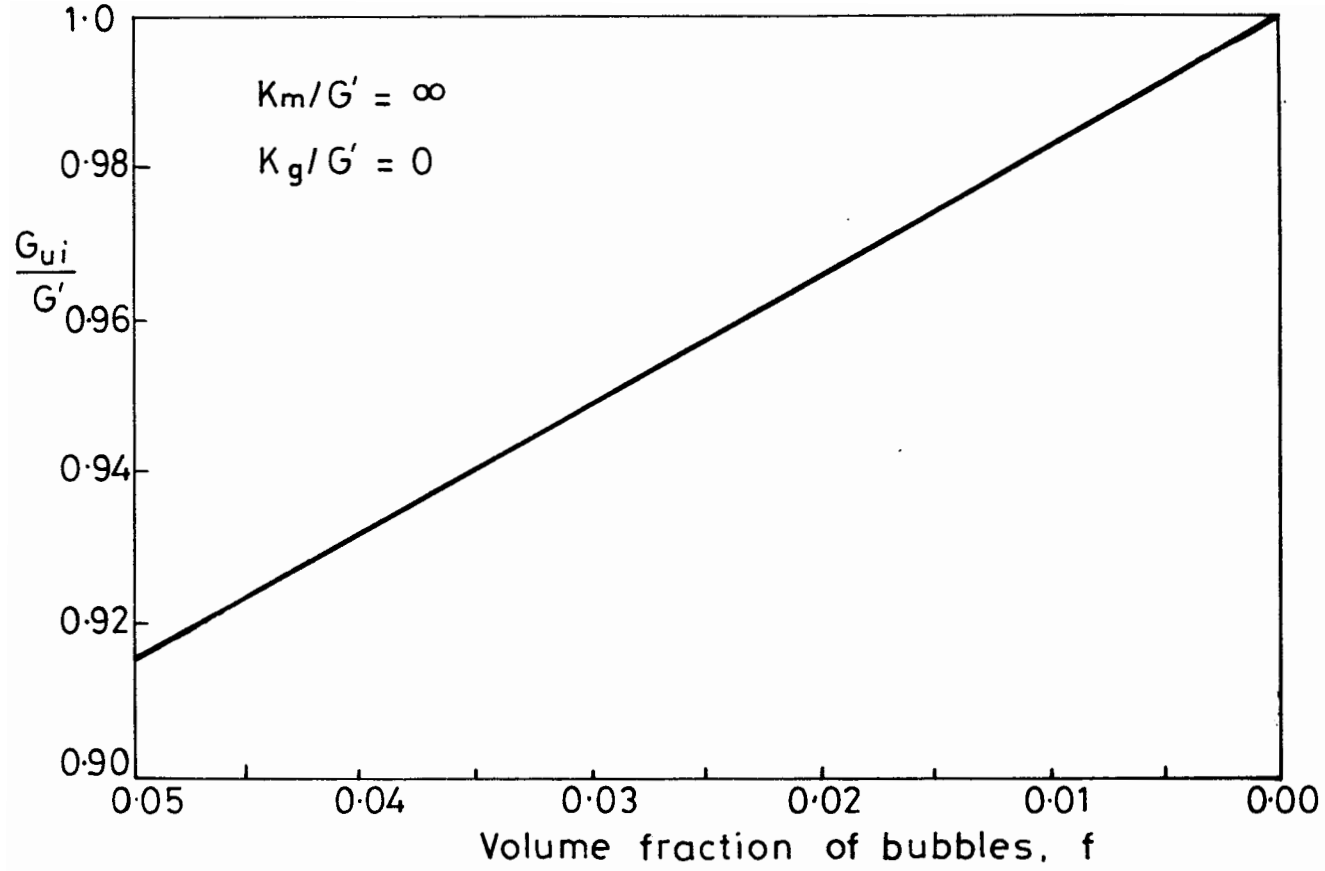

Fig. 6·1. INSTANTANEOUS UNDRAINED SHEAR MODULUS OF MODEL.

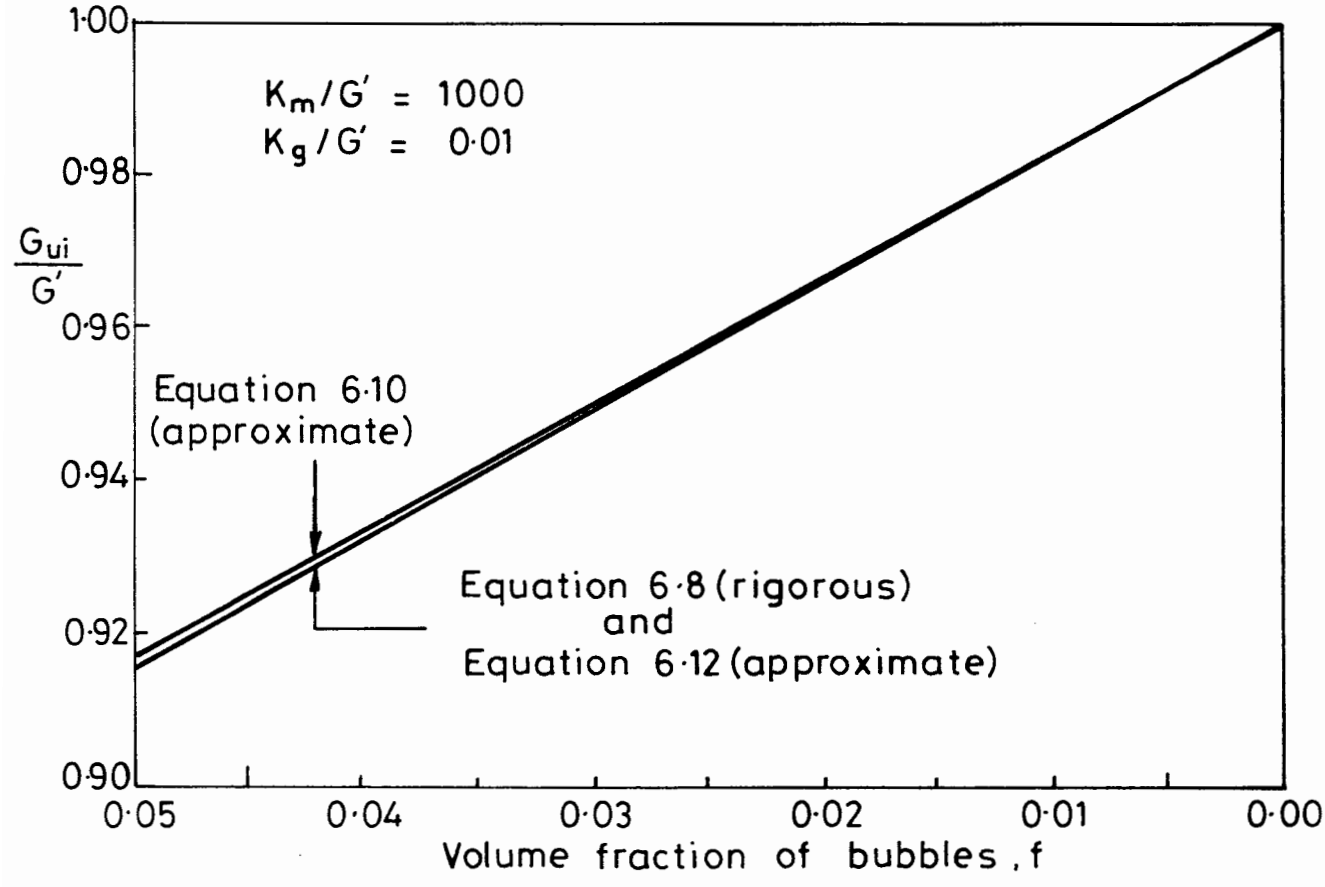

Fig. 6·2. ACCURACY OF APPROXIMATE EXPRESSIONS FOR G_{ui}

to 0.1 (which represents a reasonable upper bound for the range of conditions likely to occur in practice) G_{ui} is increased by only about 0.01%. Similarly, if K_m/G' is reduced from infinity to 100 (a reasonable lower bound) G_{ui} is reduced by about 0.03%. This means that the shear behaviour of the soil is effectively that of an incompressible matrix ($K_m = \infty$) containing empty cavities ($K_g = 0$).

The expression for G_{ui} given in Equation 6.8 can be simplified if the proportion of bubbles is very small i.e. if f is much less than 1. As f tends to zero, G_{ui} approaches G', and the first and second terms of Equation 6.8 tend to zero and $K_m/(K_m + 4G'/3)$ respectively. However the third term remains non-zero as both numerator and denominator approach zero. Therefore the equation becomes:

$$\frac{K_m}{K_m + 4G'/3} + \frac{5fG'}{G_{ui} - G'} + 2 = 0 \qquad 6.9$$

This can be rearranged to give an explicit expression for G_{ui}:

$$G_{ui} = G' \left[1 - \frac{5f(K_m + 4G'/3)}{3K_m + 8G'/3} \right] \qquad 6.10$$

Equation 6.10 can also be produced from the results of Mackenzie (1950) or Eshelby (1957). Both of these authors considered the special case of a very low volume fraction of inclusions.

Inspection of Equation 6.10 indicates that G_{ui} is independent of the bulk modulus of the gas K_g if the volume fraction of bubbles is small. This confirms the fact that the shear behaviour is very similar to that of a soil containing empty cavities.

Figure 6.2 compares the approximate relationship of Equation 6.10 with the rigorous analysis of Equation 6.8, for a typical set of conditions ($K_m/G' = 1000$, $K_g/G' = 0.01$). The errors introduced by the approximate expression are quite small.

If the compressibility of the water can be ignored K_m tends to infinity, and Equation 6.10 becomes:

$$G_{ui} = G'(1 - 5f/3) \qquad 6.11$$

If the compressibility of the water and the stiffness of the bubbles are ignored, an alternative approximate expression for G_{ui} can be derived, without assuming that the volume fraction of bubbles is small. Putting K_m as infinity and K_g as zero in the full expression for G_{ui} (Equation 6.8) produces the following result:

$$G_{ui} = \frac{3G'(1 - 2f)}{3 - f} \qquad 6.12$$

This expression is the same as Equation 6.11 if second order terms in f are ignored.

Under the range of conditions likely to occur in practice, Equation 6.12 is a better approximation than either Equations 6.10 or 6.11. For the typical conditions shown in Figure 6.2 ($K_m/G' = 1000$, $K_g/G' = 0.01$), the values of G_{ui} predicted by Equation 6.12 are indistinguishable from those given by the rigorous formula.

The value of G_{ui} given by Equation 6.12 can be used as a good first approximation in Equation 6.8, if a more accurate value of G_{ui} is required. One further iteration with Equation 6.8 normally produces an answer of six-figure accuracy.

6.2.2 Instantaneous Undrained Bulk Modulus

Combining Hill's second and third relationships (Equations 6.2 and 6.3), and inserting the component moduli of Equation 6.4, gives an expression for the instantaneous undrained bulk modulus K_{ui}, in terms of the shear modulus G_{ui}:

$$K_{ui} = \frac{4G_{ui}\{5fG' - 2(G' - G_{ui})\}}{3\{3(G' - G_{ui}) - 5fG'\}} \qquad 6.13$$

The value of G_{ui} calculated from Equation 6.8 can be substituted into Equation 6.13 to give a value for K_{ui}. It is essential to use a very accurate value for G_{ui} (typically six-figure accuracy), because Equation 6.13 is extremely sensitive to small changes in G_{ui}. Values of G_{ui} calculated from the approximate formulae of Equations 6.10, 6.11 or 6.12 should not be used in Equation 6.13.

Figure 6.3 illustrates how K_{ui} varies with the volume fraction of bubbles. The values of K_{ui} have been normalised by dividing by G'. This means that K_{ui} is presented in terms of the shear modulus of the saturated soil matrix G', rather than either the drained or undrained bulk modulus of the matrix (K' or K_m). This is the most logical form of presentation. When the large bubble model is subjected to a hydrostatic boundary stress, shear stresses are set up in the saturated soil matrix, as the stress field is distorted in the region of each bubble. The undrained deformation of the sample therefore depends upon the undrained shear modulus of the matrix G', as well as the undrained bulk modulus of the matrix K_m. Because G' is much smaller than K_m, the deformation depends mainly on G'.

Figure 6.3 shows curves for two values of the parameter K_g/G' and two values of K_m/G', covering the range of conditions likely to occur in practice. The figure shows that the bulk modulus K_{ui}, like the shear modulus G_{ui}, is very insensitive to the value of the gas modulus K_g i.e. the behaviour is effectively that of a material containing empty cavities. However, unlike G_{ui}, the value of K_{ui} may be influenced significantly by the undrained bulk modulus of the matrix K_m.

If the volume fraction of bubbles is very small, the expressions given above for K_{ui} can be replaced with an approximate solution from the results of Eshelby (1957):

$$K_{ui} = \frac{K_m(K_g + 4G'/3)}{(K_g + 4G'/3) + f(1 - K_g/K_m)(K_m + 4G'/3)} \qquad 6.14$$

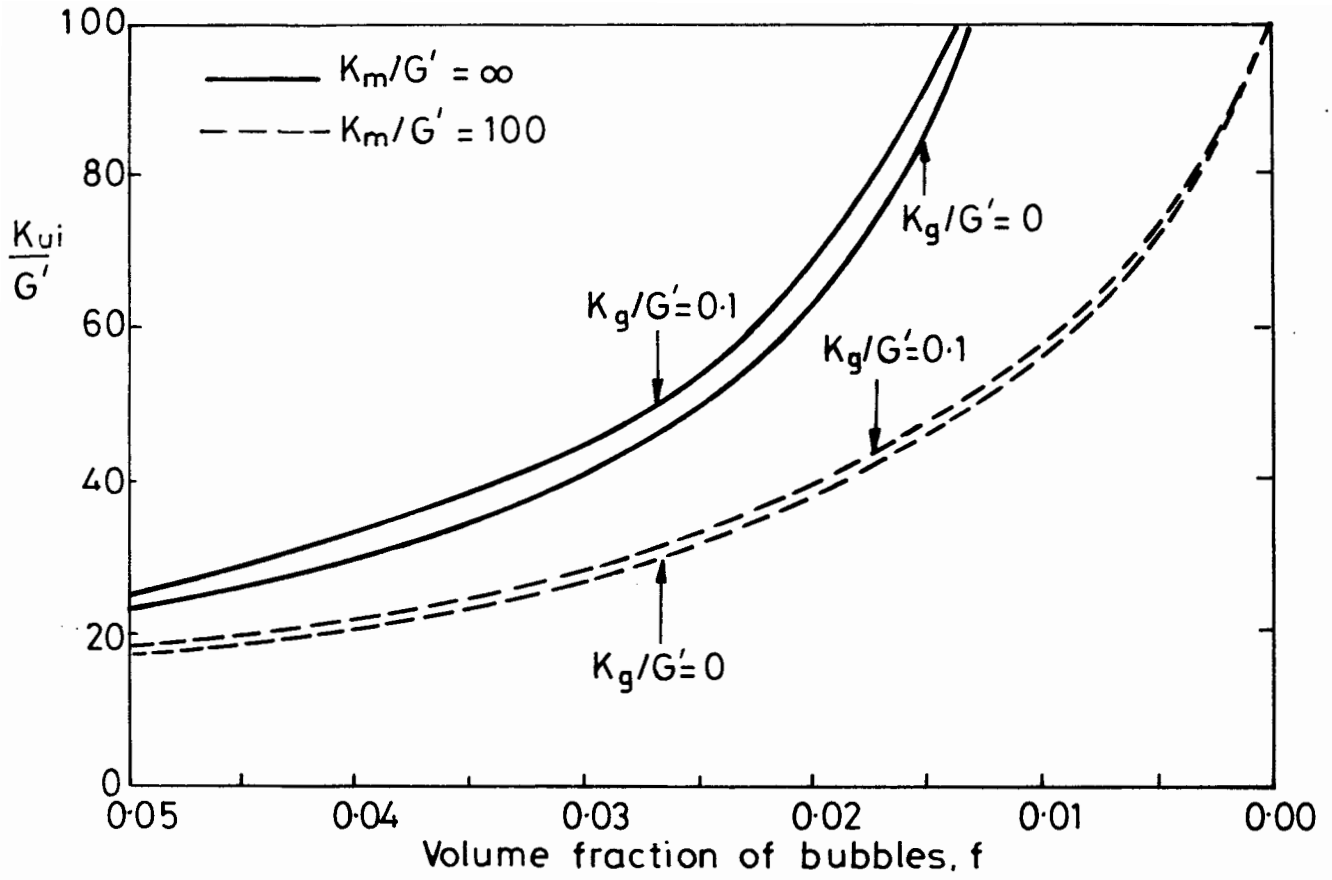

Fig. 6·3. INSTANTANEOUS UNDRAINED BULK MODULUS OF MODEL.

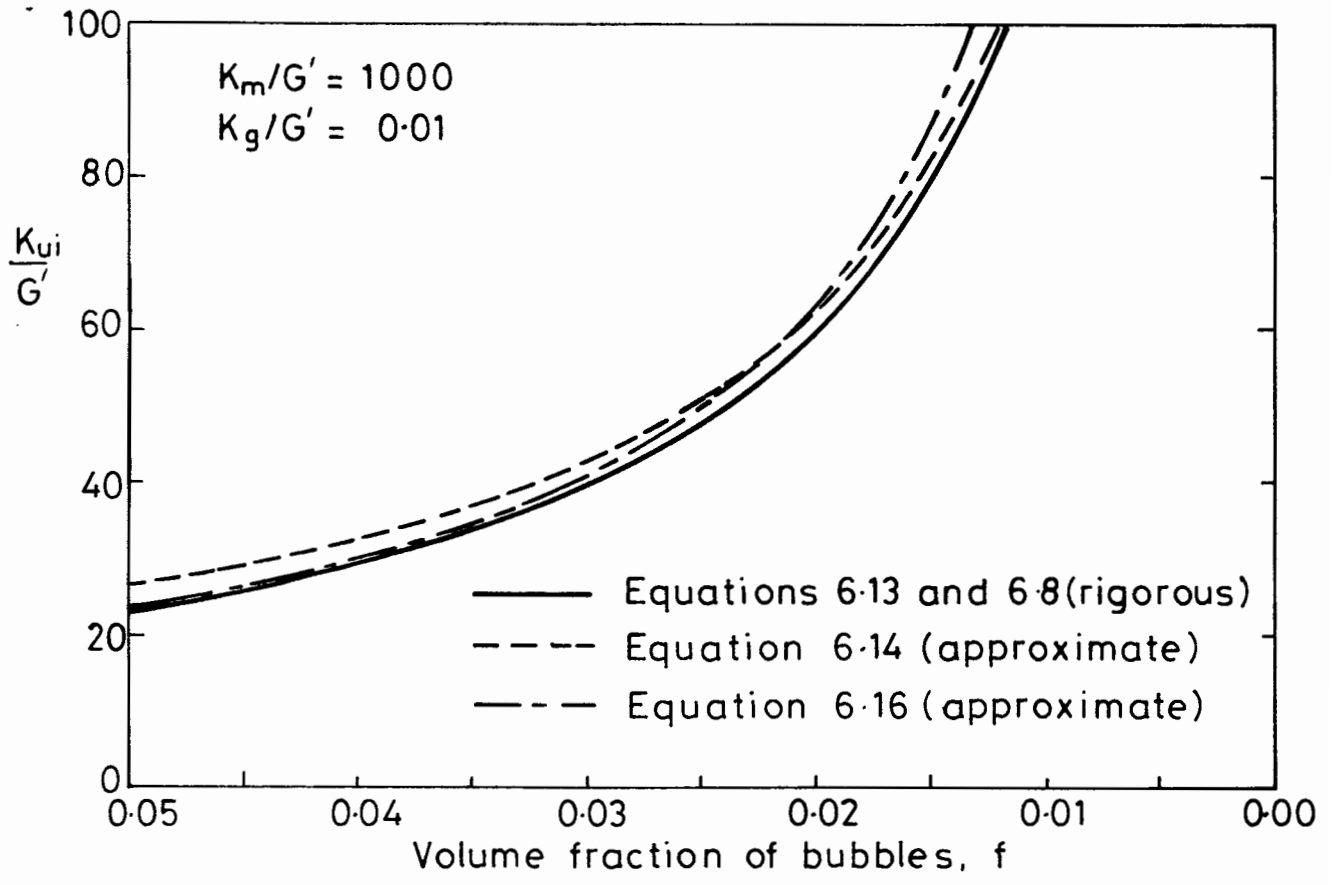

Fig. 6·4. ACCURACY OF APPROXIMATE EXPRESSIONS FOR K_{ui}

With K_g equal to zero, Equation 6.14 is identical to the solution of MacKenzie (1950) and Walsh and Brace (1966), who considered the case of empty cavities.

Figure 6.4 compares the approximate relationship of Equation 6.14 with the rigorous analysis of Equations 6.8 and 6.13. The figure shows that, under a typical set of conditions ($K_m/G' = 1000$, $K_g/G' = 0.01$), Equation 6.14 overestimates K_{ui} by about 15% when $f = 0.05$.

If the compressibility of the water can be ignored, K_m tends to infinity and Equation 6.14 simplifies to:

$$K_{ui} = \frac{K_g + 4G'/3}{f} \qquad 6.15$$

If the compressibility of the water and the stiffness of the bubbles are ignored, an alternative approximate expression for K_{ui} can be derived, without assuming that the volume fraction of bubbles is small. If K_m is infinite and K_g is zero, then G_{ui} is given by Equation 6.12, and inserting this expression in Equation 6.13 gives the following equation for K_{ui}:

$$K_{ui} = \frac{4G'}{f} \frac{(1 - 2f)(1 - f)}{(3 - f)} \qquad 6.16$$

Equations 6.15 and 6.16 reduce to the same expresson if K_g and f tend to zero.

The accuracy of Equation 6.16 can be judged by inspection of Figure 6.3. In this figure the values predicted by Equation 6.16 correspond to the curve with $K_m/G' = \infty$ and $K_g/G' = 0$. It is clear that the accuracy of Equation 6.16 is not as good as the equivalent approximate expression for the shear modulus (Equation 6.12), which produced results that were almost identical to the rigorous values. However, considering that $K_m/G' = 100$ and $K_g/G' = 0.1$ probably represent the worst possible cases, it is evident that Equation 6.16 may often be an acceptable approximation.

Figure 6.4 shows the values of K_{ui} prediced by the two approximate expressions (Equations 6.14 and 6.16) and the rigorous analysis (Equations 6.13 and 6.8). The figure represents a typical set of conditions ($K_m/G' = 1000$, $K_g/G' = 0.01$). Under these conditions, Equation 6.16 is a better approximation than Equation 6.14 provided that f is greater than about 0.02.

In summary, the expressions for G_{ui} and K_{ui} are given by Equations 6.8 and 6.13. Approximate expressions, based on the assumptions that $K_w = \infty$ and $K_g = 0$, are given in Equations 6.12 and 6.16. These are normally more accurate than the alternative approximate expressions given in Equations 6.10 and 6.14, which are based on the assumption that f is much less than unity.

6.3 LONG TERM UNDRAINED MODULI

The long-term undrained moduli differ from the instantaneous values because of two separate effects: the movement of gas into solution and localised consolidation within the matrix. These effects are described in Sections 5.3 and 5.5 of Chapter 5.

The effect of gas moving into solution is very easy to calculate. The gas modulus K_g is simply replaced by the apparent long-term gas modulus K_g^* (defined in Equation 5.11, Chapter 5).

If K_g^* is substituted for K_g in Equation 6.8, the effect on the shear modulus is very, very small (the previous section described how G_{ui} is hardly affected by much larger changes in the gas modulus). Indeed, if the approximate formulae of Equation 6.10 or 6.12 are used, instead of Equation 6.8, replacing K_g with K_g^* has no effect whatsoever.

Although the change in the shear modulus appears to be totally insignificant, if the modified value is used in Equation 6.13, the effect on the bulk modulus may be large enough to be of importance (because of the sensitivity of Equation 6.13). The approximate formula of Equation 6.14 can also be used to estimate the effect on the bulk modulus of replacing K_g with K_g^*.

The analysis of the localised consolidation effect is rather more difficult. To study the effect of any localised consolidation and swelling it is first necessary to calculate the pattern of initial water pressures set up in the matrix by a stress increment. This involves studying the field of total stresses produced by the application of a uniform total stress increment to the boundary of a sample. The problem can be simplified to a manageable level by ignoring the compressibility of the water and assuming that the volume fraction of bubbles is small.

Goodier (1933) studied the behaviour of an elastic material containing a small volume fraction of spherical inclusions. He calculated the stresses resulting from the application of a uniaxial stress at the boundary. His results can be used to calculate the field of total stresses resulting from the application at the boundary of either a hydrostatic stress increment Δp or an increment of axisymmetric pure shear Δq.

In Appendix 1, Goodier's results are employed to show that a hydrostatic boundary stress increment Δp causes an increment Δp_* in the local mean total stress at any point in the saturated soil matrix that is given by:

$$\Delta p_* = \Delta p \qquad 6.17$$

Equation 6.17 indicates that the local mean total stress increment Δp_* is independent of the position within the matrix.

For an increment of pure shear Δq at the boundary the local mean total stress increment within the matrix Δp_* is calculated in Appendix 1 as:

$$\Delta p_* = \frac{-5\Delta q a^3(1 + 3\cos 2\theta)}{18r^3} \qquad 6.18$$

r is the radial distance from the nearest bubble centre and θ is the angle from the axis of symmetry, as defined in Figure 6.5. Equation 6.18 indicates that a pure shear stress applied to the sample boundary produces a mean total stress within the matrix which varies with the position relative to a bubble.

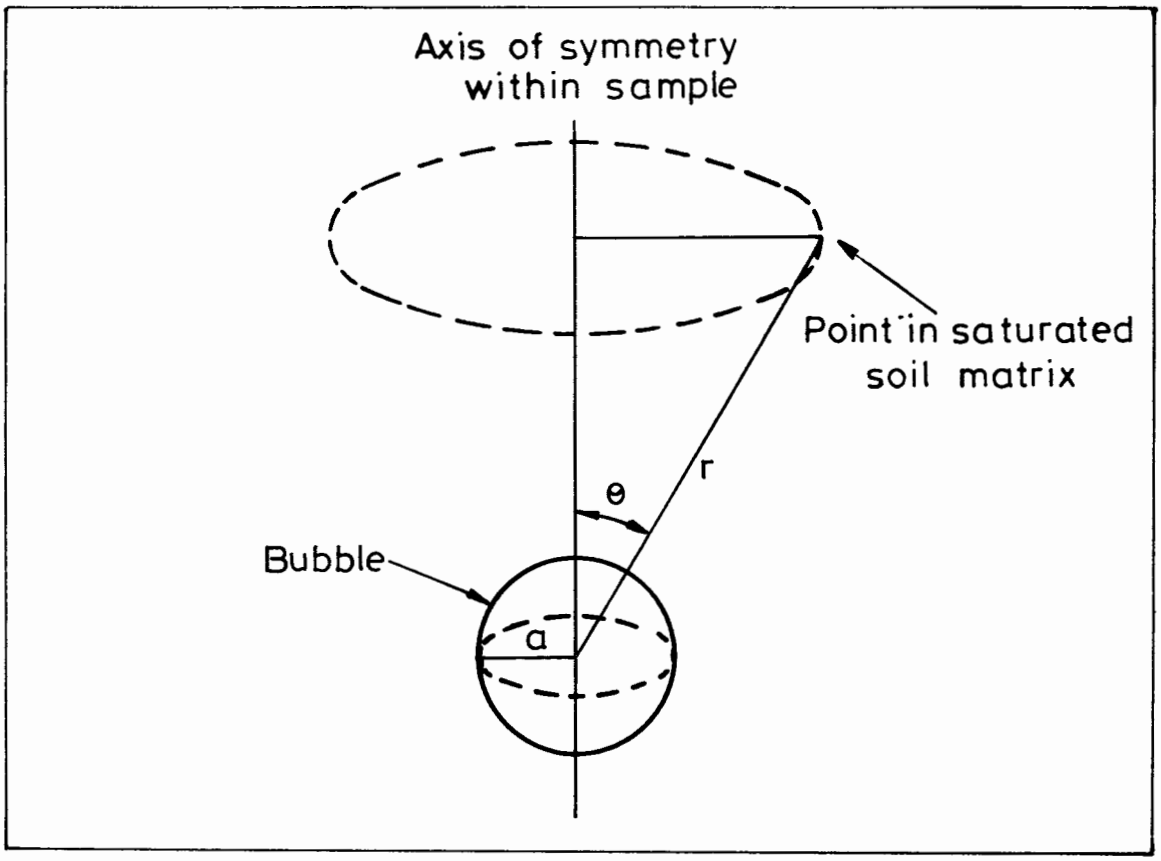

Fig. 6.5. DEFINITION OF PARAMETERS r AND θ

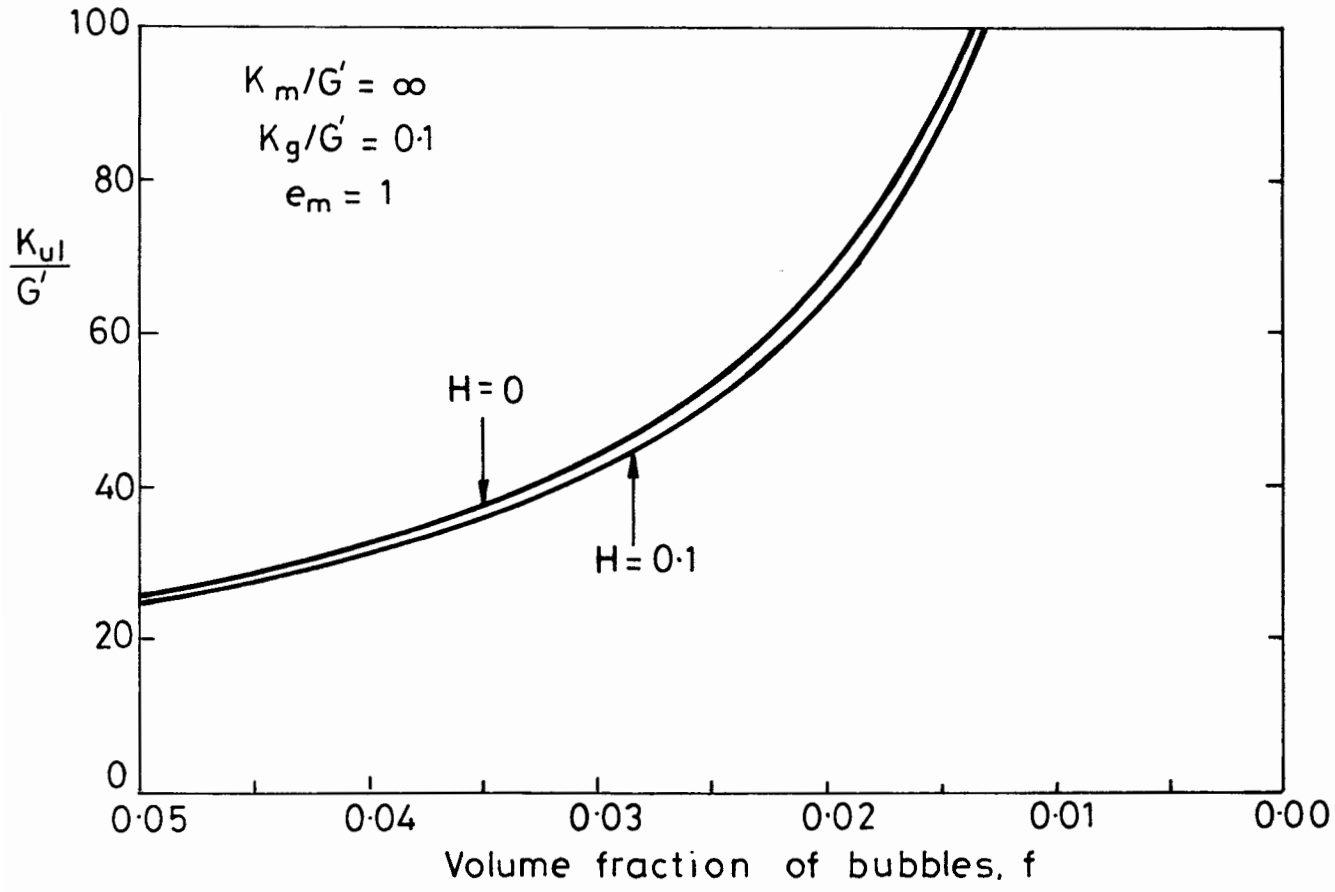

Fig. 6·6. LONG-TERM UNDRAINED BULK MODULUS OF MODEL.

With Δp_* defined by Equation 6.17 or 6.18, all that is required to calculate the initial pattern of pore water pressures is a knowledge of the change in the local mean effective stress $\Delta p'_*$ throughout the matrix. However, the instantaneous response of the matrix must be undrained, with zero volume change (because the compressibility of the water is being ignored). This means that the instantaneous change in p'_* must be zero at all points, because elastic behaviour is being assumed (a change in the mean effective stress must produce a volume change in an isotropic elastic material: Atkinson and Bransby, 1978). Therefore the initial change in the local pore water pressure is given by:

$$\Delta u_w = \Delta p_* - \Delta p'_* = \Delta p_* \qquad 6.19$$

Combining Equation 6.17 or 6.18 with Equation 6.19 gives the initial pattern of pore water pressures set up by either a hydrostatic boundary stress or a pure shear boundary stress:

$$\Delta u_w = \Delta p \qquad 6.20$$

$$\Delta u_w = \frac{-5\Delta q a^3(1 + 3\cos 2\theta)}{18r^3} \qquad 6.21$$

Equation 6.20 shows that the pore water pressure set up by the application of a hydrostatic boundary stress increment is constant throughout the saturated soil matrix. There is thus no tendency for any localised consolidation or swelling. Therefore, the long-term undrained bulk modulus $K_{u\ell}$ is unaffected by localised consolidation.

In contrast, Equation 6.21 shows that the application of a pure shear stress to the boundary of a sample results in an initial distribution of pore water pressure which varies with θ, the direction from the nearest bubble centre, and decays with the third power of r, the distance from the bubble centre. Equalisation of these water pressures will result in localised consolidation which will affect the long-term undrained shear modulus $G_{u\ell}$.

It is interesting to note that, if the volume fraction of bubbles is small, the undrained shear modulus is affected by localised consolidation but not by gas moving into solution, while the reverse is true of the undrained bulk modulus.

6.4.1 Long-Term Undrained Bulk Modulus

Because the behaviour under hydrostatic stresses is unaffected by localised consolidation, the difference between the long-term and instantaneous undrained bulk moduli is due simply to the replacement of K_g with K_g^*, as described above. By inspection of Equations 6.13 and 6.8, $K_{u\ell}$ is given by:

$$K_{u\ell} = \frac{4G_u^*\{5fG' - 2(G' - G_u^*)\}}{3\{3(G' - G_u^*) - 5FG'\}} \qquad 6.22$$

where G_u^* is given by:

$$\frac{fK_g^*}{K_g^* + 4G_u^*/3} + \frac{(1 - f)K_m}{K_m + 4G_u^*/3} + \frac{5fG'}{G_u^* - G'} + 2 = 0 \qquad 6.23$$

G_u^* is not the actual long-term undrained shear modulus $G_{u\ell}$, because $G_{u\ell}$ is affected by the localised consolidation effect. G_u^* would be the value of the undrained shear modulus if gas was allowed to move into solution, but localised consolidation was somehow prevented.

Figure 6.6 illustrates how $K_{u\ell}$ varies with the volume fraction of bubbles, for the case when $K_g/G' = 0.1$. The figure shows curves for two different values of the solubility coefficient H : zero and 0.1. It is clear that $K_{u\ell}$ is only slightly less than the instantaneous modulus K_{ui} (which corresponds to the curve with $H = 0$), even if H is as high as 0.1. If the parameter K_g/G' is reduced, the effect of varying H becomes even smaller. For $K_g/G' = 0.01$ the curves for $K_{u\ell}$ and K_{ui} are indistinguishable for values of H right up to 0.1.

If the approximate expression of Equation 6.16 is used, there is no apparent difference between K_{ui} and $K_{u\ell}$, because the reduction in the gas modulus from K_g to K_g^* has no effect on this expression (which already assumes that the gas stiffness is zero). Therefore the approximate expression for $K_{u\ell}$ is:

$$K_{u\ell} = \frac{4G'}{3f} \frac{(1 - 2f)(1 - f)}{(3 - f)} \qquad 6.24$$

The alternative approximate expression given in Equation 6.14, which assumes that the volume fraction of bubbles is small, does indicate a very slight difference between K_{ui} and $K_{u\ell}$. If K_g is replaced with K_g^*, Equation 6.14 becomes:

$$K_{u\ell} = \frac{K_m(K_g^* + 4G'/3)}{(K_g^* + 4G'/3) + f(1 - K_g^*/K_m)(K_m + 4G'/3)} \qquad 6.25$$

If the water is incompressible, Equation 6.25 reduces to:

$$K_{u\ell} = \frac{K_g^* + 4G'/3}{f} \qquad 6.26$$

6.3.2 Long-Term Undrained Shear Modulus

The expression for the long-term undrained shear modulus $G_{u\ell}$ must take account of the localised consolidation effect, because Equation 6.21 indicates that a pure shear stress applied to the boundary of a sample causes pore water pressures within the matrix which vary with position. Integration of Equation 6.21 over any hollow spherical element centred on a bubble shows that the volume average of the initial water pressure in such an element is zero. This is irrespective of the wall thickness or internal radius of the spherical element (provided that the latter is greater than the bubble radius). This means that, provided the elastic response of the soil skeleton is linear, the pore water pressures set up throughout the matrix by an increment of pure shear at the boundary will dissipate completely during localised consolidation.

Because the long-term undrained response of the soil to a pure shear stress produces no change in pore water pressure, the saturated soil matrix is effectively acting under drained conditions. Therefore, in the expression for the long-term undrained shear modulus $G_{u\ell}$, the matrix behaviour is defined by the drained moduli K' and G'. This means that Equation 6.23 is replaced by:

$$\frac{fK_g^*}{K_g^* + 4G_{u\ell}/3} + \frac{(1 - f)K'}{K' + 4G_{u\ell}/3} + \frac{5fG'}{G_{u\ell} - G'} + 2 = 0 \qquad 6.27$$

The expression for $K_{u\ell}$ and $G_{u\ell}$ (Equations 6.22 and 6.27) are apparently inconsistent, in that they do not fit Hill's relationships (Equations 6.1 to 6.3). This is because the matrix appears to have different properties, depending on whether a hydrostatic stress or a shear stress is applied to the sample boundary. If a hydrostatic stress is applied, the matrix behaves in an undrained fashion, because the positive pore water pressure set up in the matrix does not vary with position. If a pure shear stress is applied, the matrix behaves in a drained fashion, because the initial pore water pressure varies with position in such a way that the average value throughout the matrix is zero. Obviously, the matrix is only capable of exhibiting these apparently different properties under different applied stresses because it is not a simple single phase material. It consists of two phases: the soil skeleton and the pore water.

Figure 6.7 shows how $G_{u\ell}$ varies with the volume fraction of bubbles. The values of $G_{u\ell}$ have been normalised by dividing by G'. Inspection of Equation 6.27 shows that $G_{u\ell}$ depends upon both G' and K', so that $G_{u\ell}/G'$ varies with the ratio K'/G'. This ratio is controlled by the value of the drained Poisson's ratio of the matrix ν'. Figure 6.7 shows curves for $\nu' = 0.2$ and $\nu' = 0.3$, together with a curve for the instantaneous modulus G_{ui} (which corresponds to $\nu = 0.5$). It is clear that $G_{u\ell}$ is always slightly less than G_{ui}.

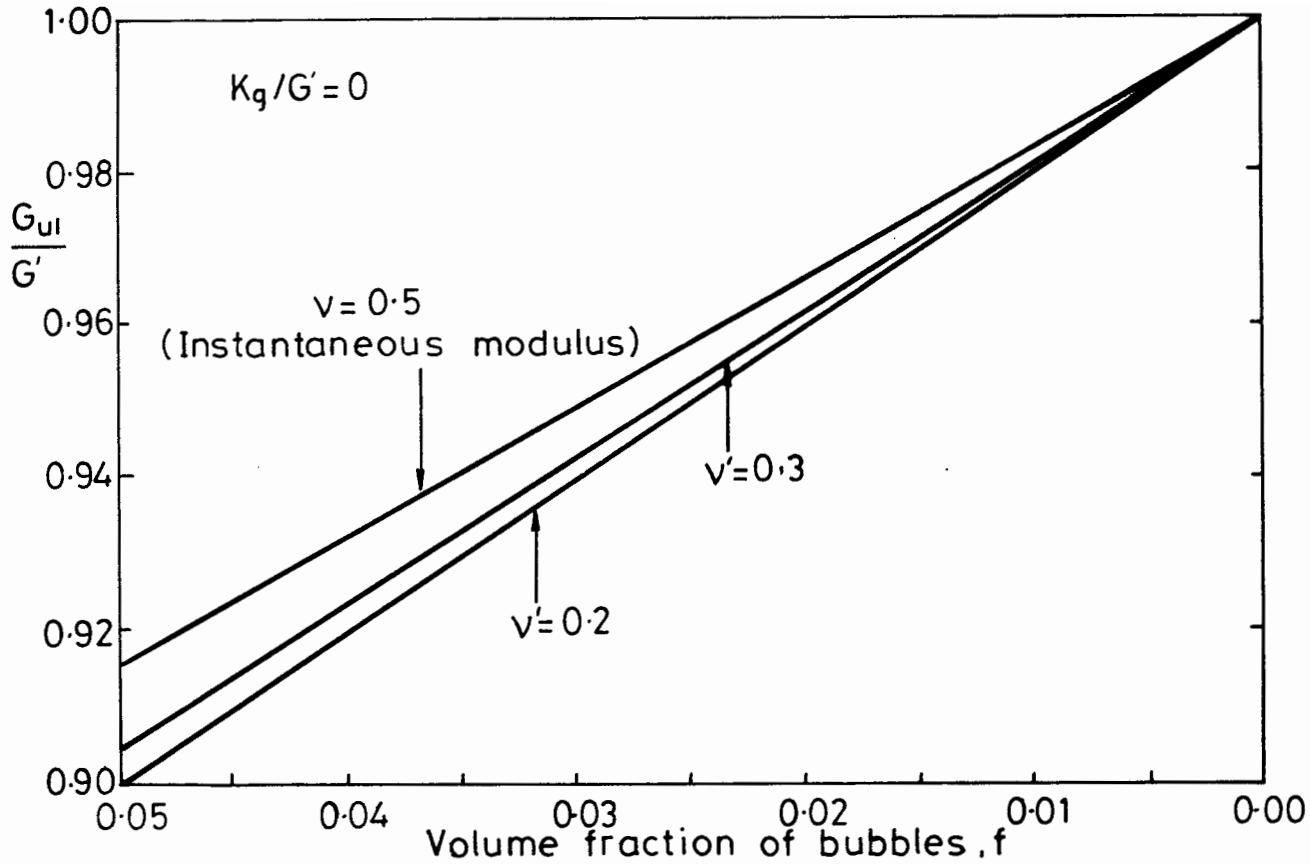

Fig. 6.7. LONG-TERM UNDRAINED SHEAR MODULUS OF MODEL.

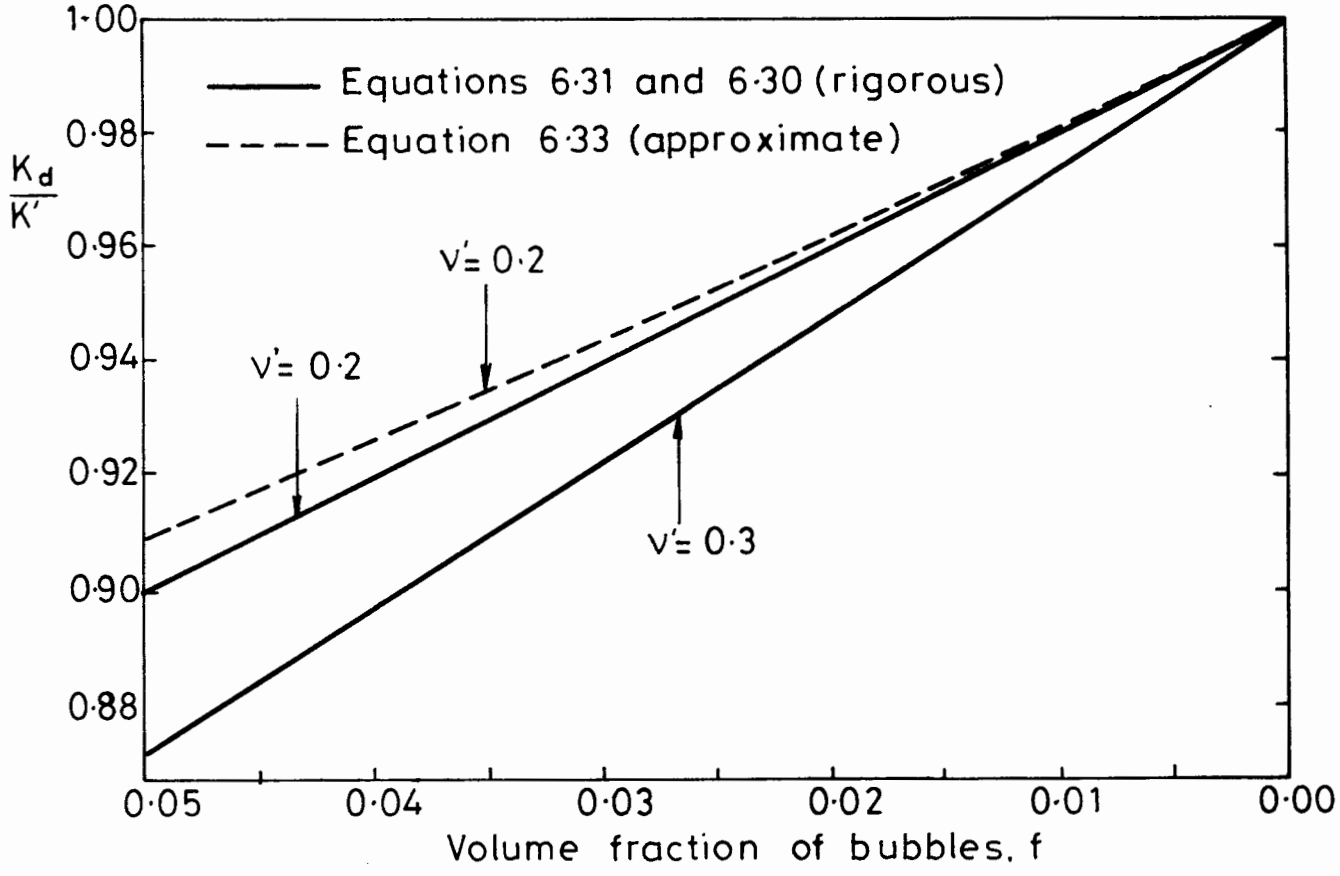

Fig. 6·8 DRAINED BULK MODULUS OF MODEL.

An approximate expression for $G_{u\ell}$ can be derived by ignoring the stiffness of the gas. If $K_g = 0$, Equation 6.27 reduces to:

$$\frac{(1 - f)K'}{K' + 4G_{u\ell}/3} + \frac{5fG'}{G_{u\ell} - G'} + 2 = 0 \qquad 6.28$$

The compressibility of the water has no effect on Equation 6.28, because the saturated soil matrix is acting in a drained fashion. Therefore, this approximate expression cannot be simplified any further by assuming that the water is incompressible.

An alternative approximate expression for $G_{u\ell}$ can be derived by assuming that the volume fraction of bubbles is very small. As f tends to zero $G_{u\ell}$ approaches G' and Equation 6.27 becomes:

$$G_{u\ell} = G'\left(1 - \frac{5f(K' + 4G'/3)}{3K' + 8G'/3}\right) \qquad 6.29$$

In summary, the most rigorous expression for $G_{u\ell}$ is given by Equation 6.27, and the most rigorous expression for $K_{u\ell}$ by Equations 6.22 and 6.23. Approximate expressions, based on the assumptions that $K_w = \infty$ and $K_g = 0$, are given in Equations 6.28 and 6.24. These are normally more accurate than the alternative approximate expressions given in Equations 6.29 and 6.25, which are based on the assumption that f is much less than unity.

It should be noted that Equations 6.22, 6.23 and 6.27, which are the most accurate expression for $K_{u\ell}$ and $G_{u\ell}$, are not entirely rigorous. This is because the analysis of the localised consolidation effect includes the assumptions that the water is incompressible and the volume fraction of bubbles is small (although these assumptions are not used in the earlier parts of the analysis).

6.4 DRAINED MODULI

The drained moduli G_d and K_d can be calculated by substituting the relevant component moduli in Hill's formulae (Equations 6.1 to 6.3). The saturated soil matrix is represented by the drained moduli G' and K', but the choice of bulk modulus for the gas is less obvious. In fact, the choice depends upon the precise nature of the boundary conditions on the drained face of the soil.

If the water supply to the drained boundary is in contact with the atmosphere (or some large reservoir of gas) diffusion of gas occurs from the bubbles to the atmosphere, so that the bubbles always remain at atmospheric pressure (see Section 5.3 of Chapter 5). Under these conditions the bulk modulus of the gas is effectively zero, because there is never any change in gas pressure. However, if the water supply to the drained face is not in direct contact with a large volume of gas, diffusion to the drained boundary does not occur. Only localised diffusion of gas takes place, as the gas moves into or out of solution from each bubble, and the effective gas modulus is K_g^*.

Of the two different boundary conditions described above, the former is by far the most likely. This was the condition that applied in the laboratory tests described in Chapters 3 and 4, and it is also likely to be the situation that occurs in the field. Therefore, the expressions for the drained moduli G_d and K_d are based on the assumption that the effective gas modulus is zero. In practice, it would make very little difference if the gas modulus was increased to K_g^*, because the results are very insensitive to this variable.

6.4.1 Drained Shear Modulus

Insertion of the relevant moduli in Equation 6.7 gives the following expression for the drained shear modulus G_d:

$$\frac{(1-f)K'}{K' + 4G_d/3} + \frac{5fG'}{G_d - G'} + 2 = 0 \qquad 6.30$$

This quadratic equation can be solved for G_d.

The expression for G_d given in Equation 6.30 is very similar to the expression for the long-term undrained modulus $G_{u\ell}$ given in Equation 6.27. The only difference is that the gas modulus has been reduced from K_g^* to zero. In fact the expression for G_d is the same as the approximate expression for $G_{u\ell}$ given in Equation 6.28, which ignores the gas stiffness.

The fact that G_d is very similar to $G_{u\ell}$ is hardly surprising in the light of the analysis presented in the previous section. This analysis suggests that a pure shear stress applied to the sample boundary produces a field of pore water pressure in the matrix which completely dissipates during localised consolidation. If large scale drainage of the soil is then allowed, there is obviously no tendency for any further movement of water. The only drainage that does occur is the diffusion of gas to the drained boundary (reducing the gas modulus from K_g^* to zero).

The expression for G_d given in Equation 6.30 is not affected by the gas modulus K_g (because the effective gas modulus is zero) or the water modulus K_w (because the saturated soil matrix is behaving in a drained fashion). Therefore the expresson cannot be simplified any further by assuming that $K_g = 0$ and $K_w = \infty$.

An approximate expression for G_d can be derived if the volume fraction of bubbles is small. If f is much less than unity, Equation 6.30 reduces to:

$$G_d = G'\left(1 - \frac{5f(K' + 4G'/3)}{3K' + 8G'/3}\right) \qquad 6.31$$

This is precisely the same as the approximate expression for $G_{u\ell}$ (Equation 6.29), for the reasons already explained. The values of G_d and $G_{u\ell}$ predicted by this equation are almost indistinguishable from the rigorous values.

As $G_{u\ell}$ and G_d are effectively equal, the variation of G_d with the volume fraction of bubbles is shown by Figure 6.7.

6.4.2 Drained Bulk Modulus

Hill's formulae can also be used to provide an expression for the drained bulk modulus K_d:

$$K_d = \frac{4G_d\{5fG' - 2(G' - G_d)\}}{3\{3(G' - G_d) - 5fG'\}} \qquad 6.32$$

The values of G_d calculated from Equation 6.30 can be substituted in Equation 6.32 to evaluate K_d.

The drained bulk modulus K_d is very different from the long-term undrained bulk modulus $K_{u\ell}$, because a hydrostatic stress applied to the sample boundary produces pore water pressures that do not dissipate during localised consolidation. If the sample is allowed to drain, the subsequent dissipation of these pore pressures produces large-scale consolidation.

Figure 6.8 shows the drained bulk modulus K_d plotted against the volume fraction of bubbles. The values of K_d have been normalised by dividing by K', because K_d is predominantly controlled by K'. This contrasts with the undrained bulk moduli K_{ui} and $K_{u\ell}$, which are mainly dependent on G'. However the figure shows that K_d is still somewhat affected by G', as demonstrated by the dependence on the drained Poisson's ratio of the matrix ν'.

The value of K_d is unaffected by the gas modulus K_g or the water modulus K_w, for the same reasons that the shear modulus G_d is independent of these parameters. Therefore the expression for G_d cannot be simplified by assuming $K_g = 0$ and $K_w = \infty$.

An approximate expression for K_d can be derived if the volume fraction of bubbles is small, by using Eshelby's relationship (see Equation 6.14). Insertion of the relevant component moduli gives:

$$K_d = \frac{G'K'}{G' + f(G' + 3K'/4)} \qquad 6.33$$

Figure 6.8 illustrates the value of K_d predicted by Equation 6.33 for the case of $\nu' = 0.2$. The figure shows that the approximate expression overestimates slightly the value of K_d.

6.5 SUMMARY OF IMPORTANT FORMULAE

Table 6.1 gives a list of the various expressions for the elastic moduli of the large bubble model. The table provides simply the numbers of the relevant equations, which can be found in the text. The table lists three equations for each modulus; first a rigorous formula and then two approximate expressions.

Table 6.2 gives representative expressions for the elastic moduli of the model, together with the corresponding values for saturated soil. The formulae presented in the table are approximate expressions, with the water assumed to be incompressible and the gas completely compressible. These approximate expressions are normally quite adequate.

Table 6.1 Summary of Equations for Elastic Moduli

			Rigorous Expressions	Approximate Expressions $K_g = 0$, $K_w = \infty$	$f \ll 1$
Instantaneous undrained moduli	Bulk modulus	K_{ui}	6.13 & 6.8	6.16	6.14
	Shear modulus	G_{ui}	6.8	6.12	6.10
Long-term undrained moduli	Bulk modulus	$K_{u\ell}$	6.22 & 6.23	6.24	6.25
	Shear modulus	$G_{u\ell}$	6.27	6.28	6.29
Drained moduli	Bulk modulus	K_d	6.32 & 6.30	6.32 & 6.30	6.33
	Shear modulus	G_d	6.30	6.30	6.31

Table 6.2 Elastic Moduli of the Large Bubble Model

			Saturated soil	Large bubble model
Instantaneous undrained moduli	Bulk modulus	K_{ui}	∞	$\frac{4G'(1 - 2f)(1 - f)}{f(3 - f)}$
	Shear modulus	G_{ui}	G'	$\frac{3G'(1 - 2f)}{3 - f}$
Long-term undrained moduli	Bulk modulus	$K_{u\ell}$	∞	$\frac{4G'(1 - 2f)(1 - f)}{f(3 - f)}$
	Shear modulus	$G_{u\ell}$	G'	$\frac{(1 - f)K'}{K' + 4G_{u\ell}/3} + \frac{5fG'}{G_{u\ell} - G'} + 2 = 0$
Drained moduli	Bulk modulus	K_d	K'	$\frac{4G_d\{5fG' - 2(G' - G_d)\}}{3\{3(G' - G_d) - 5fG'\}}$
	Shear modulus	G_d	G'	$\frac{(1 - f)\,K'}{K' + 4G_d/3} + \frac{5fG'}{G_d - G'} + 2 = 0$

All expressions are based on the assumptions $K_g = 0$ and $K_w = \infty$.

CHAPTER 7

THEORETICAL ANALYSIS : CONSOLIDATION BEHAVIOUR

CHAPTER 7

THEORETICAL ANALYSIS : CONSOLIDATION BEHAVIOUR

The previous chapter covered the elastic behaviour of the large bubble model under the application of any small load increment, with either drained or undrained boundary conditions. In this chapter, and Chapter 8, the analysis is extended to large load increments, when the soil cannot be considered as an elastic material. However, a very restricted range of loading and drainage conditions is considered. The present chapter covers the drained response under either isotropic or one-dimensional conditions i.e. the consolidation behaviour. Chapter 8 deals with the undrained response as the soil is sheared to failure i.e. the undrained shear strength.

7.1 THE TIME-DEPENDENT PROCESS OF CONSOLIDATION

Figure 7.1 shows how the matrix void ratio e_m and the volume fraction of bubbles f might vary during either isotropic or one-dimensional consolidation. Under the application of a load increment at time t_o there is an immediate reduction of f, due to the compression of the gas bubbles. However, there is no immediate change in e_m, because the saturated soil matrix is incompressible until drainage occurs. The matrix simply distorts at constant volume to accommodate the change in size of the bubble cavities. After the initial load application the value of e_m does fall with time, as water drains from the matrix during the process of consolidation.

The localised and large-scale drainage that occurs during consolidation results in deformation of the matrix. This matrix deformation affects the size of the bubble cavities, causing additional changes in the volume fraction of bubbles f. Further variation of f occurs because of the movement of gas in andout of solution under the influence of the changing bubble pressure.

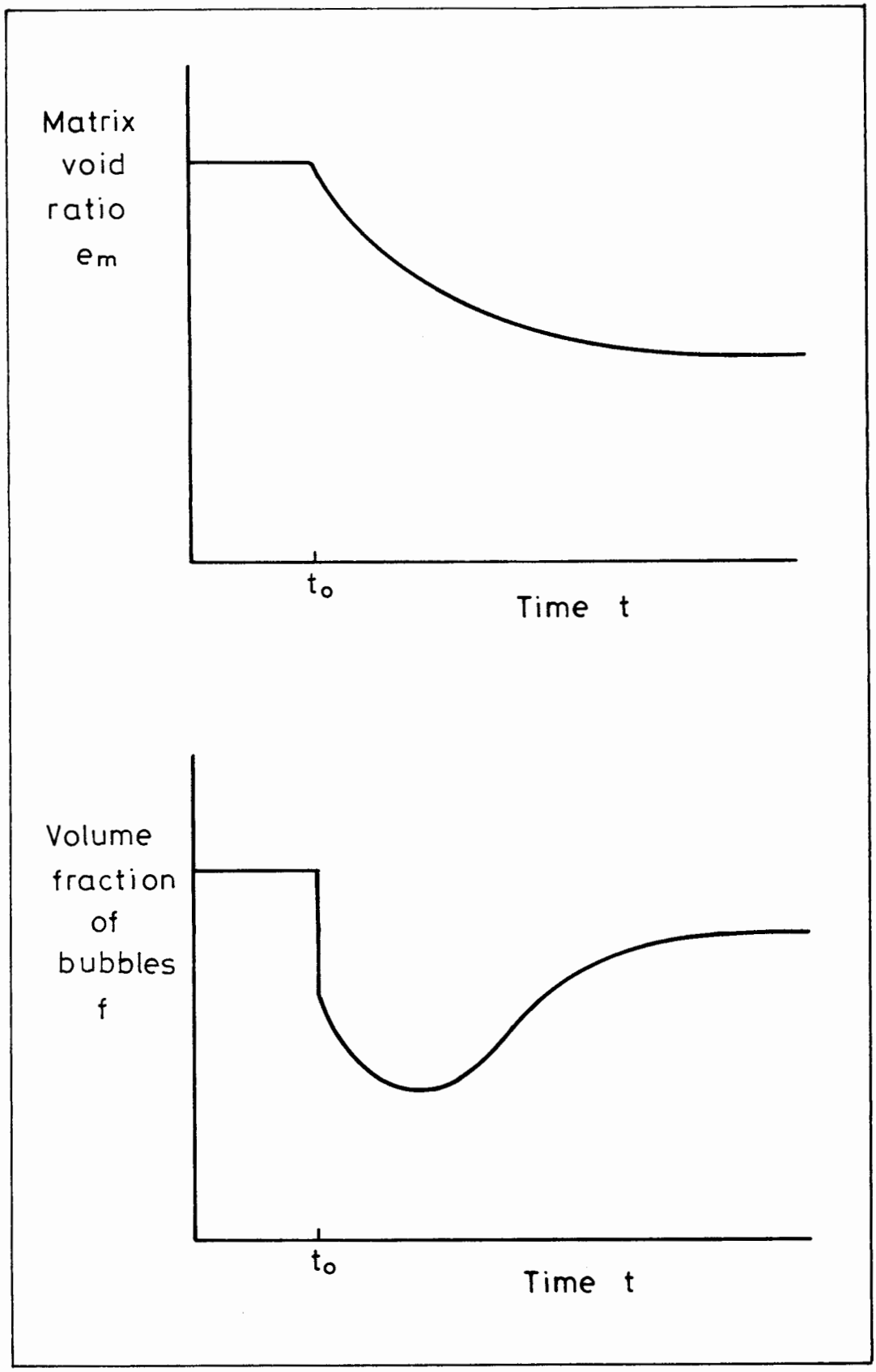

Fig. 7·1. VARIATION OF e_m AND S DURING CONSOLIDATION.

Figure 7.1 shows that both the matrix void ratio e_m and the volume fraction of bubbles f should ultimately reach final equilibrium values, when all drainage of water and gas is complete (including the diffusion of dissolved gas).

A full analysis of the consolidation behaviour, to predict the complete variation of e_m and f with time, would obviously be very difficult. The governing equations of the consolidation process, derived by Biot (1941), would have to be suitably modified to take account of localised consolidation and the movement of dissolved gas. No attempt has been made to tackle this very difficult problem. This chapter simply covers the final state of the soil, once all consolidation is complete. The model developed in Chapter 5 has been analysed to try and predict the ultimate values of e_m and f, in the hope of predicting the final values of the void ratio e and the degree of saturation S (see Equations 5.2 and 5.3, Chapter 5). This was considered to be the most important aspect of the consolidation behaviour, and the problem of most relevance to the series of experimental tests described in Chapters 3 and 4.

7.2 ISOTROPIC CONSOLIDATION

The final value of the matrix void ratio e_m after isotropic consolidation depends upon the effective stresses within the saturated soil matrix. Unfortunately the distribution of stresses within the matrix at the end of consolidation is not known. Even if the initial distribution of stresses immediately after the load application could be calculated, there would be a redistribution of these stresses during the consolidation process. However, it is possible to consider a number of feasible stress distributions, to see what these would suggest as a final value for e_m.

The type of stress distribution produced in the matrix by isotropic consolidation can be studied by considering the effect of a hydrostatic stress p applied to the boundary of the soil. It is important to realise that the pressure p is an average stress applied to the soil boundary, and is not the stress at any particular point within the matrix. By the end of consolidation the pore water pressure throughout the matrix dissipates to a value u_w, and the gas pressure within the bubbles settles at a value u_g. The total stresses within the matrix must obey the equilibrium conditions, and must fit the boundary stresses (u_g at the bubble boundary and p at the distant boundary). However this still leaves an infinite number of possible stress distributions, depending upon the material properties of the matrix.

7.2.1 Elastic Stress Distribution

One of the many possible stress distributions can be calculated by assuming that the matrix behaves as a linear elastic material. Love (1959) produced expressions for the stresses within a thick-walled spherical shell of elastic material loaded with an external pressure p and an internal pressure u_g. If the volume fraction of bubbles is very small, each bubble (of radius a) is effectively surrounded by matrix extending to infinity. With the outer radius set at infinity, Love's equations reduce to the following expressions for the radial stress σ_r and the hoop stress σ_θ at a radius r from the bubble centre:

$$\sigma_r = p - \frac{a^3}{r^3}(p - u_g) \qquad 7.1$$

$$\sigma_\theta = p + \frac{a^3}{2r^3}(p - u_g) \qquad 7.2$$

Figure 7.2 shows the variation of σ_r and σ_θ.

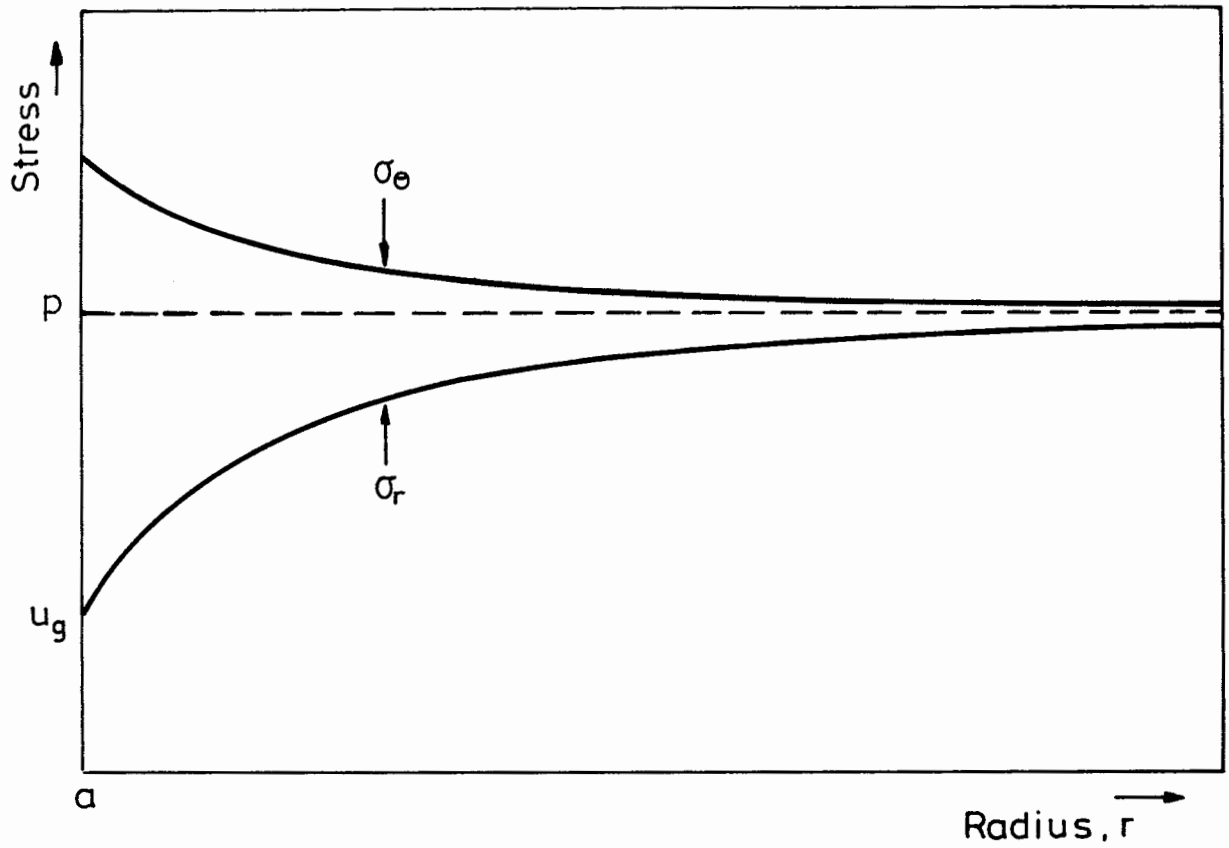

Fig. 7·2. ELASTIC STRESS DISTRIBUTION WITHIN LARGE BUBBLE MODEL.

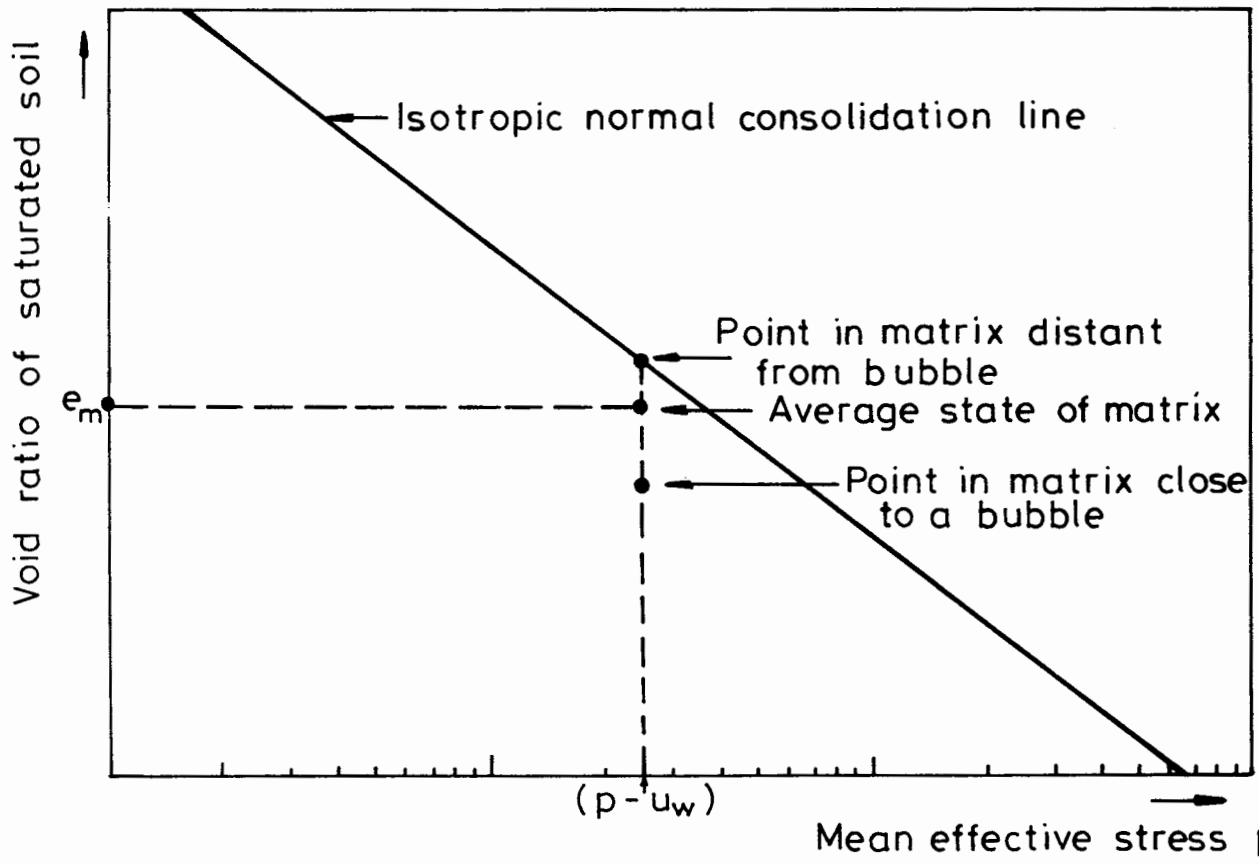

Fig. 7·3. MATRIX VOID RATIO FOR ELASTIC STRESS DISTRIBUTION.

The local value p_* of the mean total stress, at any point within the matrix, is defined by:

$$p_* = \frac{1}{3}(\sigma_r + 2\sigma_\theta) \qquad 7.3$$

Inserting the values of σ_r and σ_θ from Equations 7.1 and 7.2 into Equation 7.3:

$$p_* = p \qquad 7.4$$

Equation 7.4 indicates that the local value of the mean total stress is independent of the position within the matrix for an elastic stress distribution. This is in agreement with the analysis presented in Chapter 6 (see Equation 6.17), which was based on the work of Goodier (1933).

At the end of consolidation the pore water pressure dissipates to a value u_w throughout the matrix. Thereore, the local value p'_* of the mean effective stress is constant throughout the matrix, and is given by

$$p'_* = p - u_w \qquad 7.5$$

The local value q_* of the deviator stress within the matrix is defined by:

$$q_* = \sigma_r - \sigma_\theta \qquad 7.6$$

Inserting the values of σ_r and σ_θ from Equations7.1 and 7.2:

$$q_* = -\frac{3a^3}{2r^3}(p - u_g) \qquad 7.7$$

Equation 7.7 indicates that the magnitude of the deviator stress decays with the third power of the distance from the bubble centre. The negative sign shows that the saturated soil matrix is locally in a state of triaxial extension.

Equations 7.5 and 7.7 can be used to estimate the matrix void ratio e_m for the elastic stress distribution. In the parts of the matrix that are a long way from the nearest bubble, the deviator stress is almost zero (Equation 7.7), so the local matrix void ratio will be that of a saturated soil

consolidated isotropically to an effective stress $(p - u_w)$. However, in the region of each bubble the deviator stress is non-zero, so the local matrix void ratio is rather lower, because saturated samples can only exist on the normal consolidation line if the deviator stress is zero; all other saturated samples must fall below this line (Figure 7.3).

The average matrix void ratio e_m, for an elastic stress distribution, will lie somewhere between the two extreme values described above, as illustrated in Figure 7.3. For typical low values of f, the majority of the matrix material will be reasonably distant from a bubble, and the average matrix void ratio e_m will be only slightly less than the void ratio of a saturated soil consolidated isotropically to a stress $(p - u_w)$.

7.2.2 Plastic Stress Distribution

For the elastic stress distribution, illustrated in Figure 7.2, the difference between the radial stress σ_r and the hoop stress σ_θ varies with the distance from the bubble. Figure 7.4 shows an alternative, equally valid, stress distribution, in which the stress difference $(\sigma_\theta - \sigma_r)$ is constant throughout the matrix. This can be referred to as a plastic stress distribution, although the stress difference $(\sigma_\theta - \sigma_r)$ is not necessarily equal to the yield value of the matrix. The pattern of stresses shown in Figure 7.4 is simply one of the many possible distributions that obey the equilibrium equations and fit the boundary conditions.

If the stress difference $(\sigma_\theta - \sigma_r)$ is non-zero, the plastic stress distribution shown in Figure 7.4 cannot continue to infinite radius. The matrix must be considered as extending only a finite distance R from each bubble. The radius R should sensibly represent the point at which the effect of one bubble is overshadowed by the influence of the next bubble. Green (1972) suggests that the isotropic behaviour of a material containing a small volume fraction f of spherical cavities with radius a, can be

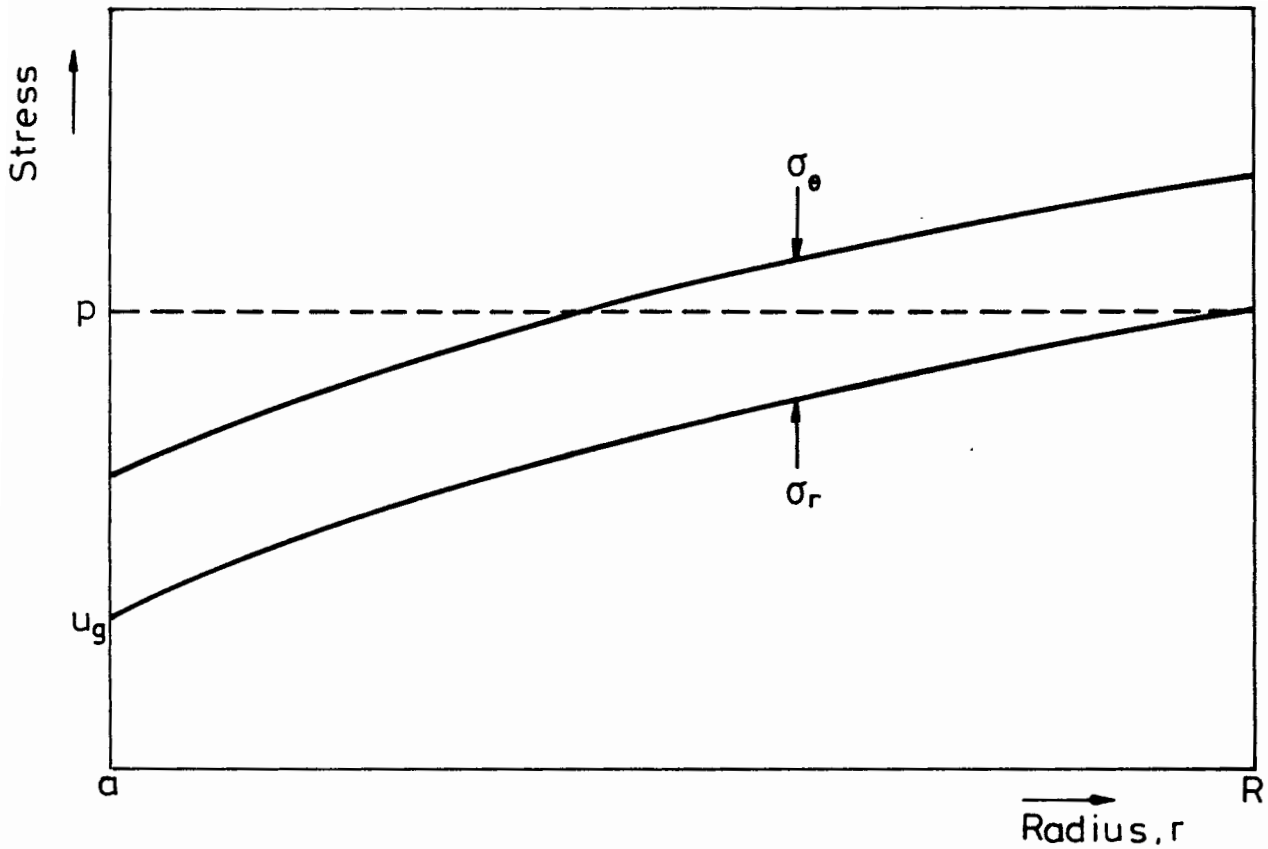

Fig. 7·4. PLASTIC STRESS DISTRIBUTION WITHIN LARGE BUBBLE MODEL.

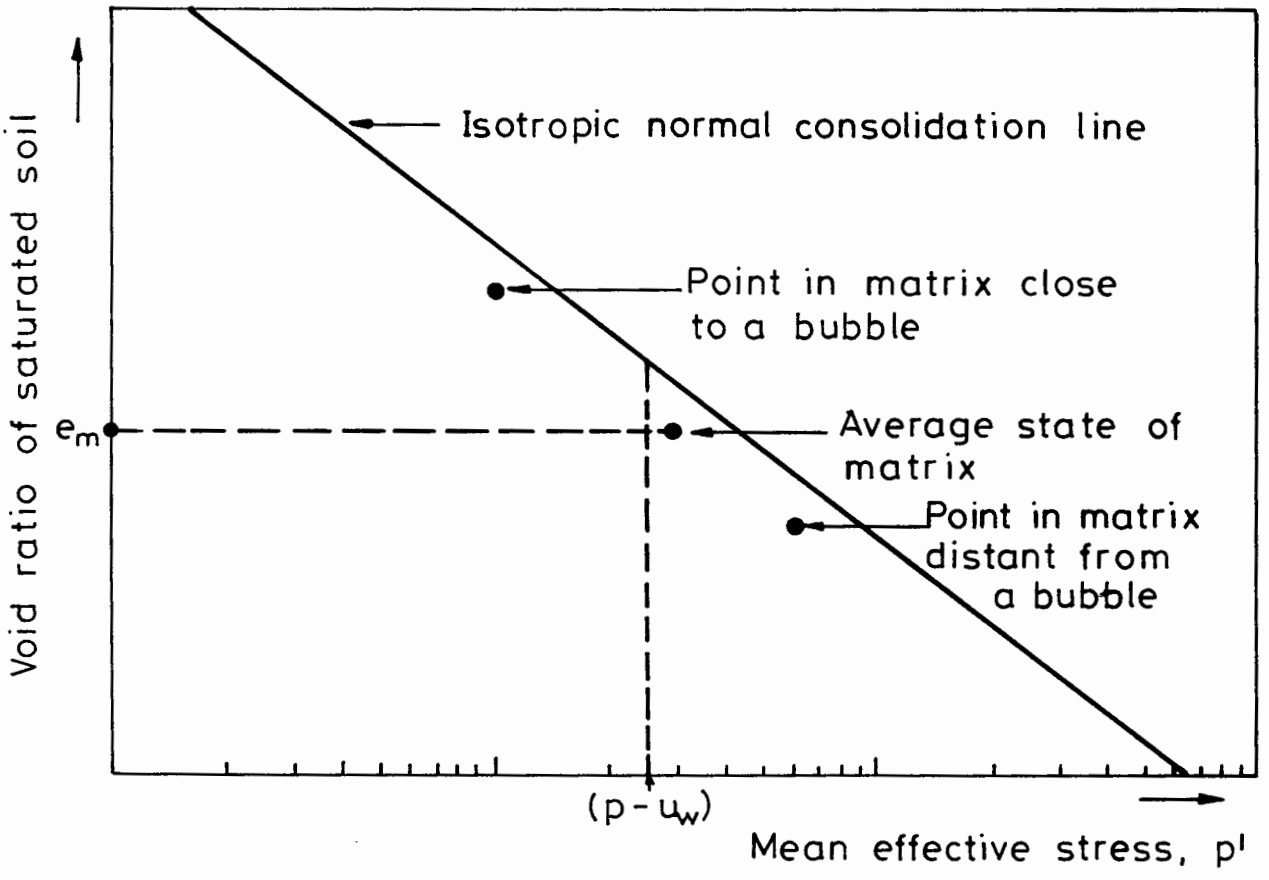

Fig. 7·5. MATRIX VOID RATIO FOR PLASTIC STRESS DISTRIBUTION.

represented by the behaviour of a single thick-walled shell with an outer radius R given by:

$$R^3 = \frac{a^3}{f} \qquad 7.8$$

Equation 7.8 states that the single cavity at the centre of the shell forms a volume fraction f of the total shell volume. This idea is developed further in Chapter 8, but in the present chapter it is sufficient to say that the radius R is much greater than the bubble radius a, provided that the volume fraction of bubbles is very small.

The stresses within the plastic distribution shown in Figure 7.4 can be calculated by invoking the equilibrium equation for a spherically symmetric condition (Vesic, 1972):

$$\frac{d\sigma_r}{dr} = \frac{2(\sigma_\theta - \sigma_r)}{r} \qquad 7.9$$

Rewriting Equation 7.9 in terms of the local deviator stress q_*, and using the convention that q_* is negative for triaxial extension:

$$\frac{d\sigma_r}{dr} = -\frac{2q_*}{r} \qquad 7.10$$

For the plastic stress distribution q_* is constant, so Equation 7.10 can be integrated to give:

$$\sigma_r = -2q_* \log_e r + \text{constant} \qquad 7.11$$

Inserting the boundary conditions ($\sigma_r = u_g$ at $r = a$, and $\sigma_r = p$ at $r = R$) into Equation 7.11 gives the following expressions for q_* and σ_r:

$$q_* = \frac{-(p - u_g)}{2\log_e(R/a)} \qquad 7.12$$

$$\sigma_r = p - (p - u_g)\frac{\log_e(R/r)}{\log_e(R/a)} \qquad 7.13$$

The corresponding expression for the hoop stress σ_θ is:

$$\sigma_\theta = p + (p - u_g)\frac{\{1 - 2\log_e(R/r)\}}{2\log_e(R/a)} \qquad 7.14$$

The local value p_* of the mean total stress within the matrix can be calculated by inserting Equations 7.13 and 7.14 into Equation 7.3:

$$p_* = p + (p - u_g)\frac{\{1 - 3\log_e(R/r)\}}{3\log_e(R/a)} \qquad 7.15$$

At the end of consolidation the pore pressure dissipates to a value u_w throughout the matrix, and the local value p'_* of the mean effective stress is given by:

$$p'_* = p - u_w + (p - u_g)\frac{\{1 - 3\log_e(R/r)\}}{3\log_e(R/a)} \qquad 7.16$$

Equations 7.12 and 7.16 indicate the variation of q_* and p'_* for the plastic stress distribution. In contrast to the elastic stress distribution, the deviator stress q_* is constant and the mean effective stress p'_* varies with the distance from the bubble centre. The value of p'_*, given by Equation 7.16, rises as the distance from the bubble is increased. In the parts of the matrix that are a long way from the nearest bubble the value of p'_* is greater than $(p - u_w)$. Close to each bubble p'_* is less than $(p - u_w)$, provided that the volume fraction of bubbles is small i.e. provided that R is much greater than a. This means that the local matrix void ratio will be high in the region of each bubble and low in the areas well away from any bubble (see Figure 7.5). In all regions the local state of the matrix will fall below the isotropic normal consolidation line for saturated soil, because the deviator stress q_* is non-zero.

The value of the average matrix void ratio e_m can be estimated by considering the average value of the mean effective stress within the matrix. The volume average of p'_* is given by integrating throughout the thick-walled shell:

$$(p')_{av} = \frac{\int_a^R 4\pi r^2 \, p'_* \, dr}{4\pi(R^3 - a^3)/3} \qquad 7.17$$

Inserting the value of p'_* from Equation 7.16 into Equation 7.17 and solving the integral:

$$(p')_{av} = p - u_w + \frac{a^3(p - u_g)}{R^3 - a^3} \qquad 7.18$$

Equation 7.18 clearly indicates that the average value of the mean effective stress in the matrix is larger than $(p - u_w)$. However, if the volume fraction of bubbles is small, so that R is much greater than a, $(p')_{av}$ is only slightly larger than $(p - u_w)$.

Equations 7.12 and 7.18 can be used to infer the approximate value of the average matrix void ratio e_m for the plastic stress distribution. It seems likely that e_m will be slightly less than the void ratio of a saturated soil consolidated isotropically to an effective stress $(p - u_w)$, because $(p')_{av}$ is slightly greater than $(p - u_w)$ and q_* is non-zero (see Figure 7.5).

There is rather more uncertainty in the prediction of e_m for the plastic stress distribution than is the case for the elastic stress distribution, because the mean effective stress p'_* varies throughout the matrix. Simply using the average value $(p')_{av}$ is not entirely rigorous. The average value of the matrix void ratio e_m cannot be directly related to $(p')_{av}$ for two reasons. Firstly the local void ratio at any point in the matrix varies linearly with the logarithm of p'_* and not linearly with p'_* itself. Secondly, the overall matrix void ratio e_m cannot be calculated by simply averaging the local values of the void ratio throughout the matrix; density can be averaged in this way but not void ratio. This second point is illustrated by Figure 7.6. However, these two factors can be shown to act in opposition to each other, suggesting that the value of e_m calculated on the basis of $(p')_{av}$ is reasonably accurate.

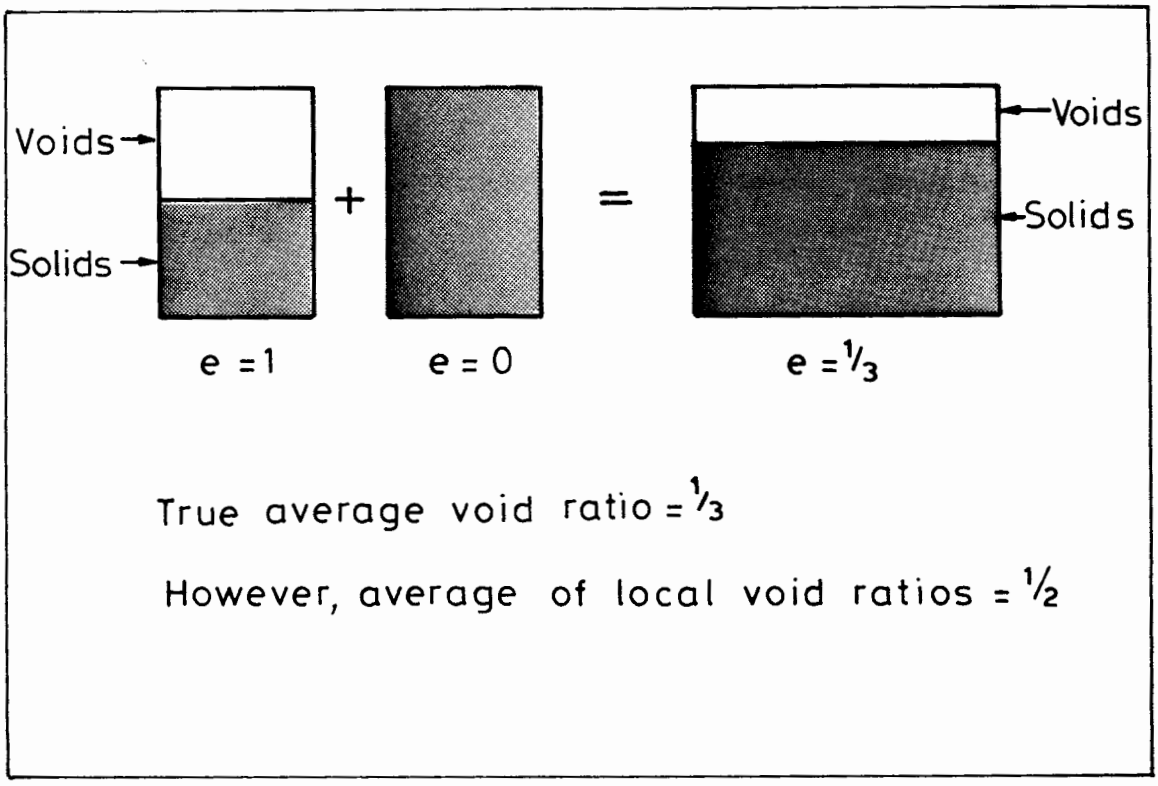

Fig. 7·6. CALCULATING AVERAGE VOID RATIOS

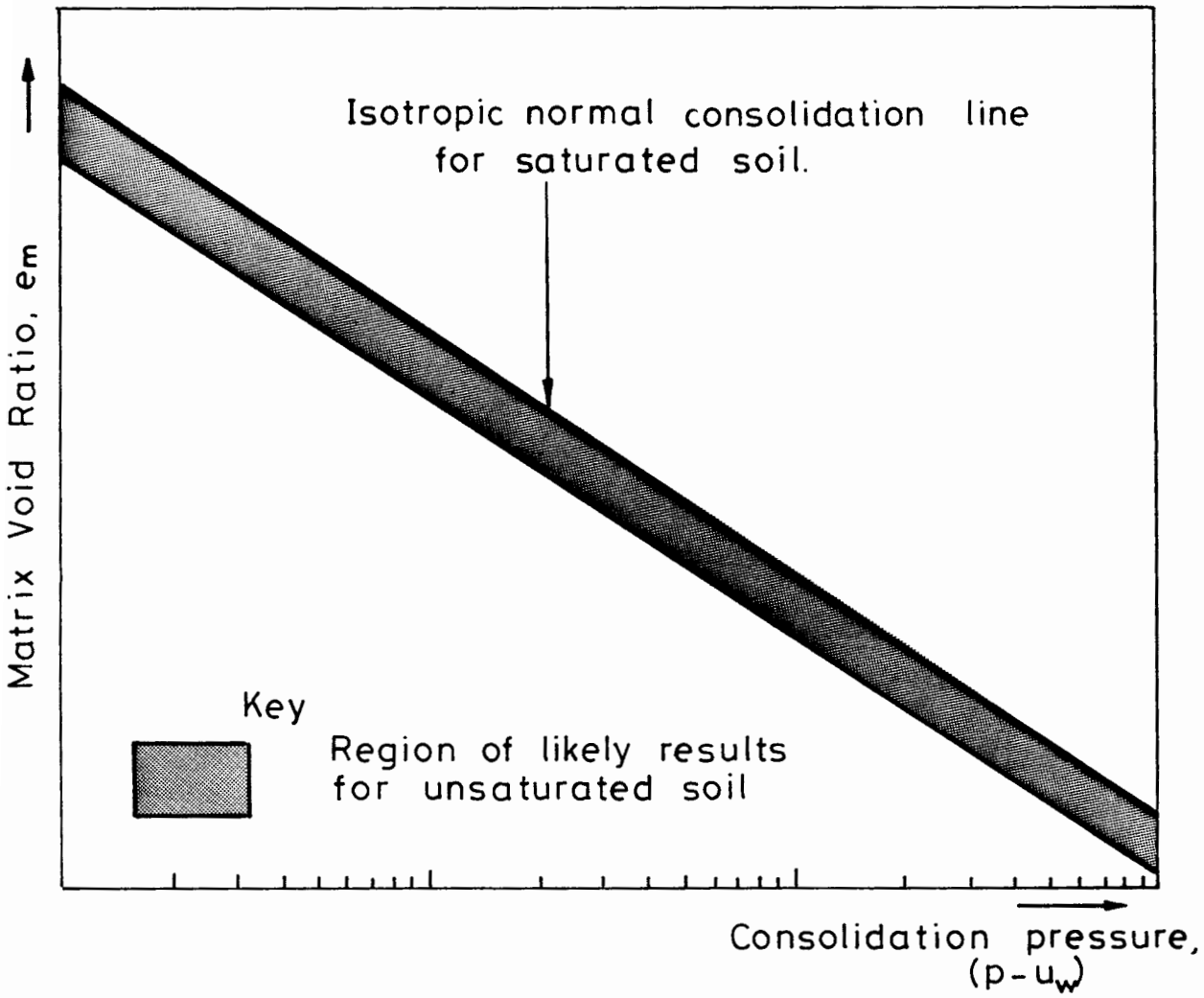

Fig. 7 7. ISOTROPIC CONSOLIDATION OF LARGE BUBBLE MODEL.

7.2.3 Matrix Void Ratio after Isotropic Consolidation

Two different analyses, based on two entirely different stress distributions (elastic and plastic), have both resulted in the same general conclusion on the value of the average matrix void ratio e_m after isotropic consolidation. In practice the true stress distribution is likely to lie somewhere between these two theoretical assumptions, because the saturated soil matrix behaves as an elasto-plastic material. Therefore the actual matrix void ratio is probably very similar to the value suggested by the two analyses i.e. slightly less than the void ratio of a saturated soil consolidated isotropically to an effective stress $(p - u_w)$ (see Figure 7.7).

Although the two theoretical stress distributions (elastic and plastic) both suggest roughly the same average matrix void ratio e_m, they result in very different local variations in the matrix void ratio. The elastic stress distribution produces a region of low void ratio around each bubble (Figure 7.3), while the plastic stress distribution results in areas of high void ratio around the bubbles (Figure 7.5). Therefore it is difficult to draw any firm conclusion on the true nature of the localised variation of the matrix void ratio. In the absence of any better information, it seems sensible to make the simplest possible assumption i.e. the void ratio is constant throughout the matrix. This means that the properties of the matrix will not vary with position. This assumption was made implicitly in the previous chapter (Elastic Moduli) and is made again in the next chapter (Undrained Shear Strength).

7.3 ONE-DIMENSIONAL CONSOLIDATION

One-dimensional consolidation of the large bubble model is rather harder to analyse than isotropic consolidation, because the problem is no longer spherically symmetric. This means that it is much more difficult to devise a range of possible stress distributions within the matrix. However,

by analogy with the isotropic case, if the large bubble model is consolidated one-dimensionally under a vertical stress σ_v and a back pressure u_w, it seems likely that the matrix void ratio e_m will be related to the stress difference $(\sigma_v - u_w)$.

Before extending the analogy between one-dimensional consolidation and isotropic consolidation too far, it is important to consider whether there are any significant differences in the logic involved. For the isotropic case, the analysis suggests that the matrix void ratio e_m is probably slightly less than the void ratio of a saturated soil consolidated to the same stress level. This conclusion is based on two facts. Firstly, the mean effective stress p'_* within the matrix (or at least the average value of p'_*) is greater than or equal to the mean effective stress $(p-u_w)$ within the equivalent saturated soil. Secondly, the magnitude of the deviator stress q_* within the matrix is greater than or equal to the deviator stress in the equivalent saturated soil (which is, of course, zero). However, neither of these two points necessarily apply when the one-dimensional consolidation of the large bubble model is compared with similar consolidation of a saturated soil.

An indication that the first point may not apply to one-dimensional consolidation is given by the elastic analysis presented in the previous chapter. Equation 6.18, which is based on the results of Goodier (1933), indicates that the application of an axially symmetric pure shear stress to the boundary (as occurs in one-dimensional consolidation) results in a decrease of the local mean stress p'_* throughout large sections of the matrix. The equation shows that p'_* is decreased in the regions of the matrix where θ is between zero and 55^o, and increased only in the regions where θ is between 55^o and 90^o (the parameter θ is defined in Figure 6.5). This suggests that the average value of p'_* in the matrix may be less than the value of p' in the equivalent saturated soil (where p' is unaffected by the application

of a pure shear stress). Obviously this conclusion is only tentative, because it is based on an elastic stress distribution, which is unlikely to be the true situation at the end of consolidation.

It is easy to see that the second point may not apply to one-dimensional consolidation, because the deviator stress in a saturated soil is non-zero under one-dimensional loading. This means that the deviator stress q_* within the matrix of the large bubble model may be either higher or lower than the deviator stress in the equivalent saturated soil.

The fact that the two points discussed above do not apply to one-dimensional consolidation means that prediction of the average matrix void ratio e_m is rather more difficult than is the case for isotropic consolidation. The best prediction that can be made is that e_m is similar to the void ratio of a saturated soil consolidated one-dimensionally to a stress $(\sigma_v - u_w)$, but e_m may be either slightly greater or slightly less than the void ratio of the saturated soil (see Figure 7.8).

7.4 GENERAL CONCLUSIONS ON CONSOLIDATION BEHAVIOUR

The analysis presented above suggests that for both isotropic and one-dimensional consolidation the final matrix void ratio e_m is related to the difference between the applied stress (p or σ_v) and the pore water pressure u_w. For isotropic consolidation the suggestion is that e_m is slightly less than the void ratio of a saturated soil consolidated to the same stress level (Figure 7.7). For one-dimensional consolidation e_m may be either slightly greater or slightly less than the void ratio of the equivalent saturated soil (figure 7.8). However, for either isotropic or one-dimensional consolidation, a reasonable first approximation would be to assume a unique relationship between e_m and the relevant stress difference (either $(p - u_w)$ or $(\sigma_v - u_w)$), independent of the volume fraction of bubbles (see Figure 7.9(a)).

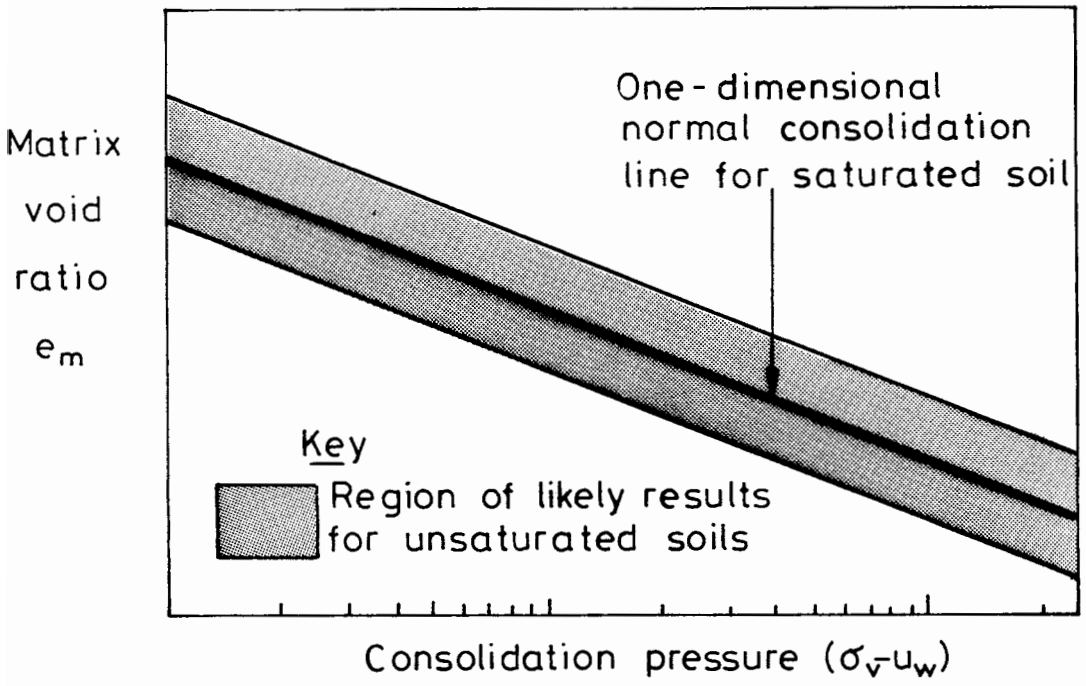

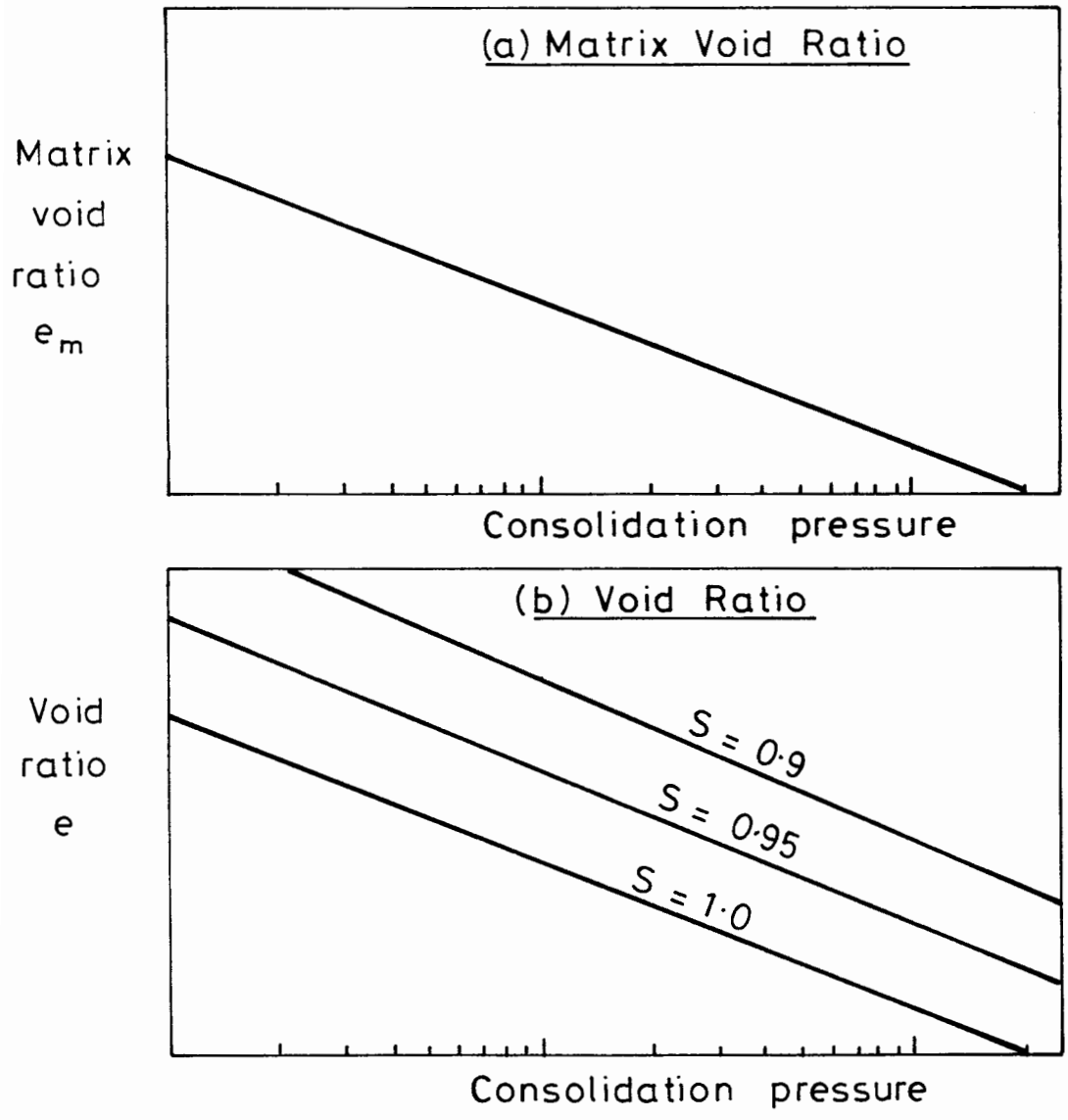

Fig. 7·9. GENERAL CONCLUSIONS ON CONSOLIDATION BEHAVIOUR.

To define completely the state of the large bubble model at the end of consolidation it is necessary to specify the volume fraction of bubbles f, as well as the matrix void ratio e_m. Unfortunately this appears to be impossible without a full analysis of the complex consolidation process, because the final value of f cannot be calculated by studying simply the conditions at the end of consolidation.

As the value of f at the end of consolidation cannot be specified, there is no way of predicting the final values of the saturation S and the overall void ratio e. However, it is possible to predict the form of the results. A unique relationship between e_m and either $(p - u_w)$ or $(\sigma_v - u_w)$ means that the overall void ratio e at the end of consolidation is dependent on the final degree of saturation. The lower the degree of saturation, the greater is the value of the void ratio e (see Figure 7.9(b)).

CHAPTER 8

THEORETICAL ANALYSIS : UNDRAINED SHEAR STRENGTH

CHAPTER 8

THEORETICAL ANALYSIS : UNDRAINED SHEAR STRENGTH

This chapter covers the undrained shear strength of the large bubble model. The analysis presented in the chapter is particularly relevant to the experimental work described in Chapters 3 and 4, because the primary objective of the experimental programme was to study the effect of gas bubbles on the undrained shear strength.

To analyse the shear strength of the model, an assumption has to be made on the state of the matrix at the start of shearing. On the basis of the previous chapter, it seems reasonable to assume that the matrix is homogeneous when shearing begins, and the matrix void ratio e_{mo} is dependent solely on the consolidation pressure $(\sigma_3 - u_{wo})$.

The undrained shear strength of the large bubble model is time-dependent, in the same way that the elastic behaviour under undrained conditions is time-dependent. If the soil is sheared extremely fast there is no time for either localised consolidation or the movement of gas into solution. However, in the experimental tests described in Chapters 3 and 4 the soil was sheared in a period of 10 to 12 hours : ample time for both localised consolidation and the movement of gas into solution. Therefore, the most relevant theoretical development would be an analysis of the long-term undrained shear strength.

For a real geotechnical problem on the seabed it is rather hard to predict the rate of shearing. It seems likely that the shearing process would be slow enough to allow localised consolidation (which takes only a few seconds), but perhaps not slow enough for the movement of gas into solution (which takes minutes or hours). However, an expression for the long-term undrained shear strength can be modified to allow for incomplete solution of gas by simply reducing the value of the solubility coefficient H.

8.1 METHOD OF ANALYSIS

A completely rigorous analysis of the long-term undrained shear strength of the large bubble model would be very hard to achieve. Difficulties arise from the localised consolidation which occurs during the shearing process because of the stress concentrations caused by the presence of the gas bubbles. The localised consolidation results in variations of the void ratio throughout the matrix. This means that the strength and stress-strain properties of the matrix are no longer homogeneous. Strictly, the local changes in matrix strength should be linked to the corresponding changes in local void ratio. This could be done by using some sort of critical state model for the matrix (Schofield and Wroth, 1968). However this would be very complicated, and would require a numerical technique, such as the finite element method. If an analytical approach is to succeed, the problem must be simplified.

To calculate the ultimate load under undrained conditions, it is probably acceptable to model the matrix as a rigid - perfectly plastic material with a yield stress σ_y in uniaxial tension or compression. The yield stress σ_y is twice the undrained shear strength of saturated soil at the matrix void ratio e_m. Therefore, at the start of shearing, when the matrix void ratio is e_{mo}, the matrix yield stress σ_y is given by $2(C_u)_{sat}$, where $(C_u)_{sat}$ is the undrained shear strength of a saturated soil consolidated to the same stress level.

The approximation of the matrix as a simple rigid-perfectly plastic material means that the effects of localised consolidation are ignored. Some of the consequences of this approximation are discussed later in Section 8.5.3.

Various authors working in the fields of solid mechanics or metallurgy have analysed the problem of the strength of a rigid-perfectly plastic material containing cavities. Some of these authors were interested in the practical application of this work to the phenomenon of ductile

fracture of metals, where cavities form within the material prior to failure. Other authors were concerned with the strength of sintered metals, where components are formed by the compression of metal powder such that the resulting material contains small voids and cavities. The work of many of these authors is directly relevant to the analysis of the large bubble model.

8.2 YIELD STRESS

The first part of the analysis concerns the value q_y of the applied deviator stress at which the entire material yields. This occurs when a plastic collapse mechanism is formed within the matrix. Although particular sections of the matrix may yield at lower values of q (because of the stress concentrations around the bubble cavities), the entire material will not yield until sufficient material has reached a plastic state to form a mechanism. This is a consequence of the fact that the matrix is assumed to be rigid when the local deviator stress is below σ_y. Prior to the formation of a mechanism, the yielded areas of the matrix are unable to deform because of the restraint provided by the neighbouring areas which are still unyielded and therefore rigid.

The yield stress q_y may not be the same as the final deviator stress at failure q_f. Although the matrix is assumed to be perfectly plastic after yield, the entire material may show significant work-hardening because of the compression of the gas bubbles which occurs when the material starts to deform. Further complications arise from the possibility of bubbles flooding during shearing (see Section 5.6, Chapter 5). The post-yield behaviour and the effects of bubble flooding are considered in subsequent sections.

8.2.1 Early Theoretical Studies

Haynes (1971) was one of the first authors to analyse the strength of a material containing cavities. As he did not consider the work-hardening effect produced by the shrinkage of the cavities after the formation of a collapse mechanism, his work is strictly relevant to the yield stress q_y, and not the failure stress q_f.

Haynes showed that an upper bound to the yield stress of a rigid-perfectly plastic material containing cavities is given by the "rule of mixtures", where the total load is uniformly spread throughout the reduced volume of matrix material:

$$q_y = \sigma_y(1 - f) \qquad 8.1$$

This expression ignores the stress-concentrating effect of the cavities. Various other authors, including Kahlow and Avitzur (1974), confirmed Equation 8.1 as an upper bound expression.

Haynes (1971) also noted that a lower bound to the overall yield stress q_y is given by the stress at which local yield first occurs in the matrix. This can be calculated from a purely elastic analysis (see Chapter 6). However, Haynes recognised that the lower bound given by the elastic approach and the upper bound given by Equation 8.1 would often be very far apart.

8.2.2 The Work of Green (1972)

Green (1972) presented a detailed analysis of the yield behaviour of a rigid-perfectly plastic von Mises type matrix containing empty spherical cavities. He assumed that a criterion for overall yield could be expressed as a function of the volume fraction of cavities f and the three stress invariants I_1, I_2 and I_3 (see Wroth and Houlsby (1985) for the definition of the stress invariants). Green proposed that any dependence on the third stress invariant could be ignored, so that yield was simply a function of

the first two stress invariants and the volume fraction of cavities. Expressing this proposition in terms of parameters more widely recognised in soil mechanics:

$$\text{function } (q^2, p, f) = \sigma_y^2 \qquad 8.2$$

Green (1972) suggested that the coupling between q and p could be ignored, and he proposed an elliptical yield curve:

$$\alpha q^2 + \beta p^2 = \sigma_y^2 \qquad 8.3$$

α and β are functions of f, such that:

$$\alpha \geq 1 \ , \quad \beta \geq 0 \qquad 8.4$$

Equation 8.3 represents a spheroidal yield surface in principal stress space. The most significant difference between this equation and a conventional yield criterion for a material without cavities is the dependence on the mean stress p, which means that yield can occur under a purely isotropic stress state. When $\alpha = 1$ and $\beta = 0$, Equation 8.3 reduces to von Mises' yield criterion.

Green derived an expression for α by considering the case of yield under an axisymmetric pure shear stress. For this part of the analysis he made the simplifying assumption that the cavities were arranged in a cubic close-packed formation, allowing him to consider only the plane of minimum section cutting through cavities at their equator. Green assumed that throughout the plane of minimum section the matrix material was in a state of plastic flow, and applied the conditions of equilibrium, compatibility and the flow rule of von Mises to this section. However, to do this he assumed a uniform strain rate on the minimum section, and he also chose an arbitrary function for the variation of the principal stress direction at the minimum section. This part of Green's paper is very similar to the classic work of Bridgman (1944) on the stress distribution at the neck of a tension specimen. Green's analysis suggests the following expression for the parameter α:

$$\alpha = \left(\frac{3 - 2f^{\frac{1}{4}}}{3(1 - f^{1/3})}\right)^2 \qquad 8.5$$

Green derived an expression for β by considering yield under a hydrostatic pressure. He analysed a thick spherical shell of matrix material containing a single cavity. The shell thickness was chosen so that the proportion of the shell volume taken up by the cavity was equal to the volume fraction of cavities f for the entire material (see Equation 7.8, Chapter 7). The problem was very easy to analyse, because of the spherical symmetry. Applying the equation of equilibrium and the yield criterion of von Mises to the matrix material, Green arrived at the following expression for β:

$$\beta = \left(\frac{3}{2\log_e f}\right)^2 \qquad 8.6$$

The complete yield criterion proposed by Green is given by substituting the expressions for α and β, from Equations 8.5 and 8.6, into Equation 8.3:

$$\left(\frac{3 - 2f^{\frac{1}{4}}}{3(1 - f^{1/3})}\right)^2 q^2 + \left(\frac{3}{2\log_e f}\right)^2 p^2 = \sigma_y{}^2 \qquad 8.7$$

The yield curve presented in Equation 8.7 refers to the case of a material containing empty cavities, where each cavity is at zero pressure. However, in the large bubble model for soils the cavities are at an elevated pressure u_g. Under these conditions the mean stress p in Green's analysis must be replaced with the stress difference $(p - u_g)$, as described by Keife and Ståhlberg (1980). The modified expression for the yield curve is:

$$\left(\frac{3 - 2f^{\frac{1}{4}}}{3(1 - f^{1/3})}\right)^2 q^2 + \left(\frac{3}{2\log_e f}\right)^2 (p - u_g)^2 = \sigma_y{}^2 \qquad 8.8$$

Equation 8.8 may be more useful if the mean stress p is expressed in terms of the deviator stress q and the lateral stress σ_3 (which remains constant during a conventional triaxial test):

$$p = \sigma_3 + q/3 \qquad 8.9$$

This results in the following quadratic equation for the deviator stress at yield q_y:

$$\left[\frac{3 - 2\,f^{\frac{1}{4}}}{3(1 - f^{1/3})}\right]^2 q_y^{\,2} + \left[\frac{3}{2\log_e f}\right]^2 (\sigma_3 - u_g + q_y/3)^2 = \sigma_y^{\,2} \qquad 8.10$$

Figure 8.1 illustrates how Green's prediction of the yield stress q_y varies with the volume fraction of bubbles f. The values of q_y calculated from Equation 8.10 have been normalised by dividing by the yield stress of the matrix material σ_y, and the curves are shown for two different values of the parameter $(\sigma_3 - u_g)/\sigma_y$. The figure clearly indicates that the presence of the bubble cavities causes a reduction in the yield stress, and the effect becomes increasingly detrimental as $(\sigma_3 - u_g)/\sigma_y$ is increased. For each value of $(\sigma_3 - u_g)/\sigma_y$ the yield stress q_y falls to zero at a critical volume fraction of bubbles f_c (f_c = 0.05 for the bottom curve and 0.22 for the top curve). At this critical volume fraction of bubbles the hydrostatic stress $(\sigma_3 - u_g)$ is sufficient to cause yield without the application of any deviator stress.

Hayne's upper bound expression for q_y given by Equation 8.1 is shown in Figure 8.1, for comparison with Green's predictions.

8.2.3 The Work of Gurson (1977)

Gurson (1977) was another author who considered axisymmetric loading of a rigid-perfectly plastic von Mises type matrix containing empty spherical cavities. Gurson used the upper bound approach of plasticity theory, employing only the compatibility of strains and the material properties of the matrix (Calladine, 1969). This contrasted with the approach of Green (1972), which involved an "exact" method using the equilibrium of stresses as well as compatibility and material properties. In practice the expressions derived by both Gurson and Green are simply approximate solutions, because of the various simplifications employed by the two authors. Gurson's main

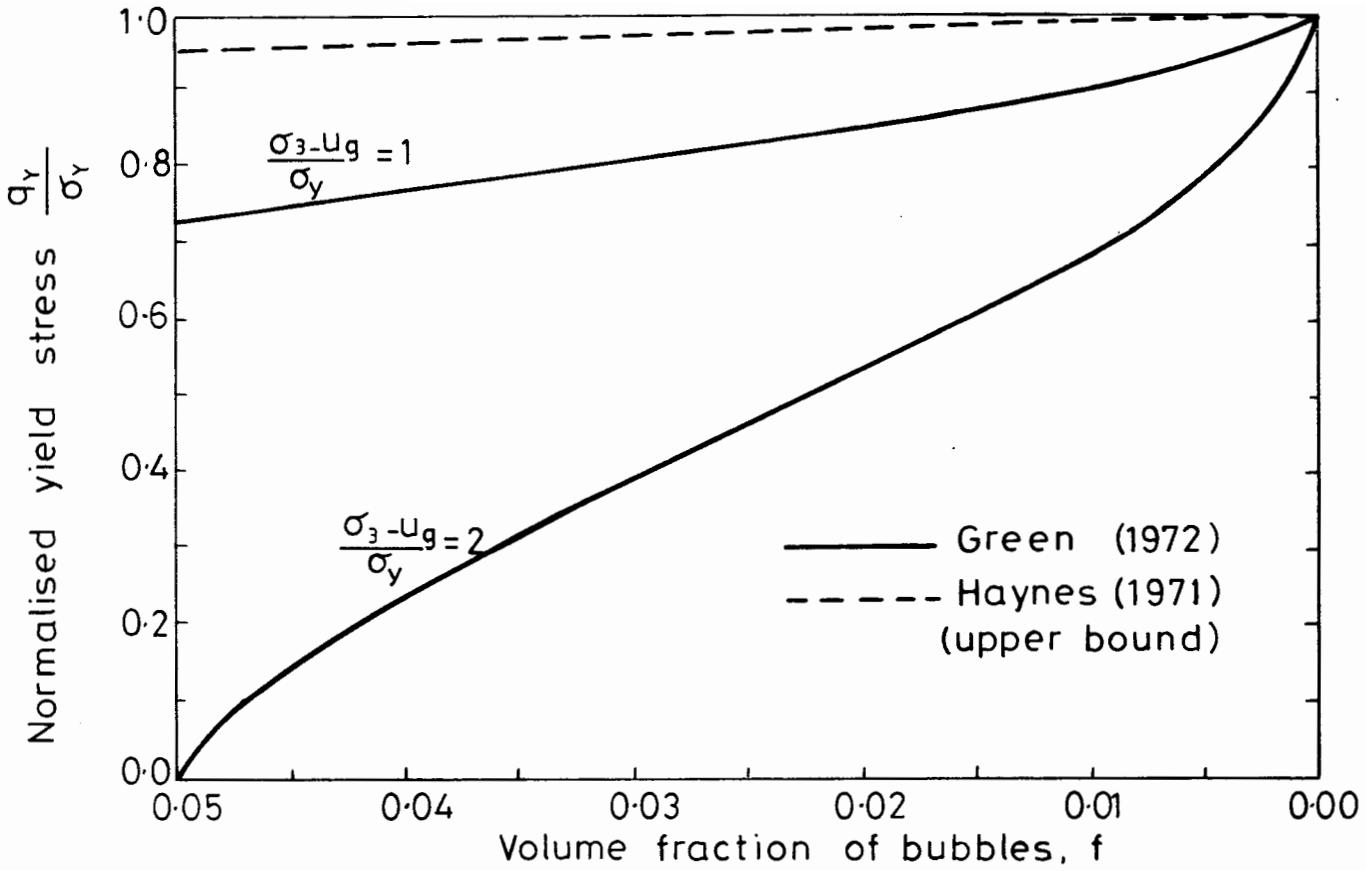

Fig. 8·1. GREEN'S PREDICTIONS OF YIELD STRESS.

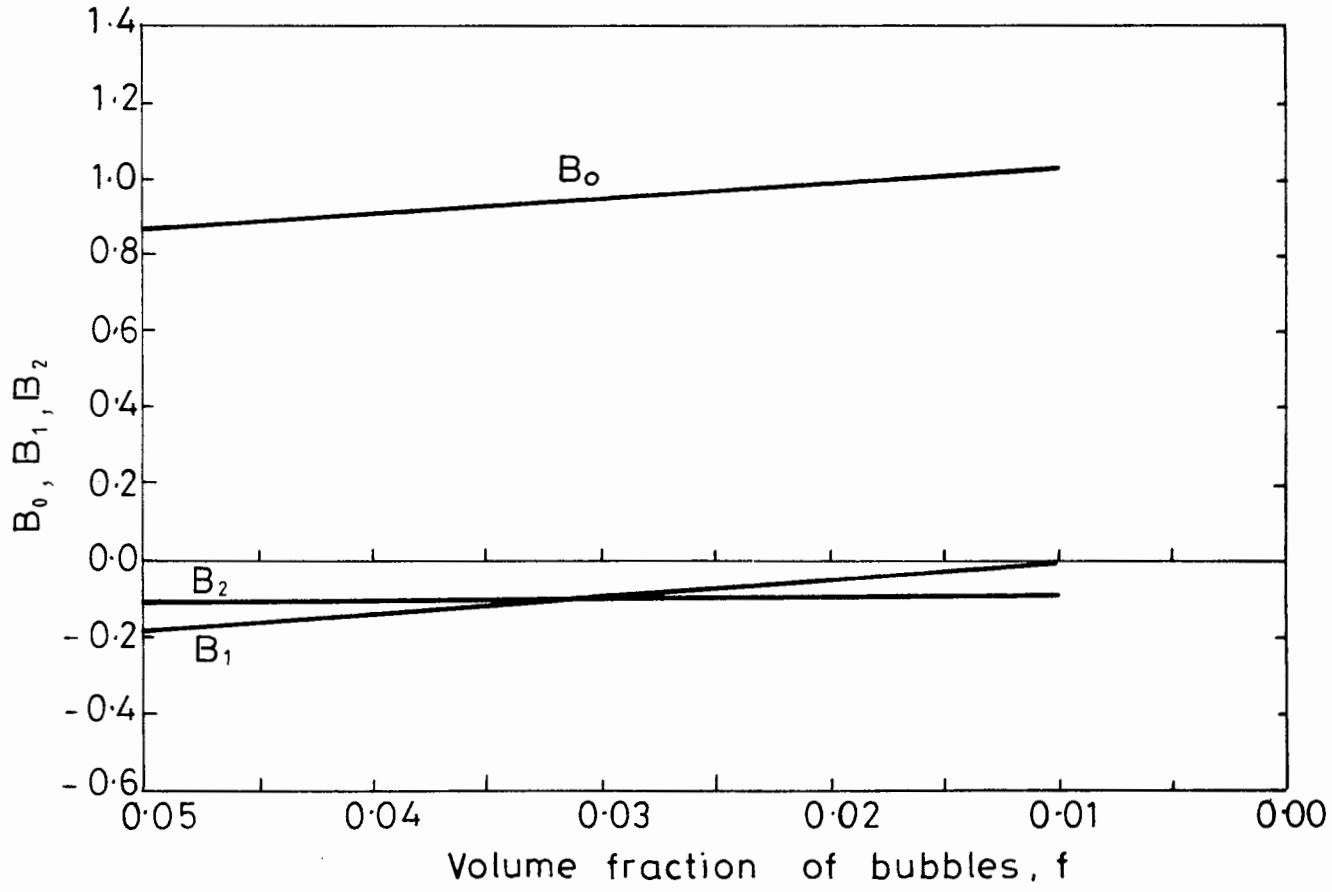

Fig. 8·2. GURSON'S CONSTANTS.

simplification was to consider only a single cavity surrounded by a spherical shell of matrix material. The shell thickness was chosen so that the proportion of the shell volume taken up by the cavity was equal to the overall volume fraction of cavities f (see Equation 7.8, Chapter 7).

Gurson (1977) selected an approximate form for the velocity field in the matrix, on the assumption that the entire matrix was in a plastic state. The velocity field, which obeyed compatibility and incompressibility, was in two parts: one associated with a change of shape of the cavity at constant cavity volume, the other associated with volume change but no change in shape. Combining this velocity field with the von Mises yield criterion for the matrix material, Gurson arrived at the following expression for the shape of the yield curve:

$$\left(\frac{q}{\sigma_y}\right)^2 + 2f\cosh\left(\frac{3p}{2\sigma_y}\right) - 1 - f^2 = 0 \qquad 8.11$$

Gurson also considered an alternative velocity field with parts of the matrix remaining rigid. The rigid sections were conical in shape, with axes coincident with the axes of symmetry of the external loading. Gurson tried this approach after studying the results of some finite element calculations (Needleman, 1972; Haward and Owen, 1973) and slip line calculations (Nagpal, McClintock, Berg and Subudhi, 1972), which all suggested that parts of the matrix remained unyielded under certain conditions. Gurson's analysis of this problem of a velocity field with a rigid section did not lead to a closed form solution. However, he fitted the results to the following expression:

$$\left(\frac{q}{\sigma_y}\right)^2 - B_o - B_1\left(\frac{p}{\sigma_y}\right) - B_2\left(\frac{p}{\sigma_y}\right)^2 = 0 \qquad 8.12$$

B_o, B_1 and B_2 are functions of f, as shown in Figure 8.2.

Like Green, Gurson considered only the case of empty cavities. To extend his results to the general case of cavities at a pressure u_g, the

mean stress p in Equations 8.11 and 8.12 must be replaced with the stress difference $(p - u_g)$. The mean stress p can then be expressed in terms of σ_3 and q (Equation 8.9), to give two alternative expressions for the yield stress q_y:

$$\left(\frac{q_y}{\sigma_y}\right)^2 + 2f\cosh\left[\frac{3(\sigma_3 - u_g) + q_y}{2\sigma_y}\right] - 1 - f^2 = 0 \qquad 8.13$$

$$\left(\frac{q_y}{\sigma_y}\right)^2 - B_o - B_1\left[\frac{\sigma_3 - u_g - q_y/3}{\sigma_y}\right] - B_2\left[\frac{\sigma_3 - u_g - q_y/3}{\sigma_y}\right]^2 = 0 \qquad 8.14$$

Figure 8.3 shows Gurson's predictions of q_y plotted against f for two different values of the parameter $(\sigma_3 - u_g)/\sigma_y$. Under many circumstances the velocity field with a rigid section (Equation 8.14) is an improvement over the fully plastic velocity field (Equation 8.13) i.e. it leads to a lower solution.

Hayne's original upper bound expression for q_y (Equation 8.1) is included in Figure 8.3 for comparison with Gurson's predictions.

Figure 8.4 shows the values of q_y predicted by both Green (1972) and Gurson (1977). The sharp discontinuity of slope in one of Gurson's curves corresponds to the point at which Equation 8.13 replaces Equation 8.14 as the preferred solution. The agreement between the results of the two authors is excellent.

8.2.4 General Conclusions on the Yield Behaviour

The results of Green and Gurson are consistent with those of other authors such as McClintock (1968), Needleman (1972), Kahlow and Avitzur (1974) and Keife and Ståhlberg (1980). All these authors analysed the behaviour of a rigid-perfectly plastic matrix containing cavities, but they considered cylindrical or cubic cavities rather than the spherical cavities considered by Green and Gurson. Experimental work on metals containing

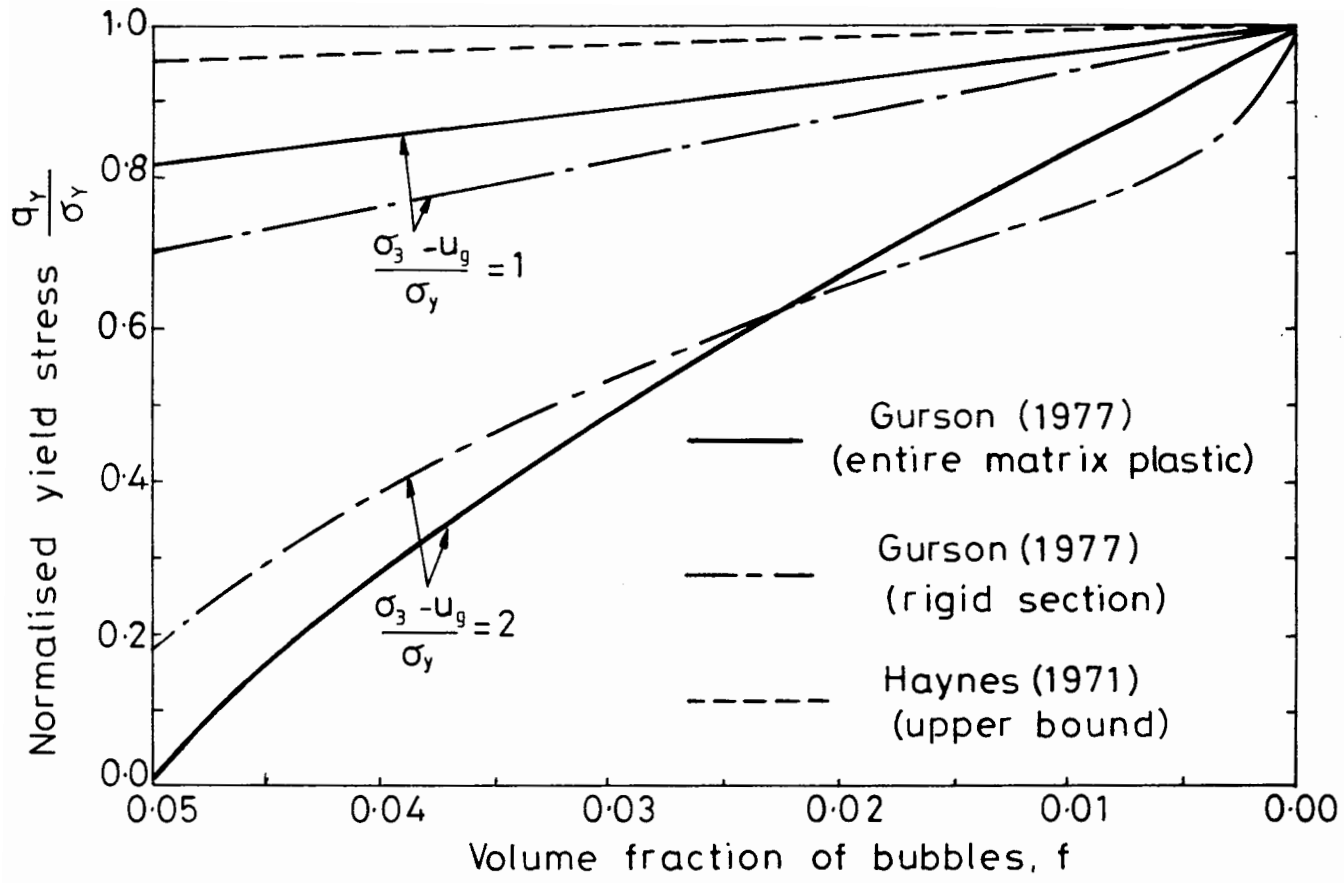

Fig. 8·3. GURSON'S PREDICTIONS OF YIELD STRESS.

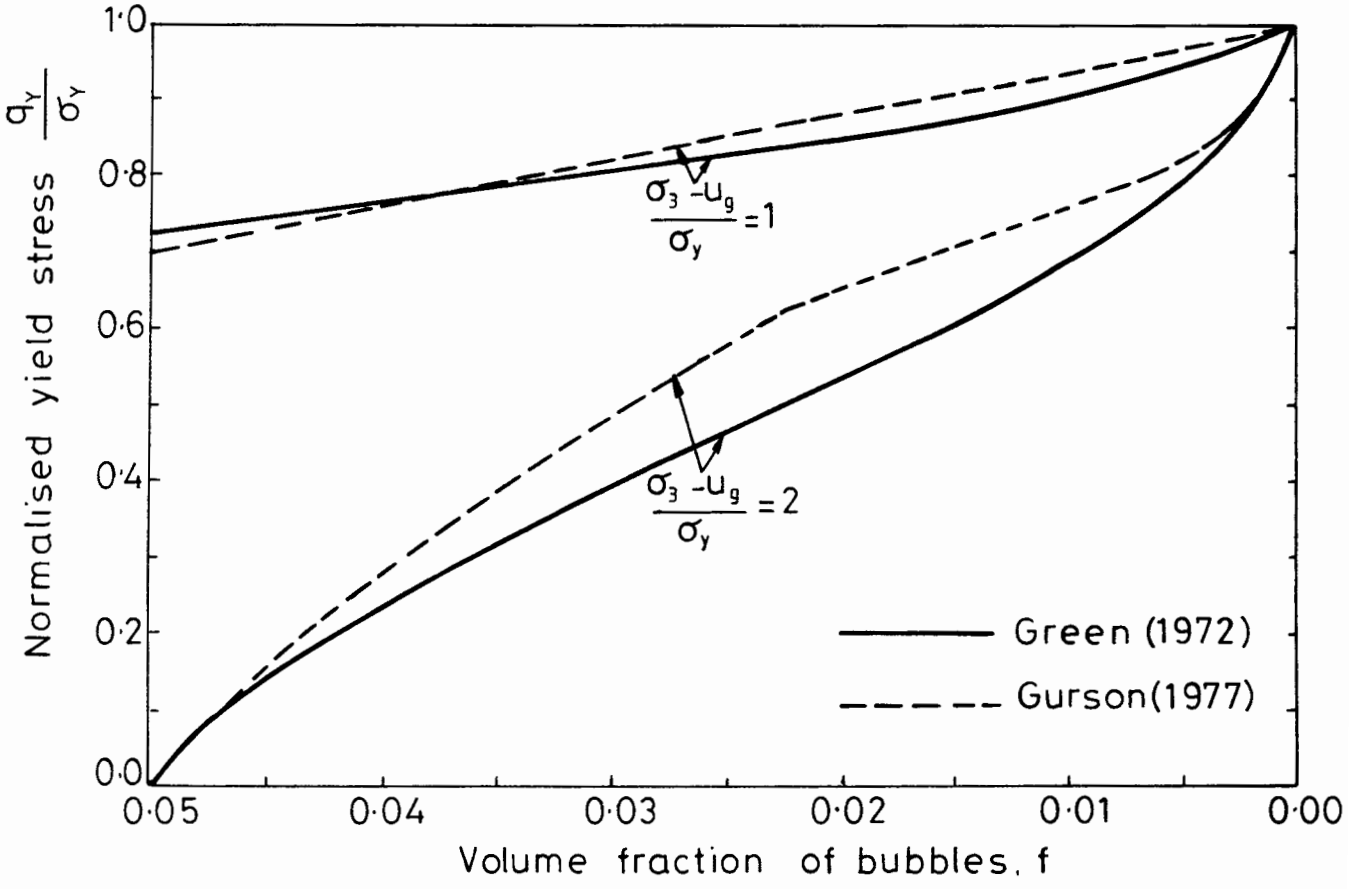

Fig. 8·4. THEORETICAL PREDICTIONS OF YIELD STRESS.

cavities has also tended to confirm the analytical predictions of Green and Gurson. This experimental work includes tests on sintered metals (Kuhn and Downey, 1971; Shima and Oyane, 1976) and tests on metals containing large artificially introduced cavities (Kahlow and Avitzur, 1974).

Before proceeding further with the analysis of the large bubble model, it is helpful if a single preferred expression for the normalised yield stress q_y/σ_y can be selected. There is little to choose between the expressions of Green and Gurson (see Figure 8.4), but Green's yield curve is considered slightly preferable, because it avoids the sharp discontinuity of slope in Gurson's curve. The elliptical shape of Green's yield curve is also in agreement with the experimental curves for sintered metals (Kuhn and Downey, 1971; Shima and Oyane, 1976).

As the material is rigid at stresses below q_y, the values of f and u_g at yield are unchanged from the initial values f_o and u_{go}. Therefore, Green's expression for the normalised yield stress q_y/σ_y (Equation 8.10) becomes:

$$\left\{\frac{3 - 2f_o^{\frac{1}{4}}}{3(1 - f_o^{1/3})}\right\}^2 \left(\frac{q_y}{\sigma_y}\right)^2 + \left\{\frac{3}{2\log_e f_o}\right\}^2 \left\{\frac{\sigma_3 - u_{go}}{\sigma_y} + \frac{1}{3}\left(\frac{q_y}{\sigma_y}\right)\right\}^2 = 1 \qquad 8.15$$

8.3 POST-YIELD BEHAVIOUR

The post-yield behaviour of a rigid-perfectly plastic matrix containing cavities is rather complicated, because the cavities can change in size (either shrinking or growing) once the material starts to deform. This affects the value of the stress required to cause further deformation, because the geometry of the collapse mechanism alters (Calladine, 1969). If the cavities shrink the value of f falls, and the weakening effect of the cavities is reduced. This leads to an increase in the stress required to cause further deformation, producing a work-hardening effect. Conversely, if the cavities increase in size there is a work-softening effect, as the

stress required to cause further deformation falls because of the increasing value of f. Thus, the entire material shows either a work-hardening or a work-softening type of behaviour, despite the fact that the matrix itself is assumed to be perfectly plastic after yield.

8.3.1 Materials Containing Empty Cavities

By assuming normality of the strain increment vector to the yield curve, Green (1972) showed that empty cavities would shrink if the mean stress p were positive, and grow if p were negative.

Green (1972) assumed that the cavities remained approximately spherical during the post-yield behaviour, so that the shape of the yield curve was still given by Equation 8.7. By combining the normality condition with the shape of the yield curve, he derived an expression relating the change in axial strain ε_1 to the change in the volume fraction of cavities f:

$$-\frac{d\varepsilon_1}{df} = \frac{3\alpha q + \beta p}{3(1-f)\beta p} \qquad 8.16$$

α and β are functions of f, given in Equations 8.5 and 8.6.

Green produced stress-strain curves for materials containing cavities, by using Equation 8.16 (the flow rule) and Equation 8.7 (the yield curve). The procedure that he used was to allow for a small change δf in the volume fraction of cavities, and on the basis of this he calculated the value of q corresponding to the new value of f (from the yield curve). Knowing values of f and q at the beginning and end of the small change δf he was able to calculate average values for the current strain increment. The average values of f and q were used to calculate average values of α, β and p; and then all these values were inserted into the flow rule (Equation 8.16), together with the size of the increment δf, to arrive at a value for the strain increment $\delta\varepsilon_1$. By repeating this procedure over many strain increments, Green produced a stress-strain curve relating the deviator stress q and the axial strain ε_1.

Green derived stress-strain curves for samples tested in uniaxial compression and uniaxial tension. The material exhibited a work-hardening response in the compression tests, because the cavities shrank under the influence of the positive mean stress p. At very high strain the deviator stress q approached the yield stress of the matrix σ_y, as the value of f tended towards zero. In contrast, the tensile tests showed a work-softening type of behaviour, because the negative value of p resulted in expansion of the cavities.

8.3.2 Materials Containing Gas-Filled Cavities

If the cavities are filled with gas at a pressure u_g, the mean stress p in Green's analysis must be replaced with the stress difference $(p - u_g)$. This means that the bubbles shrink if $(p - u_g)$ is positive, and grow if $(p - u_g)$ is negative. In the triaxial compression tests described in Chapters 3 and 4 $(p - u_g)$ was probably positive, suggesting shrinkage of the bubbles and a work-hardening type of behaviour.

Green's expression relating the axial strain increment to the change of f (Equation 8.16) must be modified by replacing the mean stress p with the pressure difference $(p-u_g)$. Also, p can be expressed in terms of σ_3 and q (Equation 8.9), so that Equation 8.16 is modified to:

$$-\frac{d\varepsilon_1}{df} = \frac{3\alpha q + \beta(\sigma_3 - u_g + q/3)}{3(1 - f)\beta(\sigma_3 - u_g + q/3)} \qquad 8.17$$

Equation 8.17 can be combined with Equation 8.10 (the yield curve) to produce stress-strain curves for the large bubble model. However, the problem is more complicated than Green's analysis of a material containing empty cavities, because the gas pressure u_g will change during straining, as the bubbles change in size. This change in u_g affects the value of the stress difference $(\sigma_3 - u_g)$ in both the yield curve (Equation 8.10) and the flow rule (Equation 8.17).

At any point in the straining process the value of $(\sigma_3 - u_g)$ can be expressed in terms of the initial value $(\sigma_3 - u_{go})$ and the initial and current values of the absolute gas pressure $(u_g + p_a)$:

$$\sigma_3 - u_g = (\sigma_3 - u_{go}) + (u_{go} + p_a) - (u_g + p_a) \qquad 8.18$$

The current value of $(u_g + p_a)$ can be calculated by considering the compression of the gas. A volume of soil containing unit volume of matrix contains a volume $f/(1 - f)$ of gas, and a volume $e_m/(1 + e_m)$ of water. The volume of water remains unchanged during undrained behaviour, but the volume of gas may change. Applying Boyle's Law and Henry's Law:

$$(u_g + p_a)\left(\frac{f}{1 - f} + \frac{He_{mo}}{1 + e_{mo}}\right) = (u_{go} + p_a)\left(\frac{f_o}{1 - f_o} + \frac{He_{mo}}{1 + e_{mo}}\right) \qquad 8.19$$

Inserting the value of $(u_g + p_a)$ from Equation 8.19 into Equation 8.18, and combining the terms in $(u_{go} + p_a)$:

$$\sigma_3 - u_g = (\sigma_3 - u_{go}) - (u_{go} + p_a)\left(\frac{f_o/(1 - f_o) - f/(1 - f)}{f/(1 - f) + He_{mo}/(1 + e_{mo})}\right) \qquad 8.20$$

Equation 8.20 can be combined with Equations 8.17 and 8.10 to produce a stress-strain curve. The procedure is as follows. The volume fraction of bubbles f is assumed to change by a small amount δf. The new value of f is inserted into Equation 8.20, to give a new value for the stress difference $(\sigma_3 - u_g)$. The new values of f and $(\sigma_3 - u_g)$ are then inserted into the yield curve (Equation 8.10), to produce a new value for the deviator stress q. Knowing values of f, $(\sigma_3 - u_g)$ and q at the beginning and end of the small change δf, average values can be calculated for the current strain increment. These average values of f, $(\sigma_3 - u_g)$ and q are inserted into Equation 8.17, together with the size of the increment δf, to produce a value for the strain increment $\delta\varepsilon_1$.

Figure 8.5 shows some typical stress-strain curves, for a material with an initial bubble fraction f_o of 0.05. Curves are included for a single value of the normalised initial stress difference $(\sigma_3 - u_{go})/\sigma_y$ and two values of the normalised initial gas pressure $(u_{go} + p_a)/\sigma_y$. The figure clearly illustrates the work-hardening effect, as the straining of the material produces shrinking of the bubbles and a consequent reduction in the value of f. This reduction in the volume fraction of bubbles is indicated by the values of f marked on both curves.

Figure 8.5 shows that work-hardening occurs most rapidly when the parameter $(u_{go} + p_a)/\sigma_y$ is high. Increasing the initial gas pressure actually has two counteracting effects, both of which are illustrated in Figure 8.5. Firstly, the increased stiffness of the gas bubbles means that a greater axial strain is required to produce a given reduction in f. Secondly, the deviator stress corresponding to a given value of f is increased, because the stress difference $(\sigma_3 - u_g)$, which falls during shearing and so increases the deviator stress, drops most dramatically when the bubbles are very stiff. The second effect always predominates, so that the stiffness of the gas bubbles enhances the work-hardening effect.

Figure 8.6 shows the influence of solubility on the post-yield behaviour. The movement of gas into solution reduces the apparent stiffness of the gas bubbles, so that the work-hardening effect is reduced. Equation 8.20 indicates that the effect of solubility on the work-hardening is actually controlled by the value of the parameter $He_{mo}/(1 + e_{mo})$.

8.3.3 Deviator Stress at Failure

The effect of work-hardening is to bring the deviator stress q up towards the yield stress of the matrix σ_y. As the true axial strain tends towards infinity (a nominal compressive strain of 100%) the volume fraction of bubbles approaches zero, and q tends towards σ_y. However, in practice

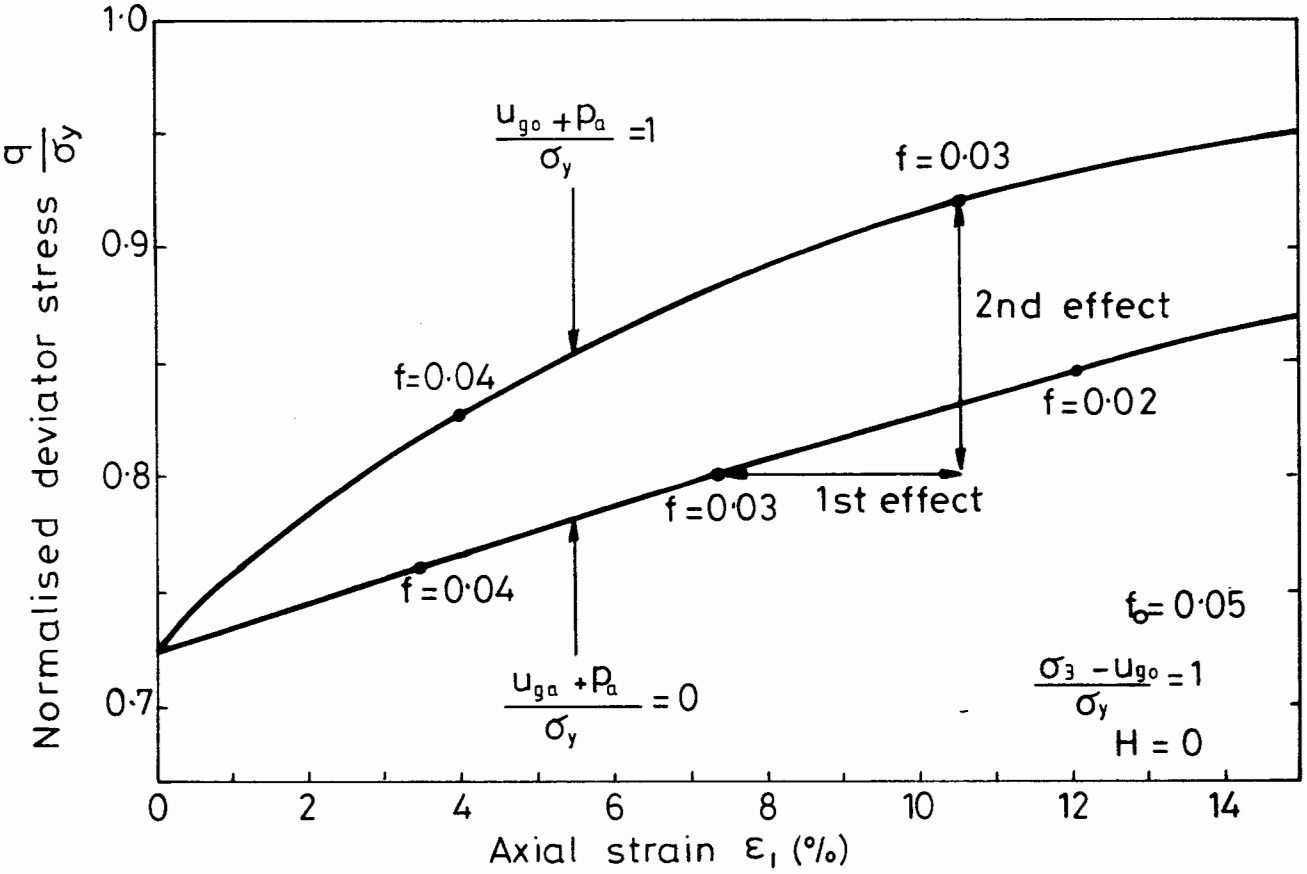

Fig. 8·5. STRESS-STRAIN CURVES FOR MATERIALS CONTAINING CAVITIES.

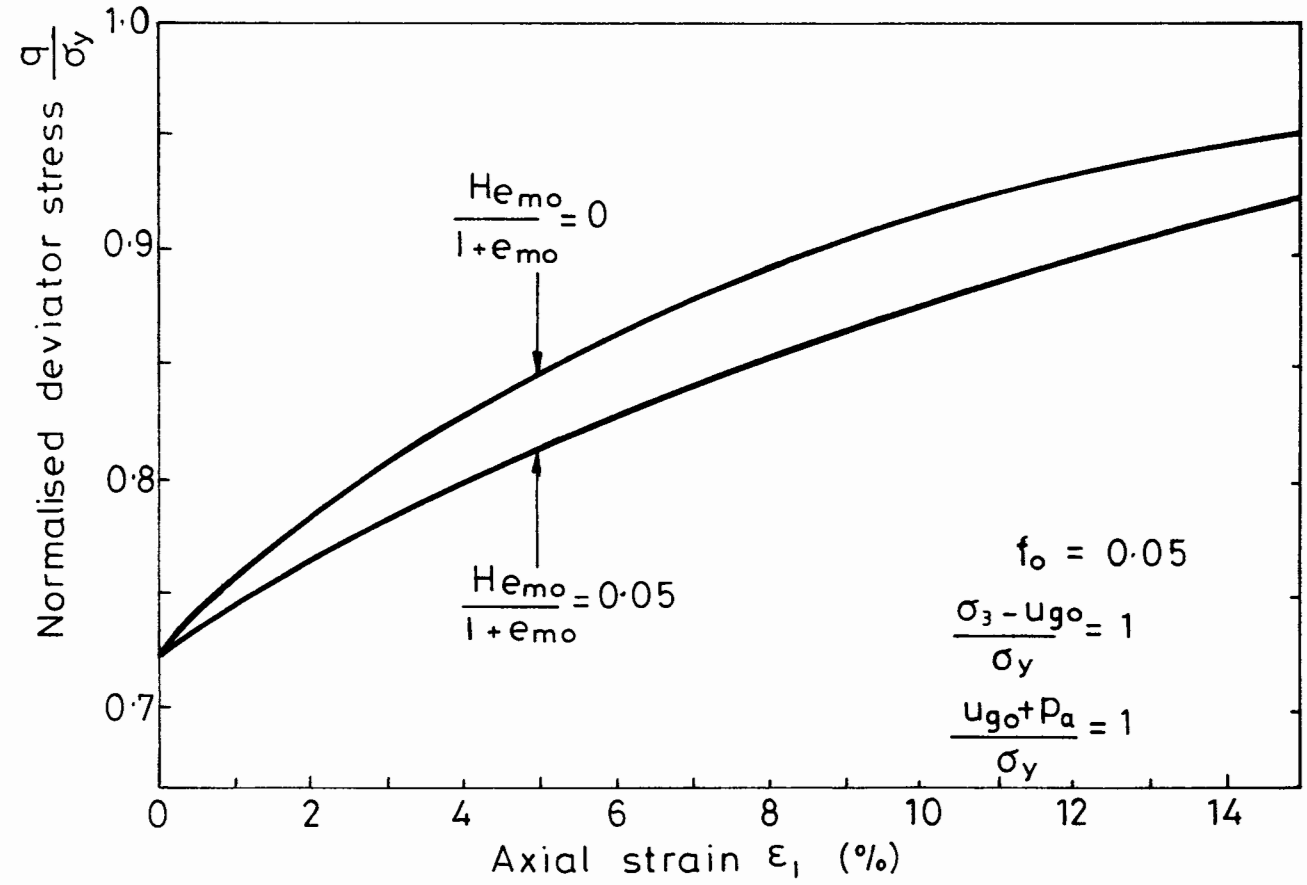

Fig. 8·6. INFLUENCE OF SOLUBILITY ON THE STRESS-STRAIN CURVES.

the strength of the saturated soil matrix probably starts to fall at some finite strain, so that the deviator stress q never reaches the ultimate value σ_y. Bearing this in mind, it seems likely that the value of the deviator stress at failure q_f will be greatest when $(u_{go} + p_a)/\sigma_y$ is high and $He_{mo}/(1 + e_{mo})$ is low, because work-hardening occurs most rapidly under these conditions (see Figures 8.5 and 8.6).

It is difficult to derive an expression for the deviator stress at failure, because q_f is dependent on the behaviour of the matrix at very high strains. However, the relationships governing the post-yield behaviour (Equations 8.10, 8.17 and 8.20) do indicate the parameters that are likely to influence the value of q_f:

$$\left(\frac{q_f}{\sigma_y}\right) = \text{function}\left[f_o, \frac{\sigma_3 - u_{go}}{\sigma_y}, \frac{u_{go} + p_a}{\sigma_y}, \frac{He_{mo}}{1 + e_{mo}}\right] \qquad 8.21$$

Despite the work-hardening effect q_f/σ_y is always less than unity. Figures 8.4 to 8.6 suggest that the value of q_f/σ_y is highest when f_o, $(\sigma_3 - u_{go})/\sigma_y$ and $He_{mo}/(1 + e_{mo})$ are low and $(u_{go} + p_a)/\sigma_y$ is high.

8.4 BUBBLE FLOODING

During undrained shear of a normally consolidated soil the pore water pressure u_w normally increases dramatically. In contrast, the gas pressure u_g increases only slightly, because the gas is highly compressible (in the extreme case of a material containing empty cavities, the cavity pressure must remain absolutely constant at zero). This means that the pressure difference $(u_g - u_w)$ probably becomes negative during shearing. If $(u_g - u_w)$ reaches the limiting condition described in Section 5.6 of Chapter 5 bubble flooding will occur. The flooding of bubble cavities during shearing will obviously affect the value of the deviator stress at failure q_f.

8.4.1 The Process of Bubble Flooding

Flooding of the first bubble cavity occurs when the stress difference $(u_g - u_w)$ reaches the lower limit given in Equation 5.14, Chapter 5:

$$(u_g - u_w) = - \frac{2T}{R_c} \qquad 8.22$$

The minimum radius of curvature of the menisci R_c will be a function of the soil type (the size, grading and shape of the particles) and the matrix void ratio e_m (which determines the packing of the particles).

If the matrix is modelled as a rigid-perfectly plastic material with a yield stress σ_y, dimensional analysis would suggest that the flooding of the first bubble would be dependent on the value of the normalised parameter $2T/R_c\sigma_y$. The lower the value of this parameter, the more likely flooding is to occur.

The bubble cavities within the soil will not all flood simultaneously. As a bubble cavity floods with water, gas diffuses from the cavity to the remaining unflooded bubbles (see Section 5.6, Chapter 5). Diffusion of this additional gas into the remaining bubbles causes an increase of the pressure within these bubbles, thus reducing, at least temporarily, the difference between the gas pressure u_g and the water pressure u_w. This delays any flooding of the remaining bubbles. However, as shearing proceeds the water pressure u_w continues to rise, and further bubble flooding occurs if the limiting condition of Equation 8.22 is reached once more.

The influence of the diffusing gas on the pressure in the remaining bubbles is dependent on the stiffness of the bubbles. This can be demonstrated by considering two bubbles, each at pressure u_{go}. The first bubble is of volume V_1 and contains a mass m_1 of gas, while the second bubble, of volume V_2, contains a mass m_2. By the Gas Law:

$$(u_{go} + p_a) = \frac{m_1 R_a T_a}{V_1} \qquad 8.23$$

$$(u_{go} + p_a) = \frac{m_2 R_a T_a}{V_2} \qquad 8.24$$

R_a is the gas constant and T_a is the absolute temperature. If the first bubble floods and the gas originally within this bubble all diffuses to the second bubble, the final pressure u_{gf} in the second bubble is given by:

$$(u_{gf} + p_a) = \frac{(m_1 + m_2)R_a T_a}{V_2} \qquad 8.25$$

In Equation 8.25 the volume of the second bubble is assumed to remain constant, and any movement of gas into solution is ignored. Subtracting Equation 8.24 from Equation 8.25 gives the change of pressure in the remaining bubble:

$$(u_{gf} - u_{go}) = \frac{m_1 R_a T_a}{V_2} \qquad 8.26$$

Substituting the value of m_1 from Equation 8.23 into Equation 8.26:

$$(u_{gf} - u_{go}) = (u_{go} + p_a) \frac{V_1}{V_2} \qquad 8.27$$

Equation 8.27 indicates that the higher the absolute pressure within the bubbles (i.e. the stiffer the bubbles) the greater is the pressure increase in the remaining bubbles caused by gas diffusing from a flooded bubble of given size.

The analysis presented above suggests that the process of bubble flooding will be dependent on the value of the normalised parameter $(u_{go} + p_a)/\sigma_y$. The higher the value of this parameter the more the pressure in the remaining bubbles would be increased by gas diffusion from a flooded bubble. Therefore, a high value of $(u_{go} + p_a)/\sigma_y$ would tend to inhibit further flooding.

Bubble flooding is also influenced by the solubility coefficient H, because the solubility affects the apparent stiffness of the gas bubbles. Equation 5.11 (Chapter 5) shows that the solubility reduces the long-term

stiffness of the bubbles, and the effect is dependent on the value of the parameter $He_{mo}/(1 + e_{mo})$. A high value of $He_{mo}/(1 + e_{mo})$ would produce a large reduction in the bubble stiffness, and the analysis presented above indicates that this would tend to encourage widespread flooding of the bubbles.

A final parameter affecting the process of bubble flooding is the permeability of the saturated soil matrix. The permeability controls the rate at which water can drain into the bubble cavities from the surrounding matrix. However, the maximum drainage path for the flooding process is likely to be a few bubble diameters, so that the time required for drainage is very short (a few minutes for the samples of Combwich Mud used in the experimental tests). If the shearing takes place over a much longer time period, as was the case in the experimental tests, the flooding process will hardly be affected by the matrix permeability.

8.4.2 Effect of Flooding on the Matrix Properties

When a bubble floods, the water drains into the bubble cavity from the surrounding saturated soil matrix, bringing down the value of the matrix void ratio e_m. This increases the strength of the matrix.

The effect of bubble flooding on the strength of the saturated soil matrix is very difficult to calculate precisely, because it is hard to predict how many of the bubbles will flood during shearing. There is also the problem that the volume of water required to flood a bubble is affected by any change in bubble size which occurs during the shearing process. This latter point can be thought of as the interaction of bubble flooding with the cavity shrinkage described in Section 8.3.

An upper bound to the matrix strength at failure can be computed by assuming that all the bubbles flood with water, and that the bubble cavity size remains unchanged during shearing. These two assumptions maximise

the flow of water from the matrix into the bubble cavities. This gives a minimum value for the matrix void ratio at failure e_{mf}, which leads in turn to a maximum value for the strength of the matrix at failure.

The matrix void ratio after complete bubble flooding can be calculated by considering a volume of soil containing unit volume of solid particles. The volume of soil will contain a volume e_{mo} of water (where e_{mo} is the initial matrix void ratio), so that the initial volume of saturated soil matrix is $(1 + e_{mo})$. The initial volume of gas bubbles will be $(1 + e_{mo})f_o/(1 - f_o)$, because a volume of soil containing unit volume of matrix would contain a volume $f/(1 - f)$ of bubbles. If all the bubbles flood with water, and the bubble cavities do not change in size, a volume $(1 + e_{mo})f_o/(1 - f_o)$ of water must drain from the matrix into the bubble cavities. Therefore the final matrix void ratio e_{mf} is given by:

$$e_{mf} = e_{mo} - \frac{(1 + e_{mo})f_o}{1 - f_o} \qquad 8.28$$

If there is no change in the size of the cavities during flooding there will actually be an increase in the volume fraction of cavities f, because the total volume of the soil must fall as water flows into the cavities. A simple calculation shows that complete bubble flooding with no change in cavity size increases the volume fraction of cavities to a value f_f given by:

$$f_f = \frac{f_o}{1 - f_o} \qquad 8.29$$

The change in matrix void ratio will produce a change in the matrix strength, which can be calculated by using the critical state approach to link the stresses and the void ratio at failure (Schofield and Wroth, 1968). Figure 8.7 shows the failure conditions for the saturated soil matrix represented by a critical state line with a slope λ. If the matrix void ratio remains constant at a value e_{mo}, the mean effective stress within

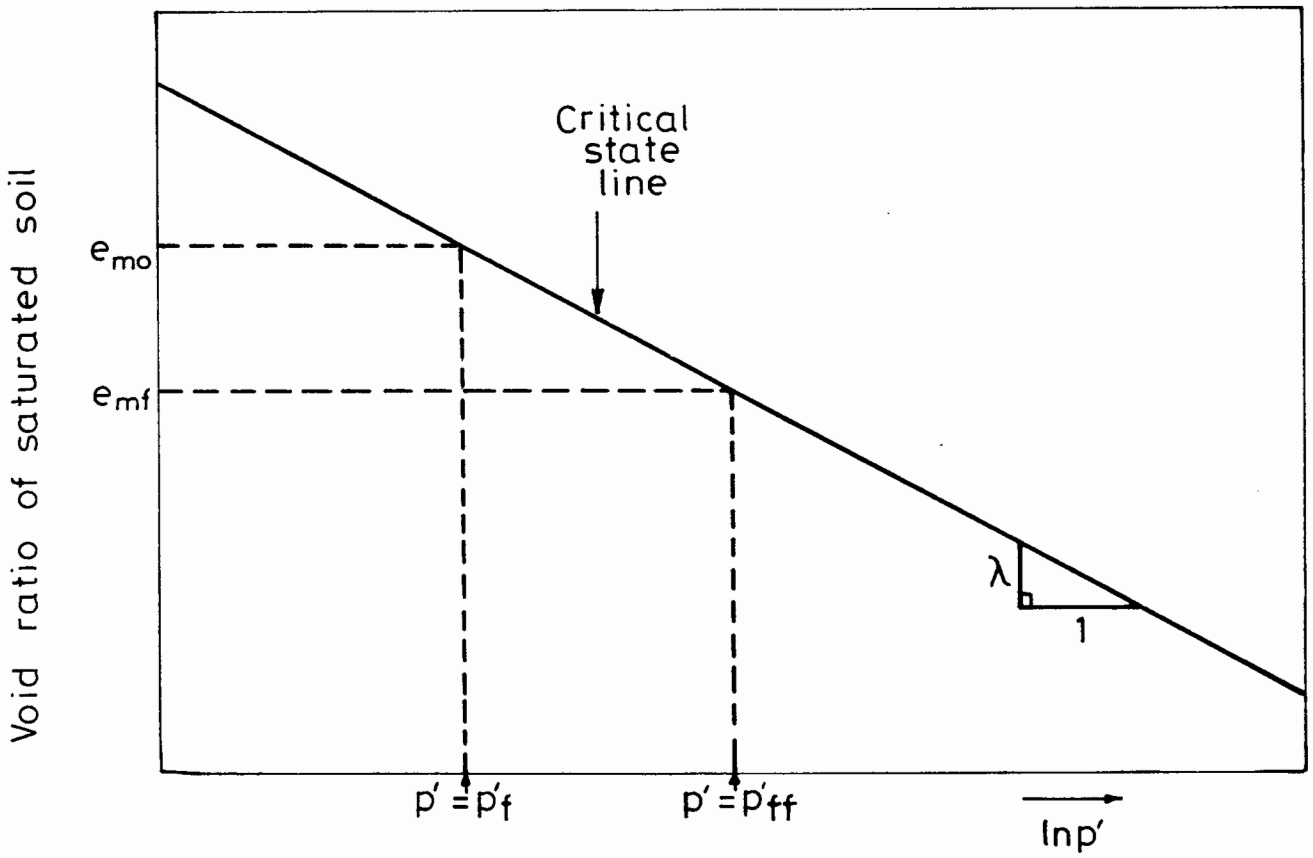

Fig. 8·7. FAILURE CONDITIONS FOR SATURATED SOIL MATRIX.

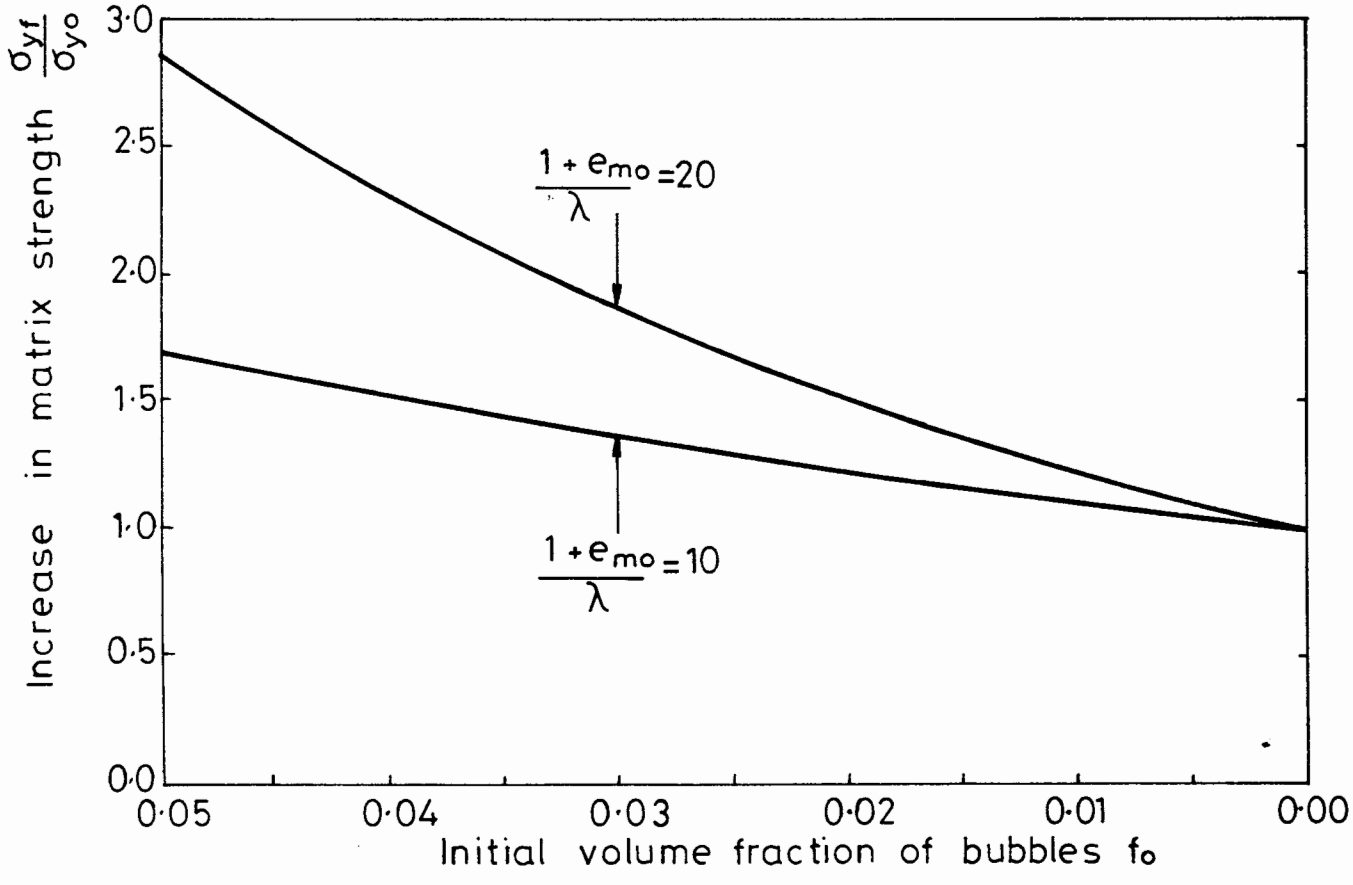

Fig. 8·8 INCREASE IN MATRIX STRENGTH CAUSED BY FLOODING.

the matrix at failure will be p'_f. However if the matrix void ratio falls during shearing to a value e_{mf}, the mean effective stress in the matrix at failure will increase to p'_{ff}. From the geometry of Figure 8.7:

$$p'_{ff} = p'_f \exp\left(\frac{e_{mo} - e_{mf}}{\lambda}\right) \qquad 8.30$$

But critical state theory suggests that the deviator stress at failure is proportional to the mean effective stress at failure for a saturated soil ($q = Mp'$). This means that the uniaxial yield stress of the matrix changes during bubble flooding from an initial value σ_{yo} to a final value σ_{yf}, that is given by:

$$\frac{\sigma_{yf}}{\sigma_{yo}} = \frac{p'_{ff}}{p'_f} \qquad 8.31$$

Substituting Equations 8.28 and 8.30 into Equation 8.31:

$$\sigma_{yf} = \sigma_{yo} \exp\left(\frac{(1 + e_{mo})f_o)}{\lambda(1 - f_o)}\right) \qquad 8.32$$

Figure 8.8 shows σ_{yf}/σ_{yo} plotted against f_o for two different values of the parameter $(1 + e_{mo})/\lambda$, covering the range of values likely to occur in practice. The figure clearly indicates that the flooding process increases the yield stress of the matrix most dramatically when the initial volume fraction of bubbles is large. This appears sensible, because when f_o is high a large volume of water must drain from the matrix to flood all the bubble cavities. The figure also shows that σ_{yf}/σ_{yo} is greatest when the parameter $(1 + e_{mo})/\lambda$ is high. This is because a high value of $(1 + e_{mo})/\lambda$ means that a given volume of water flowing into the bubble cavities causes a large increase in the matrix strength.

The values of σ_{yf} shown in Figure 8.8 are upper bound values, based on the two assumptions that all the bubbles flood with water and the bubble cavities do not change in size. In practice some of the bubbles may not flood during shearing, and the post-yield behaviour means that the bubble

cavities are likely to shrink (see Section 8.3). Therefore, the actual value of the matrix yield stress at failure σ_{yf} is likely to lie between the initial value σ_{yo} and the upper bound value given by Equation 8.32.

8.4.3 Influence of Flooding on the Deviator Stress at Failure

The precise effect of flooding on the applied deviator stress at failure q_f is difficult to calculate. A calculation might be possible if there was complete flooding of all the bubbles. After complete flooding the large bubble model described in Chapter 5 would still apply, with the single difference that the cavities would be filled with water instead of gas. The situation could be analysed as a rigid-perfectly plastic matrix, with a yield stress σ_{yf}, containing a volume fraction f_f of water-filled cavities at a pressure u_{wf}. Therefore an expression for q_f could be derived by modifying the yield curve given in Section 8.2 (Equation 8.15):

$$\left(\frac{3 - 2f_f^{\frac{1}{n}}}{3(1 - f_f^{1/3})}\right)^2\left(\frac{q_f}{\sigma_{yf}}\right)^2 + \left(\frac{3}{2\log_e f_f}\right)^2\left(\frac{\sigma_3 - u_{wf}}{\sigma_{yf}} + \frac{1}{3}\left(\frac{q_f}{\sigma_{yf}}\right)\right)^2 = 1 \qquad 8.33$$

If there was no change in cavity size during the shearing process, the values of f_f and q_{yf} given in Equations 8.29 and 8.32 could be used in Equation 8.33. However, the analysis would still be very difficult, because it would be hard to predict the value of the water pressure after flooding u_{wf}.

The deviator stress at failure would be even more difficult to predict if there was incomplete flooding of the bubbles during shearing. Under these circumstances some of the bubble cavities would be filled with water at a pressure u_w while the remaining cavities would be filled with gas at a different pressure u_g. This situation would obviously be extremely difficult to analyse.

The arguments presented above suggest that it is impossible to derive a rigorous theoretical expression for the effect of bubble flooding on the deviator stress at failure q_f. However, the analysis presented in Sections

8.4.1 and 8.4.2 does indicate some of the parameters that are likely to influence the flooding effect:

$$\text{bubble flooding} = \text{function}\left(f_o, \frac{2T}{R_c\sigma_{yo}}, \frac{u_{go} + p_a}{\sigma_{yo}}, \frac{He_{mo}}{1 + e_{mo}}, \frac{1 + e_{mo}}{\lambda}\right) \qquad 8.34$$

The parameters f_o, $2T/R_c\sigma_{yo}$, $(u_{go} + p_a)/\sigma_{yo}$ and $He_{mo}/(1 + e_{mo})$ control the amount of flooding that takes place, while the parameter $(1 + e_{mo})/\lambda$ determines the effect of this flooding on the yield stress of the matrix.

Any condition that encourages bubble flooding tends to increase the yield stress of the matrix, which is likely in turn to increase the strength of the entire material. Therefore, conditions that might lead to a large increase in q_f would include: low values of $2T/R_c\sigma_{yo}$ and $(u_{go} + p_a)/\sigma_{yo}$; and high values of $He_{mo}/(1 + e_{mo})$. A high value of $(1 + e_{mo})/\lambda$ would also be beneficial, because this would maximise the effect of any bubble flooding on the matrix strength.

8.5 UNDRAINED SHEAR STRENGTH

The undrained shear strength C_u is equal to half the deviator stress at failure q_f. The analysis presented in the previous sections suggests that the values of C_u could be normalised by dividing by the initial yield stress of the saturated soil matrix σ_{yo}. However, the theoretical predictions would be easier to assimilate if C_u could be normalised by dividing by $(C_u)_{sat}$, the undrained shear strength of a saturated soil consolidated to the same stress level. This does not present any additional problems, because $(C_u)_{sat}$ is simply half the value of σ_{yo} (see Section 8.1).

8.5.1 Factors Affecting the Undrained Shear Strength

Derivation of a rigorous expression for the undrained shear strength C_u is impossible, because of the interaction of the post-yield behaviour (described in Section 8.3) and the bubble flooding (described in Section 8.4).

However, the various analyses presented in Sections 8.2 to 8.4 do indicate the parameters that are likely to influence the value of C_u:

$$\frac{C_u}{(C_u)_{sat}} = \text{function}\left[f_o, \frac{\sigma_3 - u_{go}}{(C_u)_{sat}}, \frac{u_{go} + p_a}{(C_u)_{sat}}, \frac{He_{mo}}{1 + e_{mo}}, \frac{2T}{R_c(C_u)_{sat}}, \frac{1 + e_{mo}}{\lambda}\right] \quad 8.35$$

Although it is not possible to derive the precise form of the relationship inferred in Equation 8.35, the work presented in Sections 8.2 to 8.4 can be used to predict whether each of the parameters listed in Equation 8.35 has a positive or a negative effect on the value of $C_u/(C_u)_{sat}$. The analysis of the yield stress, in Section 8.2, indicates that $C_u/(C_u)_{sat}$ would be reduced by increasing the value of $(\sigma_3 - u_{go})/(C_u)_{sat}$. Similarly, Section 8.4 suggests that $C_u/(C_u)_{sat}$ would be increased by either reducing $2T/R_c(C_u)_{sat}$ (which encourages bubble flooding) or increasing $(1 + e_{mo})/\lambda$ (which maximises the effect of bubble flooding). Unfortunately, the same type of prediction cannot be made for the parameters $(u_{go} + p_a)/(C_u)_{sat}$ and $He_{mo}/(1 + e_{mo})$, because each of these parameters has two counteracting effects. Raising $(u_{go} + p_a)/(C_u)_{sat}$ and lowering $He_{mo}/(1 + e_{mo})$ tends to promote the work-hardening effect (Section 8.3), suggesting an increase in $C_u/(C_u)_{sat}$, but at the same time these changes tend to prevent widespread bubble flooding (Section 8.4), suggesting a decrease in $C_u/(C_u)_{sat}$. It is difficult to say which of these two effects would dominate.

8.5.2 Upper and Lower Bound Values

The work-hardening effect and the process of bubble flooding both tend to increase the undrained shear strength. Therefore a lower bound to the value of C_u can be calculated by ignoring both work-hardening and bubble flooding, so that C_u is simply half the value of the yield stress q_y given in Equation 8.15:

$$\left(\frac{3 - 2 f_o^{\frac{1}{4}}}{3(1 - f_o^{1/3})}\right)^2 \left(\frac{C_u}{(C_u)_{sat}}\right)^2 + \left(\frac{3}{2\log_e f_o}\right)^2 \left(\frac{\sigma_3 - u_{go}}{2(C_u)_{sat}} + \frac{C_u}{3(C_u)_{sat}}\right)^2 = 1 \quad 8.36$$

The lower bound value of $C_u/(C_u)_{sat}$ given in Equation 8.36 is dependent on only f_o and $(\sigma_3 - u_{go})/(C_u)_{sat}$.

Figure 8.9 shows the lower bound values of $C_u/(C_u)_{sat}$ plotted against f_o, for two different values of the parameter $(\sigma_3 - u_{go})/(C_u)_{sat}$. The lower bound curves shown in Figure 8.9 are identical to the curves for the normalised yield stress q_y/σ_y shown in Figure 8.1. The lower bound values of $C_u/(C_u)_{sat}$ given by Equation 8.36 are always less than unity.

The post-yield behaviour increases the value of C_u above the lower bound given by Equation 8.36. The work-hardening effect is due to the shrinkage of the bubble cavities, and as the cavities approach total closure the value of C_u tends towards $(C_u)_{sat}$ (see Section 8.3). Therefore, $C_u/(C_u)_{sat}$ can never rise above unity by the action of work-hardening alone.

The process of bubble flooding, described in Section 8.4, may increase $C_u/(C_u)_{sat}$ above unity. The effect of bubble flooding is maximised by complete flooding of all the bubbles.

The interaction of cavity shrinkage (previously referred to as work-hardening) and bubble flooding is complicated. Cavity shrinkage always brings the value of C_u closer to $(C_u)_{sat}$, irrespective of whether bubble flooding has already occurred, because the shrinkage ultimately results in a saturated soil with a void ratio e_{mo}. Therefore, in a situation where complete bubble flooding has increased the strength above $(C_u)_{sat}$, subsequent cavity shrinkage would actually tend to reduce the strength. The physical explanation for this reduction in strength is that shrinkage of water-filled cavities would force water back into the saturated soil matrix, with a consequent weakening of the matrix.

The analysis presented above indicates that an upper bound value of $C_u/(C_u)_{sat}$ can be calculated by assuming that complete bubble flooding occurs with no shrinkage of the cavities during shearing. However, if the upper bound value of $C_u/(C_u)_{sat}$ suggested by this approach is less than unity, it

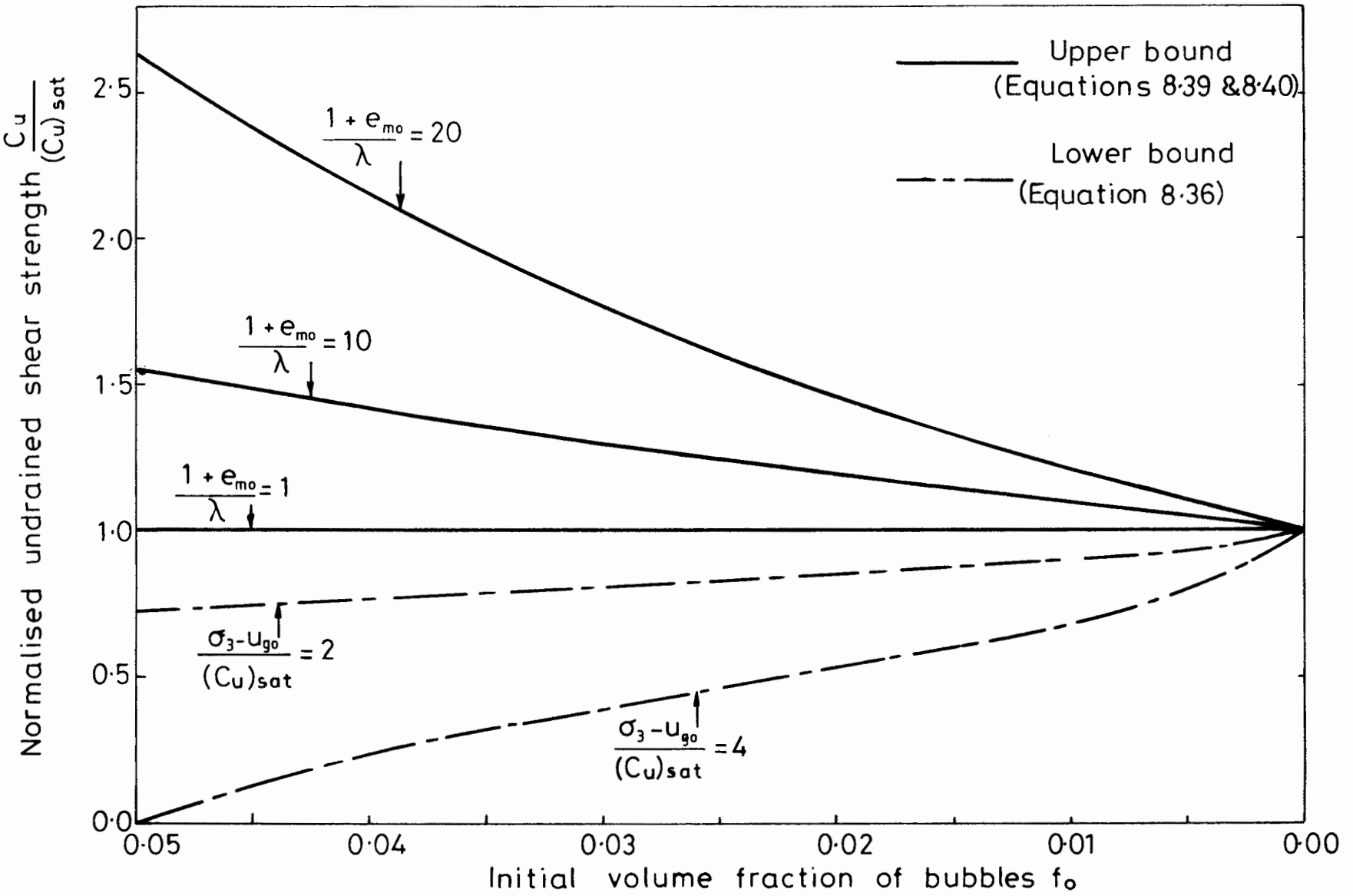

Fig. 8·9. UPPER AND LOWER BOUNDS FOR UNDRAINED SHEAR STRENGTH.

is not valid; and the upper bound to $C_u/(C_u)_{sat}$ is given instead by a value of unity (corresponding to complete closure of the cavities). This is an interesting conclusion. Bubble flooding and cavity shrinkage each tend to increase the value of C_u when acting alone, but the maximum possible value of C_u does not occur when the two processes act simultaneously. Instead the upper bound value of C_u is always given by just one of the processes occurring without interference from the other. This is because each process tends to impair the effect of the other.

The upper bound value of C_u corresponding to complete bubble flooding and no cavity shrinkage can be calculated from Equation 8.33:

$$\left(\frac{3 - 2 f_f^{\frac{1}{4}}}{3(1 - f_f^{1/3})}\right)^2\left(\frac{q_f}{\sigma_{yf}}\right)^2 + \left(\frac{3}{2\log_e f_f}\right)^2\left(\frac{\sigma_3 - u_{wf}}{\sigma_{yf}} + \frac{1}{3}\left(\frac{q_f}{\sigma_{yf}}\right)\right)^2 = 1 \qquad 8.33(a)$$

The values of f_f and σ_{yf} can be substituted from Equations 8.29 and 8.32 into Equation 8.33, but unfortunately the water pressure after flooding u_{wf} is unknown.

As the object of the exercise is to find an upper bound for C_u, the value of u_{wf} used in Equation 8.33 should be the one giving the maximum value of q_f/σ_{yf}. Because of the elliptical shape of the curve defined by Equation 8.33, it is easy to calculate the value of u_{wf} which maximises q_f/σ_{yf}:

$$u_{wf} = \sigma_3 + q_f/3 \qquad 8.37$$

Inserting this value of u_{wf} into Equation 8.33:

$$\left(\frac{3 - 2 f_f^{\frac{1}{4}}}{3(1 - f_f^{1/3})}\right)\left(\frac{q_f}{\sigma_{yf}}\right) = 1 \qquad 8.38$$

Inserting the values of f_f and σ_{yf} from Equations 8.29 and 8.32 into Equation 8.38, and replacing q_f/σ_{yo} with $C_u/(C_u)_{sat}$, produces the following expression:

$$\frac{C_u}{(C_u)_{sat}} = \frac{3(1 - (f_o/(1 - f_o))^{1/3})}{3 - 2(f_o/(1 - f_o))^{\frac{1}{4}}} \exp\left[\frac{(1 + e_{mo})f_o}{\lambda(1 - f_o)}\right] \qquad 8.39$$

Equation 8.39 gives an upper bound for $C_u/(C_u)_{sat}$ corresponding to complete bubble flooding and no cavity shrinkage. This upper bound value is dependent on only f_o and $(1 + e_{mo})/\lambda$.

The alternative upper bound expression for $C_u/(C_u)_{sat}$, corresponding to complete closure of the cavities, is very simple:

$$\frac{C_u}{(C_u)_{sat}} = 1 \qquad 8.40$$

The actual upper bound value of $C_u/(C_u)_{sat}$ is given by either Equation 8.39 or Equation 8.40, whichever is the greater.

Figure 8.9 shows the upper bound values of $C_u/(C_u)_{sat}$ plotted against f_o for three different values of the parameter $(1 + e_{mo})/\lambda$. The two highest values of $(1 + e_{mo})/\lambda$ shown in the figure (10 and 20) can be considered as typical of real soils. For these conditions the upper bound for $C_u/(C_u)_{sat}$ is given by Equation 8.39 over the full range of f_o. However, in the unlikely event of $(1 + e_{mo})/\lambda$ being as low as 1, the upper bound for $C_u/(C_u)_{sat}$ would be given by Equation 8.40 for all but the lowest values of f_o.

8.5.3 Factors Not Taken Into Account

Throughout this chapter various simplifying assumptions have been made, and a number of complicating factors have been ignored. Most of these simplifications were necessary if an analytical approach was to have any success. Hopefully the various factors that have been ignored would only produce second-order effects, so that the general conclusions of the chapter are still valid. However, it is worth considering briefly some of the more important simplifications.

The first simplification was to assume that the saturated soil matrix would be homogeneous at the start of shearing. The previous chapter, on the consolidation behaviour, provided no conclusive evidence on this point, simply indicating that a homogeneous matrix was a reasonable assumption in the absence of any better information. If the matrix was not homogeneous at the start of shearing, this could obviously affect the value of the undrained shear strength. However it is not clear whether the strength would be increased or reduced by any initial heterogeneity.

The second simplification was to ignore any localised consolidation occurring during the shearing process, which could produce further heterogeneity within the matrix. Again it is not immediately obvious whether this localised consolidation would tend to increase or reduce the shear strength.

Another point that was ignored was the variation in matrix yield stress σ_y with the local stress state within the matrix. Many previous authors have shown that the strength of a saturated soil depends upon the value of the intermediate principal stress (Bishop, 1966; Wroth, 1984). For example, the strength in triaxial extension is always less than the strength in triaxial compression. During a triaxial test on a soil containing gas bubbles the saturated soil matrix would not be in a state of uniform triaxial compression, because of the stress concentrations caused by the bubble cavities. This point was illustrated by the analysis of Section 7.2, Chapter 7, which showed that an isotropic stress state applied to the soil boundary would actually produce a state of local triaxial extension in the matrix around each bubble. The variation of σ_y with the local stress state would tend to reduce the value of $C_u/(C_u)_{sat}$, if $(C_u)_{sat}$ was the strength of a saturated soil tested in triaxial compression.

Perhaps the most obvious simplification concerning the saturated soil matrix was to model the matrix as a rigid-perfectly plastic material. In practice the matrix would have a finite stiffness even at very low loads, and matrix deformation would begin as soon as any load was applied. This would complicate the soil behaviour considerably, because cavity shrinkage would occur right from the start of shearing.

The final simplification was to ignore the change in shape of the bubbles that would occur during the shearing process. During a triaxial compression test, spherical bubbles would tend to flatten to an oblate spheroidal shape. This would probably affect the value of the deviator stress required to cause further deformation, with a consequent change in the undrained shear strength. Unfortunately it is not clear whether the strength would be increased or reduced by the change of bubble shape.

The various complicating factors described in this section all tend to influence the value of the undrained shear strength C_u. Therefore, the upper and lower bound values of $C_u/(C_U)_{sat}$ given in Equations 8.36, 8.39 and 8.40 are not completely rigorous. This means that the true values of $C_u/(C_u)_{sat}$ could lie outside these bounds.

Although the undrained shear strength is affected by the complications described in this section, the list of non-dimensional parameters controlling the value of $C_u/(C_u)_{sat}$ (Equation 8.35) may still be reasonably valid. This is because the complicating factors are likely to be controlled mainly by the same set of parameters. Any additional parameters which should be included in Equation 8.35 are likely to have only a second-order effect on the value of $C_u/(C_u)_{sat}$.

CHAPTER 9

COMPARISON OF THEORETICAL AND EXPERIMENTAL RESULTS

CHAPTER 9

COMPARISON OF THEORETICAL AND EXPERIMENTAL RESULTS

In this chapter the theoretical predictions developed in Chapters 5 to 8 are compared with the experimental results presented in Chapter 4.

The layout of the chapter follows the same general pattern as Chapter 4, with the consolidation behaviour presented first, followed by the undrained shear strength, and finally the elastic moduli. It is helpful to consider the consolidation behaviour before the other aspects, because the state of the soil at the end of consolidation affects both the undrained shear strength and the elastic moduli.

9.1 CONSOLIDATION BEHAVIOUR

9.1.1 Isotropic Consolidation

The experimental results presented in Chapter 4 show that the void ratio after isotropic consolidation e_o is dependent on the saturation S_o, with e_o increasing as S_o falls. However, the matrix void ratio e_{mo} is independent of S_o and is purely a function of the consolidation pressure $(\sigma_3 - u_{wo})$ (see Figure 4.5). The theoretical analysis of the large bubble model suggests very much the same behaviour (see Figure 7.9, Chapter 7). This is encouraging evidence of the validity of the large bubble model.

The theoretical analysis actually predicts that the matrix void ratio e_{mo} of a soil containing gas bubbles would be slightly less than the void ratio of a saturated soil consolidated to the same stress level (see Figure 7.7, Chapter 7). It is difficult to say whether this was in fact the case in the series of triaxial tests, because the scatter of the experimental data makes detection of any slight trend very difficult (see Figure 4.4, Chapter 4). The scatter of the data was probably caused by the fact that the experimental apparatus and procedure were designed primarily for measuring undrained shear

strength, and were not ideal for the accurate monitoring of consolidation behaviour.

The pattern of isotropic consolidation behaviour observed in the experimental tests could not have been predicted with a conventional model consisting of small gas bubbles fitting within the normal void spaces. This small bubble model obeys the same effective stress law as a saturated soil, because the gas bubbles simply change the compressibility of the pore fluid (Wheeler, in preparation). Therefore the model would predict a unique relationship between the consolidation pressure and the void ratio e_o, rather than the matrix void ratio e_{mo}.

9.1.2 One-Dimensional Consolidation

The experimental work of Nageswaran (1983) indicated that the matrix void ratio e_{mo} was not quite independent of the saturation level S_o for the case of one-dimensional consolidation. Nageswaran's one-dimensional consolidation results showed that the value of e_{mo} for a soil containing gas bubbles was slightly greater than the void ratio of a saturated soil consolidated to the same stress level (see Figure 1.12, Chapter 1). This subtle trend in the one-dimensional consolidation data was detected because Nageswaran's apparatus provided very accurate measurements of void ratio and degree of saturation (due to the fact that the apparatus was designed specifically for this purpose).

The theoretical analysis of one-dimensional consolidation, presented in Chapter 7, suggests that the matrix void ratio e_{mo} should be either slightly greater or slightly less than the void ratio of the equivalent saturated soil (see Figure 7.8). Therefore the theoretical predictions are consistent with the behaviour observed by Nageswaran.

A difference between the one-dimensional and the isotropic consolidation behaviour is apparent from a comparison of the experimental results of

Nageswaran and the results presented in Chapter 4. For isotropic consolidation there appears to be a unique relationship between e_{mo} and the consolidation pressure (see Figure 4.5), while the relationship is not quite unique for one-dimensional consolidation (see Figure 1.12). It is pleasing to note that the theoretical analysis provides a possible explanation for this difference (see Section 7.3, Chapter 7).

9.2 UNDRAINED SHEAR STRENGTH

Figure 9.1 shows the experimental values of undrained shear strength C_u, which have been normalised by dividing by $(C_u)_{sat}$. In the figure the normalised values are plotted against the initial volume fraction of bubbles f_o, to allow direct comparison with the theoretical predictions presented in Chapter 8.

One of the striking, and previously unexpected, features of the experimental results is that the presence of the gas bubbles reduces the strength of the soil in some circumstances but increases the strength in other circumstances. This pattern of behaviour could not have been predicted by the conventional small bubble model. Small gas bubbles would simply make the pore fluid compressible, so that an undrained test would in effect be partly drained. Therefore small bubbles would always increase the undrained strength of normally consolidated samples (Wheeler, in preparation). However, the theoretical analysis of the large bubble model provides an explanation for the pattern of behaviour observed in the experimental tests. In the absence of bubble flooding, large bubble cavities always have a weakening effect on the soil; but if bubble flooding occurs there may be an increase in strength, because the flooding strengthens the saturated soil matrix. Whether the bubbles actually increase or decrease the soil strength depends upon the relative magnitudes of the weakening effect of the cavities and the strengthening effect of any flooding.

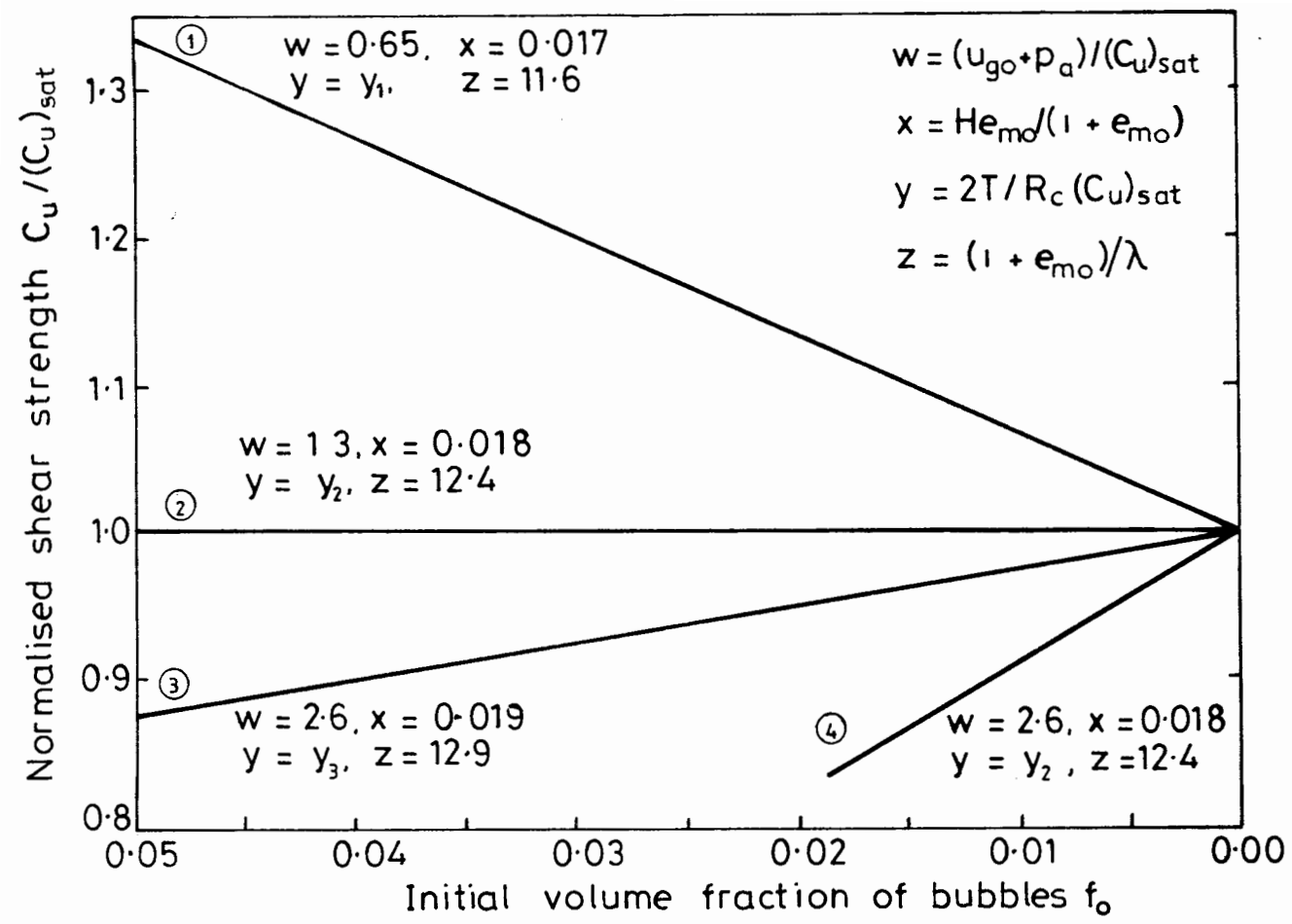

Fig. 9·1. EXPERIMENTAL VALUES OF UNDRAINED SHEAR STRENGTH.

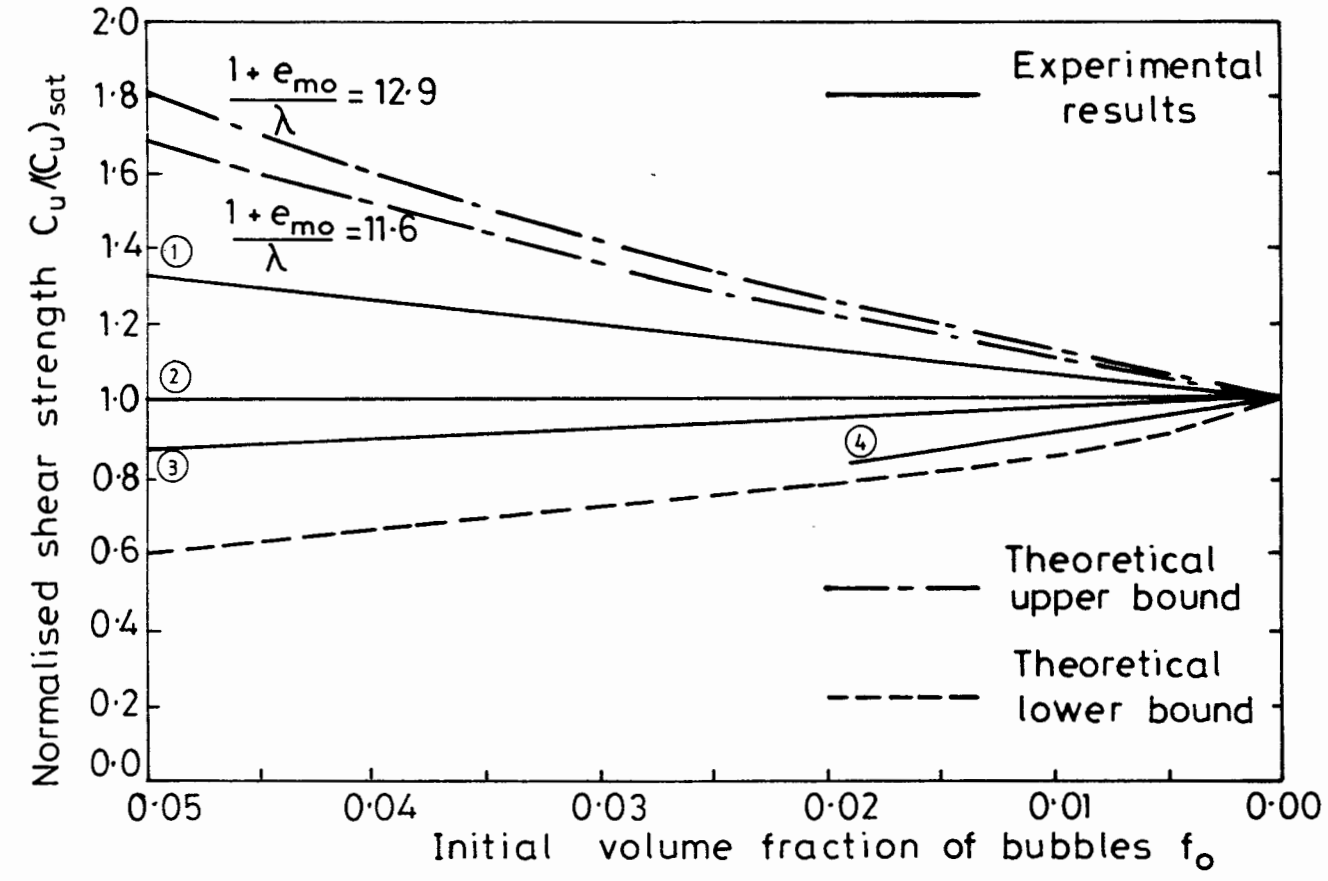

Fig. 9·2. THEORETICAL AND EXPERIMENTAL VALUES OF UNDRAINED SHEAR STRENGTH.

9.2.1 Factors Affecting the Undrained Strength

The theoretical analysis presented in Chapter 8 suggests that the normalised shear strength $C_u/(C_u)_{sat}$ should be dependent on six parameters:

$$\frac{C_u}{(C_u)_{sat}} = \text{function}\left[f_o, \frac{\sigma_3 - u_{go}}{(C_u)_{sat}}, \frac{u_{go} + p_a}{(C_u)_{sat}}, \frac{He_{mo}}{1 + e_{mo}}, \frac{2T}{R_c(C_u)_{sat}}, \frac{1 + e_{mo}}{\lambda}\right] \quad 8.35(a)$$

The parameters $(\sigma_3 - u_{go})/C_u)_{sat}$ and $(u_{go} + p_a)/(C_u)_{sat}$ both involve the initial gas pressure u_{go}, which was not measured directly in the experimental tests. However, the diffusion of gas from the soil during the consolidation stage means that it is probably reasonable to assume that the value of u_{go} was equal to the initial water pressure u_{wo} (see Section 5.3, Chapter 5).

If the initial gas pressure u_{go} was the same as the back pressure u_{wo}, then the pressure difference $(\sigma_3 - u_{go})$ was equal to the consolidation pressure $(\sigma_3 - u_{wo})$. Therefore the parameter $(\sigma_3 - u_{go})/(C_u)_{sat}$ was constant for all the experimental tests, because the denominator $(C_u)_{sat}$ was also proportional to the consolidation pressure. From Figure 4.8:

$$(C_u)_{sat} = 0.38 \quad (\sigma_3 - u_{wo}) \qquad 9.1$$

Therefore:

$$\frac{\sigma_3 - u_{go}}{(C_u)_{sat}} = \frac{1}{0.38} = 2.6 \qquad 9.2$$

Equation 9.2 indicates that the parameter $(\sigma_3 - u_{go})/(C_u)_{sat}$ was equal to 2.6 for all the experimental tests. The values of the other parameters $(u_{go} + p_a)/(C_u)_{sat}$, $He_{mo}/(1 + e_{mo})$ and $(1 + e_{mo})/\lambda$ are marked on the experimental curves shown in Figure 9.1 The parameter $(u_{go} + p_a)/(C_u)_{sat}$ varies from 0.65 for curve 1 to 2.6 for curves 3 and 4. The parameters $He_{mo}/(1 + e_{mo})$ and $(1 + e_{mo})/\lambda$ vary very little between the different curves; the only changes being due to the slight variation of e_{mo} with the consolidation pressure. The value of $(1 + e_{mo})/\lambda$ ranges from 11.6 to 12.9, while $He_{mo}/(1 + e_{mo})$ varies between 0.017 and 0.019. The latter

variation is based on a solubility coefficient H of 0.034, which is the value for methane. However, the analysis presented in Section 5.3 of Chapter 5 suggests that the bubbles may have been filled with air instead of methane by the time the samples were sheared. This would reduce all the values of $He_{mo}/(1 + e_{mo})$ by about 15% ($H = 0.029$ for air).

The experimental values of the final parameter $2T/R_c(C_u)_{sat}$ are difficult to specify, because the minimum radius of curvature of the menisci R_c is unknown. It is likely that R_c is a function of the matrix void ratio e_{mo}, which is a measure of the packing of the soil particles within the saturated soil matrix. The matrix void ratio is, in turn, a function of the consolidation pressure $(\sigma_3 - u_{wo})$. As $(C_u)_{sat}$ is also a function of the consolidation pressure, the parameter $2T/R_c(C_u)_{sat}$ probably depends solely on $(\sigma_3 - u_{wo})$, for a given type of soil. Therefore, in Figure 9.1 $2T/R_c(C_u)_{sat}$ has the same value (y_2) for curves 2 and 4 (for both of which the consolidation pressure was 200 kN/m^2), but has different values (y_1 and y_3) for the remaining curves 1 and 3. It is difficult to say whether $2T/R_c(C_u)_{sat}$ rises or falls with increasing consolidation pressure, because $(C_u)_{sat}$ increases linearly with $(\sigma_3 - u_{wo})$ while R_c decreases at some unknown rate.

The experimental curves presented in Figure 9.1 provide useful information on the effects of the various parameters listed in Equation 8.35. However the interpretation requires some care, because so many of the parameters vary between the different curves.

A comparison of curves 2 and 4 in Figure 9.1 gives a clear indication of the influence of the parameter $(u_{go} + p_a)/(C_u)_{sat}$ on the normalised strength. $(u_{go} + p_a)/(C_u)_{sat}$ has a value of 1.3 on curve 2 and a value of 2.6 on curve 4, while the remaining three variables $He_{mo}/(1 + e_{mo})$, $2T/R_c(C_u)_{sat}$ and $(1 + e_{mo})/\lambda$ have the same values on both curves. Comparing the two curves, it appears that an increase in the value of $(u_{go} + p_a)/(C_u)_{sat}$

reduces the undrained strength of the soil. The theoretical analysis presented in Chapter 8 was rather unclear on the likely influence of $(u_{go} + p_a)/(C_u)_{sat}$, because this parameter has two counteracting effects on the shear behaviour. An increase in $(u_{go} + p_a)/(C_u)_{sat}$ tends to prevent widespread flooding (suggesting a decrease in strength), but also tends to enhance the work-hardening effect (suggesting an increase in strength). The experimental results shown in Figure 9.1 seem to indicate that the influence of $(u_{go} + p_a)/(C_u)_{sat}$ on the bubble flooding is the dominant effect.

The effect of the parameter $He_{mo}/(1 + e_{mo})$ can be inferred from the effect of the previous parameter $(u_{go} + p_a)/(C_u)_{sat}$, because the two parameters both influence the soil behaviour in the same manner, by changing the stiffness of the gas bubbles. The experimental results indicate that the undrained shear strength rises when the gas stiffness is reduced, as described in the preceding paragraph. Therefore, the strength must increase with $He_{mo}/(1 + e_{mo})$, because this parameter reduces the long-term gas stiffness (see Equation 5.11, Chapter 5).

The experimental curves shown in Figure 9.1 do not provide any conclusive evidence on the influence of the two remaining parameters $2T/R_c(C_u)_{sat}$ and $(1 + e_{mo})/\lambda$, because it is impossible to isolate the effects of each parameter. However, the experimental curves are perfectly consistent with the theoretical predictions. This point can be demonstrated best by comparing curves 3 and 4, which both refer to the same value of $(u_{go} + p_a)/(C_u)_{sat}$ (so the effect of this parameter is eliminated). The parameter $He_{mo}/(1 + e_{mo})$ has a value of 0.019 on curve 3 and drops slightly to a value of 0.018 on curve 4. The preceding paragraph suggests that this reduction in $He_{mo}/(1 + e_{mo})$ is partly responsible for the observed reduction in strength between curves 3 and 4. The parameter $(1 + e_{mo})/\lambda$ also has a slightly lower value on curve 4 than on curve 3 (down from 12.9 to 12.4), and the theory indicates that this is

consistent with the drop in strength (see Section 8.5.1, Chapter 8). The final parameter $2T/R_c(C_u)_{sat}$ changes from an unknown value y_3 on curve 3 to another unknown value y_2 on curve 4. It seems likely that the change in this parameter is responsible for a major part of the drop in strength between curves 3 and 4, because the very small changes in the parameters $He_{mo}/(1 + e_{mo})$ and $(1 + e_{mo})/\lambda$ are probably not sufficient to explain the large reduction in strength.

9.2.2 Upper and Lower Bound Values

Figure 9.2 shows the experimental curves of $C_u/(C_u)_{sat}$ plotted on the same axes as the theoretical upper and lower bound curves described in Section 8.5.2, Chapter 8. The theoretical lower bound is dependent solely on the value of $(\sigma_3 - u_{go})/(C_u)_{sat}$. The lower bound curve shown in the figure is for $(\sigma_3 - u_{go})/(C_u)_{sat} = 2.6$ which is applicable to all the experimental results. The theoretical upper bound is dependent on the parameter $(1 + e_{mo})/\lambda$. In the experimental tests $(1 + e_{mo})/\lambda$ varied between 11.6 and 12.9, and the two upper bound curves shown in the figure refer to these extreme values.

The agreement between the experimental results and the theoretical bounds is very pleasing indeed. Figure 9.2 shows that the various experimental curves all fit neatly within the theoretical upper and lower bounds. This provides further confirmation of the validity of the large bubble model.

One interesting point is clearly apparent from the lower bound curve in Figure 9.2. Simple extrapolation of the experimental results would suggest ever decreasing values of normalised strength as the parameter $(u_{go} + p_a)/(C_u)_{sat}$ was increased or the parameters $He_{mo}/(1 + e_{mo})$ and $(1 + e_{mo})/\lambda$ were reduced. However, the theoretical results indicate that curve 4 in Figure 9.2 may already be approaching a limiting condition, and that further changes to the parameters would not reduce the normalised strengths substantially. Full confirmation of this very significant conclusion would require additional experimental data.

When considering the minimum possible value of the undrained shear strength, it is important to remember that the theoretical lower bound expression is not entirely rigorous (see Section 8.5.3, Chapter 8). This means that the normalised strength could actually fall slightly below the lower bound curve illustrated in Figure 9.2. It is also important to note that the lower bound curve shown in the figure is based on the assumption that the initial gas pressure u_{go} is equal to the back pressure u_{wo}. This assumption appears entirely reasonable (see Section 5.3, Chapter 5), but it has not been verified experimentally. The theoretical lower bound curve would change from that shown in the figure if u_{go} was not equal to u_{wo}, because the value of u_{go} affects the parameter $(\sigma_3 - u_{go})/(C_u)_{sat}$.

Figure 9.2 shows that all the experimental values of normalised strength fall considerably below the theoretical upper bound curve. It is unlikely that the normalised strength would ever reach the theoretical upper bound value, because this would only happen if there was no change in the cavity size during the shearing process (see Section 8.5.2, Chapter 8). The finite stiffness of the matrix makes a change in cavity size inevitable.

9.2.3 The Importance of Bubble Flooding

The importance of bubble flooding is clearly apparent from the experimental results shown in Figures 9.1 and 9.2. Without bubble flooding the normalised strength $C_u/(C_u)_{sat}$ could never rise above unity. The occurrence of bubble flooding also explains the fact that the normalised strength increases as $(u_{go} + p_a)/(C_u)_{sat}$ is reduced or $He_{mo}/(1 + e_{mo})$ is increased. In the absence of bubble flooding exactly the opposite effect would be expected.

There is further evidence of the link between high shear strengths and bubble flooding in Figure 4.12 (Chapter 4), which shows the degree of saturation at failure S_f for the various experimental tests. One of the consequences of bubble flooding would be a high value of S_f. The curves presented in

Figure 4.12 indicate that high values of S_f occurred most often in the series of tests with a consolidation pressure of 400 kN/m^2, suggesting that flooding was most widespread in this test series. The values of normalised strength recorded in this series of tests were higher than for any other tests (see curve 1, Figures 9.1 and 9.2).

The bubble flooding also enables two otherwise anomalous features of the soil behaviour to be explained. Both of these features are apparent in the results of those tests where the soil became fully saturated during shearing ($S_f = 1.0$).

The first point concerns the strain required to cause total closure of the bubble cavities. The analysis of the large bubble model presented in Section 8.3, Chapter 8, indicates that the cavities would close only if the true axial strain approached infinity (a nominal compressive strain of 100%). In practice, this means that the large bubble model could never achieve the full saturation observed in some of the experimental tests without the process of bubble flooding.

The second point concerns the strength of the samples that reach full saturation during shearing. The experimental results show that if several samples all reach failure in a saturated state at the same void ratio e_f, they may have widely differing shear strengths (the strength depending upon the initial saturation S_o). This behaviour would be difficulty to understand if the samples were homogeneous, but it is very easy to understand if the samples contain large water-filled cavities at the time of failure (the number or size of the cavities varying with the initial saturation).

9.3 ELASTIC MODULI

In Chapter 6 theoretical expressions were derived for two sets of undrained elastic moduli. These refer to the instantaneous and the long-term behaviour. The long-term moduli $G_{u\ell}$ and $K_{u\ell}$ are probably most

relevant for the series of experimental tests, because the tests were conducted slowly enough to allow both localised consolidation and the movement of gas into solution.

9.3.1 Undrained Shear Modulus

Figure 9.3 shows the experimental values of the normalised shear modulus G_u/G_{sat}. The results are plotted against the initial volume fraction of bubbles f_o, to facilitate comparison with the theoretical predictions.

In Chapter 6 the theoretical values of the undrained shear modulus G_u were normalised by dividing by the shear modulus of the saturated soil matrix G'. However G' is equal to G_{sat}, because the matrix void ratio after consolidation e_{mo} is equal to the void ratio of a saturated soil consolidated to the same stress level. Therefore the normalised curves presented in Chapter 6 can be compared directly with the experimental results. The theoretical curve for G_u/G_{sat} shown in Figure 9.3 is for a soil containing empty cavities ($K_g = 0$). In practice the experimental values of the normalised gas stiffness K_g/G_{sat} varied between 0.005 and 0.02, but these very low gas stiffnesses have no noticeable effect on the theoretical values of G_u/G_{sat}. The theoretical curve in the figure also corresponds to a matrix Poisson's ratio ν' of 0.2, but the curve would change very little for other values of ν'.

Figure 9.3 shows that the theoretical predictions seriously overestimate the shear modulus of a soil containing gas bubbles. This is probably due to the fact that the theoretical expressions for G_u take no account of any bubble flooding. In practice bubble flooding may be quite significant, because the experimental measurements of G_u are secant values taken over fairly large strain increments, so that there was ample opportunity for flooding to occur. Although bubble flooding increases the degee of saturation,

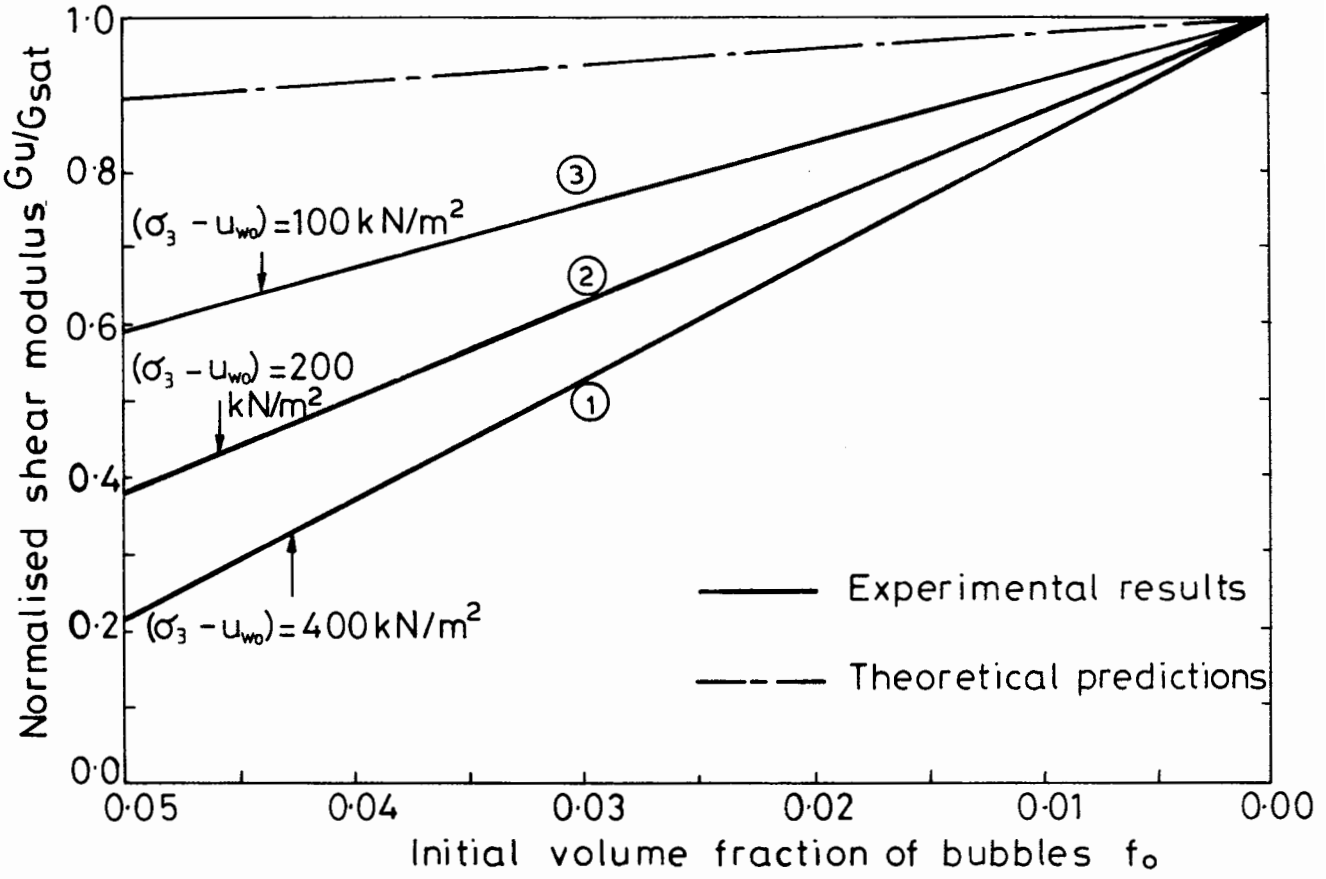

Fig. 9·3. UNDRAINED SHEAR MODULUS.

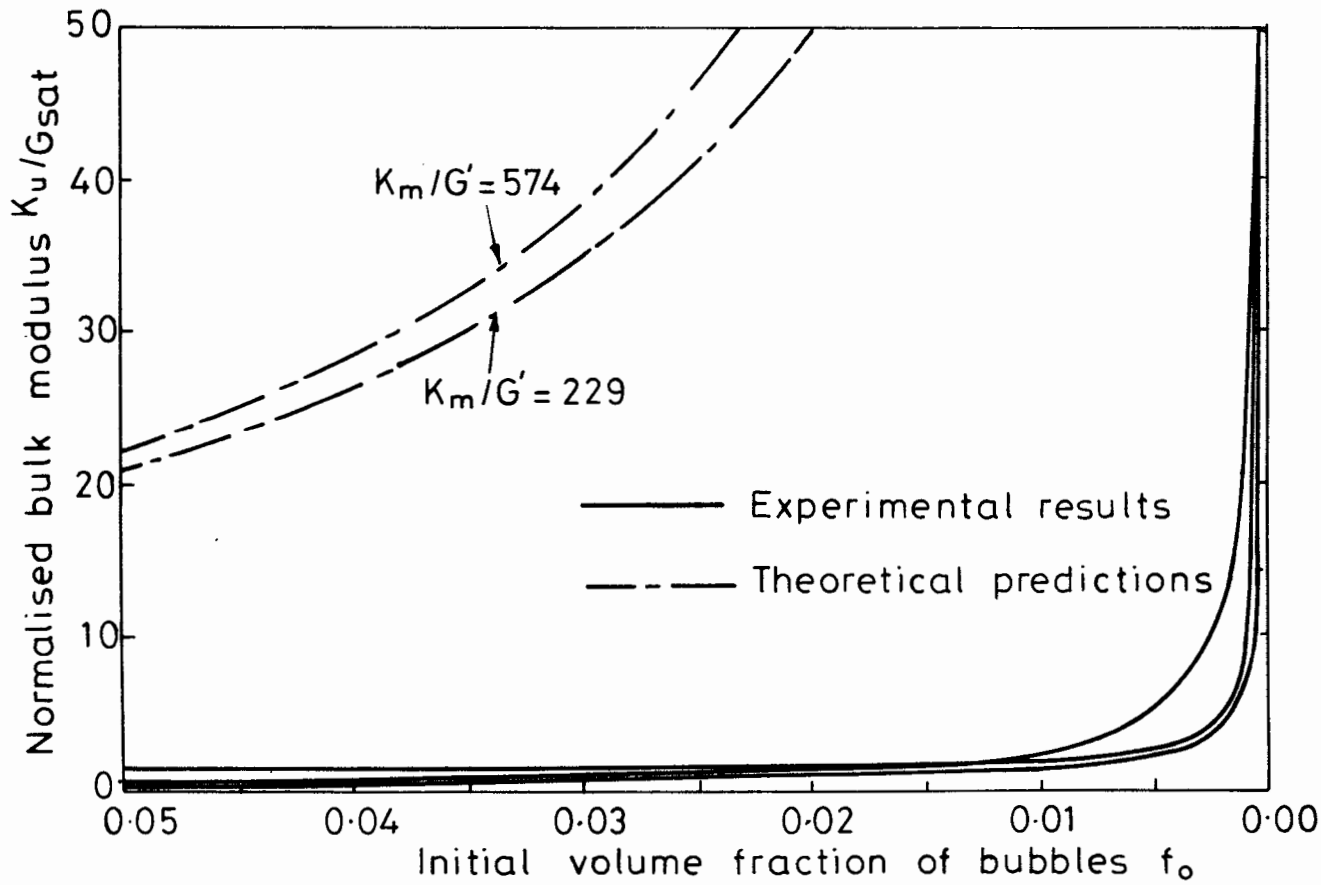

Fig. 9·4 UNDRAINED BULK MODULUS.

the flooding process would not necessarily bring the value of G_u up towards G_{sat}, because the presence of large water-filled cavities means that the soil structure after flooding is not homogenous. As a result the bubble flooding could actually reduce the value of G_u.

Figure 9.3 shows that the experimental values of G_u/G_{sat} are lowest for curve 1, which represents the conditions most suitable for bubble flooding (see Section 9.2.3). This supports the idea that the discrepancies between the theoretical and experimental values of G_u/G_{sat} are due to the effects of flooding.

If experimental values of G_u were measured at very small strains they might show better agreement with the theoretical predictions, because flooding would be unlikely to occur at low strains. Small strain measurement of G_u would require very careful experimental technique, including direct measurement of strain on the sample (Jardine, Symes and Burland, 1984). The theoretical expressions for the elastic moduli might also describe the acoustic behaviour quite well (Anderson and Hampton, 1980), because the strains caused by an acoustic signal would probably be small enough to avoid the problem of bubble flooding.

Although the theoretical predictions of G_u based on the large bubble model are significantly above the values measured in the experimental tests, they are at least a slight improvement on the predictions of the conventional small bubble model. The latter model would suggest that the gas bubbles have no effect whatsoever on the shear modulus, because all shear stresses are carried by the soil skeleton (Wheeler, 1984).

9.3.2 Undrained Bulk Modulus

Figure 9.4 shows the experimental and theoretical values of the normalised bulk modulus K_u/G_{sat} plotted against f_o. Theoretical curves are shown for two values of the normalised matrix bulk modulus K_m/G_{sat}

(229 and 574). These values of K_m/G_{sat} cover the range of conditons that occurred in the experimental tests (K_m was calculated from Equation 6.5, Chapter 6). The experimental values of the normalised gas stiffness K_g/G_{sat} varied between 0.005 and 0.02, but these very low stiffnesses have negligible effect on the theoretical curves.

The curves presented in Figure 9.4 indicate that the theoretical predictions of K_u/G_{sat} are an order of magnitude larger than the measured values. This is very disappointing, and once more is probably a reflection of the fact that the theoretical expressions for K_u take no account of any bubble flooding. The process of bubble flooding would affect the volumetric behaviour very dramatically, reducing the values of K_u considerably from the theoretical predictions.

The conventional small bubble model would actually predict values of K_u that are closer to the experimental values than the large bubble model predictions shown in Figure 9.4 (Wheeler, 1984). However, bearing in mind how poorly the small bubble model describes the other aspects of the soil behaviour, the agreement is probably coincidental.

CHAPTER 10

CONCLUSIONS AND RECOMMENDATIONS

CHAPTER 10

CONCLUSIONS AND RECOMMENDATIONS

This chapter covers the main conclusions of the research described in this thesis, together with recommendations for future work on the behaviour of soils containing gas bubbles.

10.1 CONCLUSIONS

The programme of experimental and theoretical research has provided considerable insight into the behaviour of soils containing gas bubbles. In addition, much has been learnt on the experimental techniques required for the testing of these gas-bearing soils.

10.1.1 Experimental Procedure

The zeolite molecular sieve technique for forming gas bubbles within reconstituted soil samples has proved to be highly successful at low back pressures. However, the present technique is unsuitable for producing gassy samples under high back pressures (see Section 4.1, Chapter 4).

The modified triaxial apparatus designed and built for the experimental testing programme has also been very successful. The apparatus, which is described in Chapter 2, allows changes of sample volume to be monitored throughout a test, so that the degree of saturation can be calculated at any point in the test (in addition to all the measurements available from a conventional triaxial test). Using the experimental procedure outlined in Chapter 3, the saturation S can be measured to an accuracy of ± 0.0025 ($\pm 0.25\%$ if the saturation is expressed as a percentage).

The experimental tests were conducted too fast to allow full equalisation of pore water pressure throughout each sample. The time required for this equalisation appeared to be much greater for the samples containing a considerable volume of gas bubbles than was the case for the saturated or near-saturated samples (see Section 4.7, Chapter 4). The lack of equalisation

meant that the measurements of pore water pressure u_w were rather suspect. An obvious improvement in any future programme of tests would be to conduct the tests more slowly, so that better accuracy would be achieved in the measurements of pore water pressure.

The direct measurement of pore gas pressure u_g was not possible in the experimental tests, and measurement of u_g will continue to be a problem in any future work on soils containing discrete gas bubbles (see Section 2.8, Chapter 2). However, the variation of gas pressure can be inferred from the change of sample volume, if the initial gas pressure u_{go} is known (see Section 3.8, Chapter 3).

10.1.2 Isotropic Consolidation Behaviour

The experimental results show that, for a given value of consolidation pressure $(\sigma_3 - u_{wo})$, the void ratio after isotropic consolidation e_o is dependent on the degree of saturation S_o. As S_o falls the value of e_o rises. However the product of saturation and void ratio $S_o e_o$ is independent of the value of S_o and is solely a function of the consolidation pressure (see Section 4.2, Chapter 4).

The predictions of the theoretical model described in Chapter 5, show reasonable agreement with the consolidation behaviour observed in the experimental tests. The model consists of large spherical gas bubbles surrounded by a matrix of saturated soil, and the analysis presented in Chapter 7 suggests that the matrix void ratio after consolidation e_{mo} (which is equal to the product $S_o e_o$) should be purely a function of the consolidation pressure.

10.1.3 Undrained Shear Strength

The experimental results indicate that the undrained shear strength C_u can be either increased or decreased by the presence of the gas bubbles, depending upon the values of the consolidation pressure $(\sigma_3 - u_{wo})$ and the initial pore water pressure u_{wo} (the back pressure). The effects of the gas

bubbles on the undrained strength are most detrimental when $(\sigma_3 - u_{wo})$ is low and u_{wo} is high (see Section 4.4, Chapter 4).

The theoretical analysis of the large bubble model presented in Chapter 8 suggests that the normalised strength $Cu/(Cu)_{sat}$ is a function of six non-dimensional parameters:

$$\frac{C_u}{(C_u)_{sat}} = \text{function}\left[f_o, \frac{\sigma_3 - u_{go}}{(C_u)_{sat}}, \frac{u_{go} + p_a}{(C_u)_{sat}}, \frac{He_{mo}}{1 + e_{mo}}, \frac{2T}{R_c(C_u)_{sat}}, \frac{1 + e_{mo}}{\lambda} \right] \quad 8.35(b)$$

These predictions are entirely consistent with the experimental results. Included in the theoretical analysis of the undrained shear strength is the effect of bubble flooding, as water drains from the saturated soil matrix into the bubble cavities. The experimental results confirm the importance of this bubble flooding process.

The theoretical analysis of the large bubble model suggests upper and lower bound values for the normalised strength $C_u/(C_u)_{sat}$ (see Section 8.5.2, Chapter 8). These theoretical expressions fit the experimental results very well, with the various experimental curves all falling between the theoretical bounds (see Section 9.2.2, Chapter 9).

10.1.4 Elastic Moduli

The experimental results provide secant values for the undrained elastic moduli G_u and K_u. The results show that both G_u and K_u are reduced by the presence of gas bubbles, with the reduction in bulk modulus K_u being particularly dramatic.

The analysis of the large bubble model overestimates considerably the values of both G_u and K_u (see Section 9.3, Chapter 9). This is because the theoretical analysis takes no account of any bubble flooding. The process of bubble flooding is likely to have a significant effect on the elastic moduli, if the moduli are measured as secant values over a large increment of strain.

10.2 RECOMMENDATIONS FOR FUTURE WORK

The experimental and theoretical developments reported in this thesis have resulted in a better understanding of the behaviour of soils containing gas bubbles. However, many questions are still unanswered, and there are several lines of research which could usefully be pursued in the future. These future research opportunities include laboratory tests, theoretical developments and field-work.

10.2.1 Laboratory Tests

The experimental tests documented in this thesis cover only one type of soil (Combwich Mud) containing bubbles of only one type of gas (methane). It is obviously important to confirm that the general pattern of behaviour observed in these tests also applies to other types of soil and other gases. This is one of the objectives of a research project which has just started at the Queen's University of Belfast.

The main objective of the new research programme at Belfast is to examine further the effect of gas bubbles on the undrained shear strength. In particular, the new project is concerned with the influence of the parameter $(u_{go} + p_a)/(C_u)_{sat}$, and what happens to the undrained strength when the value of this parameter is increased above the maximum level achieved in the current study. In the seabed $(u_{go} + p_a)/(C_u)_{sat}$ could easily exceed 20, whereas the maximum value reached in the laboratory tests was only 2.6. The theoretical work suggests that the shear strength should reach a limiting lower bound value as the parameter $(u_{go} + p_a)/(C_u)_{sat}$ is increased (see Section 9.2.2, Chapter 9), and it is important to see whether this limiting effect actually occurs in practice.

Testing at high values of $(u_{go} + p_a)/(C_u)_{sat}$ will require a change to the sample preparation technique, so that samples containing gas bubbles can be produced at higher back pressures. In the present technique the gas

is released during the initial one-dimensional consolidation stage, when the back pressure is zero, and this limits the amount of gas that can be introduced into the soil (see Section 4.1, Chapter 4). The first approach to this problem will be to try and delay the release of most of the gas until the sample is under a back pressure in the triaxial cell. This will be achieved by the combination of a different zeolite (which releases the gas more slowly) and a faster-draining soil (so that the one-dimensional consolidation takes less time). If this approach fails, it may be possible to solve the problem by applying a back pressure throughout the one-dimensional consolidation stage. However this would require very sophisticated experimental apparatus, as the back pressure would have to be maintained during the transfer from the one-dimensional mould to the triaxial cell.

Another objective of the new research programme at Belfast is to examine the influence of the parameter $(\sigma_3 - u_{go})/(C_u)_{sat}$ on the undrained strength. The theoretical analysis suggests that this parameter should have an important effect on the strength (see Section 8.2, Chapter 8). The present study did not provide any experimental verification of this point, because the parameter $(\sigma_3 - u_{go})/(C_u)_{sat}$ was constant in all the tests. This was due to the fact that both $(\sigma_3 - u_{go})$ and $(C_u)_{sat}$ were proportional to the consolidation pressure $(\sigma_3 - u_{wo})$ (see Section 9.2.1, Chapter 9).

There are at least three ways of varying the parameter $(\sigma_3 - u_{go})/(C_u)_{sat}$. Firstly, slight variation in the parameter could be achieved without any change in the experimental procedure, simply by varying the soil type (different soils would have different values of $(C_u)_{sat}$ for a given consolidation pressure). Secondly, $(\sigma_3 - u_{go})/(C_u)_{sat}$ could be reduced by using overconsolidated samples, which would have higher values of $(C_u)_{sat}$ than normally consolidated samples at the same value of $(\sigma_3 - u_{wo})$. However, the most versatile and realistic way of varying the parameter $(\sigma_3 - u_{go})/(C_u)_{sat}$ would be to change the experimental procedure so that the initial gas pressure u_{go} could be

varied without changing the initial water pressure u_{wo}. This could probably be achieved by using the arrangement shown in Figure 10.1, with the air-water interface on the drainage line positioned some distance h above the triaxial cell. During the consolidation stage the gas would be expected to diffuse from the sample, up the drainage line to the interface, until the pressure within the bubbles was equal to the interface pressure. If this occurred, the initial gas pressure u_{go} would be given by:

$$u_{go} = u_{wo} - h\gamma_w \qquad 10.1$$

The arrangement shown in Figure 10.1 would be a good representation of the situation that actually occurs in the marine environment. After gas generation ceases within the seabed the bubble pressure falls towards zero as the gas diffuses to the atmosphere (see Section 5.3, Chapter 5).

In addition to the work on the undrained shear strength, it would be useful to investigate the strength under drained conditions. A research project looking at just this problem is about to start at Oxford. Drained tests with a variety of different stress paths will provide fundamental information on the failure conditions for soils containing gas bubbles.

Another useful development would be a more detailed experimental study of the elastic moduli. In particular, it would be instructive to look at the behaviour at very small strains and the behaviour during unload-reload tests (see Section 9.3, Chapter 9). This would require high quality measurements of axial and lateral strain directly on the sample (Jardine, Symes and Burland, 1984). An important aspect of such a study would be a careful examination of the influence of bubble flooding on the elastic behaviour, including an investigation of the factors controlling the strain (or stress) at which flooding first occurs.

A programme of experimental measurements of the elastic moduli would be highly complementary to work currently in progress at Oxford on the acoustic

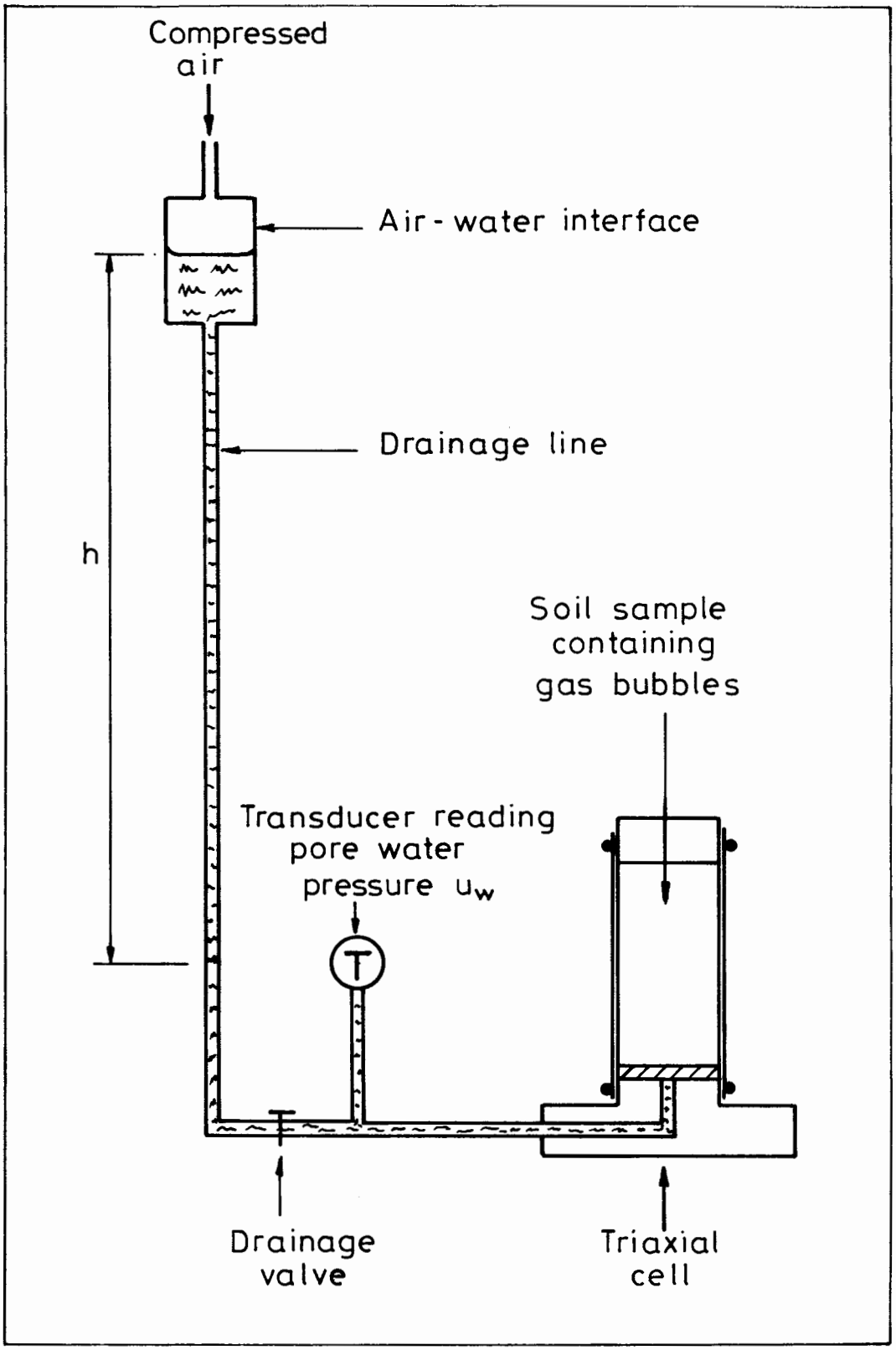

Fig. 10-1. MODIFIED EXPERIMENTAL LAYOUT.

response of soils containing gas bubbles, because the sound speed is dependent on the elastic moduli of the soil (Anderson and Hampton, 1980). The work at Oxford may ultimately lead to the development of an acoustic probe for use in the marine environment. This probe could be used both to detect the presence of gas bubbles in the seabed and to measure the degree of saturation in-situ.

Another part of the programme of laboratory work presently being undertaken at Oxford is a detailed examination of the structure of soils containing gas bubbles with an electron microscope. Prior to viewing under the microscope the soil is impregnated with a resin which fills all the void spaces, including any bubble cavities. When the resin sets, polished samples of the soil can be prepared for viewing under the microscope. This work should provide some indication of whether the theoretical large bubble model developed in this thesis is a reasonable approximation of the true soil structure.

10.2.2 Theoretical Developments

The theoretical analysis of the undrained shear strength presented in Chapter 8 would be improved if some allowance could be made for the deformation of the bubble cavities from spherical during shearing (see Section 8.5.3). This is a problem which will be tackled as part of the new research project at Belfast. It should be possible to calculate the approximate change of shape by developing the work of Rice and Tracey (1969), who analysed the changing shape of initially spherical empty cavities in a rigid-perfectly plastic matrix. The effect on the undrained strength of this change in cavity shape would be very hard to calculate precisely. However, Kahlow and Avitzur (1974) managed an approximate analysis of the effect of the length : diameter ratio of cylindrical cavities, and their work should at least indicate whether the strength would be increased or reduced by the change in cavity shape.

A complete analysis of the shear strength of a rigid-perfectly plastic matrix containing gas-filled cavities would have to include the effects of cavity shrinkage and change of cavity shape, both of which would occur after the initial yield. This would probably require a numerical method. It would be interesting to look at the possibility of using either the finite element method or the method of characteristics for analysing the behaviour of the large bubble model.

A numerical analysis could be simplified by assuming that the bubbles were arranged in a regular three-dimensional grid pattern. Because of the symmetry of this situation, it would be possible to consider just a unit cell consisting of one bubble and the surrounding matrix material. Ideally the analysis should be for a spherical bubble, using an axi-symmetric formulation of the problem. Failing this, a two-dimensional analysis of the plane-strain behaviour of a cylindrical cavity within a rigid-perfectly plastic matrix might at least give some indication of the likely behaviour. In fact, the plane-strain problem has been largely covered by Needleman (1972), who conducted a finite element analysis of a material containing empty cylindrical cavities. A plane-strain analysis would also have certain similarities with the work of Davis et al (1980), who studied the problem of tunnel collapse by using the upper and lower bound theorems of plasticity (a cylindrical bubble cavity is just a scaled-down version of a tunnel).

The major limitation of a numerical analysis in which the matrix is modelled as a simple rigid-perfectly plastic material is that no account can be taken of the bubble flooding process. The drainage of water from the matrix during bubble flooding causes a change in matrix strength, and this can only be analysed properly by using a critical state model for the matrix (see Section 8.4.2, Chapter 8). To analyse the flooding process correctly, a numerical model must also cover a volume of soil containing several bubble cavities, because an analysis of only a single bubble could not take any

account of the progressive nature of bubble flooding (see Section 8.4.1, Chapter 8). To prevent all the bubbles flooding simultaneously in the numerical analysis, the flooding criterion would have to vary slightly from bubble to bubble.

The arguments presented above suggest that the ideal numerical approach would be a three-dimensional finite element model consisting of several bubble cavities within a critical state matrix. This model would have the additional advantage that it could take full account of the heterogeneities that would build up in the matrix because of localised consolidation during the shearing process. Unfortunately, such a model would be very difficult to set up. However, it would be interesting to have a look at the numerical modelling approach, to see what progress could be made in this direction.

As well as improvements to the analysis of the undrained shear strength, theoretical developments would also be useful in other areas. The theoretical analysis of the elastic moduli could be drastically improved if there was some way of taking account of the effects of bubble flooding. Hopefully this problem will be tackled as part of the continuing research at Belfast.

The theoretical work currently in progress at Oxford includes an attempt to model the consolidation behaviour of soils containing gas bubbles by using a finite element approach . The study is concerned with the entire time-dependent process of consolidation, rather than just the initial and final conditions analysed in Chapter 7 of this thesis. A rigorous anlaysis of the consolidation process is extremely difficult, as the governing equation derived by Biot (1941) must be modified to take account of factors such as the movement of dissolved gas and the localised consolidation around each bubble.

10.2.3 Field-Work

The major conclusions of the theoretical and laboratory based research should be checked by conducting tests on real marine soils containing gas

bubbles. Ideally these tests should be conducted in-situ, to avoid the severe problems of sampling disturbance described in Section 1.2 of Chapter 1. However, a comprehensive programme of field testing is probably best delayed until a reliable method has been developed for measuring the in-situ degree of saturation. Hopefully the work at Oxford on the acoustic behaviour will ultimately provide a solution to this problem.

REFERENCES

Aitchison, G.D. and Bishop, A.W. (1960). Discussion. Pore pressure and suction in soils. Butterworths, London. p 150.

Anderson, A.L. and Hampton, L.D. (1980). Acoustics of gas-bearing sediments. J. Acoust. Soc. Am., Vol. 67, No. 6, pp 1865-1903.

Atkinson, J.H. and Bransby, P.L. (1978). The mechanics of soils: An Introduction to critical state soil mechanics. McGraw-Hill, London.

Barden, L. and Sides, G.R. (1967). The diffusion of air through the pore water of soils. Proc. 3rd Asian Reg. Conf. Soil Mech. Found. Eng., Vol. 1, pp 135-138.

Barden, L. and Sides, G.R. (1970). Engineering behaviour and structure of compacted clay. Proc. ASCE, Vol. 96, No. SM4, pp 1171-1200.

Bea, R.G. and Arnold, P. (1973). Movements and forces developed by wave induced slides in soft clays. Offshore Tech. Conf., Houston.

Bennett, R.H. (1977). Pore Water pressure measurements: Mississippi Delta submarine sediments. Marine Geotechnology, Vol. 2, pp 177-189.

Biot, M.A. (1941). General theory of three-dimensional consolidation. J. Appl. Phys., Vol. 12, pp 155-164.

Bishop, A.W. (1959). The principle of effective stress. Tek. Ukeblad, Vol. 39, pp 859-863.

Bishop, A.W. (1960). The measurement of pore pressure in the triaxial test. Pore pressure and suction in soils. Butterworths, London. pp 38-46.

Bishop, A.W. (1966). 6th Rankine Lecture: The strength of soils as engineering materials. Geotechnique, Vol. 16, No. 2, pp 89-130.

Bishop, A.W. and Blight, G.E. (1963). Some aspects of effective stress in saturated and partly saturated soils. Geotechnique, Vol. 13, No. 3, pp 177-197.

Bishop, A.W. and Donald, I.B. (1961). The experimental study of partly saturated soils in the triaxial apparatus. Proc. 5th Int. Conf. Soil Mech. Found. Eng., Paris, pp 13-21.

Bishop, A.W. and Henkel, D.J. (1962). The measurement of soil properties in the triaxial test. William Arnold, London, 2nd edition.

Blanchard, D.C. and Woodcock, A.H. (1956). Bubble formation and modification in the sea and its meteorological significance. Tellus, Vol. 9, No. 2, pp 145-158.

Breck, D.W. (1974). Zeolite molecular sieves: structure, chemistry and use. John Wiley and Sons.

Bridgman, P.W. (1944). The stress distribution at the neck of a tension specimen. Trans. Am. Soc. Metals, Vol. 32, pp 553-574.

Budiansky, B. (1965). On the elastic moduli of some heterogeneous materials. J. Mech. Phys. Solids, Vol. 13, pp 223-227.

Burland, J.B. (1964). Correspondence: Effective stresses in partly saturated soils. Geotechnique, Vol. 14, No. 1, pp 64-68.

Burland, J.B. and Symes, M. (1982). A simple axial displacement gauge for use in the triaxial apparatus. Geotechnique, Vol. 32, No. 1, pp 62-65.

Calladine, C.R. (1969). Engineering plasticity. Pergamon Press.

Chadwick, P. (1959). The quasi-static expansion of a spherical cavity in metals and ideal soils. Quart. J. Mech. Appl. Math., Vol. 12, Pt. 1.

Chang, C.S. and Duncan, J.M. (1983). Consolidation analysis for partly saturated clay by using an elastic-plastic effective stress-strain model. Int. J. Num. Anal. Methods Geomech., Vol. 7, No. 1, pp 39-55.

Claypool, G.E. and Kaplan, I.R. (1974). The origin and distribution of methane in marine sediments. Natural gases in marine sediments, Ed. I.R. Kaplan. Plenum Press. pp 99-139.

Cole, D.M. (1978). A technique for measuring radial deformation during repeated load triaxial tests. Can. Geotech. J., Vol. 15, pp 426-429.

Coleman, J.M. and Prior, D.B. (1978). Submarine landslides in the Mississippi River Delta. 10th Offshore Tech. Conf., Houston. pp 1067-1074.

Davis, E.H., Gunn, M.J., Mair, R.J. and Seneviratne, N. (1980). The stability of shallow tunnels and underground openings in cohesive material. Geotechnique, Vol. 30, pp 397-416.

Donald, I.B. (1960). Discussion session 1: General principles and laboratory measurements. Pore pressure and suction in soils. Butterworths, London. pp 69-70.

Duncan, A.R. and Pantin, H.M. (1969). Evidence for submarine geothermal activity in the Bay of Plenty. N.Z. Journal of Marine and Freshwater Res., Vol. 3, No. 4, pp 602-606.

Eshelby, J.D. (1957). The determination of the elastic field of an ellipsoidal inclusion and related problems. Proc. Roy. Soc., A241, pp 376-396.

Esrig, M.I. and Kirby, R.C. (1977). Implications of gas content for predicting the stability of submarine slopes. Marine Geotechnology, Vol. 2, pp 81-100.

Fannin, N.G.T. (1979). IGS pockmark investigations 1974-1978. IGS Report No. 98.

Fieser, L.F. and Fieser, M. (1967). Reagents for organic synthesis. Vol. 1. John Wiley and Sons. pp 703-705.

Fredlund, D.G. (1975). A diffused air volume indicator for unsaturated soils. Can. Geotech. J., Vol. 12, pp 533-539.

Fredlund, D.G. (1979). 2nd Canadian Geotechnical Colloqium: Appropriate concepts and technology for unsaturated soils. Can. Geotech. J., Vol. 16, pp 121-139.

Fredlund, D.G. (1985). Soil mechanics principles that embrace unsaturated soils. Proc. 11th Int. Conf. Soil Mech. Found. Eng., San Francisco, Vol. 2, pp 465-472.

Fredlund, D.G. and Morgenstern, N.R. (1976). Constitutive relations for volume change in unsaturated soils. Can. Geotech. J., Vol. 13, pp 261-276.

Fredlund, D.G. and Morgenstern, N.R. (1977). Stress state variables for unsaturated soils. Proc. ASCE, Vol. 103, No. GT5, pp 447-466.

Fredlund, D.G.,Morgenstern, N.R. and Widger, R.A. (1978). The shear strength of unsaturated soils. Can. Geotech. J., Vol. 15, pp 313-321.

Gibson, R.E., England, G.L. and Hussey, M.J.L. (1967). The theory of one-dimensional consolidation of saturated clays. Geotechnique, Vol. 17, pp 261-273.

Goodier, J.N. (1933). Concentrations of stress around spherical and cylindrical inclusions and flaws. Applied Mechanics (later known at J. Appl. Mech.), ASME, Vol. 1, pp 39-44.

Graham, J. and Houlsby, G.T. (1983). Anisotropic elasticity of a natural clay. Geotechnique, Vol. 33, No. 2, pp 165-180.

Green, R.J. (1972). A plasticity theory for porous solids. Int. J. Mech. Sci., Vol. 14, pp 215-224.

Grindley, J. (1955). River Thames pollution: The evolution of gas from the bottom deposits of the estuary. Dock and Harbour Authority, Vol. 36, pp 79-80.

Gurson, A.L. (1977). Continuum theory of ductile rupture by void nucleation and growth: Part 1 - Yield criteria and flow rules for porous ductile media. J. Eng. Mat. Tech., ASME, Series H. Vol. 99, pp 2-15.

Haward, R.N. and Owen, D.R.J. (1973). The yielding of a two-dimensional void assembly in an organic glass. J. Mat. Sci., Vol. 8, pp 1136-1144.

Haynes, R. (1971). Effect of porosity content on the tensile strength of porous materials. Powder Metallurgy, Vol. 14, No. 27, pp 64-70.

Hill, R. (1965). A self-consistent mechanics of composite materials. J. Mech. Phys. Solids, Vol. 13, pp 213-222.

Hirst, T.J. and Richards, A.F. (1977). In-situ pore pressure measurement in Mississippi Delta Front sediments. Marine Geotechnology, Vol. 2, pp 191-204.

Jardine, R.J., Symes, M.J. and Burland, J.B. (1984). The measurement of soil stiffness in the triaxial apparatus. Geotechnique, Vol. 34, No. 3, pp 323-340.

Jennings, J.E. (1960). A revised effective stress law for use in the prediction of the behaviour of unsaturated soils. Pore pressure and suction in soils. Butterworths, London. pp 26-30.

Jennings, J.E.B. and Burland, J.B. (1962). Limitations to the use of effective stresses in partly saturated soil. Geotechnique, Vol. 12, No. 2, pp 125-144.

Kahlow, K.J. and Avitzur, B. (1974). Void behaviour as influenced by pressure and plastic deformation. Trans. ASME, Series B, Vol. 96, pp 901-911.

Keife, H. and Ståhlberg, U. (1980). Influence of internal pressure in voids on the yield stress of metals. Int. J. Mech. Sci., Vol. 22, pp 441-446.

Kuhn, H.A. and Downey, C.L. (1971). Deformation characteristics and plasticity theory of sintered powder materials. Int. J. Powder Metallurgy, Vol. 1, pp 15-25.

Lloret, A. and Alonso, E.E. (1985). State surfaces for partially saturated soils. Proc. 11th Int. Conf. Soil Mech. Found. Eng., San Francisco, Vol. 2, pp 557-562.

Loudon, P.A. (1967). Some deformation characteristics of Kaolin. PhD thesis, Cambridge University.

Love, A.E.H. (1959). A treatise on the mathematical theory of elasticity. 4th edition. Cambridge University Press.

MacKenzie, J.K. (1950). The elastic constants of a solid containing spherical holes. Proc. Phys. Soc., Series B, Vol. 63, No. 2, pp 2-11.

Martens, C.S. and Berner, R.A. (1974). Methane production in the interstitial waters of sulphate-depleted marine sediments. Science, Vol. 185, pp 1167-1169.

Massey, B.S. (1975). Mechanics of fluids. 3rd edition. Van Nostrand and Reinhold.

Matyas, E.L. and Radhakrishna, H.S. (1968). Volume change characteristics of partially saturated soils. Geotechnique, Vol. 18, No. 4, pp 432-448.

McCartney, B.S. and Bary, B. McK. (1965). Echo-sounding on probable gas bubbles from the bottom of Saanich Inlet, British Columbia. Deep Sea Res., Vol. 12, pp 285-294.

McClintock, F.A. (1968). A criterion for ductile fracture by the growth of holes. Trans. ASME, Series E, Vol. 35, pp 363-371.

Mechalas, B.J. (1974). Pathways and environmental requirements for biogenic gas production. Natural gases in marine sediments, Ed. I.R. Kaplan. Plenum Press. pp 11-25.

Nageswaran, S. (1983). Effect of gas bubbles on the sea bed behaviour. D.Phil. thesis, Oxford University.

Nageswaran, S. and Houlsby, G.T. (1982). A study of consolidation with radial drainage. Proc. Workshop on implementation of critical state soil mechanics in finite element computations, Cambridge.

Nagpal, V., McClintock, F.A., Berg, C.A. and Subudhi, M. (1972). Traction-displacement boundary conditions for plastic fracture by hole growth. Trans. Int. Symp. on Foundations of Plasticity, Vol. 1, (A. Sawczuk, ed.), pp 365-385.

Needleman, A. (1972). Void growth in an elastic-plastic medium. J. Appl. Mech., ASME, Series E, Vol. 39, pp 964-970.

Okusa, S. (1985). Wave-induced stresses in unsaturated submarine sediments. Geotechnique, Vol. 35, No. 4, pp 517-532.

Pascoe, K.J. (1978). The properties of engineering materials. 3rd edition. Van Nostrand Reinhold. pp 216-218.

Prior, D.B. and Suhayda, J.N. (1979). Application of infinite slope analysis to subaqueous sediment instability, Mississippi Delta. Eng. Geology, Vol. 14, pp 1-10.

Rice, J.R. and Tracey, D.M. (1969). On the ductile enlargement of voids in triaxial stress fields. J. Mech. Phys. Solids, Vol. 17, pp 201-207.

Roscoe, K.H. and Burland, J.B. (1968). On the generalised stress-strain behaviour of 'wet' clay. In Engineering Plasticity (Eds. J. Heyman and F.A. Leckie). Cambridge University Press. pp 535-609.

Rowe, P.W. and Barden, L. (1964). Importance of free ends in triaxial testing. Proc. ASCE, Vol. 90, No. SM1, pp 1-27.

Schofield, A.N. and Wroth, C.P. (1968). Critical state soil mechanics. McGraw-Hill, London.

Schubel, J.R. (1974). Gas bubbles and the acoustically inpenetrable, or turbid, character of some estuarine sediments. Natural gases in marine sediments. Ed. I.R. Kaplan, Plenum Press. pp 275-298.

Schuurman, E. (1966). The compressibility of an air-water mixture and a theoretical relation between the air and water pressures. Geotechnique, Vol. 16, No. 4, pp 269-281.

Shima, S. and Oyane, M. (1976). Plasticity theory for porous metals. Int. J. Mech. Sci., Vol. 18, pp 285-291.

Sieck, H.C. (1973). Gas-charged sediment cores pose possible hazard to offshore drilling. Oil and Gas Journal, Vol. 71, No. 29, pp 148-163.

Skempton, A.W. (1960). Effective stress in soils, concrete and rocks. Pore pressure and suction in soils. Butterworths, London, pp 4-16.

Sills, G.C. and Austin, G. (1982). Pore pressure measurement in a sea-bed containing gas bubbles. Oxford Univ. Dept. Eng. Sci. Report No. SMO 28/82.

Sills, G.C. and Nageswaran, S. (1984). Compressibility of gassy soil. Oceanology Int. Exhib. Conf., Brighton, Soc. Underwater Tech., O.I.2.6.

Sills, G.C. and Nageswaran, S. (in preparation). Characteristic behaviour of laboratory prepared gassy soil. Accepted for publication by ASTM Geotech. Testing J.

Sparks, A.D.W. (1963). Theoretical considerations of stress equations for partly saturated soils. Proc. 3rd African Conf. Soil Mech. Found. Eng., Salisbury, Rhodesia, Vol. 1, pp 215-218.

Terzaghi, K. (1923). Die berechnung der durchlaessigkeitsziffer des tones aus dem verlauf der hydrodynamischen spannungsercheinungen. (Calculation of the porosity index of clay from hydrodynamic pressure conditions). Sitzbericht (Abt. 3a), Akademie der Wissenschaften, Vienna. p 132.

Terzaghi, K. (1936). The shearing resistance of saturated soils and the angle between the planes of shear. Proc. 1st Int. Conf. Soil Mech. Vol. 1, pp 54-56.

Terzaghi,K. (1944). Theoretical soil mechanics. John Wiley, pp 305-308.

Teunissen, J.A.M. (1982). Mechanics of a fluid-gas mixture in a porous medium. Mech. of Mat., Vol. 1, pp 229-237.

Vesic, A.S. (1972). Expansion of cavities in infinite soil mass. Proc. ASCE, Vol. 98, No. SM3, pp 265-290.

Walsh, J.B. and Brace, W.F. (1966). Elasticity of rock: A review of some recent theoretical studies. Rock Mech. Eng. Geol., Vol. 4, No. 4, pp 283-297.

Weast, R.C. (1984). Handbook of chemistry and physics. 65th edition. CRC Press Inc., Florida, pF-32.

Wheeler, S.J. (1984). The elastic moduli of soils containing gas bubbles: a theoretical study. Oxford Univ. Dept. Eng. Sci. Report No. SMO 47/84.

Wheeler, S.J. (1986). Soils containing gas bubbles: a review. Oxford Univ. Dept. Eng. Sci. Report No. SMO 63/86.

Wheeler, S.J. (in preparation). A model for soils containing small gas bubbles. Oxford Univ. Dept. Eng. Sci. Report.

Whelan, T. III, Coleman, J.M., Roberts, H.H. and Suhayda, J.N. (1976). The occurence of methane in recent deltaic sediments and its effect on soil stability. Bull. Int. Assoc. Eng. Geol., No. 14, pp 55-64.

Whelan, T. III, Coleman, J.M. and Suhayda, J.N. (1975). The geochemistry of Recent Mississippi River Delta sediments: Gas concentration and sediment stability. 7th Offshore Tech. Conf., Houston, pp 71-83.

Whelan, T. III, Coleman, J.M., Suhayda, J.N. and Roberts, H.H. (1977). Acoustical penetration and shear strength in gas-charged sediment. Marine Geotechnology, Vol. 2, pp 147-159.

Whelan, T. III, and Lester, G.D. (1980). Excess gas bubble pressures in modern Mississippi Delta sediments. The Delta Project, Vol. 4, pp 1-9.

Wood, D.M. (1979). The behaviour of partly saturated soils: A review. Cambridge Univ. Dept. Eng. Report CUED/D - Soils /TR69 1979.

Wroth, C.P. (1984). 24th Rankine Lecture: The interpretation of in-situ soil tests. Geotechnique, Vol. 34, No. 4, pp 449-489.

Wroth, C.P. and Houlsby, G.T. (1985). Soil mechanics: Property characterization and analysis procedures. Proc. 11th Int. Conf. Soil Mech. Found. Eng., San Francisco, Vol. 1, pp 1-55.

Wroth, C.P. Randolph, M.F., Houlsby, G.T. and Fahey, M. (1984). A review of the engineering properties of soils with particular reference to the shear modulus. Oxford Univ. Dept. Eng. Sci. Report No. 1523/84.

Wyman, J. Jr., Scholander, P.F., Edwards, G.A. and Irving, L. (1952). On the stability of gas bubbles in sea water. J. Marine Res., Vol. 11 , pp 47-62.

APPENDIX

ELASTIC STRESS FIELDS IN A MATERIAL WITH SPHERICAL GAS-FILLED CAVITIES

Goodier (1933) studied the behaviour of an elastic material consisting of spherical inclusions with shear modulus G_1 and Poisson's ratio ν_1 in a matrix with moduli G_2 and ν_2. (Goodier actually used the subscripts 1 and 2 in the reverse order, but this is not consistent with the convention adopted earlier in this thesis).

Figure A.1 shows the polar co-ordinate system used by Goodier (1933). He calculated the stresses in the matrix as the sum of two components: the stress resulting from the application of the same boundary stresses to a complete matrix (without any inclusions); and the perturbation caused by the presence of the inclusions. For a uniaxial boundary stress increment $\Delta\sigma$ applied in the z direction, the perturbation components of the normal stress increments are given by Goodier as:

$$\left.\begin{aligned}
(\Delta\sigma_{rr})^p &= 2G_2\left\{\frac{2A}{r^3} - \frac{2C\nu_2}{(1-2\nu_2)r^3} + \frac{12B}{r^5} - \left[\frac{2C(5-\nu_2)}{(1-2\nu_2)r^3} - \frac{36B}{r^5}\right]\cos 2\theta\right\} \\
(\Delta\sigma_{\theta\theta})^p &= 2G_2\left\{-\frac{A}{r^3} - \frac{2C\nu_2}{(1-2\nu_2)r^3} - \frac{3B}{r^5} + \left[\frac{C}{r^3} - \frac{21B}{r^5}\right]\cos 2\theta\right\} \\
(\Delta\sigma_{\psi\psi})^p &= 2G_2\left\{-\frac{A}{r^3} - \frac{2C(1-\nu_2)}{(1-2\nu_2)r^3} - \frac{9B}{r^5} + \left[\frac{3C}{r^3} - \frac{15B}{r^5}\right]\cos 2\theta\right\}
\end{aligned}\right\} \quad \text{A.1}$$

Where the terms A, B and C are defined by:

$$\left.\begin{aligned}
\frac{A}{a^3} = &\frac{-\Delta\sigma(G_2-G_1)\{2G_2(1-\nu_1)(6-5\nu_2) + G_1(3+19\nu_1-20\nu_1\nu_2)\}}{8G_2\{G_2(7-5\nu_2)+G_1(8-10\nu_2)\}\{2G_2(1-2\nu_1)+G_1(1+\nu_1)\}} \\
&+ \frac{\Delta\sigma\{G_1(1-\nu_2-2\nu_1\nu_2) - G_2(1+\nu_2)(1-2\nu_1)\}}{4G_2(1+\nu_2)\{2G_2(1-2\nu_1)+G_1(1+\nu_1)\}}
\end{aligned}\right\} \quad \text{A.2}$$

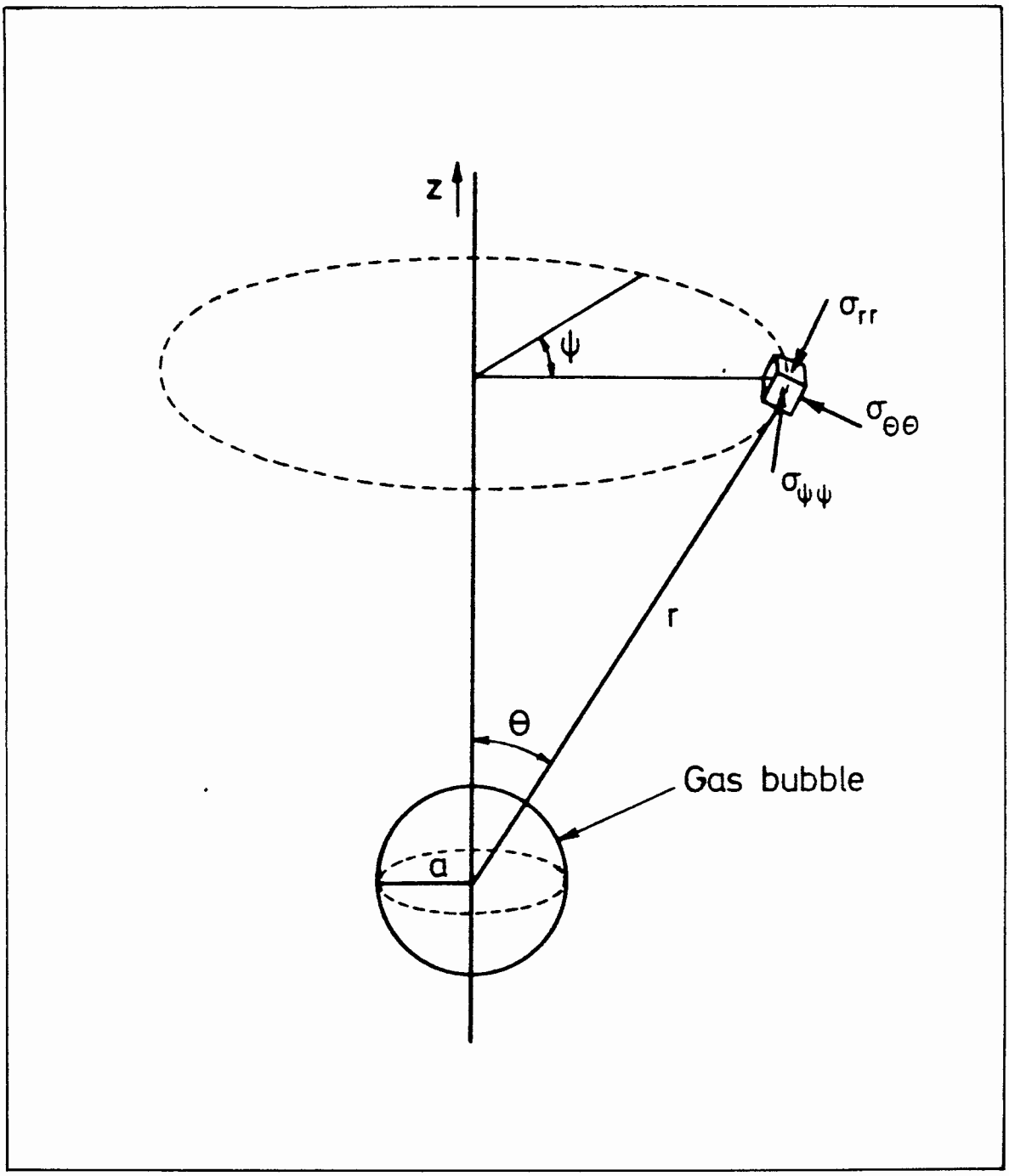

Fig. A.1. POLAR COORDINATE SYSTEM USED BY GOODIER.

$$\left.\begin{aligned} \frac{B}{a^5} &= \frac{\Delta\sigma(G_2 - G_1)}{8G_2\{G_2(7 - 5\nu_2) + G_1(8 - 10\nu_2)\}} \\ \frac{C}{a^3} &= \frac{5\Delta\sigma(G_2 - G_1)(1 - 2\nu_2)}{8G_2\{G_2(7 - 5\nu_2) + G_1(8 - 10\nu_2)\}} \end{aligned}\right\} \quad \text{A.2}$$

If the compressibility of the water can be ignored, then for a soil containing large gas bubbles the moduli of the inclusions and matrix are given by:

$$G_1 = 0, \quad \nu_1 = \tfrac{1}{2}, \quad G_2 = G', \quad \nu_2 = \tfrac{1}{2} \qquad \text{A.3}$$

It is important to note that while both G_1 and $(1 - 2\nu_1)$ are zero, the term $G_1/(1 - 2\nu_1)$ is non-zero and finite, and equal to K_g. Similarly, although the constant C is zero, the term $C/(1 - 2\nu_2)$, which occurs quite frequently in Equation A.1, is non-zero and finite.

Substituting from Equation A.3 into Equations A.1 and A.2, the perturbation components of the normal stress increments can be calculated:

$$\left.\begin{aligned} (\Delta\sigma_{rr})^p &= \frac{\Delta\sigma a^3}{6r^3}\left[\frac{-(28G' + 15K_g)}{4G' + 3K_g} + \frac{4a^2}{r^2} - \frac{(15r^2 - 12a^2)}{r^2}\cos 2\theta\right] \\ (\Delta\sigma_{\theta\theta})^p &= \frac{\Delta\sigma a^3}{6r^3}\left[\frac{4G'}{4G' + 3K_g} - \frac{a^2}{r^2} - \frac{7a^2}{r^2}\cos 2\theta\right] \\ (\Delta\sigma_{\psi\psi})^p &= \frac{\Delta\sigma a^3}{6r^3}\left[\frac{4G'}{4G' + 3K_g} - \frac{3a^2}{r^2} - \frac{5a^2}{r^2}\cos 2\theta\right] \end{aligned}\right\} \quad \text{A.4}$$

The expressions given in Equation A.4 can be superposed to calculate the stress fields resulting from the application at the sample boundary of either a hydrostatic stress or an axisymmetric pure shear stress.

A hydrostatic boundary stress increment Δp is equivalent to three mutually perpendicular uniaxial stress increments of magnitude Δp. Therefore, under these conditions the stress increments within the matrix will be given by:

$$\left.\begin{aligned} \Delta\sigma_{rr} &= \Delta p + (\Delta\sigma_{rr})^{p}_{\Delta p,\ \theta} + (\Delta\sigma_{rr})^{p}_{\Delta p,\ \frac{\pi}{2} - \theta} + (\Delta\sigma_{rr})^{p}_{\Delta p,\ \frac{\pi}{2}} \\ \Delta\sigma_{\theta\theta} &= \Delta\sigma_{\psi\psi} = \Delta p + (\Delta\sigma_{\theta\theta})^{p}_{\Delta p,\ \theta} + (\Delta\sigma_{\theta\theta})^{p}_{\Delta p,\ \frac{\pi}{2} - \theta} + (\Delta\sigma_{\psi\psi})^{p}_{\Delta p,\ \frac{\pi}{2}} \end{aligned}\right\} \quad A.5$$

Where $(\Delta\sigma_{rr})^{p}_{\Delta p,\ \frac{\pi}{2}}$ is the value of $(\Delta\sigma_{rr})^{p}$ given by Equation A.4 when $\Delta\sigma = \Delta p$ and $\theta = \frac{\pi}{2}$. In each of the relationships of Equation A.5, the first term on the right hand side is the stress increment that would occur in the absence of any cavities, while the remaining terms are the perturbation effects of the cavities on each of the three perpendicular boundary stresses.

Substituting from Equation A.4 into Equation A.5:

$$\left.\begin{aligned} \Delta\sigma_{rr} &= \Delta p\left[1 - \frac{a^3}{r^3(\,1 + 3K_g/4G')}\right] \\ \Delta\sigma_{\theta\theta} &= \Delta\sigma_{\psi\psi} = \Delta p\left[1 + \frac{a^3}{2r^3(1 + 3K_g/4G')}\right] \end{aligned}\right\} \quad A.6$$

The increment $\Delta p_{\star}$ of the local mean total stress within the matrix is given by:

$$\Delta p_{\star} = \frac{\Delta\sigma_{rr} + \Delta\sigma_{\theta\theta} \quad \Delta\sigma_{\psi\psi}}{3} \qquad A.7$$

Therefore, substituting from Equation A.6 into Equation A.7:

$$\Delta p_{\star} = \Delta p \qquad A.8$$

Equation A.8 shows that the increment of mean total stress is constant throughout the matrix, when a hydrostatic stress is applied to the soil boundary.

An increment of axisymmetric pure shear Δq can be considered as three mutually perpendicular uniaxial stresses of magnitude $2\Delta q/3$, $-\Delta q/3$ and $-\Delta q/3$. Therefore the stress increments produced in the matrix, by an increment of pure shear Δq applied to the boundary, are given by:

$$\left.\begin{aligned}
\Delta\sigma_{rr} &= \frac{\Delta q(1 + 3\cos 2\theta)}{6} + (\Delta\sigma_{rr})^{p}_{2\Delta q/3,\ \theta} + (\Delta\sigma_{rr})^{p}_{-\Delta q/3,\ \frac{\pi}{2}-\theta} + (\Delta\sigma_{rr})^{p}_{-\Delta q/3,\ \frac{\pi}{2}} \\
\Delta\sigma_{\theta\theta} &= \frac{\Delta q(1 - 3\cos 2\theta)}{6} + (\Delta\sigma_{\theta\theta})^{p}_{2\Delta q/3,\ \theta} + (\Delta\sigma_{\theta\theta})^{p}_{-\Delta q/3,\ \frac{\pi}{2}-\theta} + (\Delta\sigma_{\psi\psi})^{p}_{-\Delta q/3,\ \frac{\pi}{2}} \\
\Delta\sigma_{\psi\psi} &= \frac{-\Delta q}{3} + (\Delta\sigma_{\psi\psi})^{p}_{2\Delta q/3,\ \theta} + (\Delta\sigma_{\psi\psi})^{p}_{-\Delta q/3,\ \frac{\pi}{2}-\theta} + (\Delta\sigma_{\theta\theta})^{p}_{-\Delta q/3,\ \frac{\pi}{2}}
\end{aligned}\right\} \quad \text{A.9}$$

Again, the first term on the right hand side of each relationship of Equation A.9 is the stress that would occur in the absence of any cavities, while the remaining terms are the perturbation effects.

Substituting from Equation A.4 into Equation A.9:

$$\left.\begin{aligned}
\Delta\sigma_{rr} &= \frac{\Delta q}{6}\left[1 - \frac{a^3(5 - 4a^2/r^2)}{r^3}\right](1 + 3\cos 2\theta) \\
\Delta\sigma_{\theta\theta} &= \frac{\Delta q}{6}\left[1 - 3\cos 2\theta - \frac{a^5(1 + 7\cos 2\theta)}{r^5}\right] \\
\Delta\sigma_{\psi\psi} &= \frac{\Delta q}{6}\left[-2 - \frac{a^5(3 + 5\cos 2\theta)}{r^5}\right]
\end{aligned}\right\} \quad \text{A.10}$$

Substituting from Equation A.10 into Equation A.7, the increment of the local mean total stress is given by:

$$\Delta p_{\star} = \frac{-5\Delta q a^3(1 + 3\cos 2\theta)}{18\, r^3} \qquad \text{A.11}$$

Equation A.11 shows that the application of an axisymmetric pure shear stress to the boundary of a sample results in a pattern of mean total stress throughout the matrix which varies with θ, the direction from the nearest bubble centre, and decays with the third power of r, the distance from the bubble centre.